Mechanistic Studies for Catalytic Transformation of Small Oxygenates on Transition Metals

By

Suyash Singh

A dissertation submitted in partial fulfillment of
the requirements for the degree of

Doctor of Philosophy
(Chemical and Biological Engineering)

at the
University of Wisconsin-Madison
2014

Date of final oral examination: October 08, 2014

The dissertation is approved by the following members of the Final Oral Committee:

Manos Mavrikakis, Professor, Chemical and Biological Engineering
James A. Dumesic, Professor, Chemical and Biological Engineering
Christos T. Maravelias, Professor, Chemical and Biological Engineering
George W. Huber, Professor, Chemical and Biological Engineering
Ive Hermans, Associate Professor, Chemistry and Chemical and Biological Engineering

Abstract

Over the past century, heterogeneous catalysis has played a central role in the development of efficient chemical processes for the conversion of fossil resources to fuels and chemicals, and identification of new, sustainable routes to upgrade renewable carbon sources that minimize the ecological footprint. More recently, unprecedented advances in electronic structure theory and related computational methods have provided a major thrust to the efforts that utilize density function theory (DFT) calculations for developing fundamental atomic-level understanding of these processes, and subsequently designing new and improved catalysts.

In this dissertation, a combined theoretical and experimental approach is presented to study the reaction mechanisms for the catalytic conversion of formic acid (FA) and propylene oxide on transition metals. An iterative methodology comprising of DFT calculations, reaction kinetics measurements, and mean-field microkinetic modeling is employed to determine the nature of active sites on supported catalysts, explain the experimentally observed trends, and obtain predictions for the surface environment under reaction conditions. A detailed analysis of the DFT derived thermochemistry and kinetics parameters over a wide range of transition metal surfaces is performed to identify the key reactivity descriptors for FA decomposition on transition metal catalysts, and develop semi-empirical linear correlations that are then used to develop a microkinetic modeling based framework for the identification and design of improved (active and selective) bimetallic alloy catalysts. Finally, the possible utilization and applications of these methods and ideas in other key chemical transformations are proposed, and suggestions for future work are included.

Acknowledgements

As I complete my journey from being a dependent to an interdependent researcher, I take this opportunity to express the deep sense of gratitude that I feel for some exceptional individuals that have influenced my life, both personally and professionally, over the last 5 years.

First and foremost, I am supremely thankful to my adviser, Professor Manos Mavrikakis, for taking me under his wing and being a constant source of support, motivation, guidance, and inspiration throughout my graduate studies. His immense knowledge and expertise in the field of surface science and catalysis, uncompromising work ethics, and an infectious passion and enthusiasm for research has shaped me into a technically competent researcher, and I will forever cherish his genuinely kind and compassionate nature; it has been an absolute honor working with him and I look forward to the time when our paths cross again in future.

I would like to thank Prof. Dumesic, Prof. Klingenberg and Prof. Maravelias for serving on my preliminary committee, and Prof. Huber and Prof. Hermans for joining them on my dissertation defense committee. I am particularly indebted to Prof. Dumesic, for sharing his insights and knowledge with me during various stages of my PhD; I have greatly appreciated and benefited from the interactions that I have had with him over the years.

I have also had the pleasure to collaborate with several graduate students and researchers, both within and outside the group. I would like to thank the Institute of Atom Efficient Chemical Transformation (IACT), not only for proving the funding for my graduate studies, but also for giving me the opportunity to interact with leaders in the field of catalysis on a monthly basis. Special thanks are due to Lisa, Ronald, Jey, Brandon, and Luke; they have been excellent collaborators and are responsible for part of the data presented in this thesis.

I am grateful for the camaraderie that I have shared with the past and present Mavrikakis group members: Jeff and Guowen, for all the technical help and advice during the early stages of my PhD; Tricia and Lang for putting up with me in the office; Ahmed, Yunhai, Lisa, Jey, Tony, Luke and Fuat for the collegiality we had over the years; and Srini, for the several discussions that we had during my final year, and for sundry reasons.

I feel blessed to have developed several lasting and rewarding friendships outside work; Yan, Gretchen, Abhijeet, Tushar, Dennis, and Kyle have been great friends and have made my stay in Madison very pleasing and delightful. Special thanks to Fulya, my beloved, best friend, and confidante, for being a source of inspiration and support every day for the last four years.

Finally, I wish to thank my brother, Kushagra Singh, and my parents, Dr. Anil Pratap Singh and Dr. Sushma Singh; I owe them everything.

Table of Contents

List of Figures

List of Tables

Chapter 1

Introduction

1.1 Context and Motivation

The ever increasing global energy consumption and demands,[1] limited and depleting fossil fuel reserves,[2] and stringent environmental mandates have led to two major challenges facing the chemical and energy sector in the 21st century (1) developing novel sustainable processes from renewable carbon sources that reduce or eliminate dependence on fossil based resources while minimizing the carbon footprint, and (2) improving the efficiency of existing processes that convert fossil resources into a broad range of chemicals and fuels, by decreasing the energy consumption and developing more selective processes that generate fewer waste products.

Heterogeneous catalysis has been at the center of innovative developments in these areas over the last century; a few classic examples that underscore its contribution include the Haber-Bosch process[3, 4] that features an iron based catalyst for the production of fertilizers, the use of zeolite catalysts in the fluid catalytic cracking for the production of petroleum products such as gasoline, and the adoption of precious-metals based three-way catalysts in the internal combustion engines of gasoline and diesel driven vehicles.[5] The value of heterogeneous catalysts lies in the fact that they not only unfurl lower energy pathways for the conversion of reactants to products, but also offer a great degree of control on the rates of reactions and more importantly, the selectivity of these reactions towards desired products.

In the light of its enormous potential global impact, the prospect of having an atomic level control to tailor heterogeneous catalysts with desirable properties is extremely appealing. These properties of heterogeneous catalysts are linked closely to the electronic structure of the constituting materials, and an atomic level understanding of surfaces and processes can help explain and improve the macroscopic performance of these materials.

Over the last two decades, first principles based density functional theory (DFT) methods have been employed extensively for investigating the atomic level phenomena for different reactions on heterogeneous catalysts, and have been shown to be exceptionally successful and reliable in elucidating the mechanisms of complex chemical transformations on transition metal surfaces. In particular, these methods have contributed towards developing a better understanding of key chemical reactions like the water gas shift reaction,[6, 7] preferential oxidation and of CO in hydrogen (PROX),[8] ethylene epoxidation,[9-11] methanol decomposition and synthesis,[12] ammonia synthesis,[13, 14] and Fischer Tropsch reaction,[15] to name a few. The insights gained from these studies have then been successfully used to identify and design alloy catalysts with improved performance; some reactions for which this theory driven materials design has yielded improved catalysts are the preferential oxidation of CO, [8] hydrogen evolution reaction,[16] water gas shift reaction,[17] oxygen reduction reaction,[18, 19] selective hydrogenation of acetylene,[20] and CO methanation reaction.[21]

The DFT calculations are usually performed on highly idealized single crystal facets and the thermochemistry and kinetics information obtained from these calculations are representative of the chemistry on these model surfaces under ultra-high vacuum (UHV) conditions. Hence, there exists a pressure and materials gap between these predictions and the experimental observations that are obtained at higher pressures, on supported metal nanoparticles. This pressure and materials gap is bridged by adopting an iterative approach that involves microkinetic modeling[22] as a tool for directly incorporating the information from surface science experiments, advanced catalyst characterization techniques, and reaction kinetics measurements, together with theoretical calculations to completely describe complex reactions on supported metal catalysts over an extensive range of operating conditions.[6, 7, 12, 23-29] This combined theoretical and experimental approach provides a rigorous description of the catalyst surface under operating conditions,[6, 26, 27] serves as the means to elucidate the nature of active catalytic sites,[7, 29] and offers insights on how the catalyst properties and reaction conditions may be tailored to achieve specific goals, for instance, maximizing conversions and selectivity towards desired products.

1.2 Thesis Scope

In this thesis, the utility of a combined theoretical and experimental approach that employs DFT calculations, microkinetic modeling, reaction kinetics measurements, and catalyst characterization techniques, is illustrated through applications in the conversion of small oxygenates on transition metal catalysts. Chapter 2 provides a brief discussion on the background of the electronic structure calculations and microkinetic modeling; the exact implementation of these methods is different for each study, and is reported in detail in the individual chapters.

The two reactions that are discussed in this thesis are representative of the two key challenges that were described in the previous section. Formic Acid (FA) is a major byproduct in biomass processing, produced in equimolar quantities during levulinic acid production from cellulosic biomass.[30] The effective utilization of this sustainable source of hydrogen can not only eliminate the need for external hydrogen source for several hydrogenation reactions in biomass processing, but can also provide a boost in the efficiency of low-temperature direct formic acid fuel cells.[31] Chapter 3 first describes the first principles DFT investigation of several single crystal

Au surfaces for FA decomposition reaction. Subsequently, comparisons with experiments using microkinetic modeling provide predictions regarding the reaction mechanisms and the nature of active sites on Au catalysts, and experimental validation of these hypotheses is reported.

In Chapter 4, this study is extended to determine the nature of active sites for FA decomposition on supported Cu catalysts. Here, the importance of adopting a careful, iterative approach to obtain holistically self-consistent solutions is illustrated.

Chapter 5 describes our efforts to utilize the large thermodynamic and kinetic database that we had developed on several transition metals to perform a systematic, descriptor based search for the optimal catalyst properties, and subsequently perform rational design of bimetallic alloy catalysts that possess these particular properties, for the FA decomposition reaction.

Propylene oxide is one of the most widely produced chemicals in the world, and all existing commercial processes for its production suffer from low selectivity and/or the formation of large amount of toxic wastes. Chapter 7 discusses our efforts in developing an understanding of the reactions that limit the selectivity of direct epoxidation of propylene with air or oxygen, on supported Ag catalysts using DFT calculations and experiments.

Chapter 2

Overview of Methods

2.1 Electronic Structure Methods

The description of chemical bonds between a surface and a molecule forms the basis for understanding surface chemical reactivity. The fundamental property of interest is the energy of the atoms and molecules in a system, and more importantly, how this energy changes when these atoms and molecules are displaced, and this requires the knowledge of the ground state of the system. Obtaining this ground state energy involves solving the Schrödinger equation; a time-independent, non-relativistic form of this equation that is most applicable to the systems of our interest in heterogeneous catalysis, is shown below:

$$\left(-\frac{\hbar^2}{2m}\sum_{i=1}^{N}\nabla_i^2+\sum_{i=1}^{N}V(r_i)+\sum_{i=1}^{N}\sum_{j<i}U(r_i,r_j)\right)\Psi=E\Psi \qquad (2.1)$$

In this time-independent Shrödinger equation (TISE), ψ is the wavefunction, $\hbar$ is Planck's constant, m is the mass of an electron, N is the total number of electrons in the system, and r represents the spatial coordinates of these electrons. The three terms in the parenthesis represent the kinetic energy of electrons, interaction energy between electrons (*V*) and the nuclei, and the interaction energy between electrons (*U*), respectively. This problem can be simplified by using the Born-Oppenheimer approximation that makes use of the difference in masses of electron and nuclei to allow for the decoupling of electronic and nuclear components of the wavefunction ($\psi_{total}=\psi_{electronic}\times\psi_{nuclear}$). The TISE is then solved in an iterative manner, by first calculating the electronic structure and the *ground state energy* for a fixed nuclear configuration, and then repeating this for different nuclear arrangements. The results from these calculations are then used to construct the ground state potential energy surface (PES) for the nuclei, although it is usually only the ground state PES that is of interest in chemical analyses. For the systems of interest in heterogeneous catalysis, obtaining analytical solutions for the electronic component of the wavefunction is not feasible; hence, a number of approximate numerical schemes have been developed for this problem. In the Hartree-Fock Self-Consistent Field (HFSCF) approach, the many-electron wavefunction for the system is written as a product of one-electron wavefunctions, and consequently, the full TISE is separated into many one-electron equations. However, although this approach is quite appealing due to its simplicity, there are large inaccuracies associated with it due to the lack of explicit *electron correlation* effects. *Configuration Interaction* (CI) methods make use of unoccupied states to account for correlation effects and allow for the incorporation of excited electron configurations into the wavefunction, and by doing so, offer highly accurate, full solutions to the TISE. However, the computational costs associated with these methods are extremely high (N^7 calculations per basis set as opposed to N^4 for the HFSCF methods), which make them infeasble for the systems that typically have large number of electrons. There are numerous other methods that offer the possibility of obtaining the exact solutions to the TISE, like the Quantum/Diffusion/Variational Monte Carlo techniques, and Post-Hartree-Fock methods, but all of them are associated with exceptionally high computational demands.

In the mid 1960’s, W. Kohn, L.J. Sham, and P. Hohenberg proved that the ground state energy of a system is only a function of its electron density(ρ) of the system, and that this electron density can be expressed in terms of individual single-electron wave functions (Ψ_i).

$$E = E[\rho(\mathbf{r}), \{\mathbf{R}_\alpha\}] \quad ; \quad \rho(\mathbf{r}) = \sum_i n_i \left|\psi_i(\mathbf{r})\right|^2 \tag{2.2}$$

They also showed that the electron density that minimizes the energy of the overall functional is the one that corresponds to the full solution of the Schrödinger equation, and that one can find this electron density by solving a set of equations involving only single electron wavefunctions, as shown below:

$$\left(-\frac{\hbar^2}{2m}\nabla^2 + V_C(r) + V_H(r) + V_{XC}(r)\right)\Psi_i(r) = E_i\Psi_i(r) \tag{2.3}$$

Where V_C and V_H are the Coulomb and Hartree potentials respectively, and V_{XC} is the exchange-correlation (XC) potential which represents a heuristic way to account for the electron-electron interactions. If one could have an exact universal expression for V_{XC}, then DFT could be an exact theory. However, all XCs have been found to be explicit functionals of the electron density. In this study, PW91 generalized gradient approximation (GGA-PW91) is employed to describe these potentials, unless otherwise noted. The solution to the Kohn-Sham equations are then obtained by fist selecting a trial electron density, and solving equations 2.2 and 2.3 in an iterative manner until a self-consistent solution is obtained. Further details on these methods have been included in the individual chapters.

In this dissertation, the DFT methods have primarily been used for obtaining the thermodynamic and kinetic parameters for reaction sequences on catalyst surfaces that are then used as initial guesses in the respective microkinetic models.

2.2 Microkinetic Modeling

The importance and increasing popularity of employing microkinetic modeling as a tool for performing comparisons between the DFT predictions and experimental observations has been highlighted in Chapter 1. Here, a a brief description of the DFT derived inputs used in these microkinetic models is provided; the implementation of these models closely follows the procedure described by Gokhale et al. and Grabow et al. and additional details are provided in individual chapters.

2.2.1 Model Inputs

Equilibrium Constants

For a given elementary step, the equilibrium constant can be defined as:

$$K = \exp\left(\frac{-\Delta G^{o}}{k_B T}\right) = \exp\left(\frac{\Delta S^{o}}{k_B}\right)\exp\left(\frac{-\Delta H^{o}}{k_B T}\right) \tag{2.4}$$

Where k_B is the Boltzmann constant, T is the reaction temperature, and ΔG^{o}, ΔH^{o} and ΔS^{o} denote the change in standard-state Gibb's free energy, enthalpy and entropy respectively. The total standard entropy for all gas-phase species, adsorbed reaction intermediates, and transition states is determined by obtaining the individual contributions from the translational, rotational and vibrational modes within the molecule.

$$S^0_{total} = S^0_{trans} + S^0_{rot} + S^0_{vib} \tag{2.5}$$

For all gas phase and adsorbed species, the vibrational contribution to the entropy can be calculated accurately using the vibrational modes that are obtained from the DFT calculations, as shown below:

$$\mathrm{S_{vib}} = k_B \sum_{i}^{\#\,\text{of modes}} \left(\frac{x_i}{e^{x_i} - 1} - \ln\left(1 - e^{-x_i}\right)\right) \tag{2.6}$$

Where x_i for each vibrational mode is defined in terms of the vibrational frequency, ν_i

$$x_i = \frac{h\nu_i}{k_B T} \tag{2.7}$$

For a gaseous species, the number of vibrational modes are equal to $3N_i$-5 or $3N_i$-6 for a linear or nonlinear molecule, respectively, where N_i is the number of atoms in the molecule. The remaining contributions to the entropy from the translational and rotational degrees of freedom can be calculated using the expressions below:

$$S^0_{trans,3D} = R\left[\ln\left(\frac{(2\pi m k_B T)^{3/2}}{h^3}\right) + \ln\frac{V}{N_g} + \frac{5}{2}\right] \tag{2.8}$$

$$S^0_{rot} = R\left[\ln(q_{rot}) + \frac{3}{2}\right], \quad q_{rot} = \left(\frac{\pi T^3}{\sigma^2 \Theta_A \Theta_B \Theta_C}\right)^{1/2} \quad ,\Theta_R = \frac{h^2}{8\pi^2 I_R k_B} \tag{2.9}$$

Where m = molecular weight of the intermediates, $V/N_g = k_B T/P$ (Ideal gas approximation), I_R corresponds to the three moments of inertia about the principal axes and σ= symmetry number, which is the number of indistinguishable orientations that the molecule can adopt, and all the other symbols have their usual meanings. For adsorbed species, the translational and rotational modes are replaced by vibrational modes corresponding to frustrated translation and rotation on the surface. Hence, the total entropy of the surface species is a sum of the contributions from $3N_i$ -2 vibrational modes obtained directly from the DFT calculations, and the two-degrees of surface translational modes that are approximated as frustrated vibrations, as shown below:

$$\nu = \frac{1}{2\pi}\sqrt{\frac{k}{m}} = \sqrt{\frac{E_d}{2l^2 m}} \tag{2.10}$$

Where l is the typical length scale of diffusion, k is the spring constant describing the harmonic oscillator, and E_d is the activation barrier for the diffusion process. The entropic contributions from the two frustrated vibration modes can be obtained by substituting the frequency from equation into equations 2.10 into equations 2.7 and 2.6.

The entropy values obtained for all the gas phase and surface species are then used to obtain the Shomate parameters for all the species, as summarized below:

$$t = T(K)/1000$$

$$H^0 - H^0_{298.15}\left[\frac{kJ}{mol}\right] = At + \frac{B}{2}t^2 + \frac{C}{3}t^3 + \frac{D}{4}t^4 - \frac{E}{t} + F - H$$

$$S^0\left[\frac{J}{mol.K}\right] = A\ln(t) + Bt + \frac{C}{2}t^2 + \frac{D}{3}t^3 - \frac{E}{2t^2} + G \tag{2.11}$$

$$C_P\left[\frac{J}{mol.K}\right] = A + Bt + Ct^2 + Dt^3 + \frac{E}{t}$$

The exact procedure to obtain these parameters from the entropy values is similar to that adopted by Grabow et al., and is summarized below:

(i) The relations described above are used to calculate the value of total entropy for different temperatures in the range 10K – 298.15K.

(ii) These entropy values are then used to fit the Shomate parameters A, B, C, D, E and G. The parameters H and F are obtained using the reference enthalpy, H^0 and enthalpy at 10K,H^{10K}. Here, $H^{10K} = U_0 + ZPE$, where U_0 is the electronic energy obtained from DFT calculations. The reference temperature of 10K was used instead of 0K to ensure that we obtain a finite value of C_P , which has temperature in the denominator.

(iii) Once the Shomate parameters are obtained, they are then utilized to calculate the standard state enthalpy using the relation $H_{298.15} = U_O + ZPE + \int_{10}^{298.15} C_P(T)dT$

(iv) Steps 1 and 2 are repeated to obtain the Shomate parameters for temperatures greater than 298.15K, using the value of $H_{298.15}$ as obtained in step 3.

All microkinetic models used in this study are parameterized in terms of the Shomate parameters; this ensures that all the model inputs (except sticking coefficients, as described in next section) are obtained using rigorous DFT calculations. The temperature corrected enthalpy and entropy values are then obtained using equation 2.11, and are used for the calculation of equilibrium rate constants.

Reaction Rate Constants

The forward reaction rate constants for all bond formation/scission steps are calculated using transition state theory

$$k = \frac{k_B T}{h} exp\left(\frac{\Delta S^{0''}}{k_B}\right) exp\left(-\frac{E_A}{k_B T}\right) \tag{2.12}$$

Where E_A = Activation energy of the elementary step and $\Delta S^{0''} = S^0_{transition\ state} - \sum S^0_{reactants}$

Collision theory is used to define rate constants for adsorption processes. It can be shown that for these processes, the rate of adsorption is given by:

$$\mathrm{k} = \frac{\sigma^\circ(T)}{\sqrt{2\pi m_A k_B T}} exp\left(-\frac{E_A}{k_B T}\right) \tag{2.13}$$

Where $\sigma^\circ(T)$ denotes the sticking coefficient on a clean surface, the value of which is assumed to be 1 for initial considerations.

Chapter 3

Formic Acid Decomposition on Au catalysts: DFT, Microkinetic Modeling, and Reaction Kinetics Experiments[1]

3.1 Introduction

The effective utilization of renewable energy carriers produced from biomass based resources is one of the key challenges in the transition towards a sustainable energy future[32, 33]. Formic acid (FA, HCOOH) is a major byproduct in biomass processing[34], and it has attracted significant attention as a potential hydrogen-carrier material[35-40]. As a hydrogen-carrier, FA can be oxidized in direct formic acid fuel cells (DFAFCs)[41]. When generated as an equimolar by-product of levulinic acid [30, 42, 43] production from cellulosic biomass, FA can be used for *in-situ* harvesting H_2 that can then be utilized for the hydrogenation of levulinic acid to gamma-valerolactone (GVL)[44], thereby eliminating the need of an external hydrogen source in the production of this key biofuel precursor[45, 46]. Also, as the simplest carboxylic acid, FA has for long been considered a paradigmatic molecule in homogeneous and heterogeneous catalysis, and surface science studies, to probe the reactivity on metals[47-56], metal carbides[57-59], and metal oxides[60-65] specifically for deoxygenation of more complex carboxylic acids, which is a critical step in the selective upgrading of biomass derived platform molecules to fuels. Hence, our motivation for studying the FA decomposition reaction is based on (1) its potential application as a promising liquid hydrogen carrier for *in situ* hydrogen production, and (2) its suitability as a

---

[1] Adapted from "Formic Acid Decomposition on Au Catalysts: DFT, Microkinetic Modeling, and Reaction Kinetics Experiments", S. Singh, S. Li, R. Carrasquillo-Flores, A. C. Alba-Rubio, J. A. Dumesic, M. Mavrikakis, ***AIChE Journal*** 60, 1303 (2014). S. Li has contributed to the DFT results reported in this study; Kinetic experiments were performed by R. Carrasquillo-Flores, and TEM images were provided by A. C. Alba-Rubio.

fundamental probe molecule for understanding the reactivity of carboxylic acids on metal catalysts, and using this information to design improved catalysts for effective deoxygenation of these functional groups. FA decomposition can take place via two parallel pathways involving dehydrogenation or dehydration reactions, which are linked by the water gas shift (WGS) [6, 66, 67] reaction. In the broader context of FA decomposition on transition metals, steering selectivity towards production of $CO_2 + H_2$ (dehydrogenation), rather than $CO + H_2O$ (dehydration) presents an important selectivity challenge in this catalytic chemistry. Even though the dehydration products can be transformed to CO_2 and H_2 via the WGS reaction, forming the dehydration products may lead to partial poisoning of catalytic sites by CO, thereby limiting the efficiency of the overall catalysis. Accordingly, supported Pt catalysts have frequently been suggested to be the most active catalysts for selective FA dehydrogenation, and for this reason, they find widespread applications as anodes for DFAFCs[31, 68-73]. Yet, there exist major obstacles in using Pt based catalysts as electrode materials and as FA decomposition catalysts, because of the proneness of Pt to CO poisoning[74-76] and its dissolution under operating conditions in fuel cells.

Gold, on the other hand, is not hindered by CO poisoning under most reaction conditions. Ever since Haruta[77] and Hutchings[78] first predicted Au to be an extraordinary catalyst for CO oxidation and ethylene hydrochlorination reactions, there has been an overwhelming interest in exploring the application of supported Au catalysts in both homogeneous and heterogeneous catalysis[79-87]. More recently, Au has been studied as a catalyst for FA decomposition[88]. In particular, Ojeda et al.[89] studied the FA decomposition on supported Au catalysts and showed that the turnover frequencies (TOFs) on well-dispersed Au catalysts were higher than those on Pt catalysts. They proposed that this unprecedented activity on Au catalysts arises from small Au clusters, most likely undetected in TEM micrographs. More recently, Gazsi et al.[90] performed vapor phase experiments to study the effect of supports on the selectivity of FA decomposition to the dehydration and dehydrogenation products, and they confirmed the high activity of Au nanoparticles supported on a wide range of porous and non-porous supports. Although these experimental studies shed light on the possible nature of active sites on Au catalysts, a molecular level understanding of this reaction mechanism is still lacking. In this paper, we develop an integrated approach (Figure 3-1) by combining state-of-the-art Density Functional Theory (DFT) with reactivity experiments and microkinetic modeling that can shed additional light into the reaction mechanism and the nature of active sites on Au catalysts[25]. In particular, we choose Au(111), Au(100), and Au(211) model surfaces for our DFT calculations to derive initial guesses for the surface reaction energetics needed for our microkinetic model. We then develop a comprehensive mean-field microkinetic model including all elementary steps investigated by our DFT calculations. Comparisons between microkinetic modeling reaction rates and reaction orders with the experimental results provide critical insights for the nature of the active site on Au/SiC catalysts for FA decomposition.

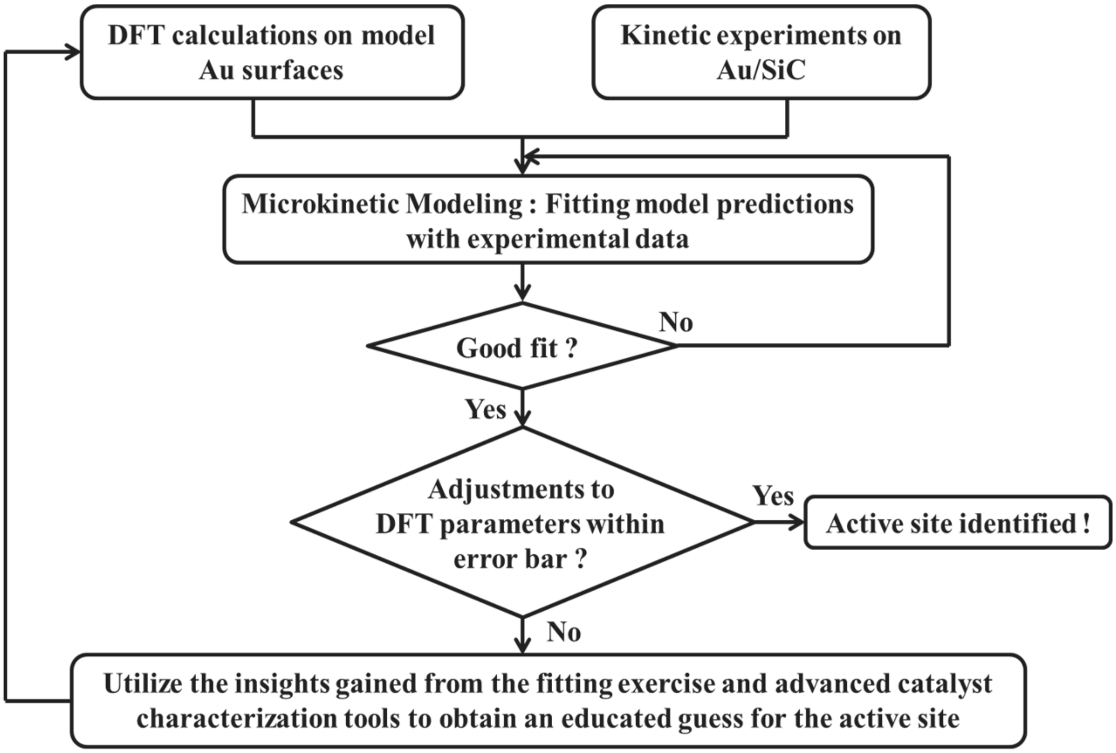

Figure 3-1 Flow chart for the identification of active sites for FA decomposition on Au/SiC.

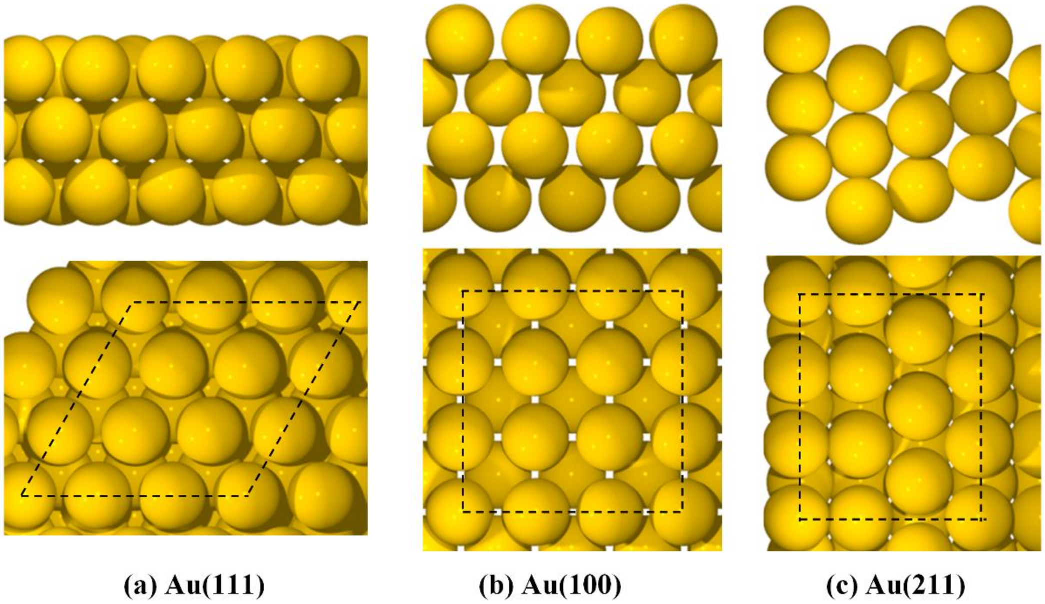

Figure 3-2 Side and top views of the three model Au surfaces employed in this study: (a) Au(111), (b) Au(100), and (c) Au(211). Dotted black lines in the top view indicate the unit cell on each surface.

3.2 Methods

3.2.1 Density Functional Theory

All calculations were performed using the DACAPO total energy code[91, 92]. The Au catalyst was modeled by the (111), (100) and (211) facets of the fcc bulk crystalline structure of Au metal (Figure 3-2).

The Au(111) surface was modeled by a three-layer slab with a p(3×3) unit cell, corresponding to 1/9 monolayer (ML) coverage for a single adsorbate in the unit cell, periodically repeated in a super cell geometry with five equivalent layers of vacuum between any two successive metal slabs. All the Au atoms in this model surface were kept fixed in their bulk truncated positions, as our systematic investigations showed that surface relaxation does not have a significant effect on the energetics for this system. The super cell used to model the Au(100) facet consists of a p(3x3) unit cell with four layers of metal atoms, top two of which were allowed to relax, and five equivalent layers of vacuum spacing separating the periodic slab images. The Au(211) slab was constructed by a 1x3 unit cell and consisted of nine Au layers (having terrace three atoms deep and three atoms wide). Successive slabs were separated by a vacuum equivalent to 12 such Au(211) layers. Adsorption was allowed on only one of the two exposed surfaces for all three slabs, and the electrostatic potential was adjusted accordingly[93, 94].

The surface Brillouin zone of (111) slabs was sampled at 18 special Chadi-Cohen[95] k points, while that for the (100) and (211) slabs was sampled by using a 4×4×1 Monkhorst-Pack[96] k-point mesh. Ionic cores were described by ultrasoft Vanderbilt pseudo-potentials[97] and the Kohn-Sham one-electron valence states were expanded in a basis of plane waves below a kinetic energy of 25 Ry. The exchange-correlation energy and potential were described self-consistently using the generalized gradient approximation (GGA-PW91)[98, 99]. The electron density was determined by iterative diagonalization of the Kohn-Sham Hamiltonian, Fermi population of the Kohn-Sham states ($k_BT = 0.1$ eV), and Pulay mixing of the resulting electronic density[100]. The total energies were then extrapolated to $k_BT = 0$ eV. The calculated equilibrium lattice constant for bulk Au was found to be 4.18 Å, in reasonable agreement with the experimental value (4.08 Å) [101].

The binding energies (BEs) were calculated with respect to the total energy of the clean slabs (E_{slab}) and the corresponding adsorbates in the gas phase ($E_{adsorbate,\ gas\text{-}phase}$), i.e., $BE_{adsorbate} = E_{total} – E_{slab} - E_{adsorbate,\ gas\text{-}phase}$. In the discussion of the DFT results, we refer to electronic energy values including the zero point energy (ZPE) corrections unless otherwise noted.

The minimum energy pathways and activation energy barriers for all elementary steps were determined using the climbing image nudged elastic band (CI-NEB) method[102]. The minimum energy path for each elementary step was discretized with at least seven images, in addition to the initial and final states. A vibrational frequency analysis[103] was performed to confirm the true nature of the saddle point by identifying a single imaginary frequency along the reaction coordinate. The frequencies were calculated using the harmonic oscillator assumption by diagonalization of the mass-weighted Hessian matrix in internal coordinates[103] .

3.2.2 Experiments

Catalyst Preparation

SiC was chosen as the preferred support for our reaction kinetics experiments because (1) it is an inert support that does not contribute to the overall reaction rate, and (2) it results in a clear contrast for Au atoms and clusters in the STEM micrographs, due to the large difference in the scattering potentials of the metal and the support. A 1 wt% Au/SiC catalyst was prepared by the deposition-precipitation method. 2.0 g of dry acid-treated silicon carbide was dispersed in 100 mL of a 1 mM chloroauric acid (Sigma-Aldrich) solution at room temperature. The pH of the mix was adjusted to 9 by drop-wise addition of 2.5 M ammonium hydroxide (Sigma-Aldrich). The mixture was aged for 6 h under vigorous stirring at room temperature and was then filtered and washed with deionized water to remove chlorine ions. The sample was dried overnight at 373 K. The dried catalyst was reduced *in situ*, prior to the reaction at a temperature between 623 and 773 K (with a heating rate of 0.5 K min^{-1}) under pure hydrogen flow (30 cm^3 (STP) min^{-1}) for four hours. Catalyst reductions at temperatures above 773 K (and up to 1073 K) were performed in a quartz flow-through cell under the same operating conditions.

Reactivity measurements

Gas phase FA decomposition studies were conducted in a fixed-bed down-flow reactor containing 500 mg of catalyst mixed with silica chips in a 1/2-inch outer diameter stainless steel tube. The temperature was measured using a K-type thermocouple attached to the outside of the reactor. The temperature of the reactor was adjusted by using a furnace connected to a variable autotransformer power source controlled with a temperature controller. The total pressure in the reactor was maintained at 1 atm, and the partial pressures of the gases were controlled by adjusting the flow-rates at the reactor inlet. The flow-rates of all gases were fixed using calibrated mass-flow meters, and the total inlet flow rate was maintained at 100 ml/min for all experimental runs. An inlet composition between 0-12% of H_2, 0-6% of CO_2 and 1-4% of FA was used, with the balance consisting of helium. The gases were used as provided, with a purity of 99.99%. Liquid FA (Sigma-Aldrich) was delivered to the reactor system at room temperature using a syringe pump (Harvard Apparatus) and vaporized at the reactor inlet. The feed and effluent gases were analyzed using gas chromatography (with a TCD). All the experimental rates reported in this study are based on FA converted, which is equal to the amount of CO_2 produced, as no measurable amount of CO is formed under any experimental condition. To ensure this, the TCD used to analyze CO in the effluent gas mixture was first calibrated by using commercial CO gas mixtures with known concentrations. Control experiments with only the SiC support in the reactor provided signals that corresponded to a concentration of 24 ± 1 ppm of CO. The CO concentrations that were obtained during our kinetic experiments under all reaction conditions were found to be very close to this value (max = 27.0 ppm, min = 23.2 ppm, average over all the runs = 25.1 ± 2 ppm). The carbon balance was verified for all experimental runs and was found to be in the range of 98.9 % - 99.9 %. Conversions were maintained below 20% to achieve differential reactor operation. To determine the apparent activation energy barrier, the temperature was varied over a range of 50K, with the concentrations kept at standard conditions. The apparent reaction orders with respect to reactants and products were determined by varying one gas concentration at a time.

Table 3-1 Reaction rates and selectivity obtained from the kinetics experiments on Au/SiC.

	Temp (K)	**y(HCOOH)**	**y(He)**	**y(H_2)**	**y(CO_2)**	**Experimental Rates (µmol gcat^{-1} min^{-1})**	**Experimental Selectivity (CO_2/(CO_2+CO))**
1	373	0.01	0.99	0.00	0.00	9.30	1.00
2	373	0.02	0.98	0.00	0.00	15.42	1.00
3	373	0.02	0.98	0.00	0.00	18.65	1.00
4	373	0.04	0.96	0.00	0.00	33.00	1.00
5	343	0.03	0.97	0.00	0.00	5.05	1.00
6	353	0.03	0.97	0.00	0.00	8.00	1.00
7	363	0.03	0.97	0.00	0.00	15.72	1.00
8	368	0.03	0.97	0.00	0.00	21.35	1.00
9	373	0.03	0.97	0.00	0.00	24.11	1.00
10	378	0.03	0.97	0.00	0.00	32.55	1.00

11	383	0.03	0.97	0.00	0.00	41.30	1.00
12	373	0.03	0.96	0.01	0.00	23.91	1.00
13	373	0.03	0.94	0.04	0.00	24.09	1.00
14	373	0.03	0.92	0.06	0.00	24.32	1.00
15	373	0.03	0.96	0.00	0.01	23.69	1.00
16	373	0.03	0.95	0.00	0.03	23.76	1.00
17	373	0.03	0.92	0.00	0.06	23.97	1.00

3.2.3 High Resolution Scanning Transmission Electron Microscopy (STEM)

The particle size distributions were determined from STEM images. STEM characterization was performed using a FEI Titan STEM with CEOS probe aberration corrector operated at 200 kV with spatial resolution of < 0.1 nm. For imaging, a high-angle annular dark-field (HAADF) Z-contrast STEM was used, with HAADF detector angle ranging from 54 to 270 mrad, probe convergence angle of 24.5 mrad, and probe current of ~25 pA. To prepare samples for STEM, the catalyst samples were first suspended in ethanol, ultrasonicated for 5 min, and then deposited onto a ~5 nm thick Si window TEM grids. STEM samples were plasma cleaned for 10 min with 20% O_2 + 80% Ar gas immediately before loading into the microscope.

The particle size distributions of the Au/SiC catalysts were calculated from the acquired STEM images. From the particle size distributions, the number average Au particle sizes were determined using the relation= $\sum_i d_i/_n$, where d_i is the particle diameter of each Au particle, n is the total number of Au particles counted from the TEM images of a given sample (Table 3-6), and the summation is performed over all the particles that were identified in the STEM images.

3.2.4 Microkinetic Modeling

A mean-field microkinetic model for FA decomposition was developed on the basis of 17 elementary steps, including some steps that are in common with the water gas shift (WGS) reaction. The initial estimates for the ZPE-corrected binding energies and activation energy barriers were derived from DFT calculations and were later adjusted to reproduce the experimental kinetic dataset collected on the Au/SiC catalysts. Entropies of adsorbed intermediates and pre-exponential factors were determined from the DFT-calculated vibrational frequencies following a procedure described elsewhere[12]. Lateral adsorbate-adsorbate interactions were neglected and all the BEs and activation energy barriers (E_As) were assumed to be coverage independent. This assumption is reasonable since we expect surface coverages to be low under our experimental conditions. The maximum surface coverage was restricted to 1 ML and multilayer adsorption was not considered. We assumed that all species occupy exactly one site on the surface, except for the bidentate formate (HCOO), which blocks two surface sites. Given the geometry of the reactor used in our experiments, the reactor was modeled as a plug-flow reactor (PFR). Hence, our reactor model comprised of 5 differential equations for the gaseous flow rate along the reactor length, 8 steady state algebraic equations for the fractional surface coverages of reaction intermediates, and 1 site-balance equation. Further details of our model formulation can be found in our previous work[12, 25, 27] .

3.3 Results and Discussion

To develop a comprehensive mean field microkinetic model that would enable us to study the structure sensitivity of this reaction on Au surfaces, we have rigorously studied the properties of 5 closed shell species and 8 reaction intermediates, as well as the reaction energetics of 17 elementary steps, on the Au(111), Au(100) and Au(211) facets using first principles DFT calculations. We first present the results from our DFT calculations; followed by the results from our attempts to fit the microkinetic model predicted rates and selectivities to the experimentally measured reaction kinetics data.

3.3.1 Structure and Adsorption Thermochemistry of Reaction Intermediates

The binding energies and preferred adsorption sites of surface species involved in this reaction network on the three Au facets studied are summarized in Table 3-1. More detailed information on adsorbed states, including vibrational frequencies of surface intermediates and gas phase species can be found in Supplementary Information (Table S.1).

The following description focuses primarily on the most favorable binding configurations for the adsorbates. Schematic representations for these configurations are shown in Figure **3-3** – Figure 3.6. In this discussion, and throughout the text, (g) stands for ‘gas phase species’ and each '*' represents a single surface site occupied by the corresponding adsorbate. Wherever available, the previously reported literature values (as obtained using DFT) for the BEs of surface species and activation energy barriers (E_A) of elementary steps are reported in parenthesis next to our DFT derived numbers.

All the closed-shell species involved in this reaction network, with the exception of CO, are found to be weakly bound to all three Au facets studied. They exhibit weak preference for their most stable binding configurations, as evidenced by the near degeneracy of their several adsorption states. Our calculations do not take into account the long-range interactions, such as van der Waals forces,[104, 105] which may contribute an additional stabilization of ~0.1 eV – 0.2 eV per carbon atom. The absolute magnitude of the binding energies of surface species on the three Au surfaces were observed to decrease in the general order: Au(211) > Au(100) > Au(111), in agreement with the general notion that adsorbates tend to exhibit stronger binding to more open facets [106].

Formic Acid exhibits two distinct stable configurations: one in which all atoms of the HCOOH* molecule lie within a plane perpendicular to the surface (HCOOH*), and another one in which this plane is parallel to the surface (HCOOHpa*). The latter orientation was found to adsorb with practically zero BE on all three surfaces. HCOOH* binds to the three facets via its carbonyl O atom on a top site with the O-H and C-H bonds pointing towards and away from the surface respectively, and has a binding energy of -0.10 eV (-0.15 eV[107]), -0.17 eV (-0.19 eV[69]), and -0.21 eV on Au(111), Au(100), and Au(211) respectively. *Formate* has long been proposed as one of the key reaction intermediates in FA decomposition and has also been frequently cited as a possible intermediate in WGS[108-110] and methanol synthesis[111-113] reactions. As a result, it has received much scientific attention[65, 89, 114-119], both in the experimental and theoretical literature. Our DFT calculations indicate that HCOO** binds on all three Au facets in a bidentate configuration (Figure 3-3) with its O ends on top of two nearest neighbor metal atoms. This structural data is in agreement with the available experimental (NEXAFS and IR)[114] and theoretical evidence. It has a BE of -1.69 eV (-1.82 eV[107]), -2.02 eV (-2.10 eV[69]) and -2.19 eV on Au(111), Au(100) and Au(211) respectively.

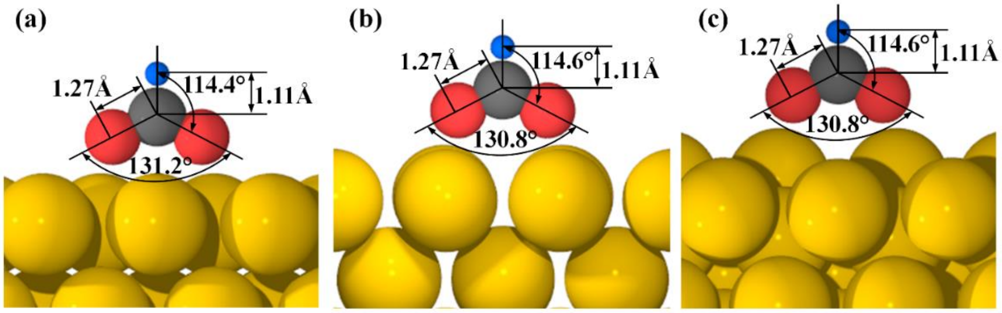

Figure 3-3 Most stable configurations of Formate (HCOO) intermediate on (a) Au(111), (b) Au(100) and (c) Au(211).

The BEs of *atomic hydrogen* on Au(111), Au(100), and Au(211) are -1.90 eV (-2.03 eV[107], -2.20 eV[120, 121]), -2.06eV (-2.29 eV[122]), -2.11eV (-2.32 eV[123]) respectively. H* binds preferentially on the bridge sites on Au(100) and Au(211), and on the three fold sites on Au(111). The most stable binding configuration on Au(111) is at the fcc sites, although the hexagonal close packed (hcp) sites are found to be energetically quasidegenerate to the fcc sites. *Atomic oxygen* prefers the three fold fcc site on Au(111), the four fold hollow site on Au(100), and the two fold bridge site on the step edge of Au(211), with BEs of -2.41 eV (-2.43 eV[124]), -2.69 eV(-2.85 eV[125]), -2.80 eV(-2.83 eV[126]) respectively. *Hydroxyl* prefers to adsorb in a top-tilted configuration on the bridge sites of all three Au facets with BEs of -1.36 eV (-1.47 eV[124]), -1.96 eV, -2.07 eV on Au(111), Au(100) and Au(211) respectively. *Carboxyl* exhibits two stable adsorption configurations: (a) one with H pointing downwards towards the surface, the trans isomer (COOH*) and (b) one with H pointing away from the surface, the cis isomer (COOHcis*). COOH* has a BE of -1.27 eV, -1.48 eV (-1.61 eV [122]) and -1.58 eV on Au(111), Au(100) and Au(211) respectively. The *formyl* radical binds preferentially through its C atom to the top sites of all three Au facets, with BEs of -1.05 eV, -1.26 eV and -1.38 eV on Au(111), Au(100), and Au(211) respectively. *Carbon monoxide* (CO) binds through the carbon atom, with the C-O bond perpendicular to the surface. It binds preferentially to the top site on Au(111), and the two fold bridge sites on Au(100) and the step-edge of Au(211), with BEs of -0.21 eV (-0.26 eV[107]), -0.62 eV (-0.62 eV[122]) and -0.67 eV (-0.65 eV[127]) respectively. *Water* binds weakly through its oxygen atom to the top site of the three Au facets with the plane containing all the atoms parallel to the surface. It has a BE of -0.10 eV (-0.11 eV[107], -0.15 eV[128], -0.12 eV[121]), -0.14 eV, and -0.20 eV (-0.19 eV[123]) on Au(111), Au(100) and Au(211) respectively. *Carbon dioxide* (CO_2) binds weakly on all three Au facets, with binding energies of -0.02 eV ~ -

0.05 eV. CO_2 retains its gas-phase linear geometry and exhibits very weak site preference with several degenerate binding configurations.

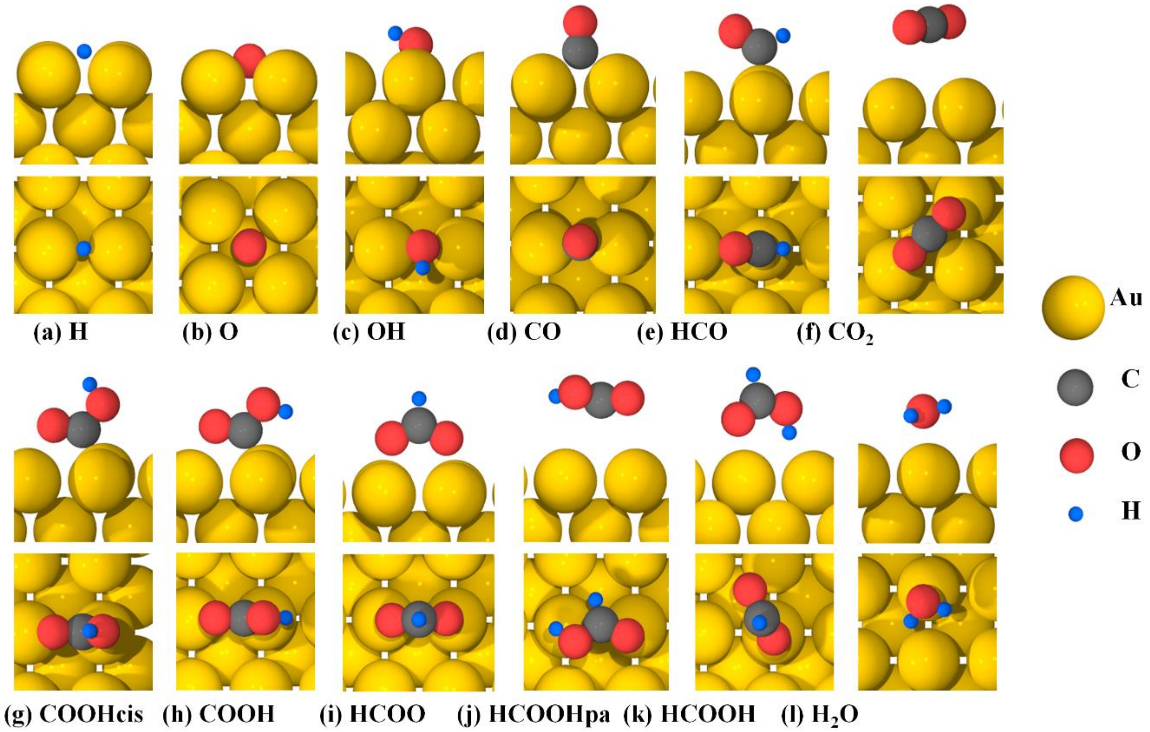

Figure 3-4 Most stable configurations of FA decomposition intermediates on Au(111) (top panel represents cross sectional view; bottom panel represents top view).

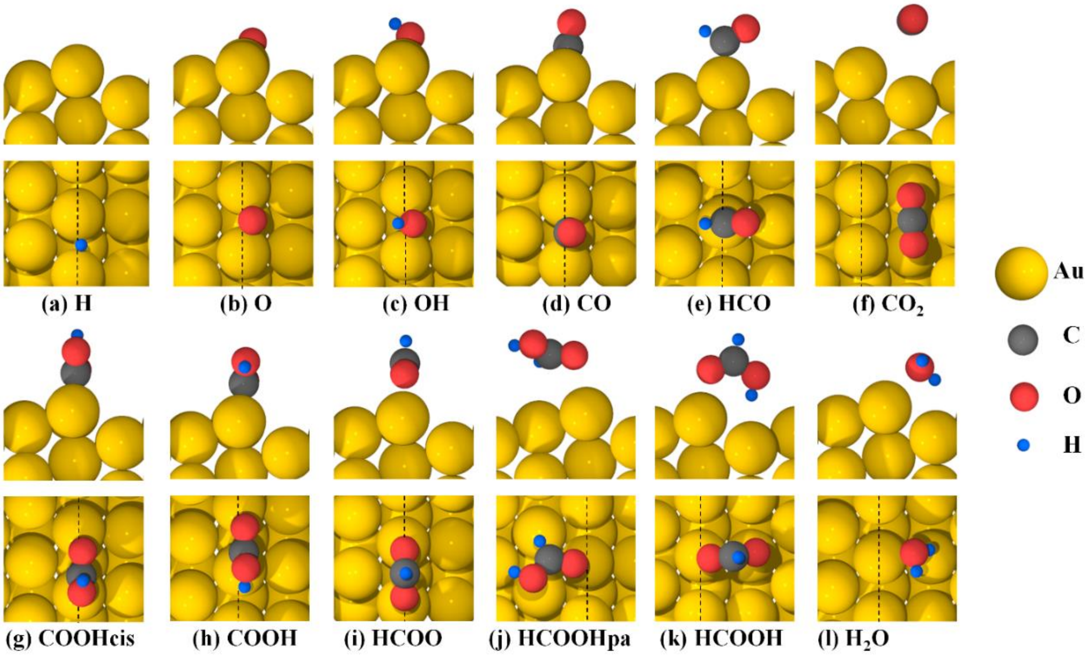

Figure 3-5 Most stable configurations of FA decomposition intermediates on Au(100) (top panel represents cross sectional view; bottom panel represents top view).

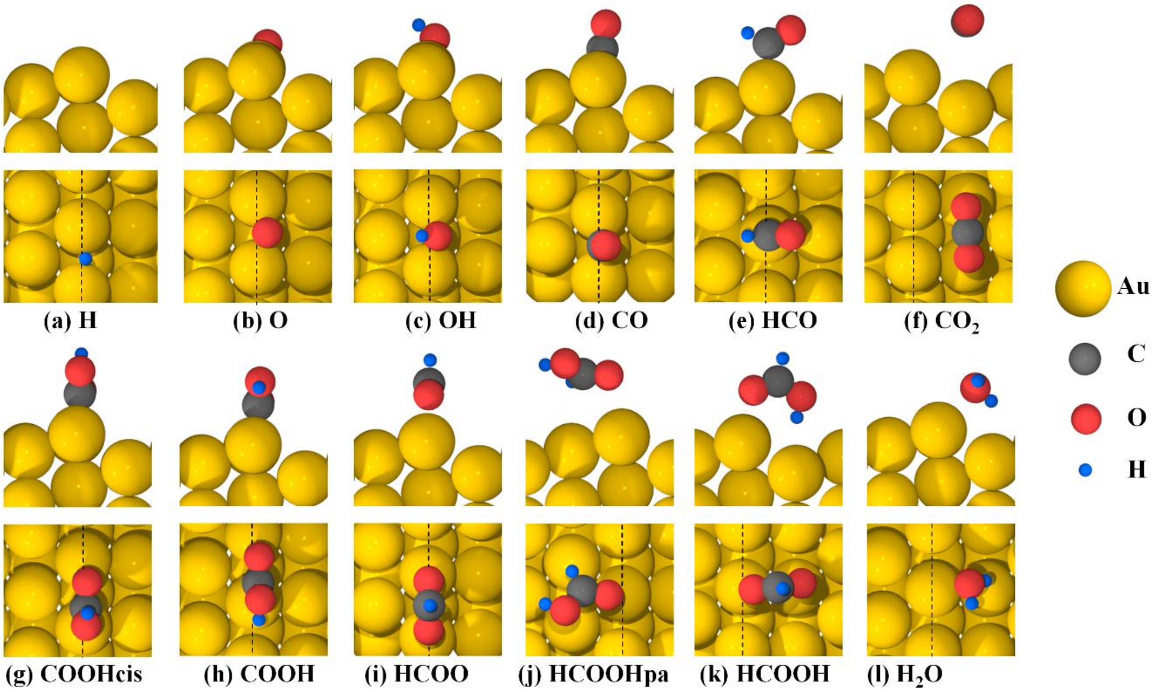

Figure 3-6 Most stable configurations of FA decomposition intermediates on Au(211) (top panel represents cross sectional view; bottom panel represents top view; dotted black lines in the top view denote the step edge of Au(211) surface)

Table 3-2 Calculated PW91 Binding Energies (BEs) of Adsorbed Species and their Preferred Adsorption Sites on Au(111), Au(100) and Au(211). Zero of the energy scale is the slab and the gas phase species at infinite separation from each other.

Species	**Au(111)**		**Au(100)**		**Au(211)**	
	Adsorption Site	**BE / eV**	**Adsorption Site**	**BE / eV**	**Adsorption Site**	**BE / eV**
H*	fcc	-1.90	bridge	-2.06	bridge	-2.11
O*	fcc	-2.41	hollow	-2.69	bridge	-2.80
OH*	bridge	-1.36	bridge	-1.96	bridge	-2.07
H_2O*	top	-0.10	top	-0.14	Off-top	-0.20
CO*	top	-0.21	bridge	-0.62	bridge	-0.67
CO_2*	physisorbed	-0.02	physisorbed	-0.02	physisorbed	-0.05
HCO*	top	-1.05	top	-1.26	top	-1.38
HCOO**	top-top	-1.69	top-top	-2.02	top-top	-2.19
COOH*	top	-1.27	top	-1.48	top	-1.58
COOHcis*	top	-1.22	top	-1.48	top	-1.59
HCOOH*	top	-0.10	top	-0.16	top	-0.21

3.3.2 Reaction Barriers of Elementary steps

The calculated activation energy barriers (E_A) and reaction energies (ΔE) for all elementary steps studied are reported in Table 3-2. All activation energy barriers and reaction energies reported in the following text are relative to the reactant and product states at infinite separation.

HCOOH activation

Here we discuss three different pathways of HCOOH activation, namely, the HCOO, the COOH, and the HCO mediated pathways (Figure 3-7).

HCOOH + 2* → HCOO** + H**

HCOOH* decomposition to HCOO** is found to proceed directly from the most stable, albeit weakly bound perpendicular configuration. The most favorable pathway involves H abstraction from HCOOH* over the top site on Au(111), but bridge site on Au(100) and Au(211) surface.

This step has a ΔE of 0.86 eV (0.89 eV[107]), 0.42 eV, and 0.26 eV, with E_A of 1.29 eV (1.36 eV[107]), 0.87 eV, and 0.98 eV on Au(111), Au(100), and Au(211) respectively.

*HCOOH** → *HCOOHpa*; HCOOHpa** + * → *COOH** + *H**

C-H bond scission in HCOOH*, yielding adsorbed COOH* and atomic hydrogen, is a two-step process. The first step is the rotation of HCOOH* to yield a metastable HCOOHpa* state. This rotation is quasi structure-insensitive, with a barrier of 0.55 eV to 0.63 eV on the three Au facets. HCOOHpa* is higher in energy than the most stable adsorbed state (HCOOH*), but it brings the carbonic hydrogen in FA closer to the three Au surfaces, thereby facilitating the C-H bond scission. The specific bond scission in HCOOHpa* to yield COOH* is an endothermic step, with E_A of 1.22 eV, 0.83 eV and 0.87 eV on Au(111), Au(100), and Au(211) respectively.

*HCOOH** + * → *HCO** + *OH**

The dehydroxylation of HCOOH* to yield HCO* and OH* has a barrier of 2.16 eV, 1.91 eV and 1.74 eV on Au(111), Au(100) and Au(211) respectively, significantly higher than the HCOO** and COOH* formation steps.

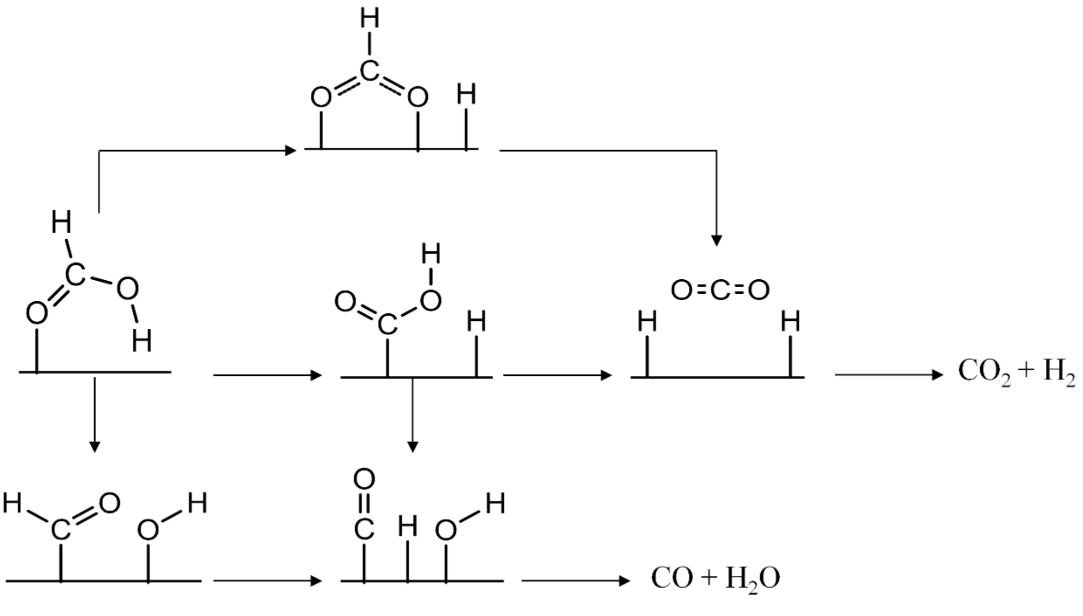

Figure 3-7 Three HCOOH decomposition pathways considered.

Product Formation

*HCOO*** → *CO_2* + H**

H abstraction from HCOO** starts with the rotation of the HCOO** molecule such that the C-H bond becomes parallel to

the Au surface, and one Au-O bond is broken just before the C-H bond scission over the top sites of all three Au facets (top site at the step edge for Au(211) facet). The H-C bond length in the transition state is 1.29 Å, 1.37 Å and 1.18 Å on Au(111), Au(100) and Au(211) respectively, as compared to the bond length of 1.11Å in adsorbed HCOO**. This step is slightly exothermic on Au(111) (ΔE = -0.35 eV) and Au(100) (ΔE = -0.17eV) and near-thermo neutral on Au(211) (ΔE = -0.08 eV). E_A for this step is relatively invariant of the model surface, with values of 0.80 eV (0.65 eV[129]), 0.84 eV, and 0.85 eV on Au(111), Au(100) and Au(211) respectively.

*COOH** + * → *CO_2* + H**

Carboxyl decomposition to CO_2 is found to proceed directly from the more stable trans configuration (COOH*). The reaction on all three facets starts with rotation of carboxyl within its molecular plane, such that O-H bond-scission takes place over the top site. Atomic hydrogen subsequently diffuses to the closest preferable site, and CO_2 settles in its physisorbed state. This step is exothermic, with ΔE of -0.54 eV (-0.49 eV[121]), -0.48 eV, and -0.46 eV, and has E_A of 0.54 eV (0.58 eV[121]), 0.68 eV, and 0.74 eV on Au(111), Au(100), and Au(211) respectively.

$COOH^* \rightarrow COOHcis^*; COOHcis^* + * \rightarrow CO^* + OH^*$

Contrary to the previous step, CO formation from carboxyl starts from the cis configuration of carboxyl. For this to take place, the most stable trans configuration of COOH* undergoes activated rotation (with E_A of 0.45 eV, 0.52 eV, and 0.44 eV on Au(111), Au(100), and Au(211) respectively), to yield the cis configuration (COOHcis*). The dissociation of COOHcis* takes place over the top site on all three Au facets, with E_A of 1.33 eV (1.25 eV[121]), 0.70 eV and 1.00 eV on Au(111), Au(100) and Au(211) respectively.

$H^* + H^* \rightarrow H_2 + 2^*$

H_2 recombinative desorption starts with two H* adsorbed on adjacent bridge sites, and the H-H bond formation takes place over the top site, for all three Au facets. The H-H bond length at the transition state are 1.38 Å, 1.38 Å and 1.34 Å on Au(111), Au(100) and Au(211) respectively, as compared to an H_2 gas phase bond length of 0.75 Å.

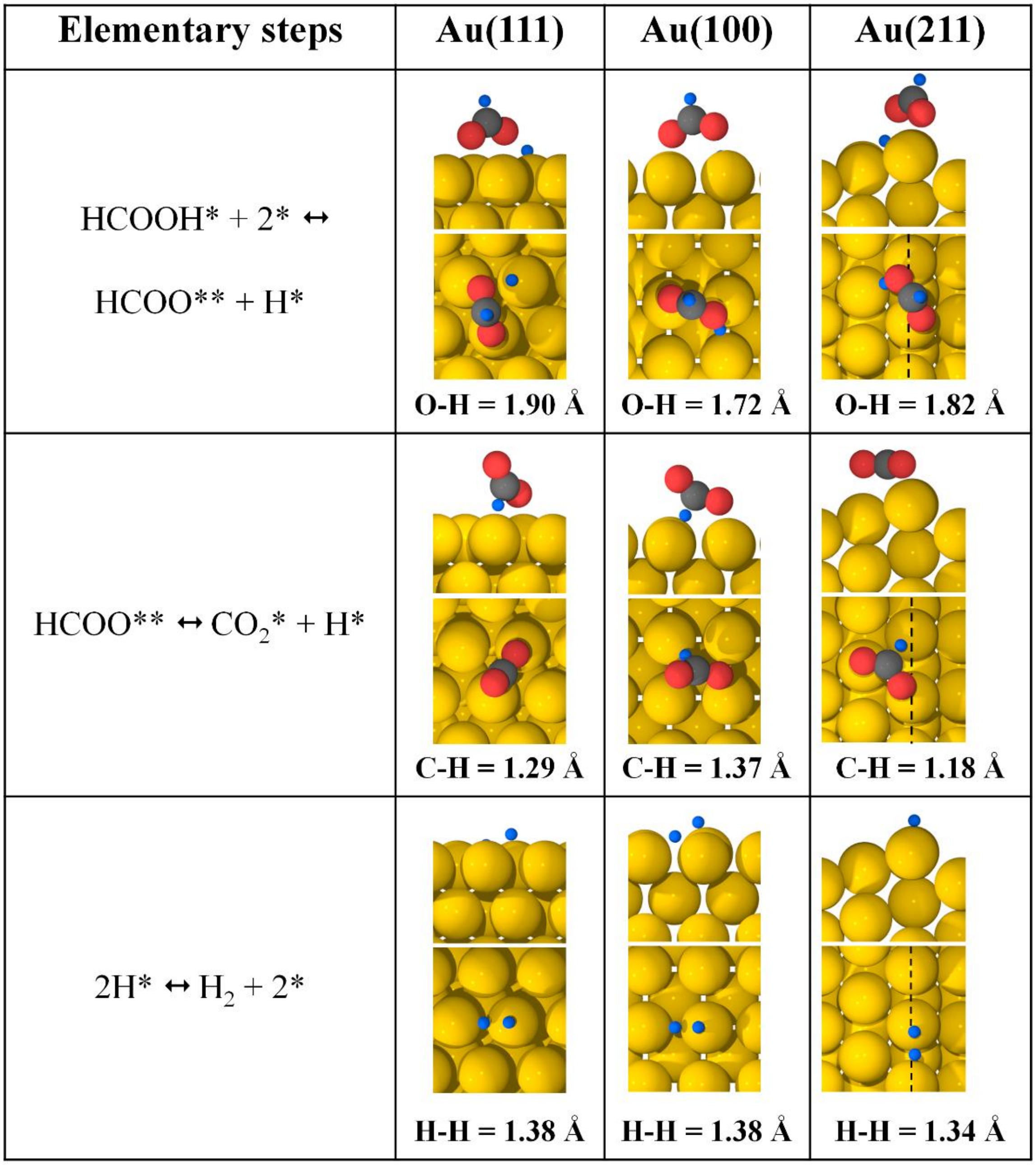

Figure 3-8 Side and top views of the transition states (TS) for the three kinetically relevant steps (as predicted by our microkinetic modeling results) on Au(111), Au(100) and Au(211) surfaces.

Table 3-3 PW91 reaction energies (ΔE) and activation energy barriers (EA) for the elementary steps considered in the HCOOH decomposition reaction network on Au(111), Au(100) and Au(211) surfaces. All the values are relative to infinite separation in initial/final states

#	**Reaction**	**Au(111)**		**Au(100)**		**Au(211)**	
		ΔE /eV	**E_A / eV**	**ΔE / eV**	**E_A / eV**	**ΔE / eV**	**E_A / eV**
1	HCOOH + * ↔ HCOOH*	-0.10		-0.16		-0.21	
2	HCOOH* ↔ HCOOHpa*	0.24	0.55	0.29	0.59	0.26	0.63
3	HCOOH* + 2* ↔ HCOO** + H*	0.86	1.29	0.42	0.87	0.26	0.98
4	HCOOHpa* + * ↔ COOH* + H*	0.80	1.22	0.44	0.83	0.37	0.87
5	HCOOH* + * ↔ HCO* + OH*	2.32	2.16	1.57	1.91	1.38	1.74
6	HCOO** ↔ CO_2* + H*	-0.35	0.80	-0.17	0.84	-0.08	0.85
7	HCOO** + H* ↔ H_2 + CO_2* + 2*	-0.84	0.99	-0.34	1.11	-0.15	1.30
8	COOH* + * ↔ CO_2* + H*	-0.54	0.54	-0.48	0.68	-0.46	0.74
9	COOH* ↔ COOHcis*	0.05	0.45	0.00	0.52	-0.01	0.44
10	COOHcis* + * ↔ CO* + OH*	1.30	1.33	0.55	0.70	0.51	1.00
11	COOHcis* + H* ↔ CO* + H_2O*	-0.33	0.55	-0.36	0.68	-0.30	0.87
12	HCO* + * ↔ CO* + H*	0.07	0.59	-0.29	0.24	-0.26	0.28
13	OH* + H* ↔ H_2O* + *	-1.64	0.26	-0.92	0.38	-0.81	0.61
14	2H* ↔ H_2 + 2*	-0.49	0.57	-0.17	0.47	-0.07	0.49
15	CO_2* ↔ CO_2 + *	0.02		0.02		0.05	
16	H_2O* ↔ H_2O + *	0.10		0.14		0.20	
17	CO* ↔ CO + *	0.21		0.62		0.67	

3.3.3 Potential Energy Surfaces

The thermochemistry and activation energy barriers of various elementary steps described in the previous sections can be summarized in the form of two-dimensional potential energy surfaces (PESs) for the three Au facets, as shown in Figure 3-9. The PESs shown in Figure 3-9(a-c) compare the HCOO** and COOH* mediated pathways on the three Au facets respectively (a-c). On the basis of the DFT-derived energetics alone, the HCOO** mediated route appears to be the minimum energy path for FA decomposition on Au(100) and Au(211), whereas both HCOO** and COOH* mediated routes appear to be competitive for the Au(111) facet. Figure 3-9(d) compares the HCOO** pathway on all three Au facets, and one can suggest from here that Au(100) and Au(211) are expected to be significantly more active than the Au(111) facet.

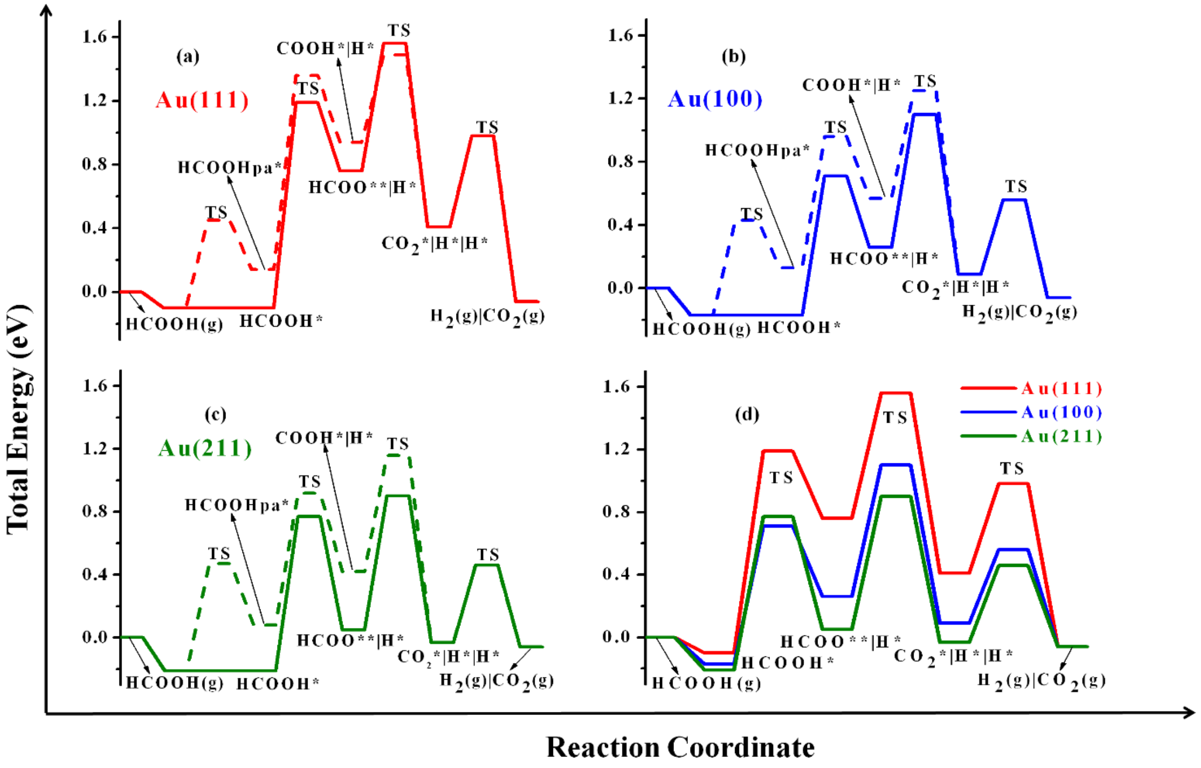

Figure 3-9 The 2-dimensional PESs of FA decomposition reaction via the HCOO (solid lines) and COOH (dashed lines) mediated pathways on Au(111) (red) (a), Au(100) (blue) (b), and Au(211) (green) (c), and a comparison of the most favorable pathways (HCOO mediated)

3.3.4 Microkinetic Modeling

A microkinetic model was developed using the results from these DFT calculations as initial guesses for the model parameters. With no adjustments to the DFT derived parameters, the microkinetic model predicts FA decomposition rates that are 11 and 5 orders of magnitude lower on the Au(111) and Au(100)/Au(211) surfaces, respectively, than the measured experimental rates on Au/SiC. The reaction is predicted to take place via the HCOO mediated route, i.e., HCOOH (g) $\rightarrow$ HCOOH* $\rightarrow$HCOO** + H* $\rightarrow$ CO_2* + 2H* $\rightarrow$ CO_2 (g) + H_2 (g), on all three facets, with 100% selectivity towards the dehydrogenation products; the rate of CO production is predicted to be negligible We next carried out studies in which the kinetic parameters were adjusted from the initial values on these three Au facets in attempts to describe the results from reaction kinetic measurements (Table 3-3) . The adjustable parameters that are modified during this process are the BEs of all surface species and transition state energies of all activated elementary steps. While this procedure gives a total of 26 parameters for our complex reaction network, sensitivity analysis showed that only the BEs of HCOO**, H*, and the transition state energies of the HCOO** formation and direct decomposition steps (steps (3) and (6) in Table 3-2) were sensitive parameters. We then made systematic adjustments in these parameters until reasonable agreement between the experimentally measured and model predicted reaction rates was reached, and we subsequently employed a gradient based optimization algorithm in Matlab to obtain optimized values and confidence intervals for our adjustable parameters. The model predicted reaction orders and apparent activation energy barriers corresponding to the best-fitted solution are reported in Table 3-4, and are in close agreement with their experimental counterparts. In addition, the experimentally observed apparent activation energy barrier (59.6 kJ/mol) in the zero-order kinetic regime is in good agreement with past experimental studies on numerous supported Au catalysts[89, [90, 130]. Figure 3-10 shows the PES for the best fitted solution, compared with the DFT derived PESs for the three Au facets. Here, we only report the energetics of the closed catalytic cycle that is found to carry the entire reaction flux; the energetics of other elementary steps, which do not carry much flux from reactants to products are not included in the figure. We can see from this figure that the adjustments needed in the DFT derived initial guesses to obtain good fits are too large to be attributed to the computational errors in our calculations, which are typically on the order of 0.1 eV – 0.2 eV. With > 0.95 ML of the surface predicted to be vacant under all conditions, we can also rule out any potential stabilization that might result from lateral adsorbate - adsorbate interactions[131]. In particular, an additional stabilization of the transition states for the HCOO** formation and decomposition steps by > 0.5 eV is required to obtain good fits with the experimental data, strongly suggesting that (i) the Au(111), Au(100) and Au(211) may not be the most accurate representation of the active sites for this reaction, and (ii) the active site might be an even more under-coordinated environment that would stabilize the transition states to a much greater extent than these three facets. This conclusion is a quantitative confirmation of a previous proposal put forward by Iglesia and coworkers based on their experimental reactivity studies for the same reaction[89]. Importantly, similar suggestions for the reactivity of single metal atoms or very small metal nanoclusters have been made in the literature for other reactions as well[132-135].

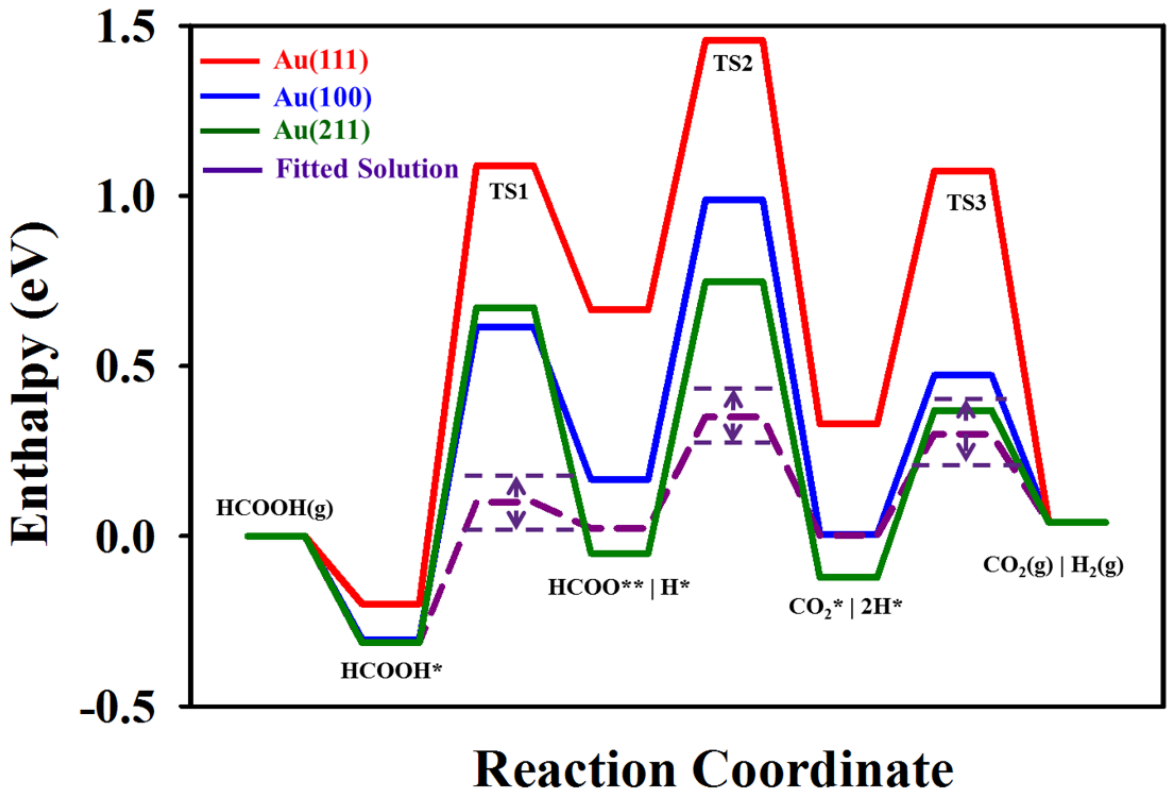

Figure 3-10 Enthalpy surfaces for FA decomposition via the HCOO** mediated pathway on Au(111), Au(100), and Au(211) facets (red, blue, green, respectively) as obtained directly from DFT calculations, and that corresponding to the best fitted solution (violet)

Table 3-4 Experimental and model predicted reaction orders and apparent activation energy barriers.

	Experiment	**Model**
HCOOH	0.95 ± 0.06	0.99
CO_2	0.01 ± 0.003	0.00
H_2	0.01 ± 0.003	0.00
E_A	59.6 ± 1.6 kJ/mol	60.2 kJ/mol

Rate determining step

The individual reaction fluxes of the elementary steps reveal that the overall reaction proceeds entirely through the 'direct HCOO**' route, and no reaction flux is observed through any of the COOH* mediated pathways. We further analyzed the reaction mechanism and the rate determining steps in the reaction scheme using Campbell's degree of rate control, [136-138] which quantifies the kinetic importance of an elementary step in a reaction scheme by computing the relative change in the overall reaction rate upon changing the forward and reverse rate constants for that step, while holding the equilibrium constant for that step as well as the rate constants for all other steps constant. In this formalism, the degree of rate control (X_{RC}) of each elementary step can be evaluated using the following relation:

$$X_{RC,i} = \frac{k_i}{r} \left(\frac{\delta r}{\delta k_i}\right)_{K_{i,eq},k_j} \tag{3.1}$$

where k_i is the rate constant for step i, $K_{i,eq}$ is the equilibrium constant for this step and r is the overall reaction rate. For all equilibrated steps (including the adsorption/desorption steps that were assumed to be quasi-equilibrated), $X_{RC,i}$ is 0. Table 3-5 gives the $X_{RC,i}$ for the kinetically relevant steps in our reaction mechanism. For the ‘best-fitted solution’, Step 6 exhibits the highest degree of rate control for all reaction conditions and hence is the most rate controlling.

Table 3-5 Campbell’s degree of rate control for kinetically relevant steps

Step #	**Elementary Step**	**X_{RC}**
3	$HCOOH^* + 2^* \leftrightarrow HCOO^{**} + H^*$	0.64
6	$HCOO^{**} \leftrightarrow CO_2^* + H^*$	0.25
14	$2H^* \leftrightarrow H_2 + 2^*$	0.10

Active Sites

The results from our microkinetic model suggest that Au(111), Au(100), and Au(211) are, in all likelihood, not the best representation of active sites for this reaction on SiC-supported Au catalysts. Thus, the major contributors to the overall rates could potentially be the Au atoms with lower (< 7) Au-Au coordination that exhibit even greater stabilization of reaction intermediates and transition states than the more open facets studied here ((100) and (211)). To gain further insights into the nature of the active sites, we synthesized different catalyst samples with a varying degree of Au dispersion by treating the initial catalyst in flowing H_2 at different temperatures (623, 673, 723, 973 and 1073 K) for 8 hours, prior to using these materials as catalysts for reaction kinetic studies. Typically, the catalysts that are pre-reduced at low temperatures are more highly dispersed (and less sintered) than the materials that are pre-reduced at high temperatures.

Particle Size distribution:

Figure 3-11 shows representative STEM images of the five catalysts that were used to determine the Au particle size distribution (Figure 3-12) in these samples. This technique allows for imaging Au nanoparticles as low as 0.3 nm in size. It was observed that reducing the catalysts under a H_2 stream at increasingly elevated temperatures resulted in increased averaged Au particle sizes, as reported in Table 3-6.

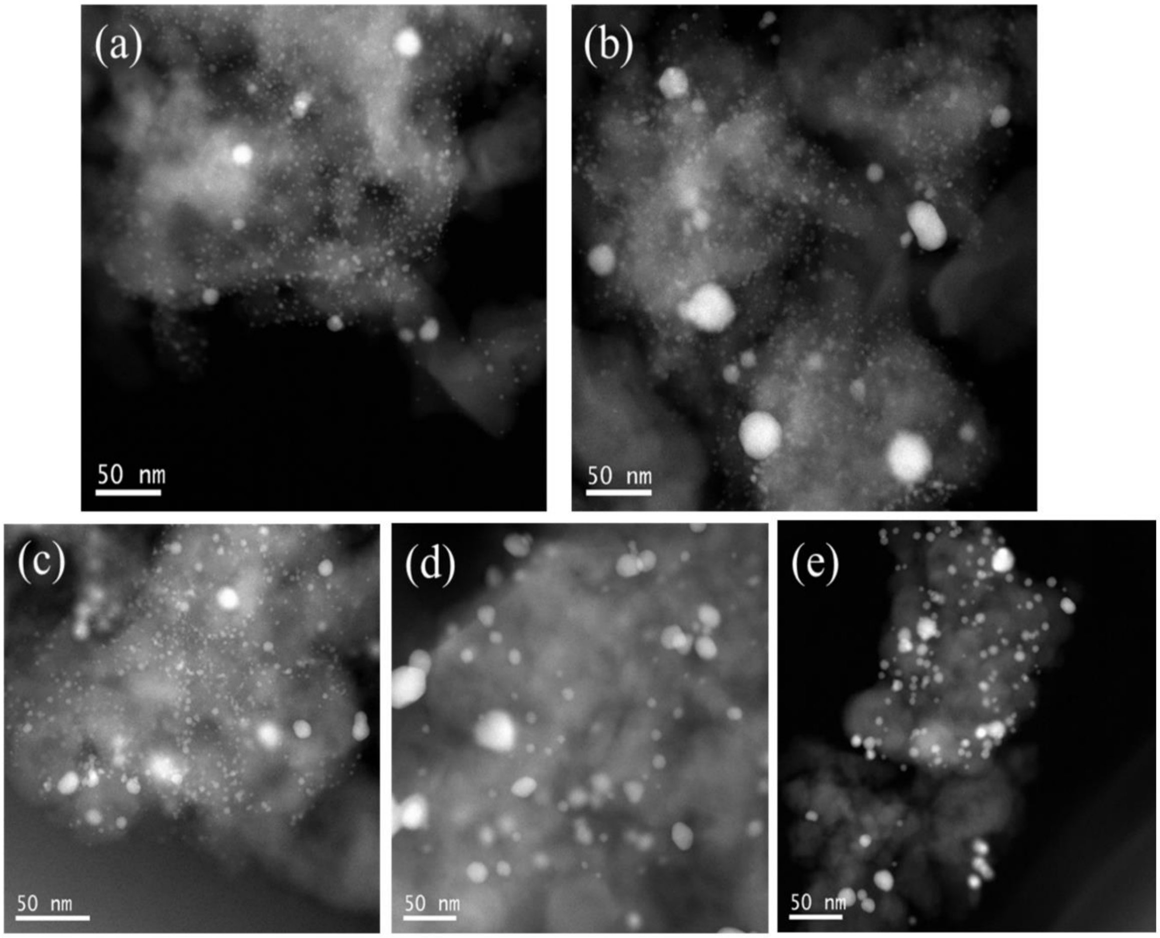

Figure 3-11 Typical TEM images of Au/SiC catalysts used to determine the Au particle size distributions. The pre-reduction temperatures for these catalysts are (a) 623 K, (b) 673 K, (c) 723 K, (d) 973 K and (e) 1073 K.

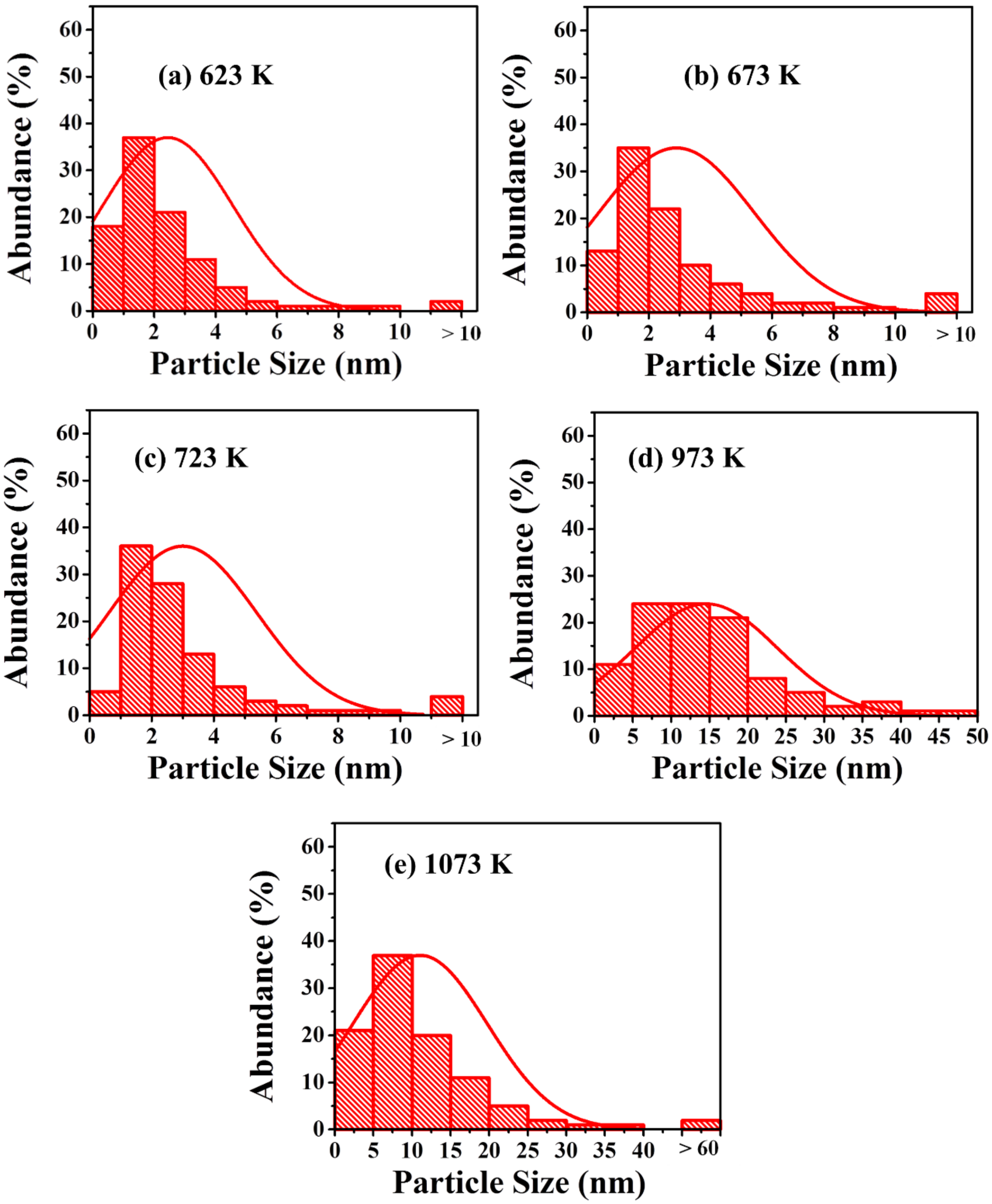

Figure 3-12 Histograms depicting the Au particle/cluster size distributions for the Au/SiC catalysts pre-reduced at 623 – 1073 K for 8 hours.

Kinetic Reaction Rate Measurements: Reaction kinetic measurements were performed to obtain the FA decomposition rates on five catalysts under same operating conditions (T = 413 K, Total inlet flow rate = 100 ml/min, Inlet feed composition = 2.5% FA and 97.5% He). A monotonic decrease in the reaction rates with an increase in the pre-reduction temperature (and the average particle size) was observed, as shown in Table 3-6.

Table 3-6 Average particle size (as determined by STEM) and experimentally measured reaction rates on the five different Au/SiC catalysts.

Catalyst Sample #	**Pre-Reduction Temperature (K)**	**Number of Total /Sub nanometer sized Au Clusters Analyzed**	**Number Average Particle Size (d (nm))**	**Experimentally Observed Reaction Rate (μmol $gcat^{-1}$ min^{-1})**
1	623	6860 / 1248	2.55	178.58
2	673	4837 / 636	3.09	129.93
3	723	3887 / 213	3.23	97.84
4	973	1119 / 0	7.53	9.02
5	1073	1153 / 0	10.74	2.64

Additionally, it is observed that the number (and relative abundance) of sub-nanometer sized Au clusters decreases sharply upon increasing the calcination temperature. Hence, these reactivity trends provide a first indication that the number of sub nanometer sized Au clusters in the catalyst may be correlated with the overall reaction rate. This hypothesis is consistent with past experimental studies[88, 89, 130] that have postulated that this remarkable activity on supported Au catalysts arises from subnanometric Au clusters that are undetected in TEM micrographs. To quantify the contributions of different Au atoms in the catalytic particles/clusters to the overall reaction rate, we first classify the different kinds of Au atoms that are present in any given cluster into four categories: (1) Corner (C) atoms: CN = 1 to 4, (2) Perimeter (P) atoms: CN = 5 and 6, (3) Terrace (T) atoms: CN = 7 to 9 and (4) Bulk (B) atoms: CN ≥ 9, where CN refers to the Au-Au coordination number. Surface (S) atoms are defined as the sum total of the C, P, and T atoms.

In their work on the WGS reaction on supported Au catalysts, Ribeiro and co-workers[139-141] employed physical models of Au clusters as truncated cuboctahedra to develop relations for determining the variation of the C, P, and T sites with the number averaged Au particle size. However, these relations hold true only for particles with diameter (d) > ~1.6 nm. Therefore, and given our TEM data, we attempted to develop physical models of Au clusters with d < 1.6 nm to obtain the corresponding relations that provide the dependence of the C, P, and T sites on the average Au particle size. For that purpose, we used the results of past computational studies which employed DFT to identify the most stable configurations of Au_n clusters (with $2 < n < 20$) in the gas-phase, [142-145] along with our physical models. The relative abundance of the C, P and T sites is highly dependent on the choice of the cluster shape for d < 1.6 nm. Since there is no general agreement in the literature on the most stable structures for these small clusters, a computational methodology must be adopted to this end. This approach would involve modeling a SiC support, performing *ab-initio* molecular dynamics (AIMD)[146-148] simulations to determine the most stable configurations of different sized Au clusters on this support under reaction conditions, and finally counting the number of C, P, and T sites in these configurations to develop the structure-site density relations for quantifying the contributions from each of these sites towards the overall rates. This approach is an ongoing endeavor and will be presented in a future report. However, as a first approximation, we treat these sites together, since the total number/fraction of surface (S) atoms (i.e. C + P + T) is invariant of the actual distribution. In particular, all atoms in clusters of d < 1.6 nm can be assumed to be surface atoms (100% dispersion) without loss of accuracy.

The total moles of surface Au in the catalysts can then be calculated by employing the following relation:

$$Total\ moles\ of\ surface\ Au = \left(\frac{\sum_n f(d)t(d)}{\sum_n t(d)}\right) * Total\ moles\ of\ Au\ in\ the\ catalyst \qquad (3.2)$$

where, *f(d)* is the fraction of surface atoms in the cluster of diameter d (Table 3-7), *t(d)* is the total number of atoms in that cluster, and the summation is performed over all the Au clusters that were identified from the STEM image of that catalyst, i.e., the full particle size distribution was used for each sample. The TOFs normalized to the surface Au moles and total Au moles are plotted against the average particle size in Figure 3-13, and these plots can be used to draw the following key conclusions:

(i) A decreasing trend in the rate per surface site with average Au particle size (Figure 3-13(a)) indicates the heterogeneity of the surface Au sites, i.e., all surface sites do not contribute equally to the overall reaction rate.

(ii) Figure 3-13(b) shows that the rate per total mole of Au catalysts varies as $d^{-2.95}$, whereas Table 3-7 suggests that the fraction of terrace, perimeter, and corner sites vary as $d^{-0.7}$, $d^{-1.8}$, and $d^{-2.9}$ respectively. Thus, the variation in FA decomposition rate per total mole of Au seems to correlate with the ‘corner model’, i.e., the rate per corner site is independent of the Au particle size, thereby implying that corner sites might be the dominant active sites for this reaction. As mentioned earlier, this conclusion is based on the assumption that the $d^{-2.9}$ dependence of the corner sites will be valid over the entire particle size range, and further studies to confirm this for smaller clusters (d <1.6 nm) will be needed.

Table 3-7 Relations used to determine the fraction of different sites from the number-average particle size obtained from the STEM images.

Type of Surface Site → / Particle Size ↓	Terrace (T)	Perimeter (P)	Corner (C)	Surface (S)
< 1.6 nm	#	#	#	1.0
≥ 1.6 nm[139]	$0.90\ d^{-0.7}$	$0.46\ d^{-1.8}$	$0.54\ d^{-2.9}$	$0.90\ d^{-0.7} + 0.46\ d^{-1.8} + 0.54\ d^{-2.9}$

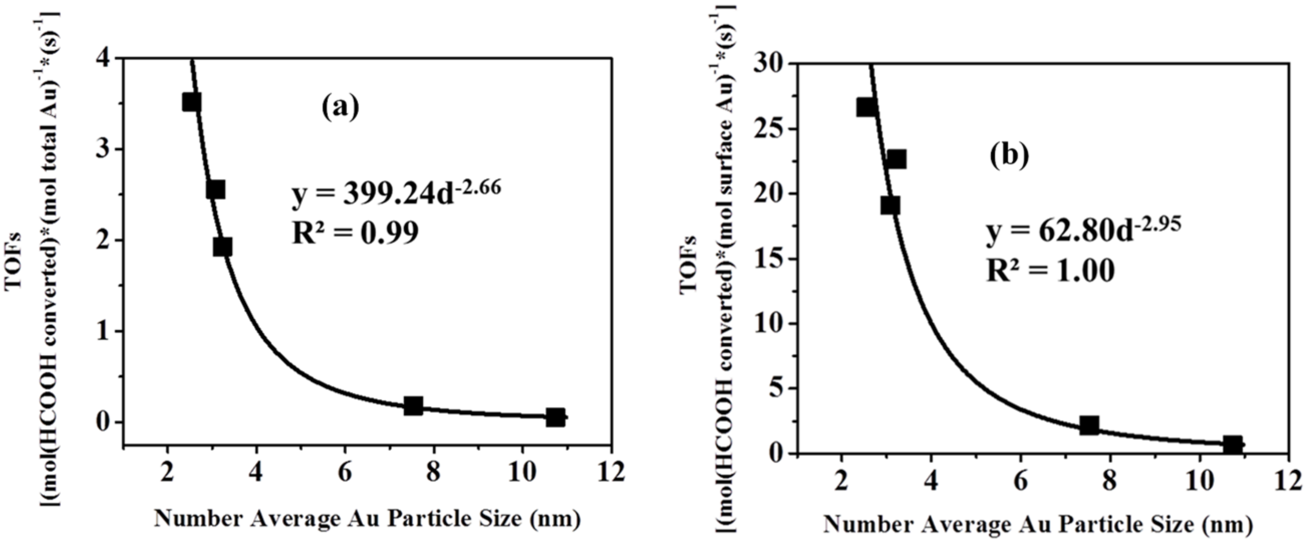

Figure 3-13 FA decomposition rate normalized by (a) surface Au moles and (b) total Au moles (2% FA inlet feed at 413 K, 1 atm) on Au/SiC catalysts.

3.4 Conclusions

Periodic, self-consistent DFT calculations were performed to determine the energetics of 13 adsorbed intermediates for FA decomposition, as well as the activation energy barriers and pre-exponential factors of 13 activated elementary steps on Au(111), Au(100), and Au(211) surfaces, which were chosen as the representative stable model facets of Au nanoparticles on SiC support. The DFT results suggest that the surface species and transition states are stabilized as the Au-Au coordination of surface atoms decreases, and the reaction rates follow the order: Au(211) ≈ Au(100) > Au(111).

A mean field microkinetic model was employed to describe the experimental rate and selectivity data that were collected under realistic conditions on Au/SiC. Our 'best fitted solution' from the microkinetic model shows a good description of the experimental data ($R^2 = 0.98$), and good agreement between the model predicted apparent activation energy barriers and reaction orders with their experimental counterparts. The reaction is predicted to proceed via the formate mediated route. Importantly, the closed catalytic cycle that adequately describes the FA decomposition mechanism on Au catalysts is found to be comprised of three elementary steps: $HCOOH^* \rightarrow HCOO^{**} + H^*$, $HCOO^{**} \rightarrow CO_2^* + H^*$ and $2H^* \rightarrow H_2(g)$.

A comparison of the DFT derived binding energies and activation energy barriers with the parameters obtained upon fitting the microkinetic model to the experimental data suggests that Au(111), Au(100) and Au(211) might not provide the most accurate representation of the active site on supported Au catalysts. Further reaction rate experiments and measurements of the Au particle size distribution using STEM corroborated this claim that the coordinatively unsaturated corner sites, with Au-Au coordination of ≤ 4, are most likely the dominant active sites for this reaction. Further DFT studies on Au clusters that possess atoms with Au-Au coordination number

≤ 4 will be needed to identify the exact nature of active site for FA decomposition on supported Au nanoparticles. We are currently exploring synthetic protocols suggested in the literature[80, 87, 88, 149-152] for synthesizing catalysts with atomically dispersed gold in order to further advance our tentative conclusion regarding the importance of highly under-coordinated Au sites in this chemistry.

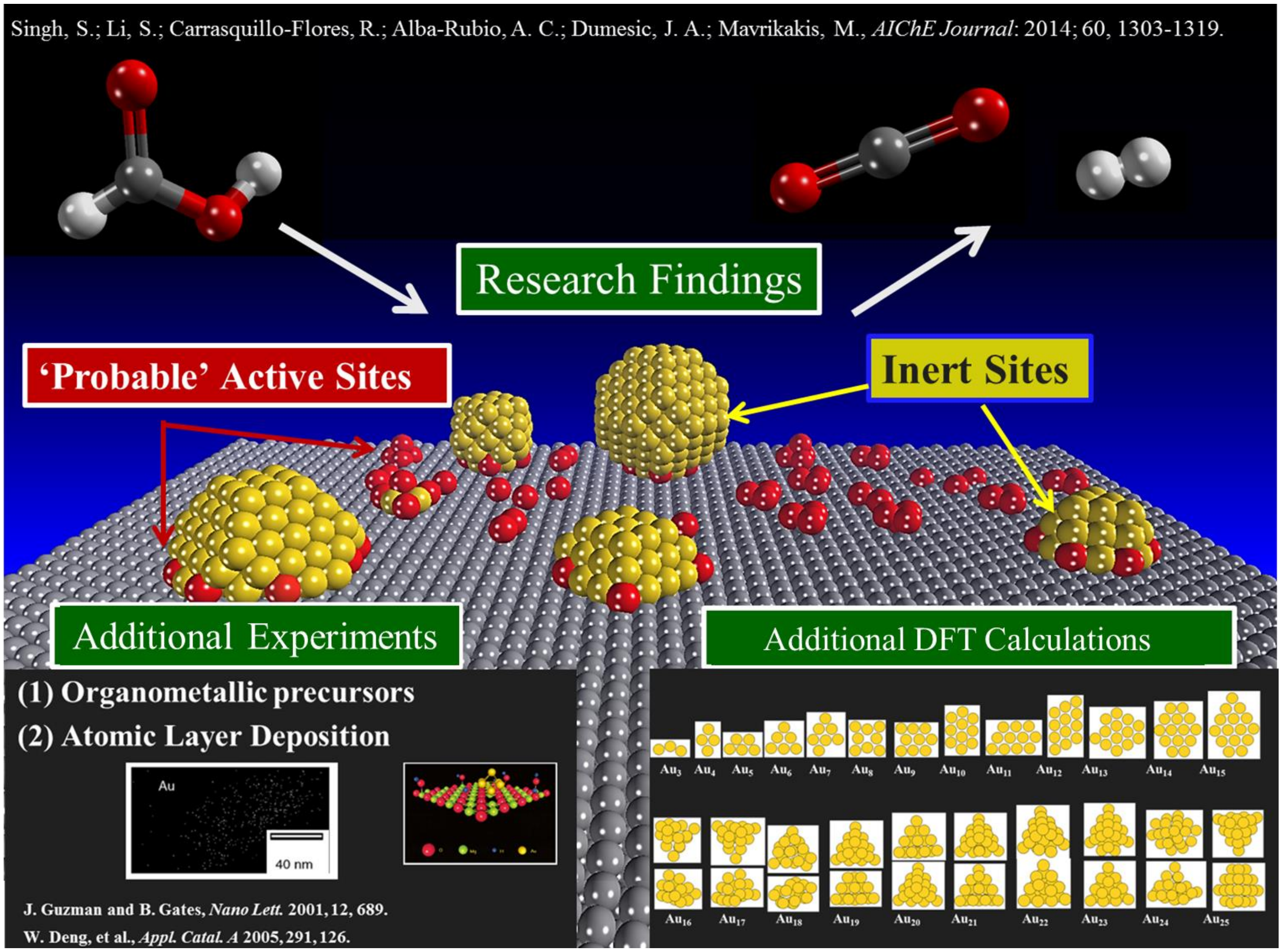

Singh, S.; Li, S.; Carrasquillo-Flores, R.; Alba-Rubio, A. C.; Dumesic, J. A.; Mavrikakis, M., *AIChE Journal*: 2014; 60, 1303-1319.

J. Guzman and B. Gates, *Nano Lett.* 2001, 12, 689.
W. Deng, et al., *Appl. Catal. A* 2005, 291, 126.

3.5 Supplementary Information

Table S. 1 Calculated Vibrational Frequencies of Gas Phase species.

Species	Frequencies [cm^{-1}]
H_2	4430
CO	2205
CO_2	2469, 1351, 629, 623
H_2O	3940, 3825, 1575
HCOOH	3693, 2980, 1725, 1281, 1025, 996, 925, 682, 402

Table S. 2 Calculated PW91 Binding Energies (BE), with (w) and without (w/o) ZPE corrections, and Vibrational Frequencies of Adsorbed Species at their Preferred Adsorption Site on Au(111).

Species	Adsorption Site	BE / eV		Frequencies [cm^{-1}]
		W/O ZPE	W ZPE	
H*	fcc	-2.04	-1.90	879.4, 681.2, 596.5
O*	fcc	-2.46	-2.41	394.2, 250.0, 247.5
OH*	bridge	-1.56	-1.36	3766.3, 576.5, 546.6, 307.3, 165.7, 125.6
H_2O*	top	-0.16	-0.10	3884.4, 3773.4, 1551.2, 339.2, 260.4, 244.4, 71.0, 66.4, 59.7
CO*	top	-0.26	-0.21	2138.5, 229.6, 222.1, 214.2, 82.2, 50.4
CO_2*	physisorbed	-0.05	-0.02	2458.8, 1349.6, 635.8, 634.3, 144.2, 117.6, 49.2, 35.5, 21.2
HCO*	top	-1.20	-1.05	2903.5, 1814.8, 1138.2, 726.9, 458.5, 263.2, 128.4, 121.0, 97.8
HCOO**	top-top	-1.79	-1.69	2927.4, 1575.7, 1303.6, 1285.0, 968.5, 729.4, 289.4, 263.3, 244.8, 107.4, 91.3, 64.6
COOH*	top	-1.35	-1.27	3446.8, 1824.6, 1200.6, 1104.1, 625.9, 588.6, 447.5, 268.6, 208.7, 126.9, 106.9, 85.7

COOHcis*	top	-1.30	-1.22	3622.3, 1765.6, 1230.1, 1042.2, 627.5, 618.6, 399.0, 267.4, 224.9, 103.0, 96.9, 59.3
HCOOH*	top	-0.16	-0.10	3437.4, 3006.4, 1748.5, 1343.8, 1273.0, 1117.5, 998.4, 663.0, 619.7, 144.3, 100.8, 88.8, 77.9, 59.3, 26.7

Table S. 3 Calculated PW91 Binding Energies (BE), with (w) and without (w/o) ZPE corrections, and Vibrational Frequencies of Adsorbed Species at their Preferred Adsorption Site on Au(100).

Species	**Adsorption Site**	**BE / eV**		**Frequencies [cm^{-1}]**
		W/O ZPE	**W ZPE**	
H*	bridge	-2.22	-2.06	1126.5, 1055.9, 361.0
O*	hollow	-2.73	-2.69	250.6, 140.9, 131.8
OH*	bridge	-2.18	-1.96	3789.3, 727.2, 556.4, 317.8, 272.3, 138.5
H_2O*	top	-0.20	-0.14	3875.4, 3760.3, 1547.9, 348.3, 334.8, 147.2, 86.9, 63.9, 30.6
CO*	bridge	-0.68	-0.62	1970.6, 293.5, 283.6, 257.1, 224.6, 88.4
CO_2*	physisorbed	-0.05	-0.02	2455.7, 1350.7, 627.1, 612.1, 116.5, 96.9, 92.1, 65.5, 51.6
HCO*	top	-1.41	-1.26	2868.4, 1803.2, 1167.5, 731.7, 479.6, 254.3, 130.7, 126.8, 116.8
HCOO**	top-top	-2.13	-2.02	2934.5, 1584.7, 1315.2, 1303.5, 976.1, 725.9, 289.1, 281.6, 257.0, 95.1, 87.8, 49.8
COOH*	top	-1.58	-1.48	3763.8, 1671.2, 1199.4, 1125.6, 665.8, 573.9, 432.3, 248.7, 232.5, 147.3, 93.1, 55.3
COOHcis*	top	-1.57	-1.48	3617.3, 1617.3, 1258.0, 1098.3, 652.1, 645.9, 395.5, 261.6, 233.1, 147.1, 59.9, 57.4
HCOOH*	top	-0.22	-0.16	3273.3, 3014.9, 1732.3, 1342.3, 1284.7, 1131.4, 1000.6, 702.5, 629.3, 170.2, 135.2, 90.4, 88.5, 64.2, 51.4

Table S. 4 Calculated PW91 Binding Energies (BE), with (w) and without (w/o) ZPE corrections, and Vibrational Frequencies of Adsorbed Species at their Preferred Adsorption Site on Au(211).

Species	Adsorption Site	BE / eV		Frequencies [cm^{-1}]
		W/O ZPE	W ZPE	
H*	bridge	-2.27	-2.11	1131.7, 1044.7, 393.4
O*	bridge	-2.86	-2.80	434.9, 398.2, 132.4
OH*	bridge	-2.29	-2.07	3804.9, 730.3, 568.7, 309.3, 262.0, 144.0
H_2O*	Off-top	-0.25	-0.20	3864.1, 3711.8, 1547.0, 414.1, 335.1, 144.2, 111.0, 71.3, 55.0
CO*	bridge	-0.73	-0.67	1967.7, 313.5, 274.5, 250.5, 212.8, 121.2
CO_2*	physisorbed	-0.06	-0.05	2454.7, 1349.5, 626.1, 622.1, 111.7, 77.2, 41.6, 35.7, 20.8
HCO*	top	-1.53	-1.38	2876.1, 1808.7, 1176.5, 733.1, 487.3, 220.7, 97.3, 94.5, 82.2
HCOO**	top-top	-2.29	-2.19	2951.7, 1589.5, 1316.7, 1301.1, 971.1, 726.0, 282.8, 277.8, 253.9, 99.4, 93.0, 87.1
COOH*	top	-1.68	-1.58	3764.5, 1637.8, 1209.8, 1134.0, 679.3, 578.1, 436.4, 278.5, 222.0, 157.8, 111.6, 93.1
COOHcis*	top	-1.68	-1.59	3604.6, 1578.9, 1268.5, 1117.7, 664.6, 660.1, 406.8, 282.9, 234.5, 167.6, 114.8, 105.9
HCOOH*	top	-0.28	-0.21	3378.6, 3023.9, 1719.3, 1342.2, 1286.0, 1117.7, 998.9, 702.7, 631.7, 179.4, 158.4, 93.9, 79.6, 58.1, 45.6

Table S. 5 PW91 reaction energies (ΔE), activation energy barriers (EA) for the elementary steps considered in the HCOOH decomposition reaction network on Au(111), with (w) and without (w/o) ZPE corrections. All the values are relative to the infinite separation of species in the initial/final states.

#	Reaction	Adsorbate Interaction / eV IS / FS	ΔE / eV		E_A / eV	
			W/O ZPE	W ZPE	W/O ZPE	W ZPE
1	HCOOH + * ↔ HCOOH*	- / -	-0.16	-0.10		
2	HCOOH* ↔ HCOOHpa*	- / -	0.24	0.24	0.60	0.55
3	HCOOH* + 2* ↔ HCOO** + H*	- / -0.06	1.02	0.86	1.46	1.29
4	HCOOHpa* + * ↔ COOH* + H*	- / -0.03	0.96	0.80	1.44	1.22
5	HCOOH* + * ↔ HCO* + OH*	- / -0.15	2.42	2.32	2.27	2.16
6	HCOO** ↔ CO_2* + H*	- / 0.00	-0.21	-0.35	0.86	0.80
7	HCOO** + H* ↔ H_2 + CO_2* + 2*	-0.06 / 0.00	-0.71	-0.84	1.08	0.99
8	COOH* + * ↔ CO_2* + H*	- / 0.00	-0.39	-0.54	0.74	0.54
9	COOH* ↔ COOHcis*	- / -	0.05	0.05	0.50	0.45
10	COOHcis* + * ↔ CO* + OH*	- / -0.07	1.41	1.30	1.48	1.33
11	COOHcis* + H* ↔ CO* + H_2O*	-0.04 / -0.04	-0.39	-0.33	0.59	0.55
12	HCO* + * ↔ CO* + H*	- / 0.04	0.23	0.07	0.77	0.59
13	OH* + H* ↔ H_2O* + *	-0.03 / -	-1.80	-1.64	0.26	0.26
14	2H* ↔ H_2 + 2*	0.01 / -	-0.49	-0.49	0.59	0.57
15	CO_2* ↔ CO_2 + *	- / -	0.05	0.02		
16	H_2O* ↔ H_2O + *	- / -	0.16	0.10		
17	CO* ↔ CO + *	- / -	0.26	0.21		

Table S. 6 PW91 reaction energies (ΔE), activation energy barriers (EA) for the elementary steps considered in the HCOOH decomposition reaction network on Au(100), with (w) and without (w/o) ZPE corrections. All the values are relative to the infinite separation of species in the initial/final states.

#	Reaction	Adsorbate Interaction / eV IS / FS	ΔE / eV		E_A / eV	
			W/O ZPE	W ZPE	W/O ZPE	W ZPE
1	HCOOH + * ↔ HCOOH*	- / -	-0.22	-0.16		
2	HCOOH* ↔ HCOOHpa*	- / -	0.29	0.29	0.65	0.59
3	HCOOH* + 2* ↔ HCOO** + H*	- / 0.01	0.56	0.42	1.09	0.87
4	HCOOHpa* + * ↔ COOH* + H*	- / -0.01	0.56	0.44	1.02	0.83
5	HCOOH* + * ↔ HCO* + OH*	- / -0.22	1.64	1.57	2.00	1.91
6	HCOO** ↔ CO_2* + H*	- / 0.00	-0.06	-0.17	1.02	0.84
7	HCOO** + H* ↔ H_2 + CO_2* + 2*	0.01 / -	-0.19	-0.34	1.29	1.11
8	COOH* + * ↔ CO_2* + H*	- / 0.00	-0.34	-0.48	0.90	0.68
9	COOH* ↔ COOHcis*	- / -	0.01	0.00	0.58	0.52
10	COOHcis* + * ↔ CO* + OH*	- / -0.04	0.62	0.55	0.78	0.70
11	COOHcis* + H* ↔ CO* + H_2O*	-0.01 / -0.05	-0.41	-0.36	0.77	0.68
12	HCO* + * ↔ CO* + H*	- / -0.01	-0.16	-0.29	0.40	0.24
13	OH* + H* ↔ H_2O* + *	-0.02 / -	-1.03	-0.92	0.45	0.38
14	2H* ↔ H_2 + 2*	-0.03 / -	-0.13	-0.17	0.53	0.47
15	CO_2* ↔ CO_2 + *	- / -	0.05	0.02		
16	H_2O* ↔ H_2O + *	- / -	0.20	0.14		
17	CO* ↔ CO + *	- / -	0.68	0.62		

Table S. 7 PW91 reaction energies (ΔE), activation energy barriers (EA) for the elementary steps considered in the HCOOH decomposition reaction network on Au(211), with (w) and without (w/o) ZPE corrections. All the values are relative to the infinite separation of species in the initial/final states.

#	Reaction	Adsorbate Interaction/eV IS / FS	ΔE / eV		E_A / eV	
			W/O ZPE	W ZPE	W/O ZPE	W ZPE
1	HCOOH + * ↔ HCOOH*	- / -	-0.28	-0.21		
2	HCOOH* ↔ HCOOHpa*	- / -	0.31	0.26	0.68	0.63
3	HCOOH* + 2* ↔ HCOO** + H*	- / 0.20	0.40	0.26	1.20	0.98
4	HCOOHpa* + * ↔ COOH* + H*	- / 0.02	0.49	0.37	1.06	0.87
5	HCOOH* + * ↔ HCO* + OH*	- / -0.03	1.47	1.38	1.85	1.74
6	HCOO** ↔ CO_2* + H*	- / 0.00	0.04	-0.08	1.03	0.85
7	HCOO** + H* ↔ H_2 + CO_2* + 2*	0.20 / 0.00	0.02	-0.15	1.39	1.30
8	COOH* + * ↔ CO_2* + H*	- / 0.00	-0.31	-0.46	0.96	0.74
9	COOH* ↔ COOHcis*	- / -	0.00	-0.01	0.50	0.44
10	COOHcis* + * ↔ CO* + OH*	- / 0.15	0.58	0.51	1.10	1.00
11	COOHcis* + H* ↔ CO* + H_2O*	0.02 / 0.02	-0.34	-0.30	0.95	0.87
12	HCO* + * ↔ CO* + H*	- / 0.02	-0.14	-0.26	0.43	0.28
13	OH* + H* ↔ H_2O* + *	0.08 / -	-0.92	-0.81	0.69	0.61
14	2H* ↔ H_2 + 2*	-0.02 / -	-0.02	-0.07	0.55	0.49
15	CO_2* ↔ CO_2 + *	- / -	0.06	0.05		
16	H_2O* ↔ H_2O + *	- / -	0.25	0.20		
17	CO* ↔ CO + *	- / -	0.73	0.67		

Chapter 4

Self-Consistent Solutions from DFT, Microkinetic Modeling and Experiments: Formic Acid Decomposition on Cu catalysts[2]

4.1 Introduction

Formic Acid (FA) decomposition on transition metal catalysts is a very well-studied system, both in heterogeneous catalysis and surface science. This reaction is of applied interest because of FA's potential as a liquid hydrogen carrier[153] with a high H:C ratio and a closed carbon cycle.[41, 153-157] FA is used as a fuel in direct FA fuel cells that operate at low temperatures and have been shown to exhibit better efficiency than alcohol fuel cells.[158, 159] Also, FA is an equimolar byproduct in the production of levulinic acid from biomass,[30, 43] and can be utilized in situ to provide H_2 for the subsequent hydrogenation of levulinic acid to gamma-valerolactone.[44, 160] Additionally, FA, being the simplest carboxylic acid, has been widely used to probe the catalytic properties of metals[50, 53, 60, 89, 114, 161, 162], metal oxides[61-63, 65], metal carbides[57-59], and alloys. Early work for FA decomposition reaction on Cu catalysts involved infrared, kinetic isotope effect, and decomposition rate measurements that shed some light on the mechanistic aspect of this reaction. Subsequently, Madix and coworkers, in their pioneering work on Cu single crystals[55, 59, 163, 164] demonstrated the key role of a very stable formate species in this reaction; this work resulted in a series of studies on Cu single crystals that continue till date.[164-171]

---

[2] S. Li and J. Scaranto contributed to the DFT results reported in this study. B.O'Neill provided the experimental dataset on Cu catalysts.

Despite the abundance of experimental studies for FA decomposition on Cu catalysts, there is a lack of general consensus regarding the active site and reaction mechanism. Iglesia and Boudart[161, 172-174] observed that the turnover rates for this reaction were insensitive to the particle size, and to the nature of support. Their results, together with several other studies that reported similar activation energy barriers for this reaction on preferentially oriented and polycrystalline Cu catalysts, [175-182] suggested that this reaction was structure insensitive. Additionally, they suggested that the catalytic FA decomposition was a bimolecular process, in which the HCOO decomposition was assisted by adsorbed FA molecules.

In contrast to these findings, Bowker and coworkers[164, 166-171, 183] showed that FA does not undergo dissociation on clean Cu(111), and that the presence of pre-dosed oxygen is required for it to exhibit any appreciable reaction rates. Clean Cu(100) and Cu(110), on the other hand, were shown to be active for this reaction under same conditions. More recently, Nakamura and coworkers[184, 185] demonstrated that formic acid decomposition was structure sensitive, with distinctively different activation energy barriers for HCOO decomposition step on Cu(111) as compared to Cu(100); they also demonstrated a strong promotional effect of H_2 co-feed on the rate of this reaction only on Cu(111), and showed that HCOO decomposition was enhanced 17 times in the presence of H_2, only on Cu(111) and not on Cu(100).

The importance and contemporary relevance of microkinetic modeling as a tool for performing comparisons between experiments and DFT predictions has been highlighted in Chapters 1 and 3. Since parameter estimation using microkinetic modeling is essentially a non-convex optimization problem,[186] the final solution, and the ensuing conclusions that are drawn from this solution, depends on the initial guesses for the thermodynamics and kinetics parameters that are obtained from DFT calculations on representative model surfaces. Hence, the importance of ensuring the accuracy of these DFT derived parameters in order to obtain reliable predictions from the microkinetic model cannot be overstated. The two primary sources of errors in these parameters are (a) the inherent errors associated with DFT calculations, and (b) the errors that arise when the model surface used in DFT calculations doesn’t accurately represent the active site and/or the surface environment under reaction conditions. While the recent advances in computational techniques have contributed towards quantifying and minimizing the former, it is the inconsistency between the surface environment (surface coverages of most abundant reaction intermediates) predicted by the model, and that employed in the DFT calculations, that is often overlooked. In this study, we employ a rigorous, iterative approach for microkinetic modeling that ensures self-consistency between the surface environment employed in the DFT calculations and that predicted by the model, and discuss the possible ramifications that this might have on the final conclusions regarding the active sites on a catalyst.

Hence, the objective of this work is two-fold, to (1) demonstrate a rigorous, iterative methodology in action that yields holistically self-consistent solutions, and (2) employ this method to resolve the unsatisfying status quo that exists regarding the reaction mechanism, nature of active sites, and structure sensitivity for FA decomposition reaction on Cu catalysts.

4.2 Methods

4.2.1 DFT Calculations

Several key elementary steps in the FA decomposition reaction network on Cu(111) were studied and reported in our earlier work, as part of the methanol synthesis reaction network.[12] For consistency, we employ the same setup here, for all additional DFT calculations on Cu(111) and Cu(100) surfaces; a description of these methods is included below.

All calculations were performed using the DACAPO total energy code.[91, 92] The Cu(111) surface was modeled by a three-layer slab with a p(3×3) unit cell, corresponding to 1/9 monolayer (ML) coverage for a single monodentate adsorbate in the unit cell, periodically repeated in a super cell geometry with five equivalent layers of vacuum between any two successive metal slabs. All the Cu atoms in the Cu(111) surface were kept fixed in their bulk truncated positions, as our systematic investigations showed that surface relaxation does not have a significant effect on the energetics for this system. The super cell used to model the Cu(100) facet consists of a p(3x3) unit cell with four layers of metal atoms, top two of which were allowed to relax, and five equivalent layers of vacuum spacing separating the periodic slab images.

Adsorption was allowed on only one of the two exposed surfaces for all three slabs, and the electrostatic potential was adjusted accordingly.[93, 94] The surface Brillouin zone of (111) slabs was sampled at 54 special Chadi-Cohen[95] k points, while that for the (100) slabs was sampled by using a 4×4×1 Monkhorst-Pack[96] k-point mesh. Ionic cores were described by ultrasoft Vanderbilt pseudo-potentials[97] and the Kohn-Sham one-electron valence states were expanded in a basis of plane waves below a kinetic energy of 25 Ry. The exchange-correlation energy and potential were described self-consistently using the generalized gradient approximation (GGA-PW91).[98, 99] The electron density was determined by iterative diagonalization of the Kohn-Sham Hamiltonian, Fermi population of the Kohn-Sham states ($k_BT = 0.1$ eV), and Pulay mixing of the resulting electronic density.[100] All total energies were then extrapolated to $k_BT = 0$ eV. The calculated equilibrium lattice constant for bulk Cu was found to be 3.66 Å, in good agreement with the experimental value of 3.62 Å.[187]

The binding energies (BEs) were calculated with respect to the total energy of the clean slabs (E_{slab}) and the corresponding adsorbates in the gas phase ($E_{adsorbate,\ gas\text{-}phase}$), i.e., $BE_{adsorbate} = E_{total} – E_{slab}$ -

$E_{adsorbate, gas\text{-}phase}$. In the discussion of the DFT results, we refer to electronic energy values including the zero point energy (ZPE) corrections unless otherwise noted. Throughout the text, (g) stands for ‘gas phase species’ and each '*' represents a single surface site occupied by the corresponding adsorbate. Our calculations do not take into account the long-range interactions, such as van der Waals forces,[104, 105] which may contribute an additional stabilization of ~ 0.1 eV – 0.2 eV per carbon atom.

The minimum energy pathways and activation energy barriers for all elementary steps were determined using the climbing image nudged elastic band (CI-NEB) method.[102, 188, 189] The minimum energy path for each elementary step was discretized with at least seven images, in addition to the initial and final states. A vibrational frequency analysis[103] was performed to confirm the true nature of the saddle point by identifying a single imaginary frequency along the reaction coordinate. The frequencies were calculated using the harmonic oscillator assumption by diagonalization of the mass-weighted Hessian matrix in internal coordinates obtained with a displacement of 0.01 Å.[103, 190] While it is straightforward to define the translational and rotational modes for gas phase species using its center of mass and principle moments of inertia,[25] it is relatively difficult to unambiguously define these frustrated modes for adsorbed species. Hence, we only treat the two frustrated translational modes of adsorbed species characterized by changes of position of the center of mass within the plane parallel to the substrate surface separately. Vibrational and frustrated rotational modes are then obtained by diagonalization of the remaining Hessian matrix.

4.2.2 Experiments

Synthesis of Cu/γAl_2O_3

Cu was deposited onto γ-Al_2O_3 (Strem) using $Cu(NO_3)_2$ x $3H_2O$ (Acros) dissolved in water via incipient wetness. The γ-Al_2O_3 support had been crushed, and the sieved fraction between 36 and 100 μm was dried for 1 hour at 110 °C before impregnation. It had a surface area of 210 m^2 g-1 as determined by BET. After deposition, the catalyst was dried for an additional 1 hour at 110 °C, followed by reduction in flowing H_2 at 300 °C (0.6 °C/min, 5 hours). After reduction, the catalyst was passivated in flowing 1%O_2/Ar at room temperature. The copper surface site density was determined to be 53 μmol g^{-1} using a standard N_2O chemisorption method.[191]

Kinetic Experiments

Reaction kinetics measurements were carried out using a quarter-inch stainless steel tube as a flow reactor. A fixed-bed, down-flow configuration was maintained by using a quartz wool plug at the bottom and top of the catalyst bed. The reactor was filled to the top of the heating zone with fused SiO_2 to facilitate heat transfer. The reactor was heated via aluminum blocks in a well-insulated furnace. The temperature was measured by type-K thermocouples (Cole Parmer) and controlled by a PID controller (Love Controls Series 16A) connected to a variable transformer (Staco Energy Products). Prior to reaction kinetics studies, the catalyst was reduced in-situ at 300 °C (0.6 C min^{-1} ramp) for 5 h. The flow rates of co-fed gasses (UHP grade, Airgas) were controlled using a mass flow controller (Hastings), and the total gas flow rate out of the system was measured using a bubble meter. The formic acid (Sigma-Aldrich, 98-100%) was used as purchased and was fed to the reactor from a stainless steel syringe and a high pressure syringe pump (Harvard Apparatus). For all experiments, gas analysis was carried out utilizing a Shimadzu GC-8A gas chromatograph with a HaySep DB 100/120 column (Alltech) and a thermal conductivity detector to detect CO and CO_2. A Shimadzu GC2014 gas chromatograph with an FID detector was used to detect gas phase alkanes, including methane, but none were detected under the conditions employed in this study. Gas phase analysis was performed throughout the duration of the experiment.

4.2.3 Microkinetic Modeling

Mean-field microkinetic modeling was employed to describe the experimentally measured FA conversions, apparent activation energy barrier, and reaction orders apropos of all gaseous components. The different aspects of the model development are reported below:

Reaction Network:

Table 4-2 includes a list of elementary steps for which the thermochemistry and kinetics was obtained using DFT calculations on clean Cu(111) and Cu(100) surfaces. These steps represent various pathways for FA decomposition: the direct and 'adsorbate-assisted' HCOO, COOH and HCO pathways, and were explicitly considered in the microkinetic model for the two surfaces. The ‘high-coverage’ models comprised of an abridged version of this reaction network, as shown in Table 4-6.

Model Inputs:

(1) DFT derived parameters: The microkinetic model was parameterized in terms of the Shomate parameters of the gas phase reactants and products, most stable adsorption states of all reaction intermediates, and the transition states of all activated elementary steps. The temperature and ZPE corrected reaction enthalpies and entropies of all these states were used to calculate the equilibrium constants, pre-exponential factors, and forward/reverse reaction rate constants for all elementary steps, using the relations described in Chapter 2.

(2) Experimental data: The experimental data that was used in this study comprised of the inlet flow rates of all gaseous components, reaction temperature, total pressure, total number of active sites in the catalyst, and the experimentally determined FA conversions and selectivity to CO_2.

Adjustable parameters and objective function:

The objective function that was used to quantitatively compare and assess the different solutions and the corresponding fits, was the normalized sum of squared residuals (nSSR); which is a measure of the absolute difference between the experimental and model predicted flow rates of the gaseous products.

$$nSSR = min\left(\sum_{i\in n}\sum_{j\in G}\left(\frac{M_{ji}^{out}}{E_{ji}^{out}} - 1\right)\right) \tag{4.1}$$

Where M_{ji}^{out} and E_{ji}^{out} are the model predicted and experimental outlet flow rates for species *j* and experimental condition *i*. The summation is performed over the flow rates of all outlet species (G) for all experimental conditions (n).

An additional metric that we have used in this study to compare the quality of different solutions is the mean absolute error (MAE), defined as MAE $= {}^{\sum_i abs\,(TOF_{model} - TOF_{experiment})}/_{n}$, where TOF stands for turnover frequencies.

The DFT derived enthalpies of thermodynamic /transition states were chosen to be the adjustable parameters for fitting purposes, while the surface entropies and pre-exponential factors were fixed to their DFT derived values..

Model Formulation

The model was formulated as a plug flow reactor (PFR), which comprised of 5 differential equations (one for each gaseous flow rate) and 7 algebraic equations (one each for all reaction intermediates, and an additional one for the vacant site), is a way described by Madon et al.[7] The inbuilt MATLAB solvers and optimization routines were employed to solve these equations and perform subsequent parameter estimation. In addition to starting with the exact DFT derived numbers as the initial guesses, we decided to sample the parameter space in the vicinity of these numbers (± 40 kJ/mol from the DFT derived initial guesses for each adjustable parameter). In this study, we have adopted a manual approach for sampling the parameter space, an automated multi-start approach using latin hypercube sampling has recently been reported by Nason et al.[186]

Rate Controlling Steps

Campbell's degree of rate control (X_{RC}) is employed to analyze the reaction mechanisms and quantitatively determine the rate determining steps for a set of experimental conditions. This approach quantifies the kinetic importance of an elementary step in a reaction scheme by computing the relative change in the overall reaction rate upon changing the forward and reverse rate constants for that step, while holding the equilibrium constant for that step as well as the rate constants for all other steps constant. In this formalism, the degree of rate control (X_{RC}) of each elementary step can be evaluated using the following relation:

$$X_{RC,i} = \frac{k_i}{r} \left(\frac{\delta r}{\delta k_i}\right)_{K_{i,eq},k_j} \tag{4.2}$$

Where k_i is the rate constant for step i, $K_{i,eq}$ is the equilibrium constant for this step and r is the overall reaction rate.

4.3 Results and Discussion

In this section, the results are presented in the order that preserves and highlights the logical progression and evolution of this project, where we started from a clean Cu(111) surface for our initial DFT calculations and eventually obtained a good description of the active site and surface environment for FA decomposition on supported Cu catalysts, under reaction conditions.

4.3.1 Cu(111) – 'Clean'

In our quest to conclusively determine the active site for this reaction on Cu catalysts, we first chose a Cu(111) model surface for our DFT calculations to obtain the thermodynamic and kinetic parameters for the elementary steps considered in the reaction mechanism. Cu(111) is the thermodynamically most stable Cu facet, it has been shown to be the preferentially exposed facet for supported Cu catalysts via TEM studies,[192] and has been proposed to be active for several reactions involving small oxygenates. HCOO species has for long been considered a key surface intermediate for several reactions on Cu(111); however, despite an overwhelming spectroscopic evidence of its existence under reaction conditions on Cu catalysts, its exact surface coverage under these conditions has never been quantified. In the absence of any definitive knowledge regarding the surface environment under reaction conditions, we employed a 'clean' Cu(111) facet (no spectator species) for our initial set of DFT calculations.

DFT Calculations

The adsorption geometries for the most stable binding configurations of all surface species on Cu(111) are illustrated in Figure 4-1, and a summary of the binding energies and preferred adsorption sites is included in Table 4-1. Table 4-2 reports the reaction energies and activation energy barriers for all elementary steps involved in this reaction network.

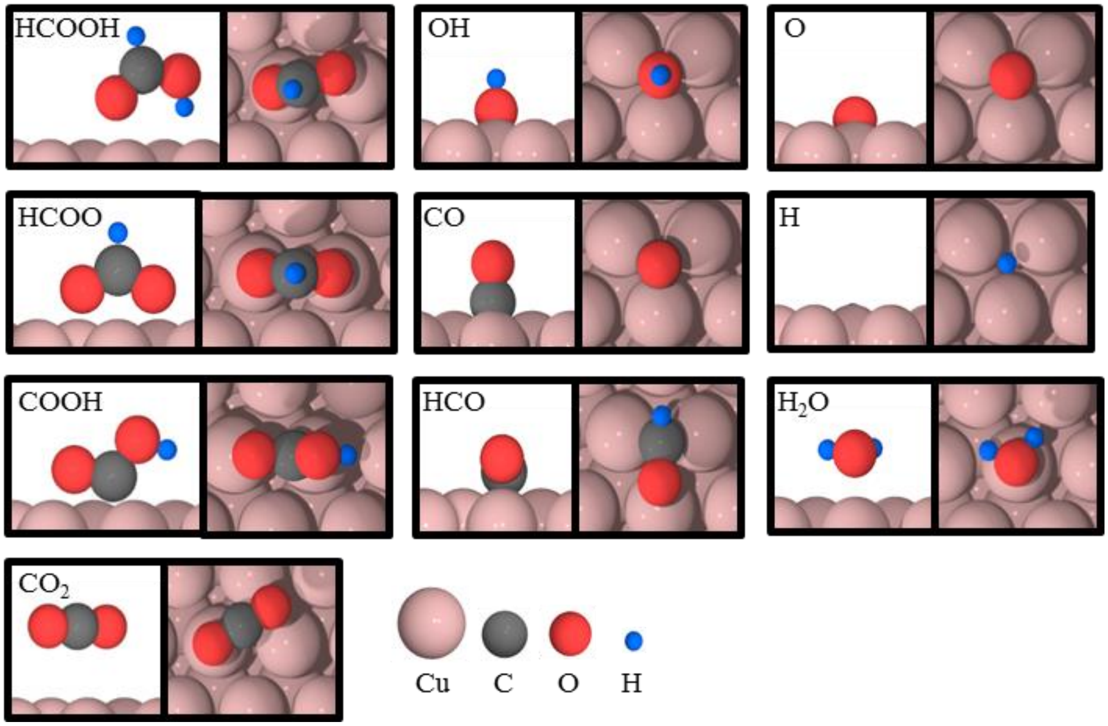

Figure 4-1 Most stable adsorption configurations for all surface adsorbates on Cu(111). The pink, grey, red and blue spheres represent Cu, C, O, and H atoms respectively

Table 4-1 Preferred Adsorption Sites and ZPE-Corrected PW91 Adsorption Energies (BE) of Surface Species on Clean Cu(111)

Species	**Adsorption Site**	**BE / eV**
H*	Fcc	-2.26
O*	Fcc	-4.18
OH*	Fcc	-2.61
H_2O*	Top	-0.16
CO*	Fcc	-0.82
CO_2*	No-Preference	-0.06
HCO*	Bridge	-1.07
HCOO*	Top-Top	-2.57
COOH*	Top	-1.44
HCOOH*	Top	-0.16

Table 4-2 ZPE-Corrected Reaction Energies and Activation Energy Barriers for all Elementary Steps on Clean Cu(111)

#	**Reaction**			**ΔE / eV**	**E_A / eV**
1[a]	HCOOH + *	↔	HCOOH*	-0.16	-
2[a]	HCOOH* + 2*	↔	HCOO** + H*	-0.33	0.48
3[a]	HCOOH* + *	↔	COOH* + H*	0.49	1.13
4[a]	HCOOH* + *	↔	HCO* + OH*	1.10	1.52
5[a]	HCOO**	↔	CO_2* + H*	0.15	0.95
6	HCOO** + O*	↔	CO_2* + OH* + *	-0.48	1.43
7	HCOO** + OH*	↔	CO_2* + H_2O* + *	0.06	1.64
8	HCOO** + H*	↔	H_2 + CO_2* + 2*	0.37	1.91
9[a]	HCOO**	↔	HCO* + O*	2.06	2.25
10[a]	COOH* + *	↔	CO_2* + H*	-0.68	0.98
11[a]	COOH* + *	↔	CO* + OH*	-0.26	0.33
12	COOH* + O*	↔	CO* + H_2O*	-1.31	-0.32
13[a]	COOH* + OH*	↔	CO_2* + H_2O*	-0.77	-0.44
14	COOH* + H*	↔	CO* + H_2O*	-0.35	1.14
15	HCOO* + COOH*	↔	HCOOH* + CO_2*	-0.35	0.11
16[a]	HCO* + *	↔	CO* + H*	-0.87	0.07
17[a]	CO* + O*	↔	CO2* + *	-1.05	0.65
18[a]	O* + H*	↔	OH* + *	-0.62	0.88
19[a]	2OH*	↔	H_2O* + O*	0.53	0.53
20[a]	OH* + H*	↔	H_2O* + *	-0.09	1.09
21	2H*	↔	H_2 + 2*	0.23	0.74
22[a]	CO*	↔	CO + *	0.82	-
23[a]	CO_2*	↔	CO_2 + *	0.06	-
24[a]	H_2O*	↔	H_2O + *	0.16	-

[a] : These values have been taken from our earlier publication.[12]

Preliminary insights from microkinetic modeling suggest that several elementary steps that have high activation energy barriers (> 1.5 eV) are highly unlikely to have any reaction flux under the operating conditions employed in this study; although all these steps have been explicitly included in the microkinetic model, we only provide succinct, in-text comments on some key elementary steps that were found to be part of the catalytic cycle and the surface intermediates that are formed during the course of the reaction; all relevant information pertaining to the other elementary steps and reaction intermediates can be found in the tables.

The most stable adsorption configuration for FA (HCOOH) is one in which all its atoms lie in a plane perpendicular to the surface. It binds to the surface via its carbonyl O atom on a top site, with the C-H and O-H bonds pointing away and towards the surface, respectively, and has a BE of -0.16 eV.[193, 194] The potential importance of the formate intermediate (HCOO) for this reaction has been highlighted in earlier sections; it binds in a bidentate configuration with both its O atoms binding to the adjacent top sites of the Cu(111) surface, consistent with the experimental observations, [195, 196] and has a BE of -2.57 eV.[193, 197] Atomic hydrogen (H) binds preferentially on the three fold sites, with a BE of -2.26 eV[193, 197]; both the fcc and hcp sites are found to be energetically quasi-degenerate. CO_2 binds extremely weakly to the surface (BE = -0.06 eV) and does not exhibit a site preference for its most stable adsorption configuration, as evidenced by the near degeneracy of its several adsorption states.

For the reaction conditions employed in our experiments, FA decomposition is found to proceed via a direct dehydrogenation pathway that involves HCOO intermediate. First, HCOOH dehydrogenation to HCOO proceeds directly from its most stable perpendicular configuration, and the HCOO-H bond cleavage takes place over a bridge site (Figure 4-2A). The E_A for this step is 0.48 eV (ΔE = -0.33 eV).[66, 193] The significantly higher activation energy barriers of 1.13 eV and 1.52 eV for the two alternate initial bond breaking steps, FA dehydrogenation to COOH and its dehydroxylation to HCO, respectively, explain why these steps do not contribute to the reaction rates. The second dehydrogenation step, HCOO conversion to CO_2 and H involves rotation of the HCOO molecule such that the C-H bond is aligned towards the surface; one Cu-O bond is first cleaved, followed by a C-H bond scission over a bridge site (Figure 4-2B), with an activation energy barrier of 0.95 eV.[198] The C-H bond length in the transition state is 1.52 Å, as compared to 1.11 Å in adsorbed HCOO. H_2 recombinative desorption starts from the two H atoms on adjacent three-fold sites, and the H-H bond formation takes place over a bridge site (Figure 4-2C), with a bond length of 0.97 Å, as compared to an H_2 gas phase bond length of 0.75 Å, and an activation energy barrier of 0.74 eV.[66, 197, 199, 200]

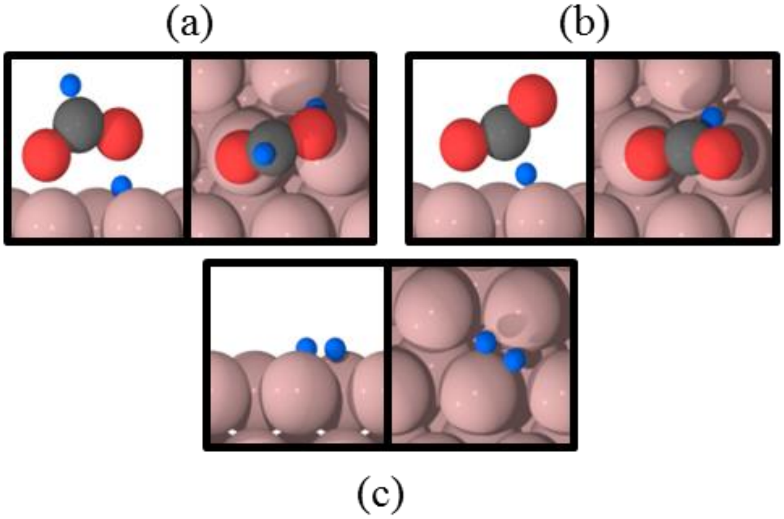

Figure 4-2 Side and top views of the transition states for the three key elementary steps: (A) HCOOH → HCOO + H, (B) HCOO → CO_2 + H, (C) 2H → H_2 (g) on Cu(111) surface.

Microkinetic Modeling:

A microkinetic model that was parameterized using the DFT derived thermodynamics and kinetics parameters was employed to analyze this reaction mechanism and perform comparisons with the experimental kinetic dataset. Prior to making any adjustments in the DFT derived initial guesses, the model predicts 100% conversion for all reaction conditions; the surface is predicted to be completely clean, and the reaction is found to proceed via the sequence of elementary steps described in the section above: $HCOOH \rightarrow HCOO + H \rightarrow CO_2 + 2H \rightarrow CO_2 + H_2$, with the first step being the rate controlling step. Since the DFT derived parameters for Cu(111) were inadequate to describe the experimental observations on supported Cu catalysts, we performed parameter optimization to try and obtain improved fits with the experimental data.

With a complex model that has 30 adjustable parameters being used to fit a kinetic dataset comprising of 18 unique conditions, one could expect multiple solutions that yield reasonably good fits with the experimental observations. Hence, in addition to employing the DFT derived parameters as the initial guesses, we sampled the parameter space in the vicinity of these initial guesses to ensure that we do not miss a feasible solution. As a result of this exercise, we found two unique solutions that provided excellent fits with the experimental dataset, both of which were able to successfully emulate the experimentally observed apparent activation energy barrier and the reaction orders for the reactants and products. Henceforth, we will refer to the two solutions as the 'HCOO solution' and the 'H solution', for reasons that will become apparent in the following section. A discussion on these two solutions is presented below:

(1) HCOO solution

Starting from the DFT derived parameters as the initial guesses, the reaction rate was found to be most sensitive to the binding energies of HCOO and the transition state energies of the direct HCOO formation and decomposition steps (Steps 2 and 5 in Table 4-2). Small (< 0.1 eV), successive adjustments were made in the most sensitive parameters until the model predictions and experimental reaction rates matched. Full optimization of the model was then performed (by nonlinear least-squares data fitting, using the nlinfit function in Matlab that makes use of the Gauss-Newton algorithm), to refine the fit and obtain the final, optimized set of parameters.

The parity plot of the experimental and model predicted TOFs corresponding to the best fit solution is shown in Figure 4-3A; it has an MAE of 0.0004 sec^{-1} and an NSSR value of 0.98.

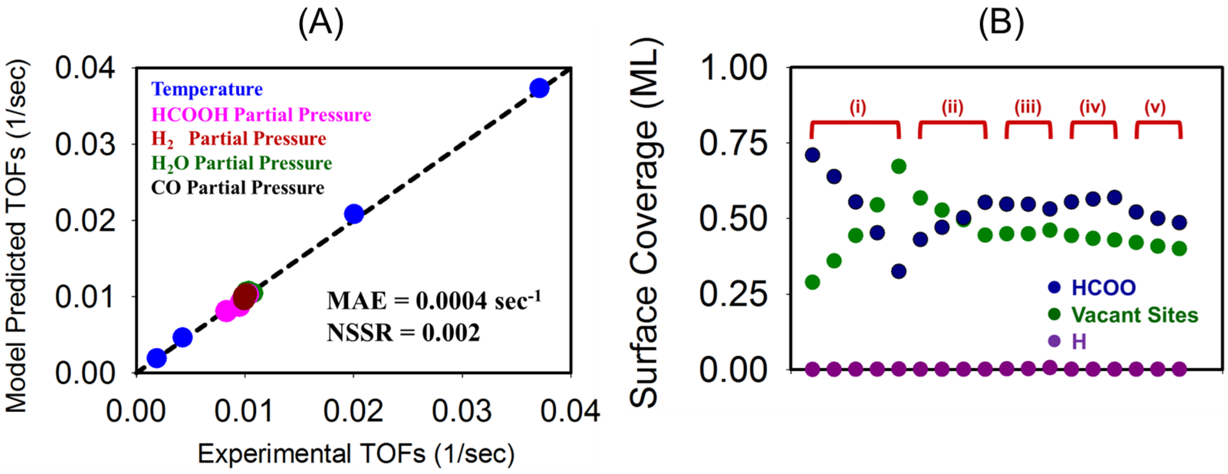

Figure 4-3 (A) Parity plot of experimental and model predicted TOFs. The different colored circles reporesent the different set of experiments. The H_2O and CO partial pressure variation points are hidden behind the H_2 Partial Pressure (dark red). (B) Surface coverage (ML) of the most abundant surface intermediates for the different experimental conditions (i) Temperature (ii) HCOOH PP (iii) H_2 PP) (iv) H_2O PP (v) CO PP variation

The adjustments made to the DFT derived initial guesses in order to obtain this solution are reported in Table 4-3 and Table 4-4. While the transition state energies for both HCOO formation and decomposition steps required modest stabilizations of -0.04 eV and -0.09 eV respectively, both of which are within the DFT error bars, the HCOO intermediate had to be stabilized by -0.32 eV. The surface was predicted to have 0.33 ML – 0.71 ML of adsorbed HCOO, the remaining sites being vacant. The HCOO surface coverage decreased (increased) with increasing temperature (FA partial pressure), accompanied by a commensurate change in the number of vacant sites. For the majority of experiments that were performed at 130°C, the ‘home temperature’ for obtaining H_2/H_2O/CO reaction orders, the HCOO surface coverage was nearly constant, ~ 0.55 ML. Campbell’s degree of rate control was calculated for all the elementary steps, and HCOO decomposition was found to be the rate controlling step under all reaction conditions, as reported in Table 4-4.

(2) H- solution

The ‘multi-start’ approach led us to an alternate solution that exhibited near-identical fits with the experimental data as the preceding HCOO solution. The quality of the fit between the model predicted and experimental TOFs is shown in Figure 4-4, and the adjustments that were required in the DFT derived parameters in order to obtain this fit are reported in Table 4-3 and Table 4-4. To obtain these fits, the transition state for the H_2 recombination step was destabilized by 0.43 eV, while those for HCOO formation and decomposition steps were stabilized by -0.18 eV and -0.22 eV respectively. The surface was predicted to have an H coverage of 0.51 ML -0.76 ML, with the remaining sites being vacant. H_2 recombination was found to be the predominantly rate controlling step under all reaction conditions, as reported in Table 4-4.

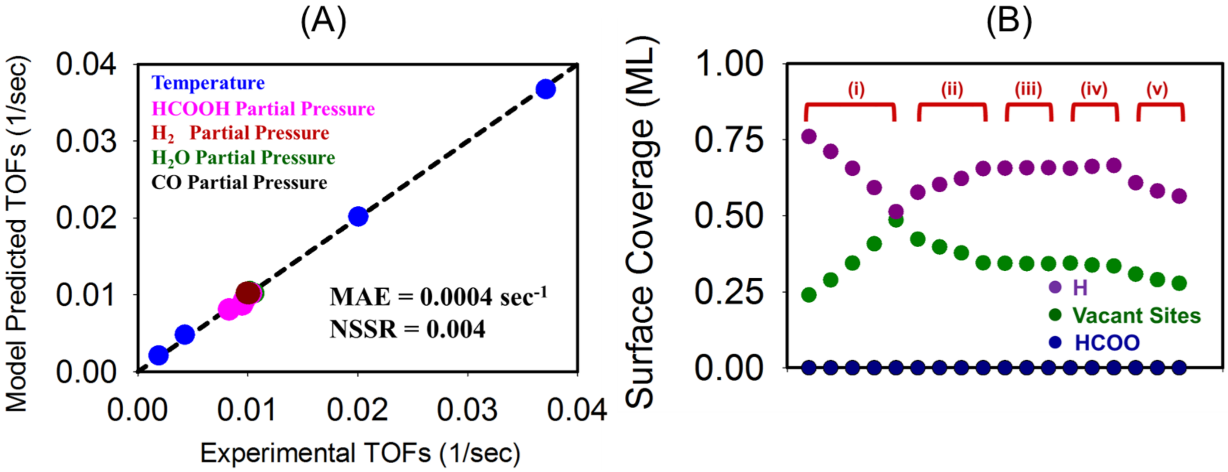

Figure 4-4 (A) Parity plot of experimental and model predicted TOFs. The different colored circles represent the different set of experiments. The H_2O and CO partial pressure variation points are hidden behind the H_2 Partial Pressure (dark red). (B) Surface coverage (ML) of the most abundant surface intermediates for the different experimental conditions (i) Temperature (ii) HCOOH PP (iii) H_2 PP (iv) H_2O PP (v) CO PP variation.

Table 4-3 Adjustments needed in the DFT derived binding energies on clean Cu(111) corresponding to the best fit

Species	HCOO Solution ΔBE / eV	H Solution ΔBE / eV
H*	0.00	-0.01
HCOO**	-0.32	0.00

Table 4-4 Adjustments needed in the DFT derived transition state energiees corresponding to the best fit, and the Cambell's degree of rate control (XRC) for the kinetically relevant elementary steps on clean Cu(111)

Reaction			HCOO Solution		H Solution	
			ΔETS / eV	XRC	ΔETS / eV	XRC
HCOOH* + 2*	↔	HCOO** + H*	-0.04	0.11-0.30	-0.18	0.01-0.02
HCOO* + *	↔	CO_2* + H*	-0.09	0.57-0.88	-0.22	0.15-0.27
2H*	↔	H_2 + 2*	0.00	0.00-0.01	0.43	0.62-0.83

After careful sampling of the parameter space, we were able to establish, with reasonable confidence, that the two solutions presented here were the only ones that were able to accurately describe all the experimental measurements: including the reaction orders, apparent activation energy barrier, and turnover frequencies. An enthalpy surface that compares the DFT derived energetics with those corresponding to 'HCOO solution' and 'H solution', at 130°C, is shown in Figure 4-5.

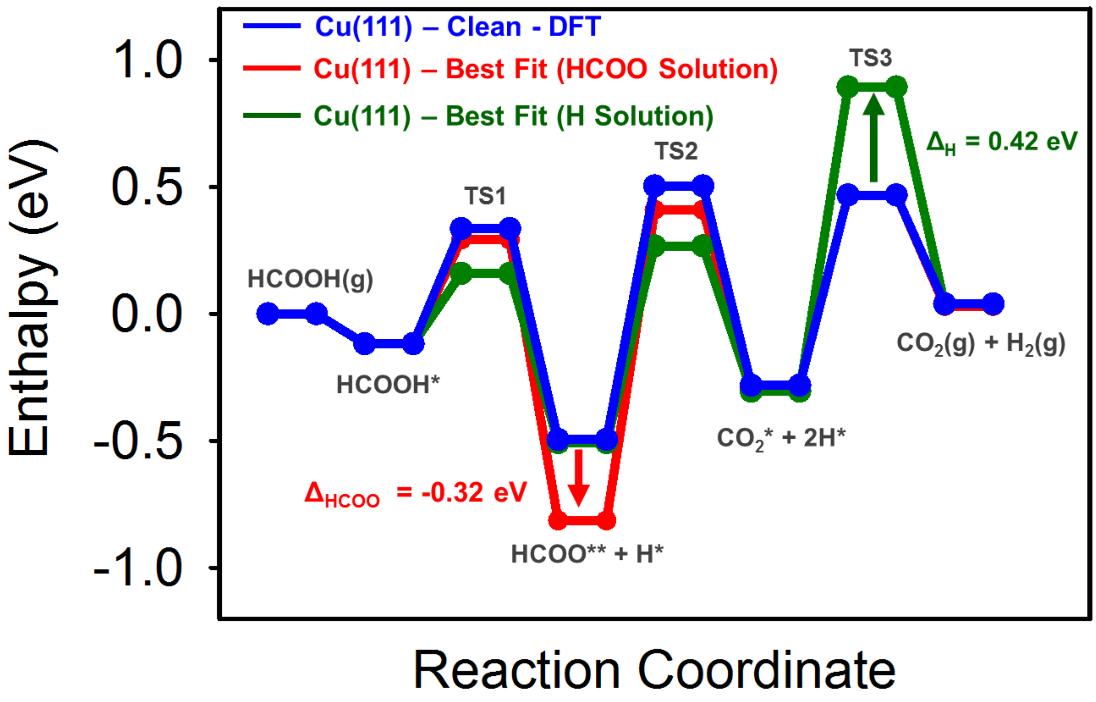

Figure 4-5 2-dimensional PESs of FA decomposition reaction via the HCOO pathway on clean Cu(111). Zero-energy corresponds to the gasphase enthalpy of FA molecule. The blue line corresponds to the DFT derived PES, and the red and green lines reflect the enthalpies of the thermodynamic and transition states for the HCOO solution and H solution, respectlively. The maximum adjustments made for both these solutions is also reported.

Although the thermodynamics and kinetic parameters used in the model were all collected on a clean Cu(111) surface, both solutions predicted substantial coverages of either HCOO or H species on the surface. Hence, there exists a disparity between the model predicted surface environment and one that was employed in the DFT calculations, and a direct comparison of the optimized thermodynamic and kinetic parameters obtained from microkinetic modeling with their DFT derived counterparts is logically fallacious. This merits further investigation, and we attempted to close this gap by performing additional DFT calculations with appropriately chosen unit cells, as described below.

4.3.2 Cu(111) - High Coverage

HCOO solution

The model predicted surface coverage of HCOO for this solution was found to vary with the experimental conditions, within a range of 0.32 ML and 0.70 ML. It should be noted here that since HCOO is a bidentate species, (a) the surface concentration of HCOO species is half that of the predicted surface coverage (in ML), and (b) for DFT calculations on a 3x3 unit cell, its coverage can only be varied in increments of 2/9 ML (as opposed to 1/9 ML for monodentate species). We decided to perform our high-coverage calculations in presence of 4/9 ML of 'spectator' HCOO, which corresponds to two HCOO species, in a (3x3) Cu(111) unit cell; this surface will be referred to as the ‘Cu(111)-HCOO’ in the subsequent sections.

DFT Calculations

HCOOH is found to exhibit significantly strong binding in presence of 2 spectator HCOO species, with a BE of -0.55 eV, as opposed to -0.16 eV on the clean slab. This is primarily because of H-bonding that exist between the hydroxyl H of HCOOH and the neighboring oxygen atom of the HCOO species, with the distance between two atoms being 1.49 Å, as illustrated in Figure 4-6A and further accentuated in Figure 4-14A. Also, the most stable binding configuration of HCOOH is one where it binds to the surface via the O atom on the bridge site (Figure 4-6A), compared to the top site on clean Cu(111). The most stable adsorption configuration of HCOO species, in presence of 2 spectator formates, is a bidentate form where one of the two O atoms is slightly displaced from the top site of Cu(111) (Figure 4-6C), and exhibits a slightly weakened binding of -2.40 eV (-2.57 eV on the clean slab). Also, in contrast with the clean surface, we found a stable monodentate adsorption state for HCOO intermediate that binds to the surface through one O atom on the hcp site (Figure 4-6B), with a BE of -2.16 eV. The existence of a monodentate HCOO on

Cu(111) was reported by Gokhale et al.[25] wherein they had employed a (2x2) unit cell for their calculations, which further underlines the importance of surface coverage effects on the structural stability of adsorbed states. As it did on the clean slab, H atom occupies a hollow site with a BE of -2.26 eV, identical to that on the clean slab.

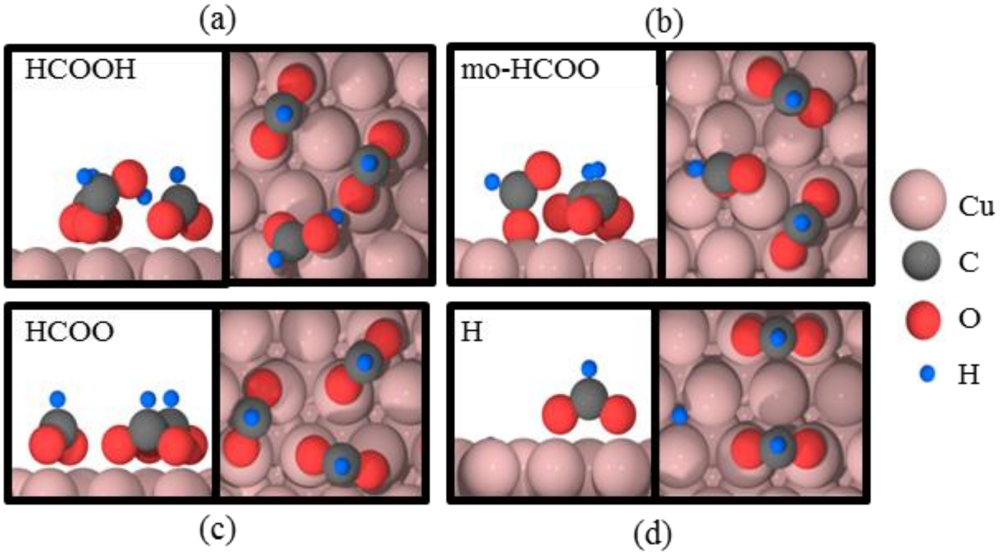

Figure 4-6 Most stable adsorption configurations for all surface adsorbates on a HCOO-covered Cu(111). The pink, grey, red and blue spheres represent Cu, C, O, and H atoms respectively

The activation energy barrier for HCOOH dehydrogenation to HCOO in presence of 4/9 ML of spectator HCOO is 1.01 eV ($\Delta E = 0.23$ eV), which is much higher than on the clean slab, primarily because the initial state is stabilized due to H-bonding. Also, the HCOO-H bond scission takes place on a 3-fold site, as opposed to a bridge site on the clean slab.

In contrast with the clean slab, the HCOO decomposition to CO_2 in presence of HCOO spectator species is a two-step process. The first step is the rotation of bidentate HCOO that involves an O-Cu bond cleavage, and results in a metastable monodentate ‘mo-HCOO’ intermediate; this step has an activation energy barrier (reaction energy) of 0.30 eV (0.24 eV). This intermediate then undergoes dehydrogenation to form CO_2 and adsorbed H, with an $E_A = 0.49$ eV and $\Delta E = -0.20$

eV. The recombinative desorption of H_2 from adsorbed H atoms is the step that is least affected by the presence of spectator HCOO species; it has an E_A and ΔE of 0.84 eV and 0.23 eV respectively, similar to the clean slab values of 0.74 eV and 0.23 eV.

Microkinetic Modeling:

With no adjustments to the DFT derived parameters on high HCOO-covered surface, the model under predicts the rates by 2 orders of magnitude. Starting from this curtailed model with a revised set of initial guesses for the DFT parameters, we perform parameter optimization and obtain good fits with the experimental data, much the same way as described in the earlier sections.

Table 4-7 and Table 4-8 report the adjustments that were made in the DFT parameters in order to obtain these fits. The model predicts a HCOO surface coverage of 0.34 ML – 0.72 ML; hence, from the surface coverage standpoint, this is a self-consistent solution in that the model predicted surface coverages are consistent with those employed in DFT calculations. However, while the adjustments made in most parameters are within the DFT error bar (0.2 eV), the HCOO binding energy requires stabilization by -0.51 eV. This adjustment is too large to be attributed solely to the errors in our DFT calculations. Hence, based on this solution alone, we cannot claim Cu(111) to be the active site.

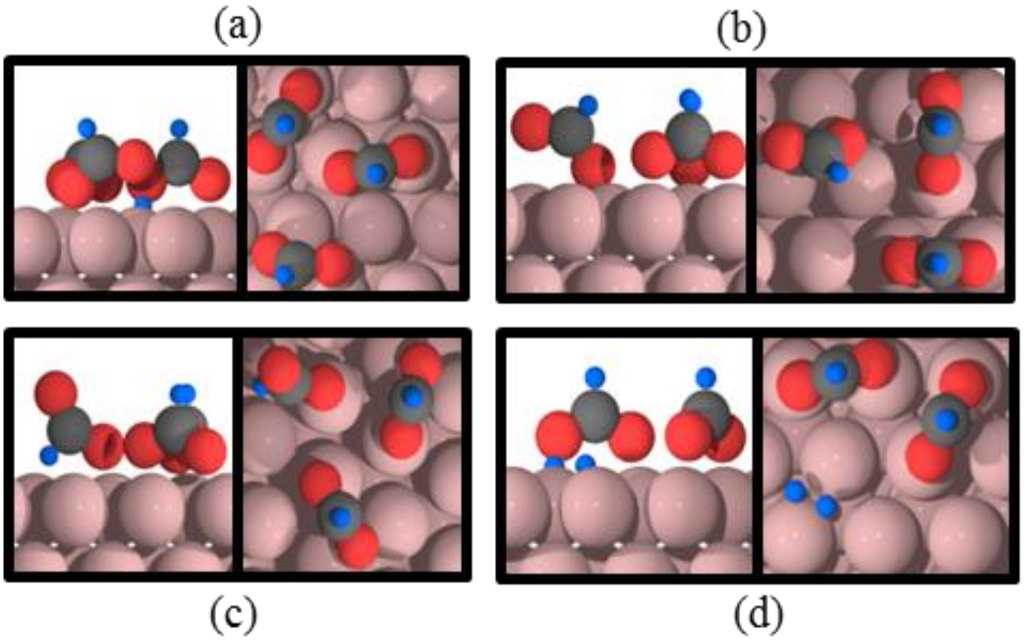

Figure 4-7 Side and top views of the transition states for the four key elementary steps: (A) HCOOH → HCOO + H, (B) HCOO → mo-HCOO (C) mo-HCOO → CO2 + H, (D) 2H → H_2 (g) on a HCOO covered Cu(111) surface.

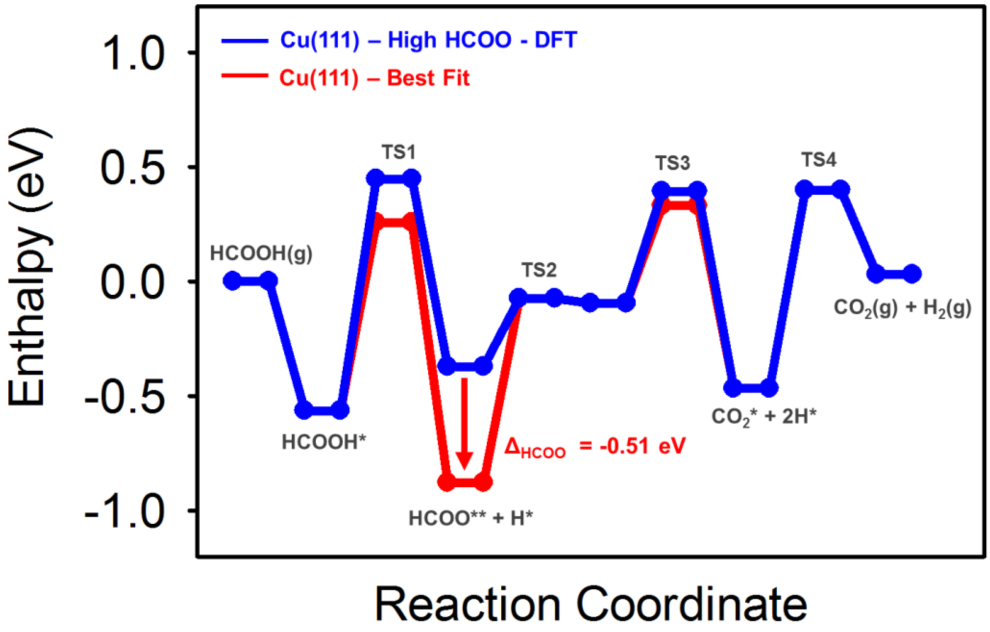

Figure 4-8 2-dimensional PESs of FA decomposition reaction via the HCOO pathway on a HCOO-covered Cu(111) surface. Zero-energy corresponds to the gasphase enthalpy of FA molecule. The blue line corresponds to the DFT derived PES, and the red line corresponds to the best-fit solution. The adjustment required in the binding energy of HCOO is also reported.

H Solution

The alternate, ‘H-solution’ suffered from the same surface-coverage inconsistencies, as it predicted high H coverages on the surface when the DFT derived initial guesses were obtained from the calculations on a clean Cu(111) facet. Hence, we performed further DFT calculations using a unit cell that mimics the surface coverages predicted by the microkinetic model to address this issue. For the ‘best-fit’ solution, the microkinetic model predicts H surface coverage in the range of 0.51 ML - 76 ML depending on the reaction temperature; for the majority of the experiments that were performed at 130°C, this coverage is predicted to be ~0.66 ML. For these reasons, we decided to repeat the DFT calculations on a unit cell that has 0.66 ML of pre-adsorbed H as spectator species. As was the case for the HCOO-solution, we decided to only repeat these calculations for the ‘key elementary steps’, i.e., the steps that were found to be part of the closed catalytic cycle.

DFT Calculations

HCOOH exhibits very weak binding (BE = -0.03 eV), with several energetically degenerate adsorption configurations, one of which is shown in Figure 4-9A. HCOO binds preferentially in a bidentate configuration, however, one of the 2 O atoms now binds on the bridge site, as opposed to both of them being on the top sites on the clean slab (Figure 4-9B). This results in a significantly weaker binding (BE = -1.96 eV, as opposed to -2.57 eV on the clean slab). Figure 4-9C shows the most stable adsorption configuration of 7 H atoms on the surface; all the H atoms are found to occupy the hollow sites and the differential BE of the seventh H atom is -2.09 eV, as opposed to the BE of -2.26 eV of H on clean Cu(111) .

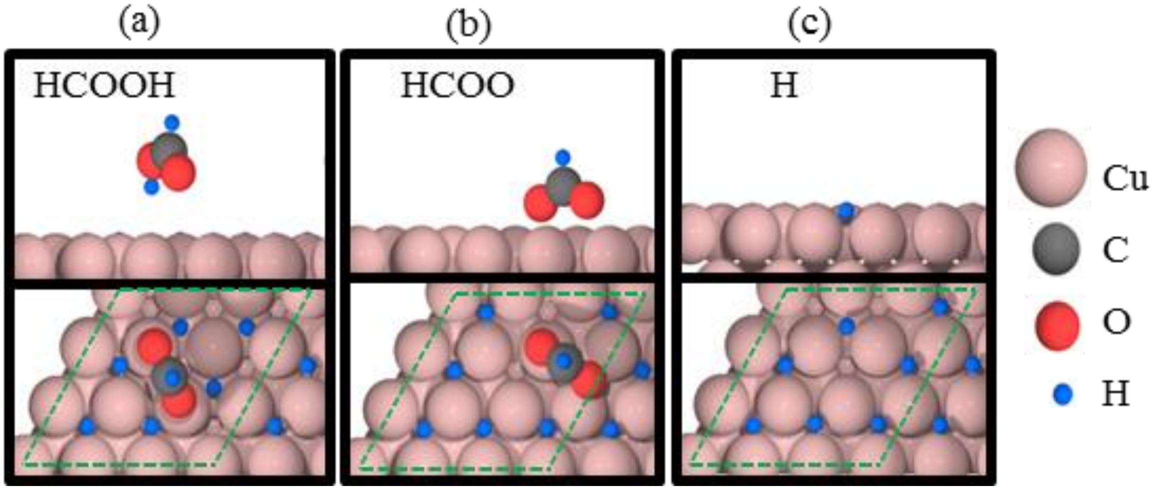

Figure 4-9 Most stable adsorption configurations for all surface adsorbates on a H-covered Cu(111). The pink, grey, red and blue spheres represent Cu, C, O, and H atoms respectively

HCOOH decomposition to HCOO + H has an activation energy barrier of 0.77 eV, with ΔE = 0.32 eV, and the O-H bond scission takes place over a threefold site, as opposed to a bridge site on clean Cu(111). The transition state geometries of HCOO dehydrogenation and H_2 recombination are both very similar to their clean-slab counterparts, and this is reflected in their activation energy barriers. Although these barriers are arguably similar to those on the clean slab, the corresponding transition states have substantially higher energies, due to the significant destabilizations in the initial states of these steps; this is illustrated in the enthalpy surface shown in Figure 4-11.

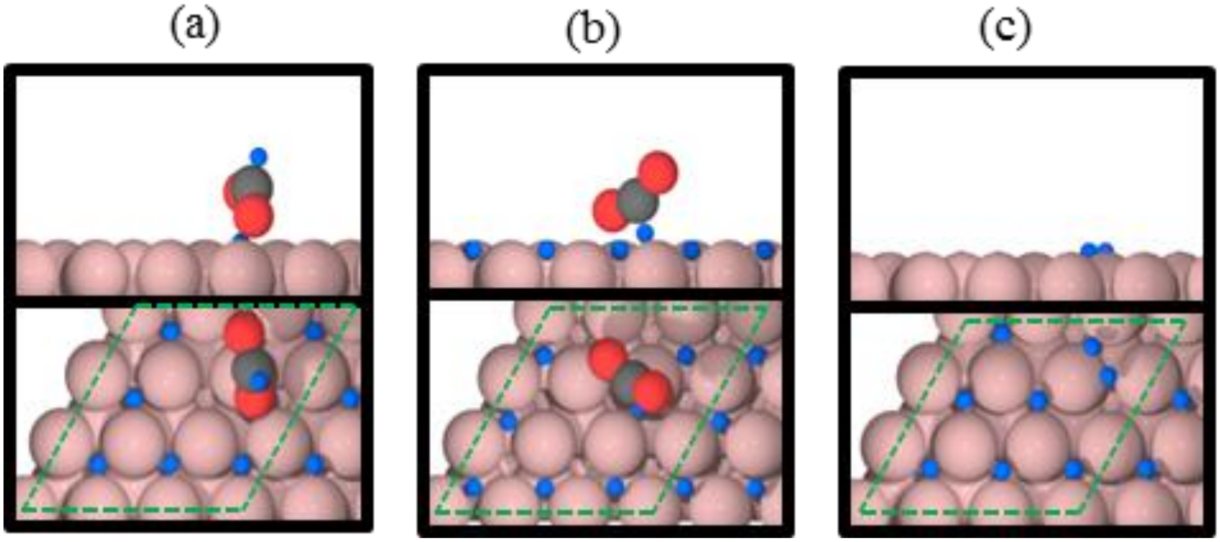

Figure 4-10 Side and top views of the transition states for the three key elementary steps: (A) HCOOH → mo-HCOO + H, (B) mo-HCOO → CO_2 + H, (C) 2H → H2 (g) on a H-covered Cu(111) surface.

Microkinetic Modeling:

A microkinetic model that makes use of these DFT numbers as the initial guesses under predicts the HCOOH decomposition rate by > 6 orders of magnitude. In order to obtain good fits with the experimental data starting from these initial guesses, significant adjustments are required for several parameter values. The adsorbed HCOOH, HCOO and H were stabilized by -0.10 eV, -0.09 eV, and -0.30 eV respectively, whereas the transition state energies of HCOO formation, HCOO decomposition, and H_2 recombination steps were adjusted by -0.56 eV, -0.72 eV and -0.23 eV respectively. As before, several of these are very large deviations that cannot be attributed simply to the inaccuracies in our DFT calculations.

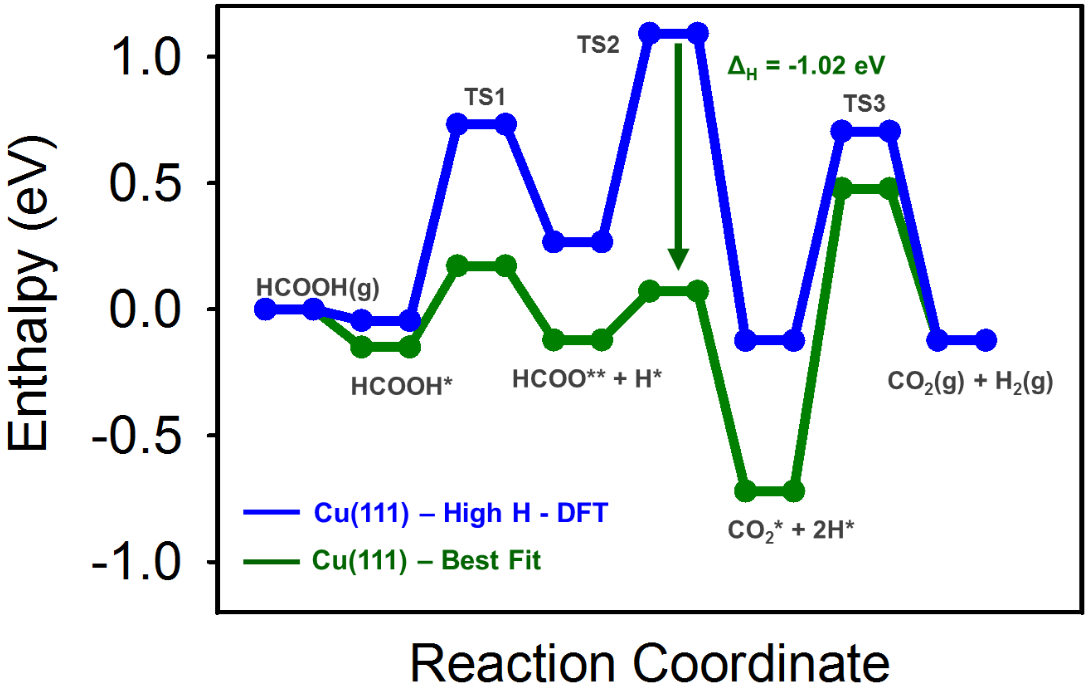

Figure 4-11 2-dimensional PESs of FA decomposition reaction via the HCOO pathway on a H-covered Cu(111) surface. Zero-energy corresponds to the gasphase enthalpy of FA molecule. The blue line corresponds to the DFT derived PES, and the green line corresponds to the best-fit solution. The adjustment required in the transition state energy for HCOO decomposition is also reported.

In this section we showed how the DFT derived parameters on all three surfaces (clean and high HCOO/H covered Cu(111)) were inadequate in describing the experimental observations. In the subsequent sections, we explore the possibility of an active site different from the Cu(111) facet for this reaction. We chose Cu(100) for our subsequent studies, as it is the next most stable facet; additionally, it is the only other facet that was visible in the TEM images under reaction conditions. We follow the same approach as was presented in this section; i.e., we first start with the DFT calculations on clean Cu(100) and make necessary adjustments based on the model predictions.

Table 4-5 Preferred Adsorption Sites and ZPE-Corrected PW91 Adsorption Energies (BE) of Surface Species on High HCOO/H covered Cu(111)

Species	**Cu(111) with 4/9ML of HCOO**		**Cu(111) with 6/9ML of H**	
	Adsorption Site	**BE / eV**	**Adsorption Site**	**BE / eV**
H*	fcc	-2.26	fcc/hcp	-2.09
HCOO**	top-top	-2.40	top-bridge	-1.96
mo-HCOO*	hcp	-2.16	-	-
HCOOH*	bridge	-0.55	top	-0.03

Table 4-6 ZPE-Corrected Reaction Energies and Activation Energy Barriers for all Elementary Steps on high HCOO/H covered Cu(111)

#	**Reaction**			**Cu(111) with 4/9ML of HCOO**		**Cu(111) with 6/9ML of H**	
				ΔE / eV	**E_A / eV**	**ΔE / eV**	**E_A / eV**
1	HCOOH + *	↔	HCOOH*	-0.55	-	-0.03	-
2	HCOOH* + 2*	↔	HCOO** + H*	0.23	1.01	0.32	0.77
3	HCOO**	↔	mo-HCOO* + *	0.24	0.30	-	-
4	mo-HCOO* + *	↔	CO_2* + H*	-0.20	0.49	-	-
5	2H*	↔	H_2 + 2*	0.23	0.84	-0.12	0.80
6	HCOO**	↔	CO_2* + H*	-	-	-0.23	0.73

Table 4-7 Adjustments needed in the DFT derived binding energies on high HCOO/H covered Cu(111) corresponding to the best fit

Species	**HCOO Solution ΔBE / eV**	**H Solution ΔBE / eV**
H*	0.00	-0.30
HCOO**	-0.51	-0.09
HCOOH*	0.00	-0.10

Table 4-8 Adjustments needed in the DFT derived transition state energiees on high HCOO/H covered Cu(111) corresponding to the best fit, and the Cambell's degree of rate control (XRC) for the kinetically relevant elementary steps

Reaction			HCOO Solution		H Solution	
			ΔETS / eV	XRC	ΔETS / eV	XRC
HCOOH* + 2*	↔	HCOO** + H*	-0.19	0.10-0.26	-0.56	0.11-0.26
HCOO**	↔	mo-HCOO* + *	0.00	0.00	--	--
mo-HCOO* + *	↔	CO_2* + H*	-0.06	0.60-0.89	--	--
2H*	↔	H_2 + 2*	0.00	0.01-0.00	-0.23	-0.73-0.88
HCOO**	↔	CO_2* + H*	--	--	-0.72	0.00-0.01

4.3.3 Cu(100) – 'Clean'

DFT Calculations

Table 4-5 reports the DFT derived binding energies for all the reaction intermediates considered in this study, and Table 4-6 contains the reaction enthalpies and activation energy barriers of all the elementary steps included in the reaction network.

HCOOH binds on the Cu(100) surface via its O atoms in a slightly off-top position, with a BE of -0.32 eV. HCOO binds in a bidentate configuration, similar to the Cu(111) surface, and has a BE of -2.95 eV. In the absence of a threefold site on Cu(100), H preferentially binds on a fourfold hollow site, with the BE of -2.27 eV. It can be seen from Tables 1 and 9 that Cu(100) exhibits stronger binding for all surface intermediates when compared to Cu(111), as was expected due to the lower coordination of surface atoms.

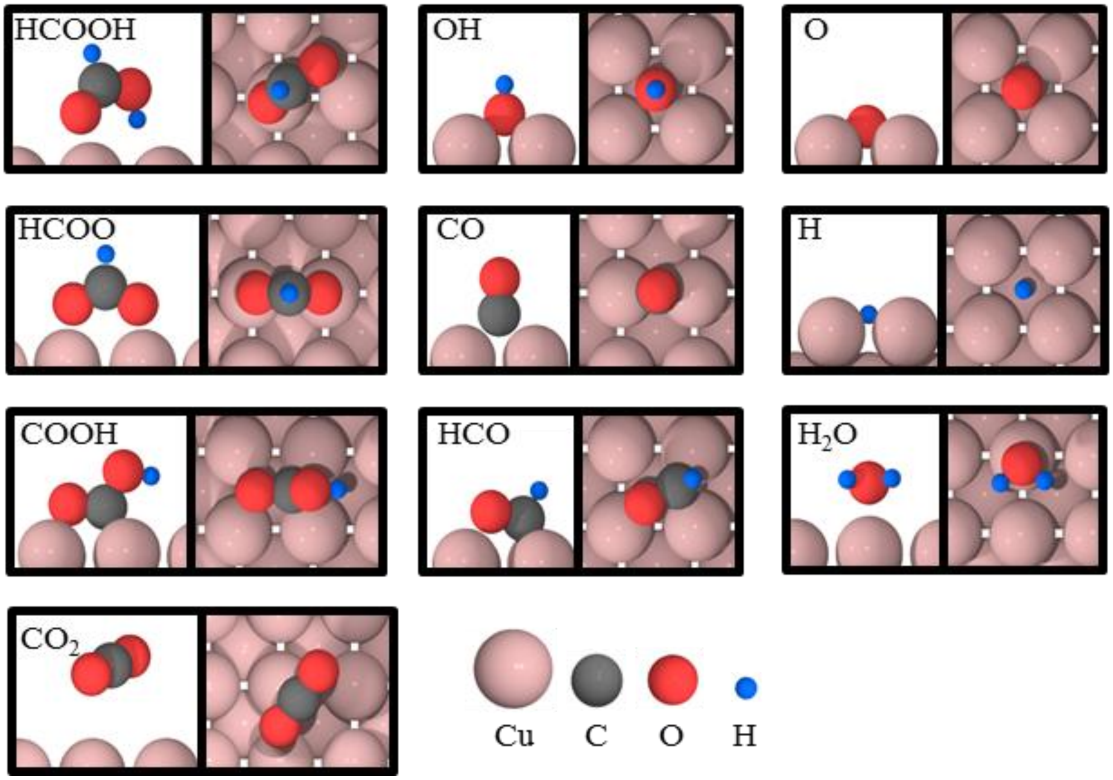

Figure 4-12 Most stable adsorption configurations for all surface adsorbates on clean Cu(100). The pink, grey, red and blue spheres represent Cu, C, O, and H atoms respectively

HCOOH decomposition to HCOO starts from its most stable adsorption configuration; the C-H bond scission takes place over the bridge site and the final state is a bidentate HCOO species with an H atom coadsorbed on an adjacent fourfold hollow site; this step has an E_A (ΔE) of 0.42 eV (-0.57 eV). The HCOO decomposition is initiated by a rotation of the bidentate HCOO molecule that entails an O-Cu bond breaking, and is followed by the C-H bond scission that takes place over a bridge site with an E_A (ΔE) = 1.21 eV (0.52 eV).

H_2 recombination reaction starts with two H atoms coadsorbed on diagonally-adjacent fourfold hollow sites and the transition state has both H atoms on adjacent bridge sites, with H-H bond length of 1.17 Å, as compared to the gas phase bond length in H_2 of 0.75 Å. This step has an E_A and ΔE of 0.72[199, 200] eV and 0.25 eV respectively, near identical to the Cu(111) surface, and is structure insensitive.

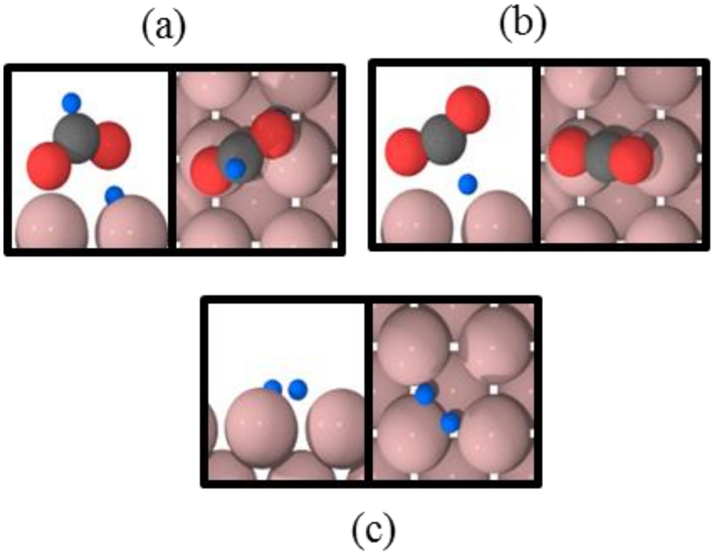

Figure 4-13 Side and top views of the transition states for the three key elementary steps: (A) HCOOH → HCOO + H, (B) HCOO → CO_2 + H, (C) 2H → H_2 (g) on clean Cu(100) surface.

Table 4-9 Preferred Adsorption Sites and ZPE-Corrected PW91 Adsorption Energies (BE) of Surface Species on Clean Cu(100)

Species	**Adsorption Site**	**BE / eV**
H*	fcc	-2.27
O*	fcc	-4.65
OH*	fcc	-2.92
H_2O*	top	-0.23
CO*	bridge	-0.86
CO_2*	physisorbed	-0.05
HCO*	bridge-top	-1.39
HCOO**	top-top	-2.95
COOH*	bridge-bridge	-1.74
HCOOH*	top	-0.32

Table 4-10 ZPE-Corrected Reaction Energies and Activation Energy Barriers for all Elementary Steps on Clean Cu(100)

#	Reaction			ΔE / eV	E_A / eV
1	HCOOH + *	↔	HCOOH*	-0.32	-
2	HCOOH* + 2*	↔	HCOO** + H*	-0.57	0.42
3	HCOOH* + *	↔	COOH* + H*	0.35	0.94
4	HCOOH* + *	↔	HCO* + OH*	0.64	1.05
5	HCOO**	↔	CO_2* + H*	0.52	1.21
6	HCOO** + O*	↔	CO_2* + OH* + *	0.07	1.47
7	HCOO** + OH*	↔	CO_2* + H_2O* + *	0.68	1.34
8	HCOO** + H*	↔	H_2 + CO_2* + 2*	0.77	1.84
9	COOH* + *	↔	CO_2* + H*	-0.39	1.12
10	COOH* + *	↔	CO* + OH*	-0.30	0.21
11	COOH* + O*	↔	CO* + H_2O*	-0.84	-0.09
12	COOH* + OH*	↔	CO_2* + H_2O*	-0.24	-0.58
13	COOH* + H*	↔	CO* + H_2O*	-0.15	1.69
14	HCOO* + COOH*	↔	HCOOH* + CO_2*	0.17	0.67
15	HCO* + *	↔	CO* + H*	-0.60	0.21
16	CO* + O*	↔	CO_2* + *	-0.54	0.63
17	O* + H*	↔	OH* + *	-0.45	1.13
18	2OH*	↔	H_2O* + O*	0.60	0.66
19	OH* + H*	↔	H_2O* + *	0.15	0.98
20	2H*	↔	H_2 + 2*	0.25	0.72
21	CO*	↔	CO + *	0.86	-
22	CO_2*	↔	CO_2 + *	0.05	-
23	H_2O*	↔	H_2O + *	0.23	-

Microkinetic Modeling

A model that is parameterized using the DFT derived thermodynamic and kinetic parameters on Cu(100) is used for parameter estimation and model optimization, using the same approach as was described earlier for clean Cu(111). With no adjustments to these parameters, this model predicts the rates that are an order of magnitude smaller than the measured rates on the supported Cu catalyst. Starting with these parameters as the initial guesses, we obtained a solution that offers excellent fits with the experimental dataset, with minimal adjustments needed in the DFT parameters. The alterations made in the DFT parameters are reported in Table 4-11 and Table 4-12; it can be seen that the maximum adjustment that was made was -0.14 eV, in the transition state energy for HCOO decomposition step, which is well within the error bars of our DFT calculations. The sequence of elementary steps that describe the reaction mechanism is the same as the Cu(111) surface, i.e. : HCOOH → HCOO + H → CO_2 + 2H → CO_2 + H_2. For this solution, the surface is predicted to have a high coverage (0.32 ML – 0.78 ML)of surface HCOO, with ~ 0.55 ML being the predicted coverage for most experimental conditions that were collected at the 'home temperature'. Hence, there exists an inconsistency between the surface coverages that are predicted by the model and those employed in the DFT calculations, and we address this issue in the following section.

As before, we also sampled the parameter space within ± 40 kJ/mol of the DFT derived initial guesses to capture any other feasible solutions that we might have missed by starting only from the DFT derived initial guesses and performing gradient based search. This led us to the 'H-solution', that also exhibits excellent fits with the experimental data, but predicts adsorbed H to be the most abundant surface intermediate (MASI) instead, with a coverage of 0.53 ML – 0.67 ML. The adjustments required in the DFT derived parameters to obtain this solution are significantly higher than the ones in the 'HCOO solution', with the transition state energy for H_2 recombination step requiring destabilization by ~ 0.42 eV.

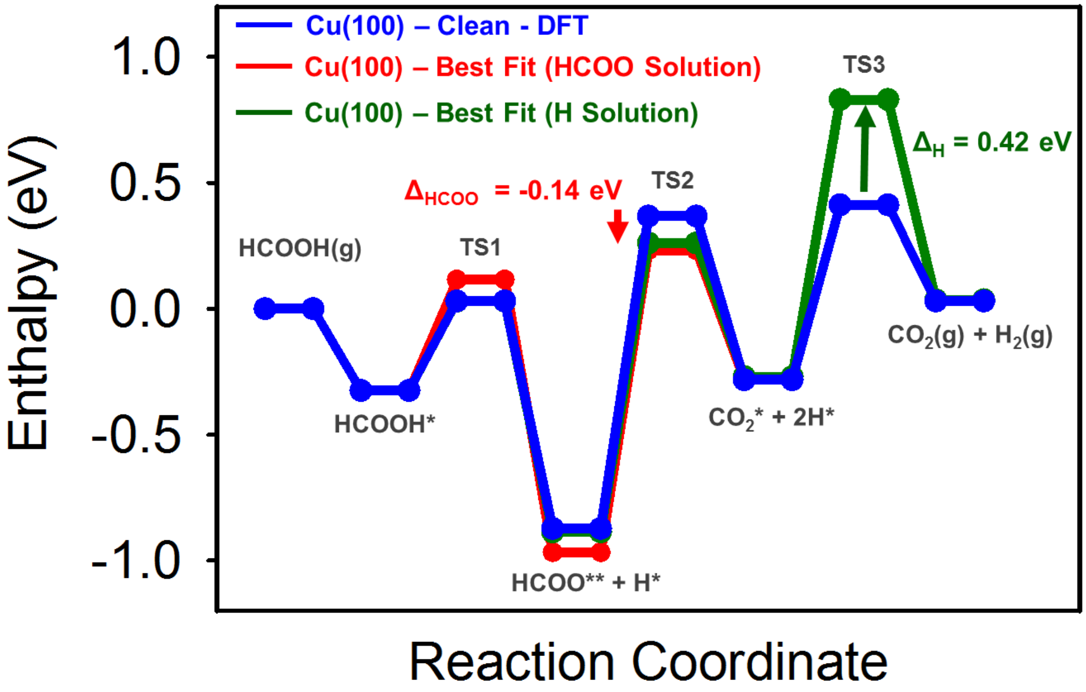

Figure 4-14 2-dimensional PESs of FA decomposition reaction via the HCOO pathway on clean Cu(100). Zero-energy corresponds to the gasphase enthalpy of FA molecule. The blue line corresponds to the DFT derived PES, and the red and green lines reflect the enthalpies of the thermodynamic and transition states for the HCOO solution and H solution, respectlively. The maximum adjustments made for both these solutions is also reported.

Table 4-11 Adjustments needed in the DFT derived binding energies on clean Cu(100) corresponding to the best fit

Species	**HCOO Solution ΔBE / eV**	**H Solution ΔBE / eV**
H*	0.00	-0.02
HCOO**	-0.09	0.00

Table 4-12 Adjustments needed in the DFT derived transition state energiees corresponding to the best fit, and the Cambell’s degree of rate control (XRC) for the kinetically relevant elementary steps on clean Cu(100)

Reaction			HCOO Solution		H Solution	
			ΔETS / eV	XRC	ΔETS / eV	XRC
HCOOH* + 2*	↔	HCOO** + H*	0.08	0.08-0.26	0.00	0.02-0.07
HCOO* + *	↔	CO_2* + H*	-0.14	0.75-0.91	-0.11	0.33-0.36
2H*	↔	H_2 + 2*	0.00	0.00	0.42	0.58-0.62

4.3.4 Cu(100): High Coverage

For both solutions described above, there exists a disparity between the surface coverages predicted by the model and those employed in the DFT calculations. Our studies on Cu(111), wherein we performed rigorous DFT calculations on high HCOO and H covered surfaces, had shown that the overall thermochemistry and kinetics was affected to a significantly greater extent by the presence of large amounts of H on the surface, than that of HCOO. Taking cues from those studies, we first performed only the thermochemistry calculations on high – H covered surface on Cu(100). The results from these calculations confirmed that the thermochemistry for the reaction in presence of large amounts of H was significantly worse than that on the clean slab, much the same way it was on Cu(111). For these reasons, we did not perform additional activation energy barrier calculations on high-H covered surface, and pursued the HCOO solution instead.

HCOO Solution

For reasons listed above, we performed additional thermochemistry and kinetics calculations for the abridged reaction network on a Cu(100) surface with 0.44 ML of spectator HCOO.

HCOOH exhibits significantly stronger binding in the presence of adjacent spectator HCOO, due to H-bonding, and has a BE of -0.69 eV (-0.32 eV) on the clean slab. This difference in BEs between the clean and high HCOO covered surface is same as the one obtained on the Cu(111) surface, suggesting that the extent of H-bonding is the same on both surfaces. The similar binding configurations of HCOOH on the two surfaces (Figure 4-15) supports this finding.

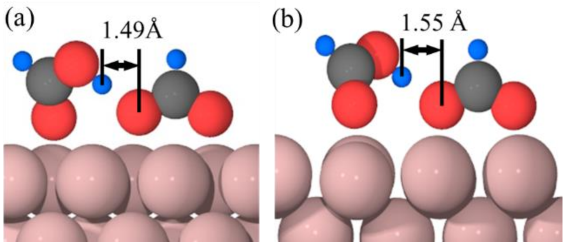

Figure 4-15 Most stable adsorption configuration of HCOOH on high HCOO covered (A) Cu(111) and (B) Cu(100), which is stabilized by the H-bonding of its hydroxyl H with neighboring HCOO species.

HCOO binds preferentially in a bidentate configuration (Figure 4-16C), with a BE of -2.85 eV (-2.95 eV on clean slab). Contrary to the clean surface, we found a stable monodentate configuration for HCOO (Figure 4-16B) that has a BE of -2.39 eV. H binds on a fourfold site (Figure 4-16D), with a BE that is near-identical to its clean slab counterpart.

HCOOH decomposition to HCOO starts from its most stable adsorption configuration and the O-H bond cleavage takes place over an off-bridge site with an E_A (ΔE) = 1.09 eV (-0.06 eV). HCOO decomposition to CO_2 and H is a two-step process; the bidentate HCOO first undergoes rotation to give a monodentate HCOO species with an E_A (ΔE) = 0.54 eV (0.46 eV). The monodentate HCOO then undergoes C-H bond cleavage over a bridge site to give gas-phase CO_2 and adsorbed H, with an E_A (ΔE) = 0.51 eV (0.03 eV). The final step is H2 recombination that starts with the two hydrogen atoms adsorbed on diagonally adjacent hollow sites and the transition state has the two atoms on the adjacent bridge sites.

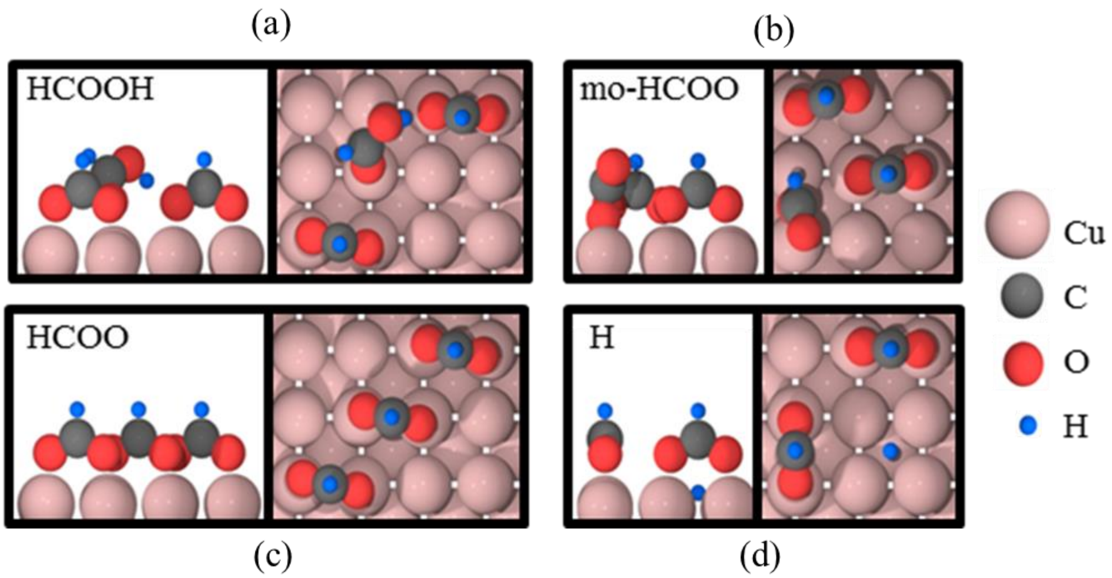

Figure 4-16 Most stable adsorption configurations of the four key surface adsorbates on a HCOO-covered Cu(100). The pink, grey, red and blue spheres represent Cu, C, O, and H atoms respectively.

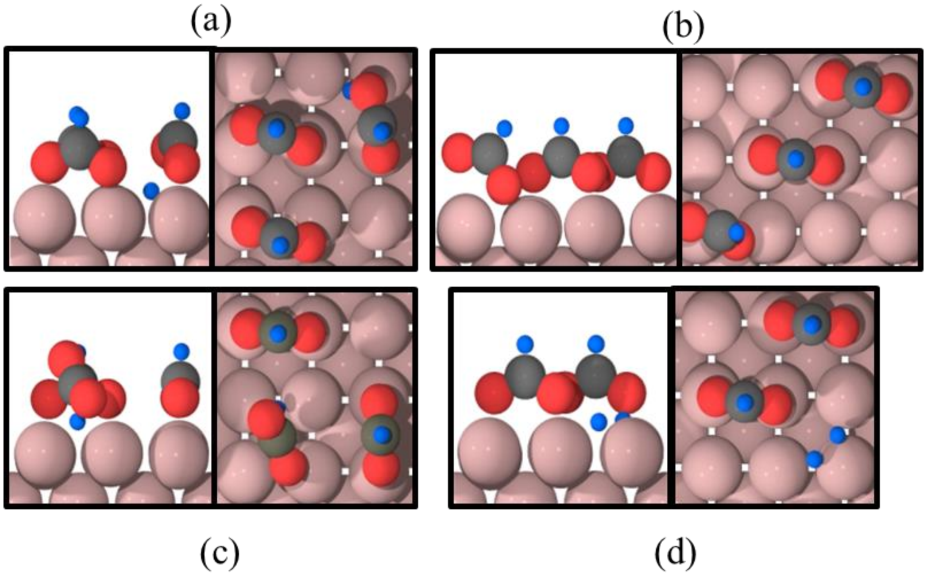

Figure 4-17 Side and top views of the transition states for the four key elementary steps: (A) HCOOH → HCOO + H, (B) HCOO → mo-HCOO (C) mo-HCOO → CO_2 + H, (D) 2H → H_2 (g) on high HCOO covered Cu(111) surface.

Table 4-13 Preferred Adsorption Sites and ZPE-Corrected PW91 Adsorption Energies (BE) of Surface Species on HCOO covered Cu(100)

Species	Adsorption Site	BE / eV
H*	fcc	-2.25
HCOO**	top-top	-2.85
HCOO*	bridge	-2.39
HCOOH*	top	-0.69

Table 4-14 ZPE-Corrected Reaction Energies and Activation Energy Barriers for all Elementary Steps on HCOO covered Cu(100)

#	Reaction			ΔE / eV	E_A / eV
1	HCOOH + *	↔	HCOOH*	-0.69	-
2	HCOOH* + 2*	↔	HCOO** + H*	-0.06	1.09
3	HCOO**	↔	HCOO* + *	0.46	0.54
4	HCOO* + *		CO_2* + H*	0.03	0.51
5	2H*	↔	H_2 + 2*	0.21	0.77

Microkinetic Modeling:

A microkinetic model that uses the DFT numbers obtained on high HCOO-covered Cu(100) as the initial guesses under predicts the TOFs by an order of magnitude; however, when we use these DFT numbers as the initial guesses, the maximum adjustment that we need to make is < 20 kJ/mol to get to the solution that gives an excellent fit with the experimental TOFs, and accurately describes the experimentally observed reaction rates and apparent activation energy barrier. The model predicts a HCOO surface coverage of 0.34 ML – 0.72 ML, with HCOO → CO_2 + H being the RCS.

Hence, for this solution, the surface coverages predicted by the model are consistent with the ones used in our DFT calculations to get the initial guesses for the energetics (thermochemistry and kinetics) for HCOOH decomposition on Cu(100).

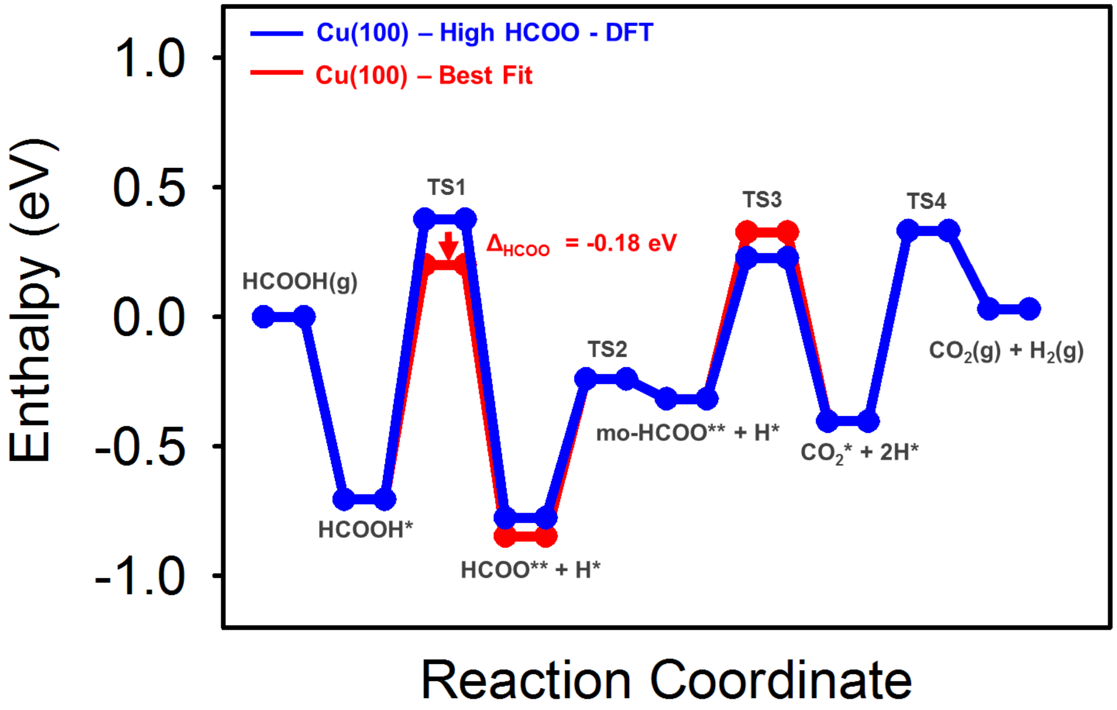

Figure 4-18 2-dimensional PESs of FA decomposition reaction via the HCOO pathway on a HCOO-covered Cu(111) surface. Zero-energy corresponds to the gasphase enthalpy of FA molecule. The blue line corresponds to the DFT derived PES, and the red line corresponds to the best-fit solution. The adjustment required in the transition state energy for the HCOO formation step is also reported.

Table 4-15 Adjustments needed in the DFT derived binding energies on high HCOO/H covered Cu(100) corresponding to the best fit

Species	**HCOO Solution ΔBE / eV**
H*	0.00
HCOO**	-0.07

Table 4-16 Adjustments needed in the DFT derived transition state energiees on high HCOO covered Cu(111) corresponding to the best fit, and the Cambell's degree of rate control (XRC) for the kinetically relevant elementary steps

Reaction			HCOO Solution	
			ΔETS / eV	XRC
HCOOH* + 2*	↔	HCOO** + H*	-0.18	0.10-0.23
HCOO**	↔	mo-HCOO* + *	0.00	0.00
mo-HCOO* + *	↔	CO_2* + H*	0.10	0.60-0.89
2H*	↔	H_2 + 2*	0.00	0.01-0.00

4.4 Conclusions

Using an iterative approach that involves first principles DFT calculations, reaction kinetics measurements, and microkinetic modeling, we systematically investigated the formic acid decomposition reaction on supported Cu catalysts. We performed an extensive set of DFT calculations on clean Cu(111) and Cu(100) surfaces as the single crystal facets representative of the supported Cu catalysts employed in our reaction kinetics experiments, to obtain the initial guesses for the thermodynamics and kinetics parameters for our microkinetic model. While we were able to obtain excellent fits with the experimental dataset starting from the initial guesses obtained from the DFT calculations on the clean slabs, the models predicted a high surface coverages (0.30 ML – 0.80 ML) of either HCOO or H species on the surface for all reaction conditions. We repeated our DFT calculations for key elementary steps, using unit cells that have spectator HCOO and H species, to address this inconsistency in the surface environment between DFT calculations model predictions.

Our studies revealed that contrary to several earlier reports, Cu(111), in all likelihood, does not contribute to the overall rates for this reaction, that Cu(100) is the most probable active site for this reaction, and that the overall energetics (thermochemistry and kinetics) of this reaction varies, to a great extent, with the surface coverages of reaction intermediates employed in the DFT calculations.

This formic acid dehydrogenation reaction is found to proceed via the following sequence of elementary steps: HCOOH → HCOO + H → CO_2 + 2H → CO_2 (g) + H_2 (g); HCOO decomposition to CO_2 and H is found to be the rate controlling step for all the experimental conditions that were studied, and the Cu(100) surface is expected to have a HCOO coverage of 0.36 ML – 0.73 ML under the reaction conditions.

This is a first study of its kind that demonstrates, in detail, the steps involved in an iterative process that ensures holistic self-consistency of the solutions with respect to the surface coverages, which is crucial in developing an accurate fundamental understanding of the chemistries of heterogeneously catalyzed reactions.

Chapter 5

Formic Acid Decomposition on Transition Metals: Catalyst Design via Microkinetic Modeling

In Chapters 1 and 2, we presented an iterative approach that employs DFT, experiments, and microkinetic modeling to obtain fundamental insights into the reaction mechanism of formic acid decomposition on supported Au and Cu catalysts. In this chapter, we build on those studies and utilize the large database of thermodynamic and kinetic parameters on transition metals to initiate a systematic, descriptor based search for the optimal alloy catalyst for this reaction.

5.1 Methods

All calculations were performed using DFT, as implemented in DACAPO, [91, 92] a total energy code. These calculations were performed on (111) and (100) facets of face-centered cubic (fcc) metals (Ag, Au, Rh, Ir, Ni, Pd, Pt and Cu) and (0001) facet of hexagonal close-packed (hcp) metals (Re, Ru, Os, Co). All the surfaces were modeled using a 3x3 unit cell, corresponding to 1/9 monolayer (ML) coverage for a single monodentate adsorbate, with 4-6 layers of metal atoms, periodically repeated in a super cell geometry with five equivalent layers of vacuum between any two successive metal slabs. All atoms were fixed to their bulk-truncated positions for the close-packed facets, while the top two layers were allowed to relax for the more open, (100) facets. Previous calculations have shown that the effect of relaxing the metal atoms is minimal for the close-packed surfaces.[201, 202] The lattice constants for all the metals were optimized and compared against their experimental values.[187, 203] The surface Brillouin zone of close-packed facets was sampled at 18 special Chadi-Cohen[95] k points, while that for the (100) facets was sampled by using a 4×4×1 Monkhorst-Pack k-point mesh.[96] Ionic cores were described by ultrasoft Vanderbilt pseudo-potentials[97] and the Kohn-Sham one-electron valence states were expanded in a basis of plane waves below a kinetic energy of 25 Ry. The exchange-correlation energy and potential were described self-consistently using the generalized gradient approximation (GGA-PW91).[98] The electron density was determined by iterative diagonalization of the Kohn-Sham Hamiltonian, Fermi population of the Kohn-Sham states ($k_BT = 0.1$ eV), and Pulay mixing of the resulting electronic density. The total energies were then extrapolated to $k_BT = 0$ eV. Adsorption was permitted on only one of the two exposed surfaces, and the dipole moment was adjusted accordingly.[93, 94] The minimum energy pathways and corresponding activation energy barriers for all bond formation/cleavage elementary steps were calculated using the climbing image nudged elastic band method (CI-NEB).[102] The elementary step trajectory was discretized over seven images, excluding endpoints. All transition states were confirmed by vibrational frequency calculations yielding a single negative curvature mode. These transition states were only calculated for Cu, Pt, Pd, Ni, and Au; this selection was made to explore a wide range of binding strengths among the catalysts, and only thermochemistry calculations were performed for all other metals.

5.2 Results and Discussion

5.2.1 Reaction Network

As was reported in Chapters 1 and 2, the closed catalytic cycle for FA decomposition on Cu and Au catalysts comprised of only three bond breaking/formation steps, via the 'direct HCOO mediated pathway' : $HCOOH \rightarrow HCOO + H \rightarrow CO_2 + 2H \rightarrow CO_2 + H_2$. Similar studies on Pt and Pd catalysts revealed that, in addition to the steps reported above, the 'direct COOH-mediated pathways' ($HCOOH \rightarrow COOH + H \rightarrow [(CO_2 + 2H)$ OR $(CO + H_2O)] \rightarrow [(CO_2 + H_2)$ or $(CO +$

H_2O)] also contribute to the overall reaction rates under certain reaction conditions. In this chapter, we have adopted a reaction network that comprises of the two pathways listed above, as shown in Figure 5-1.

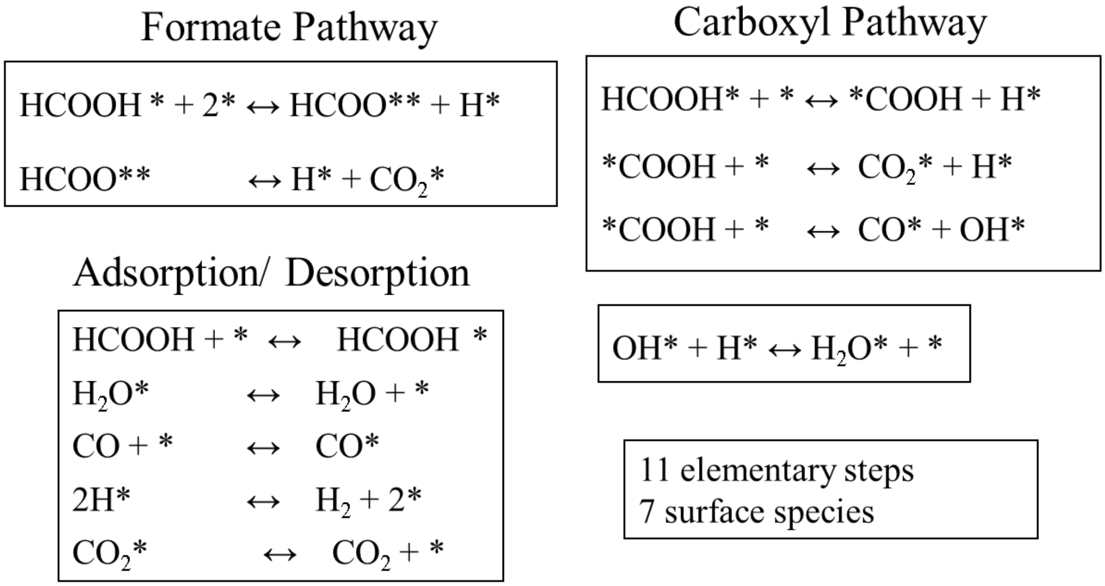

Figure 5-1The reaction network considered in the microkinetic model used for developing the reactivity and selectivity volcano plots.

5.2.2 Reactivity Descriptors and Scaling Relations

Linear Scaling Relations to Estimate Binding Energy

It has been shown in several past studies that the DFT derived binding energy (BE) of surface adsorbates scale linearly with the BEs of the atoms through which they bind to the surface. All surface species involved in FA decomposition reaction network bind to the catalyst surface via either the C or the O atom (or in rare cases, both atoms). Hence, the BE of all the intermediates can be related to the BE of these two atoms, as shown below:

$$BE = mBE_O + nBE_C + \ b$$

Where m and n are the empirically calculated slopes, b is the intercept, and BE_O and BE_C are the binding energy of oxygen and carbon atoms respectively. The adsorption energy for all reaction intermediates that were obtained on 8 fcc metals (Au, Ag, Cu, Ir, Ni, Pt, Pd, and Rh), and 4 hcp metals (Co, Os, Ru, Re) (Table 5-1 reports these values for the close-packed facets) were used to develop the linear scaling relations motivated by the bond order conservation models. Figure 5-2 and Figure 5-3 show these scaling relations for the selected adsorbates present in the reaction network, on the close-packed facets.

Table 5-1Calculated PW91 Binding Energy (BE), in eV, of adsorbed species on 12 close-packed metal facets. Zero of the energy scale is the energy of the clean slab and gas phase species at infinite separation from each other.

	C	O	OH	HCO	HCOO	HCOOH	H_2O	H	CO	COOH
Au	-3.68	-2.47	-1.56	-1.20	-1.78	-0.16	-0.15	-2.22	-0.10	-1.35
Ag	-3.15	-3.16	-2.28	-0.86	-2.31	-0.18	-0.17	-2.07	-0.10	-1.19
Cu	-4.3	-4.14	-2.69	-1.13	-2.76	-0.23	-0.21	-2.38	-0.72	-1.52
Pt	-6.57	-3.73	-2.11	-2.35	-2.35	-0.37	-0.33	-2.70	-1.74	-2.40
Pd	-6.46	-3.73	-2.22	-2.25	-2.34	-0.39	-0.30	-2.83	-1.95	-2.19
Ni	-6.38	-4.94	-2.98	-2.17	-2.80	-0.32	-0.27	-2.81	-1.90	-2.25
Rh	-7.05	-4.74	-2.72	-2.41	-2.94	-0.49	-0.39	-2.82	-1.92	-2.58
Ir	-6.88	-4.69	-2.60	-2.38	-2.94	-0.43	-0.38	-2.73	-1.83	-2.63
Co	-6.59	-5.23	-3.13	-2.04	-2.67	-0.33	-0.29	-2.98	-1.83	-2.25
Os	-7.37	-5.47	-3.05	-2.77	-3.62	-0.69	-0.60	-2.81	-2.10	-3.05
Ru	-6.99	-5.29	-3.22	-2.68	-3.50	-0.81	-0.60	-2.90	-1.98	-3.00
Re	-7.47	-6.69	-3.72	-2.72	-3.55	-0.64	-0.55	-3.04	-1.92	-2.83

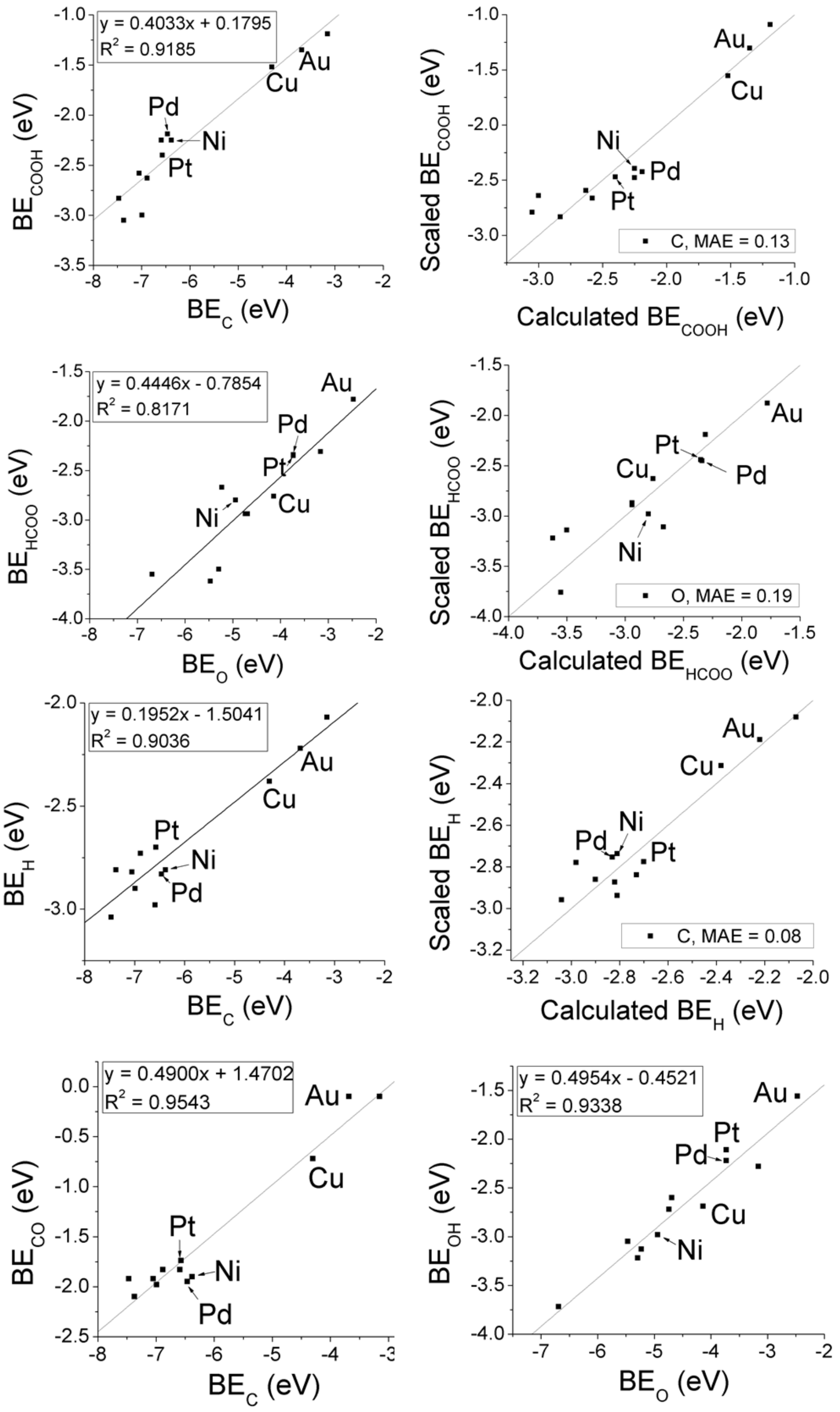

Figure 5-2 Binding energy of selected surface adsorbates plotted against the binding energy of C and O, the two reactivity descriptors for this reaction, on the close-packed facets. Also shown are plots that compare the binding energy calculated by the scaling relations with those predicted directly from DFT calculations.

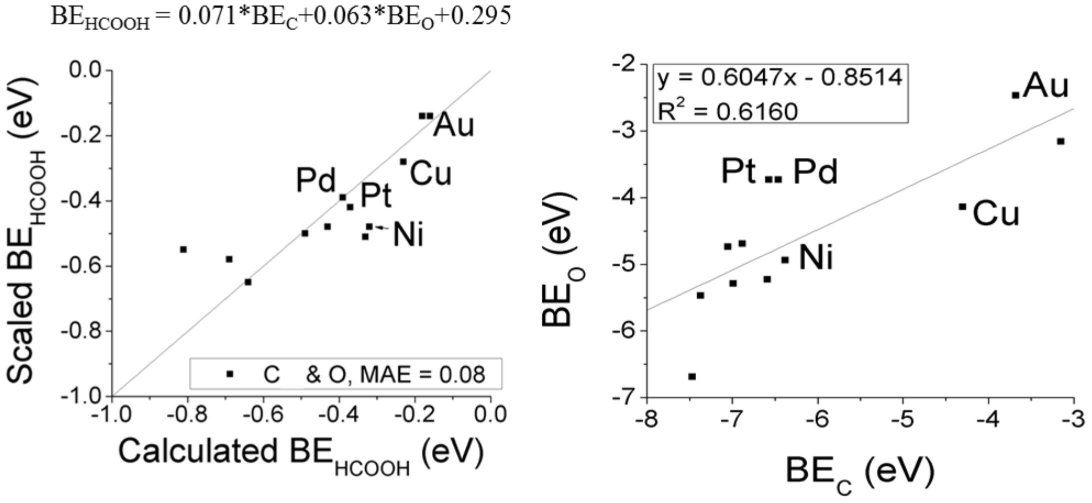

Figure 5-3 (A) Binding Energy of adsorbed FA calculated using the scaling relations plotted against the DFT values. (B) Binding Energy of atomic O plotted against that for atomic C.

With the exception of adsorbed FA, the BE for all the surface species scaled linearly with the BE of either C or O; the BE of adsorbed FA was found to scale with a linear combination of the two parameters, as shown in Figure 5-3A. Figure 5-3B shows that BE of C and O are not correlated, further underscoring the importance of having both of them as independent reactivity descriptors. Similar scaling relations were developed for the (100) facets, and are shown in Figure 5-4., The maximum mean absolute error (MAE) for all the relations is less than 0.15 eV for the COOH intermediate, while the binding energies themselves span over as much as 6 eV. This is within the intrinsic errors of 0.2 eV associated with DFT calculations.

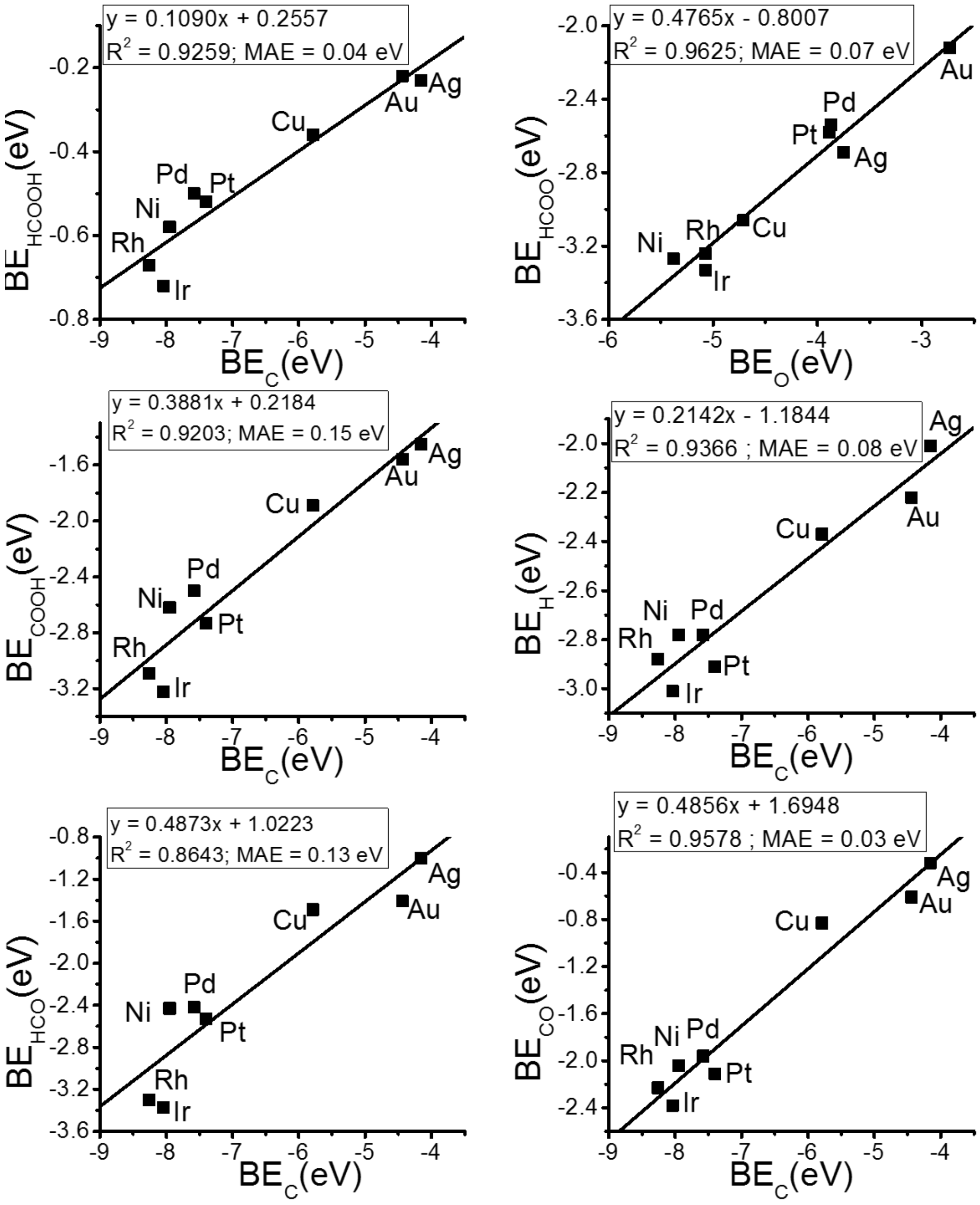

Figure 5-4 Binding energy of all surface adsorbates plotted against the binding energy of C and O, the two reactivity descriptors for FA decomposition, on the (100) facets.

Brønsted Evans Polanyi-type Correlations to Estimate Activation Barriers

The existence of strong linear correlations between the activation energy barriers of elementary surface reactions and their respective reaction energies has been reported for several heterogeneously catalyzed reactions. These Brønsted-Evans-Polanyi (BEP) type correlations, together with the linear scaling relations described in the previous section, provide a powerful methodology to map out the entire thermochemistry and kinetics of the reaction by identifying all the minima (thermodynamic states) and maxima (transition states) in the potential energy surfaces, from the knowledge of the two reactivity descriptors alone.

We utilize the results from our activation energy barrier calculations on 5 fcc metals (Au, Cu, Ni, Pt, Pd) on (111) and (100) facets to obtain these linear BEP relations between the transition state energies (or activation energy barriers) for the elementary steps listed in Figure 5-1 with their reaction energy. Figure 5-5 shows the BEP type correlations for the five key elementary steps on the (111) facets, and Figure 5-6 shows the corresponding plots for the (100) facets.

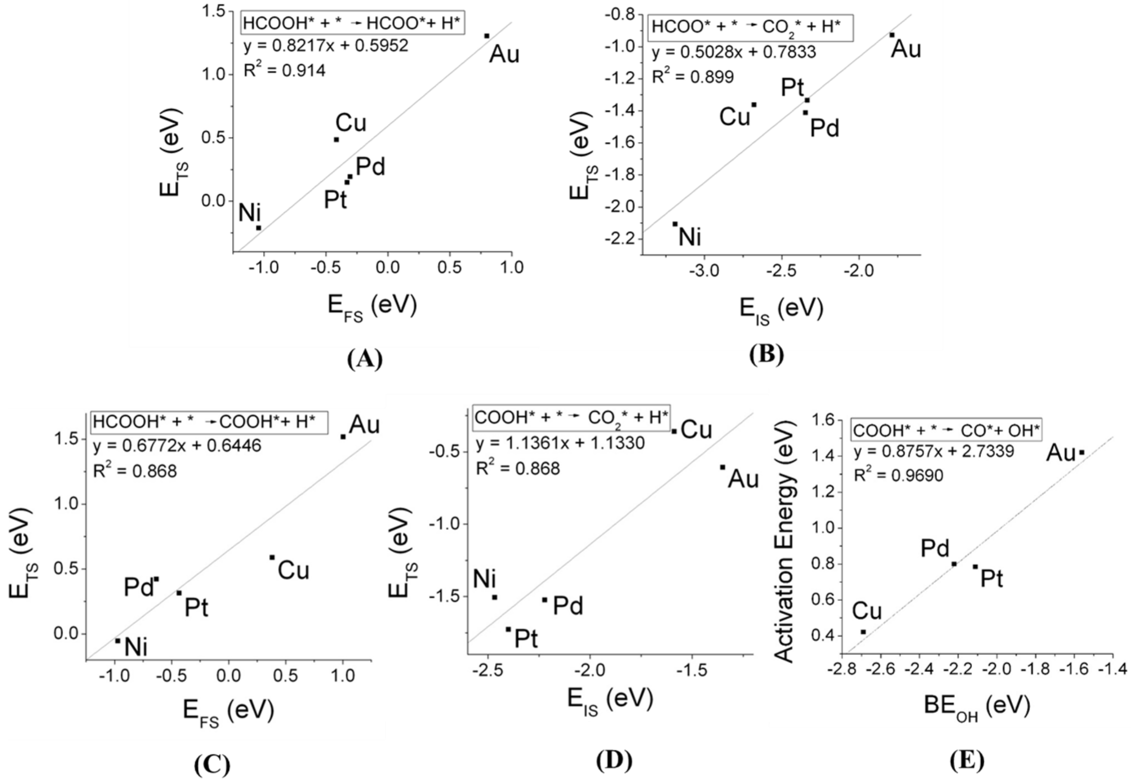

Figure 5-5 Brønsted Evans Polanyi relationships for the five key elementary steps included in the microkinetic model, for the close-packed facets

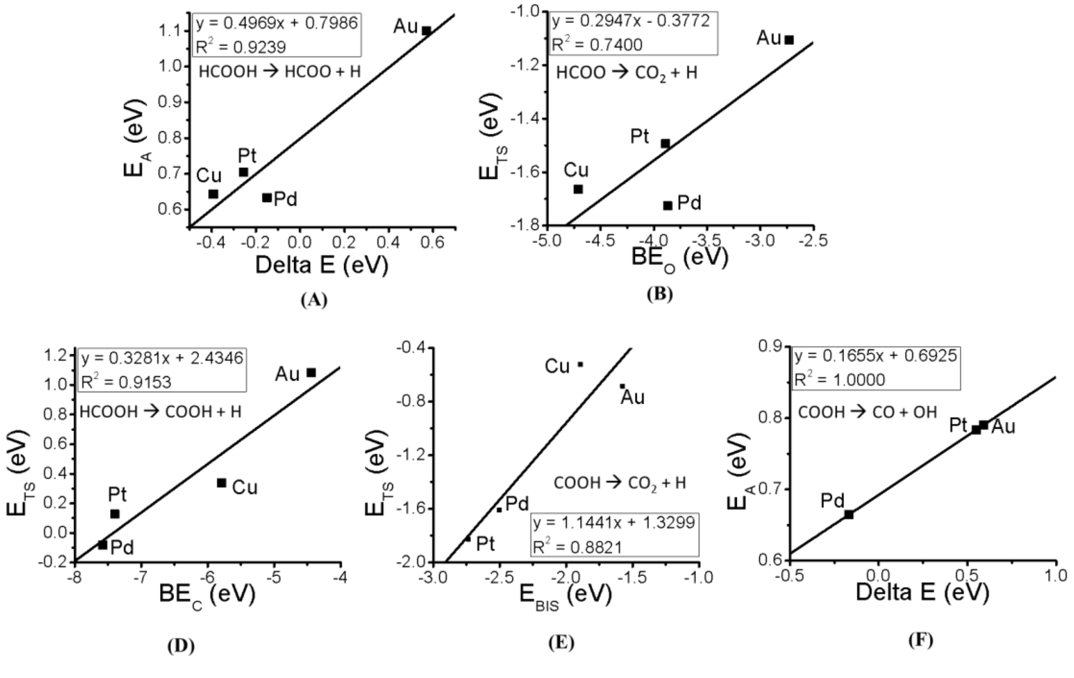

Figure 5-6 Brønsted Evans Polanyi relationships for the five key elementary steps included in the microkinetic model, for the (100) facets

5.2.3 Microkinetic Modeling

A simple mean-field microkinetic model was then developed to utilize the scaling relations and obtain accurate predictions for the reaction activity and selectivity under reaction conditions. A brief description of the model formulation and inputs is included below:

(a) Reaction Condition: The ‘home’ condition selected for these simulations was chosen to be at T = 200°C and P = 1 atm, with the inlet feed comprising of 2% FA diluted with He.

(b) Thermodynamic and Kinetics Parameters: The only DFT derived inputs to this model were the linear scaling relations reported in the earlier sections. The BEs of C and O were varied from -8 eV to -3eV, and -7 eV to –2 eV respectively, in increments of 0.1 eV each, to finely sample the entire parameter space. As a result, this parameter space was sampled at 2500 discrete data points, each of which potentially representing a unique catalyst. The scaling relations were then used to obtain the BEs of surface species and the activation energy barriers for all elementary steps. The vibrational frequencies for all surface intermediates were calculated on Pd (111) and Pd(100), and these values were assumed to be independent of the metal identity. Using these vibrational frequencies, we calculated the zero-point energies and Shomate Parameters, as described in section 2.2, which were then used to calculate the entropy of surface species and transition states, and the temperature corrections for the surface enthalpy and entropy for all states. All this information was then used to calculate the equilibrium and forward/reverse rate constants at 200°C.

(c) Model Formulation: The model was formulated as a transient CSTR, along the lines described by Madon et al.[7] Forward simulation was performed for all 2500 discrete data points (both for the close-packed and (100) models), to obtain the reactivity and selectivity under reaction conditions. This information was then used to prepare the activity and selectivity ‘volcano plots’.

5.2.4 Volcano Plots

The linear scaling relations based microkinetic model was employed to develop two dimensional activity and selectivity volcano plots that provide insights into the reaction mechanism and guidelines to identify and design alloy catalysts with improved performance.

Close-Packed Facets

The activity and selectivity volcano plots were obtained from the microkinetic model at the ‘home conditions’ and are shown in Figure 5-7for the close-packed facets. The two reactivity descriptors, i.e., the BEs of C and O are the x- and y-axes for all these plots and the red and blue regions in the parameter space correspond to higher and lower rates / selectivity respectively. Given the fine discretization of the parameter space, these graphs can be assumed to be continuous contour plots for all practical purposes.

As can be seen from Figure 5-7, Cu(111) is predicted to be the most active (TOF = 0.1 s^{-1}), and Au(111) is predicted to be the least active (TOF = 1e-10 s^{-1}) close-packed facets among the monometallic catalysts with fcc/hcp crystal structure. In comparison, a ‘full microkinetic model’, one that employs the thermochemistry and kinetics parameters obtained from the rigorous DFT calculations for a much larger reaction network predicts the TOFs of 0.08 s^{-1} and 1e-10 s^{-1} for Cu(111) and Au(111) respectively for the same reaction conditions. Hence, it can be argued here that there isn’t any appreciable loss in accuracy upon going from the full model to the curtailed and simplified scaling-relations based model, at least for the monometallic catalysts considered here. Also, there appears to be a room for improvement in the maximum achievable rates, as Cu(111) seems to lie along the fringes of the volcano (region in red); the volcano ‘peak’, which has the coordinates (BE_C, BE_O) of (eV, eV) is predicted to be ~ 3 orders of magnitude more active than Cu(111). Moreover, CO_2 and H_2 are predicted to be the exclusive products for majority of the region in the parameter space (Figure), and only the catalysts that exhibits strong C and O adsorption ($BE_C > -6.5$ eV and $BE_O > -4.5$ eV) are predicted to exhibit low selectivity for CO_2.

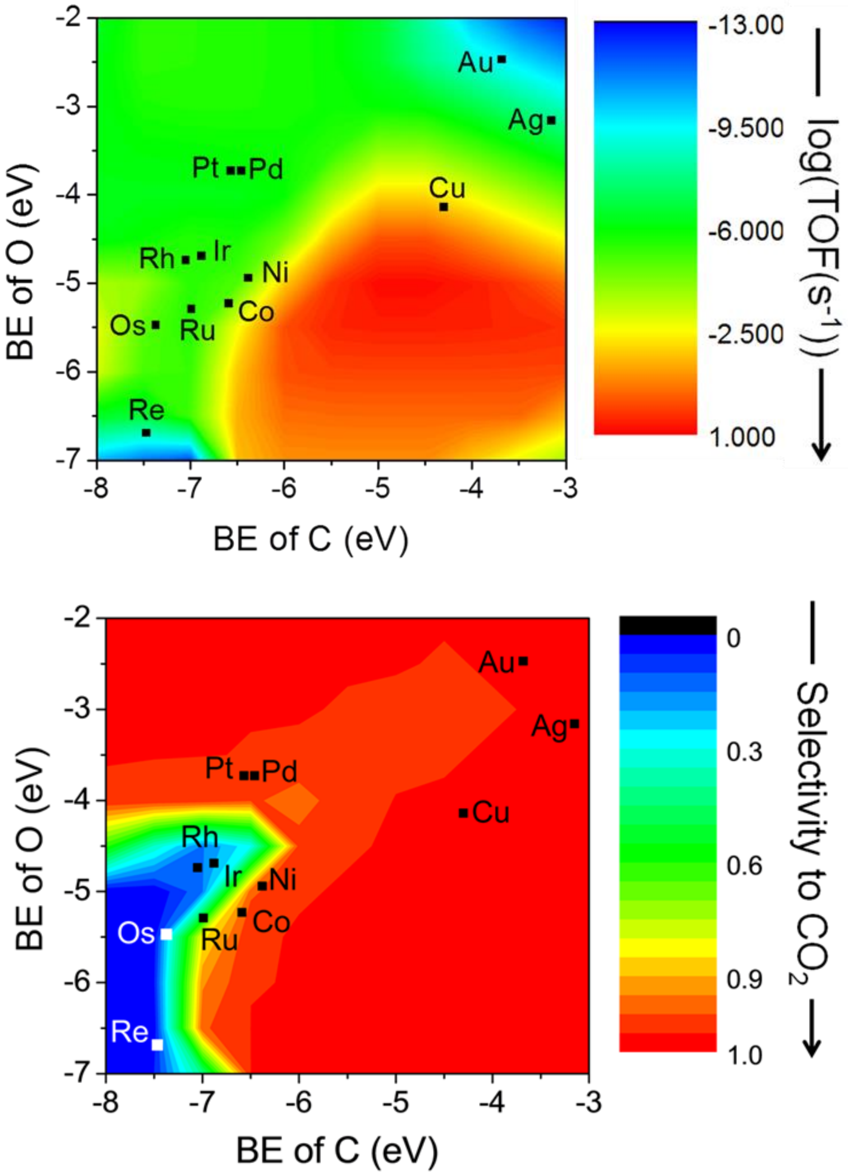

Figure 5-7 Theoretical activity and selectivity volcano plots for FA decomposition, developed using the scaling relations developed for the close-packed facets. For activity volcano, the logarithms of the turnover frequencies are plotted as functions of binding energy of atomic C and O. The selectivity to CO_2 is defined as the total outlet flow rate of CO_2 normalized by the total amount of FA converted, the only other C containing product being CO.

Closed Catalytic Cycle and Rate Controlling Steps

As was shown in Figure 5-1, the reaction network considered in this study comprises of two pathways: the ‘HCOO pathway’ and the ‘COOH pathway’. Here, we try and determine the individual contributions from these two pathways to the overall rates, and identify the closed-catalytic cycle on different catalysts. The existence of these two alternate pathways results in two unique volcano ‘peaks’: a relatively smaller, less active peak at high C binding and moderate O binding regime, corresponding to the COOH pathway (Figure 5-8A), and a more active peak at moderate C and O binding, for the HCOO pathway (Figure 5-9); at their respective peaks, the HCOO pathway is ~2.5 orders of magnitude more active than the COOH pathway.

On a related note, HCOO pathway is predicted to be the dominant pathway that carries the bulk of the reaction flux for all the catalysts that exhibit weak C binding (<-6.5 eV), and COOH pathway is predicted to be the dominant pathway for those that exhibit strong C binding (>-6.5 eV).

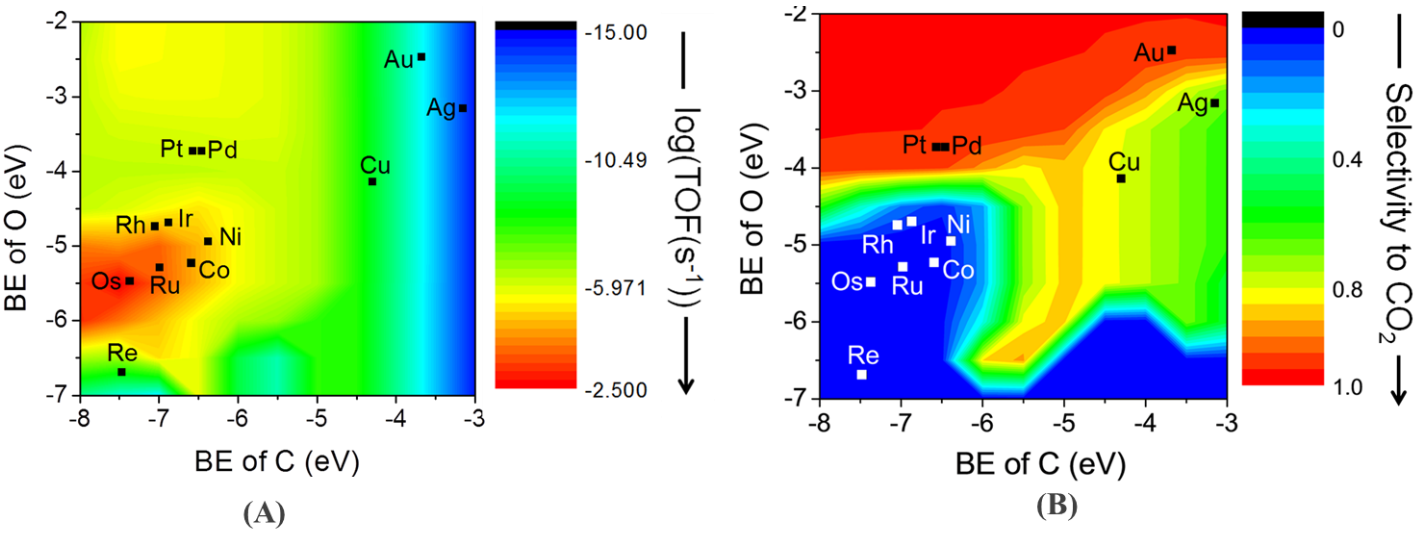

Figure 5-8 Theoretical activity and selectivity volcano plots for FA decomposition, when only the COOH pathway was considered in the microkinetic model.

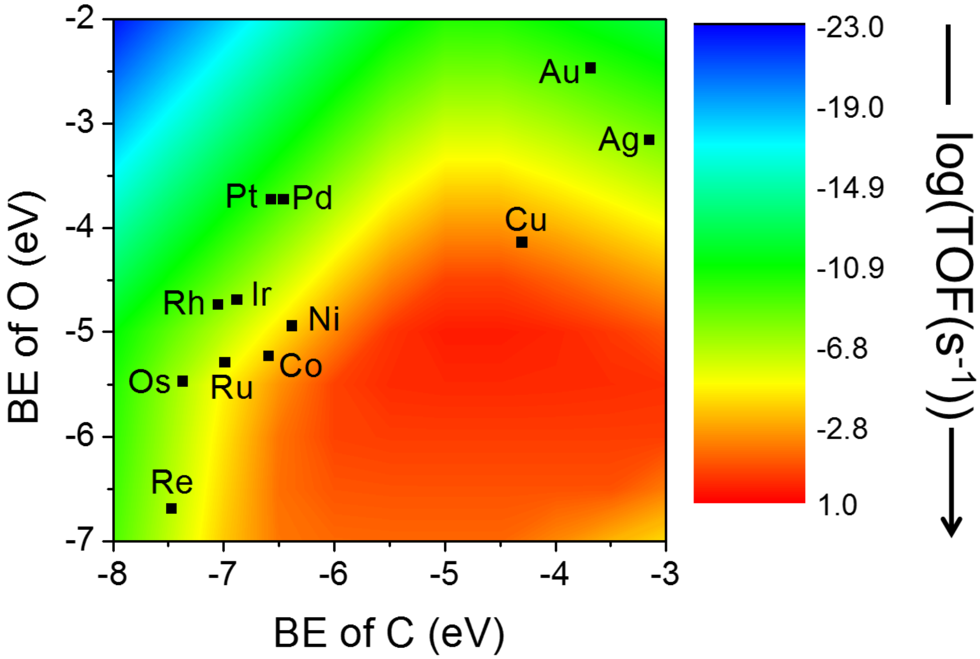

Figure 5-9 Theoretical activity and selectivity volcano plots for FA decomposition, when only the HCOO pathway was considered in the microkinetic model. Since the only route to CO formation is via the COOH pathway, the inclusion of only the HCOO pathway results in CO_2 being the only product. For these reasons, separate selectivity volcano plot is not included here.

The kinetic significance for each elementary step was quantified by calculating their respective 'Campbell's degree of rate control (XRC)', with the elementary step having the highest XRC defined as the rate controlling step; Figure 5-10 shows how the rate controlling steps vary across different regions in the parameter space. (Note: This plot appears to be more pixelated than others because we used a relatively coarse mesh to discretize the parameter space for this analysis).

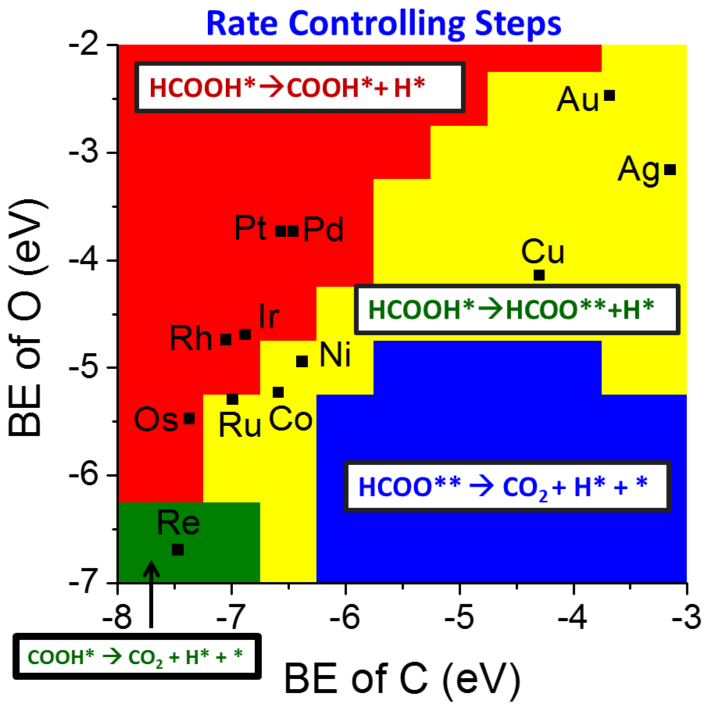

Figure 5-10 Variation of the rate controlling steps with the binding energy of atomic C and O.

Surface Coverages

In addition to the reactivity and selectivity volcano plots, similar two-dimensional plots were also developed to illustrate how the surface coverages of the key reaction intermediates vary across the parameter space. These 'surface coverage volcano plots' provide predictions regarding the most abundant surface intermediates (MASI) for different catalysts under reaction conditions.

(1) Figure 5-11A: Catalysts that exhibit strong C binding (> -5 eV) and weak O binding (< -3. eV) are predicted to have a high concentration of atomic H on the surface.

(2) Figure 5-11B: Catalysts that exhibit very strong C binding (> -7 eV) and O binding of >-3.5 eV are predicted to have CO as the MASI. Note here that the maximum surface coverage of

CO allowed by the model is 2/3 ML. This is enforced by using a coverage-dependent binding energy of CO, as was implemented by Grabow et al.[27]

(3) Figure 5-11C: Catalysts that exhibit relatively weak C binding (< -6 eV) and strong O binding (>-5 eV) are predicted to have HCOO as the MASI.

(4) Figure 5-11D: Catalysts that exhibit weak C and O binding (< 5 eV for each) are predicted to be vacant under the reaction conditions employed for these simulations.

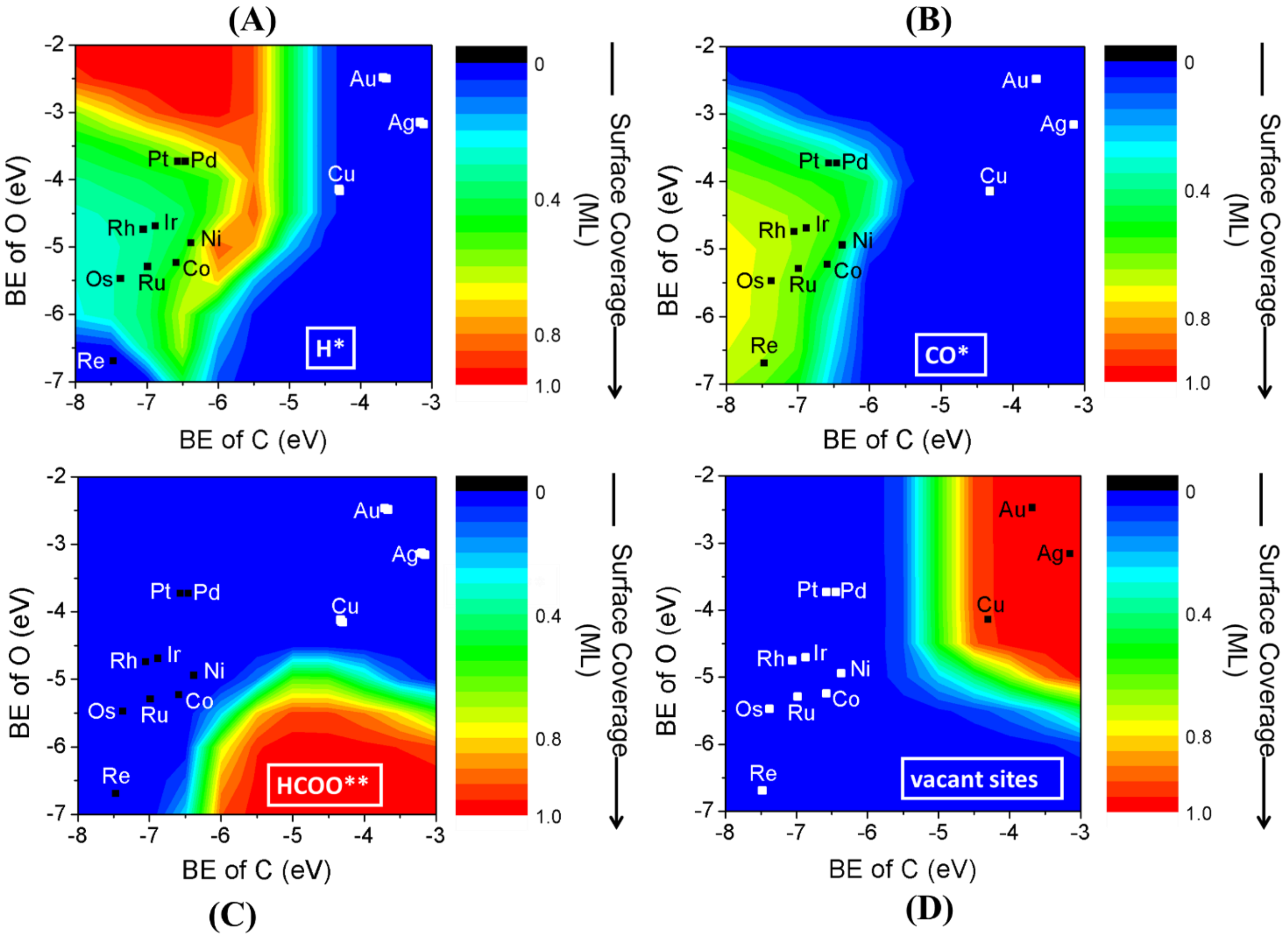

Figure 5-11 Variation of surface coverages of adsorbed (A) H (B) CO (C) HCOO (D) vacant sites, with the binding energy of atomic C and O.

Identifying Improved Alloy Catalysts

In the previous sections, we demonstrated how a descriptor based approach that uses microkinetic modeling and linear scaling relations can be used to obtain insights into the reaction mechanism, and obtain specific information regarding the rate controlling steps and the surface environment under reaction conditions, for any catalyst that exhibits the C and O binding within the range of BEs employed here. We also showed that there exists an *untapped* region in the parameter space that is predicted to have higher activity than Cu(111), which is the most active monometallic catalyst among those considered here, with 100% selectivity for the desired product. The challenge then was to screen for alloy catalysts that might possess this desirable combination of C and O BEs, and hence, lie within the promising window in the parameter space. To this end, thermochemistry calculations were performed on the close-packed facets of over 75 bimetallic alloy catalysts, to determine the BEs of C and O on these surfaces, and subsequently determine their respective positions on the reactivity and selectivity volcano plots. Figure 5-12A - C show some of the promising candidates that were identified from these calculations. In this Figure, the candidates have been classified into 3 categories: In Figure 5-12A, the bulk metal and near surface alloys (NSAs) of relatively inexpensive *base metals*, specifically, Cu, Ni, Sn, Zn, and Co are shown. Figure 5-12C shows some *exotic* combinations of the precious metals (Au, Pt, Pd, among others), while Figure 5-12B demonstrates how the reactivity might change upon changing the lattice constant of Cu. In particular, upon increasing the lattice constant of Cu from 3.66 Å to 3.94 Å, the reactivity is predicted to change by ~ 2 orders of magnitude. In practice, this change in lattice constant of Cu can be affected by overlaying Cu monolayers over metals with larger lattice constant (Au, Ag etc.).

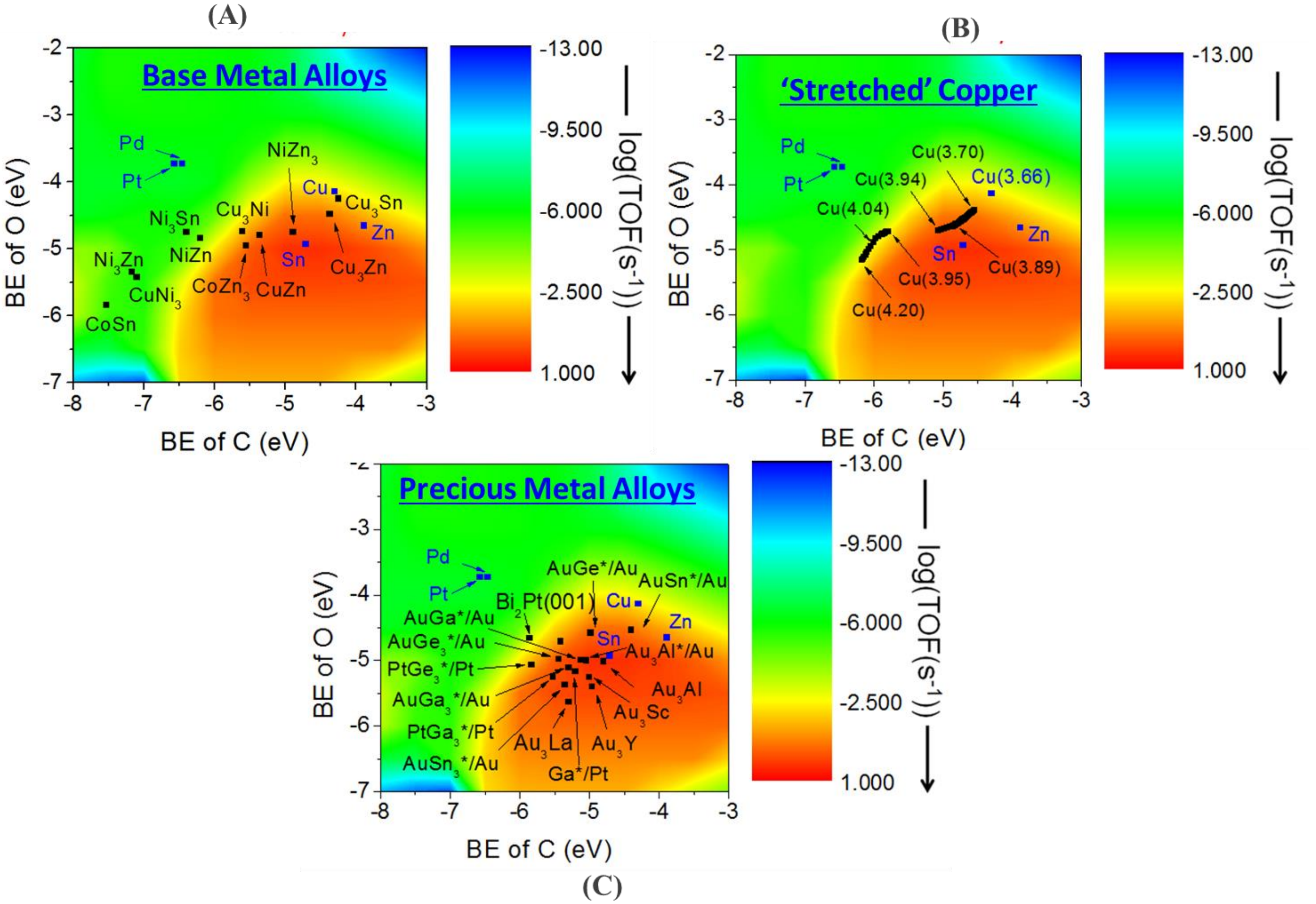

Figure 5-12 Selected promising bimetallic alloy catalysts and the activity of their (111) facets.

Figure 5-13A-C quantify the relative activity of the candidate alloy catalysts, normalized by the predicted activity on Cu(111). As can be seen from these figures, the most active alloys identified from this method predict rates that are ~ 2.5 orders of magnitude higher than those on Cu(111), the most active close-packed facet among the monometallic catalysts.

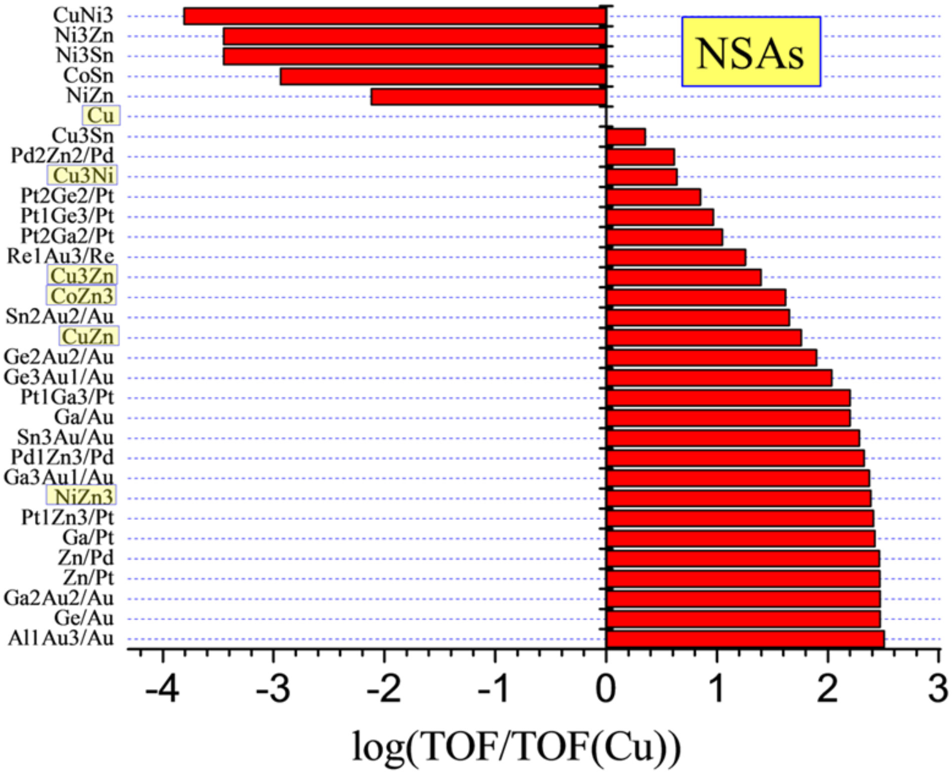
CuNi3
Ni3Zn
Ni3Sn
CoSn
NiZn
Cu
Cu3Sn
Pd2Zn2/Pd
Cu3Ni
Pt2Ge2/Pt
Pt1Ge3/Pt
Pt2Ga2/Pt
Re1Au3/Re
Cu3Zn
CoZn3
Sn2Au2/Au
CuZn
Ge2Au2/Au
Ge3Au1/Au
Pt1Ga3/Pt
Ga/Au
Sn3Au/Au
Pd1Zn3/Pd
Ga3Au1/Au
NiZn3
Pt1Zn3/Pt
Ga/Pt
Zn/Pd
Zn/Pt
Ga2Au2/Au
Ge/Au
Al1Au3/Au
NSAs
-4
-3
-2
-1
0
1
2
3
log(TOF/TOF(Cu))

(A)

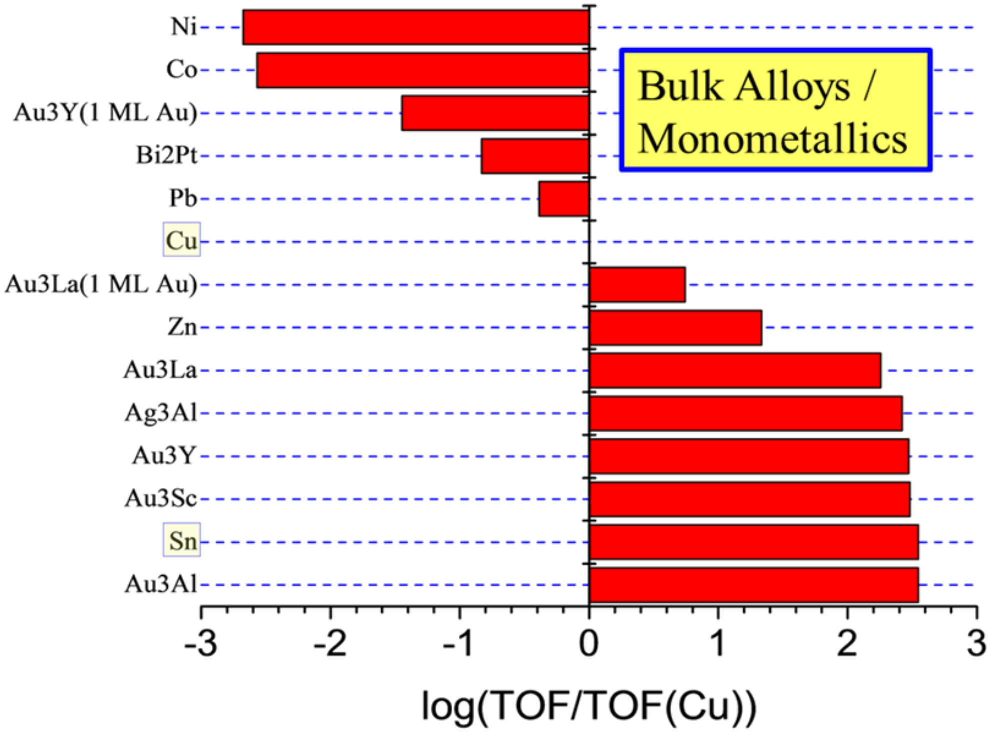
Ni
Co
Au3Y(1 ML Au)
Bi2Pt
Pb
Cu
Au3La(1 ML Au)
Zn
Au3La
Ag3Al
Au3Y
Au3Sc
Sn
Au3Al
Bulk Alloys / Monometallics
-3
-2
-1
0
1
2
3
log(TOF/TOF(Cu))

(B)

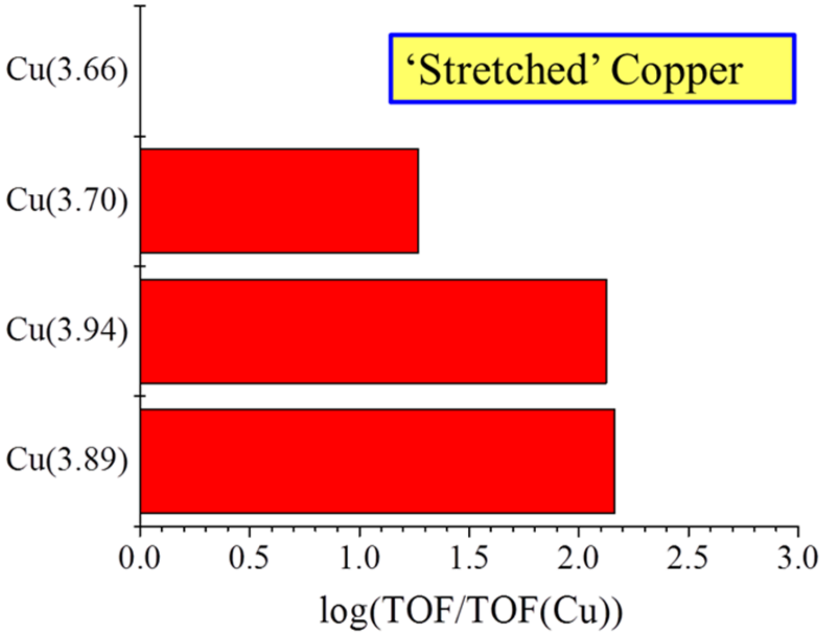

(C)

Figure 5-13 Relative rates for the promising bimetallic catalysts, as predicted by the descriptor based microkinetic model. The predicted rates on all the catalysts are normalized by the rates on Cu(111), the most active monometallic catalyst.

Cu(100) facets

Using the same approach as described in the earlier sections, the linear scaling relations developed for the (100) facets were utilized to develop the volcano plots for these more open facets (Figure 5-14). The reaction rates at the peak of the '(100) volcano' were found to be ~ 2 orders of magnitude smaller than that of the '(111) volcano'; this can be attributed to the relatively higher surface coverages of the HCOO species in that region of the parameter space, as the open surface tends to exhibit stronger binding than their close-packed counterparts. As before, thermochemistry calculations to determine the binding energy of atomic C and O were performed on the (100) facets of over 75 bimetallic alloys, and some promising candidates are included in Figure 5-14.

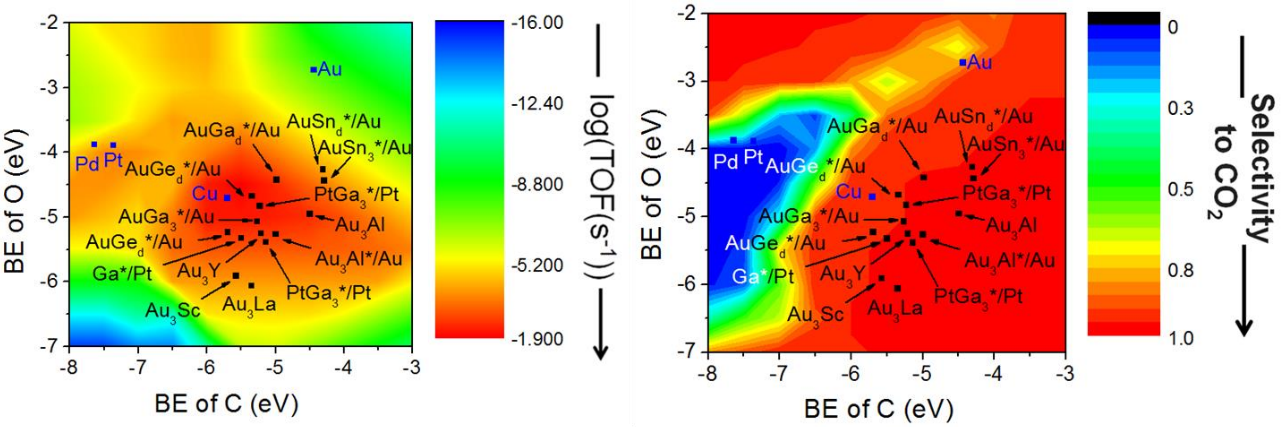

Figure 5-14 Selected promising bimetallic alloy catalysts and the activity and selectivity of their (111) facets

5.3 Conclusions

This study reports a theoretical analysis for formic acid decomposition reaction on transition metal surfaces. The database of binding energy and activation energy barriers that was obtained using rigorous DFT calculations on several fcc and hcp close-packed, and fcc(100) facets, was utilized to develop the linear scaling relations that correlated the adsorption energies of surface species to the reactivity descriptors (binding energy of C and O), and the Brønsted Evans Polanyi-type relations that correlated the activation energy barriers with the thermochemistry of elementary steps. These semi-empirical correlations were incorporated in a mean-field microkinetic model to develop two-dimensional volcano plots that described the turnover frequencies (TOFs) and selectivity to CO_2 as functions of the two descriptors. These volcano plots were then used to search for alloy catalysts that have improved performance over the most active monometallic catalysts, and several potentially promising catalysts were identified and reported.

Chapter 6

Reactions of Propylene Oxide on Supported Silver Catalysts: Insights into Pathways Limiting Epoxidation Selectivity[3]

6.1 Introduction

Propylene oxide (PO) is an important industrial chemical with wide applications in the fabrication of plastics, fuel additives, and urethane foams, among others. In 2009 the global production of propylene oxide reached 6 million tons, making it one of the most widely produced chemicals in the world [204]. All of the existing commercial processes for the production of PO suffer from drawbacks. The oldest of these, the chlorohydrin process, generates stoichiometric amounts of chloride salts. The Halcon process employs a (homogeneous) early transition metal catalyst to react an alkyl hydroperoxide with propylene, and its economics are closely coupled to the values of co-products such as tertiary butyl alcohol or styrene, produced in addition to PO. Similar processes using heterogeneous catalysts include the Shell SMPO process[205] and the recently commercialized BASF/Dow HPPO process, which uses hydrogen peroxide to oxidize propylene. The use of hydrogen peroxide introduces safety issues and, while potentially more economical than the use of alkyl hydroperoxides, is generally less economical than carrying out direct oxidations with air or oxygen, if the latter can be performed selectively. Unfortunately, although ethylene can be epoxidized directly to ethylene oxide with silver catalysts with high (80% to 90%)

---

[3] Adapted from "Reactions of Propylene Oxide on Supported Silver Catalysts: Insights into Pathways Limiting Epoxidation Selectivity", A. Kulkarni, M. Bedolla-Pantoja, S. Singh, R. F. Lobo, M. Mavrikakis, M. Barteau, *Topics in Catalysis* 55, 3 (2012). Experiments for this study were performed by A Kulkarni and M. Bedolla-Pantoja.

selectivity, direct propylene epoxidation is much less favorable. Propylene epoxidation selectivities with silver catalysts in the archival and patent literature range from less than 5% to 50% [206], with most tending toward the lower end of this range.

The low selectivity for direct propylene epoxidation over silver catalysts has been attributed to the vulnerability of the allylic hydrogen in propylene to abstraction by adsorbed oxygen, leading to complete combustion [207]. Heavy modifications, particularly with alkali metals and/or in the presence of gas-phase modifiers, such as organic chlorides, are generally required to obtain even moderate PO selectivity. The co-feeding of conjugated dienes like butadiene has also been shown to increase the PO selectivity.[208] It is unclear, however, whether these approaches involve suppression of allylic hydrogen abstraction. For instance, for olefins that do not contain allylic hydrogen such as ethylene and butadiene, epoxidation selectivity may still be limited by reactions that occur *after* the addition of oxygen to the olefin. In both cases, addition of an oxygen atom to a terminal carbon results in the formation of a surface oxametallacycle intermediate. In the case of ethylene, the corresponding oxametallacycle can ring-close to form ethylene oxide (EO), or can isomerize via a 1,2-hydrogen shift to form acetaldehyde which is then readily combusted. The branching ratio between the ring closure and isomerization channels available to the oxametallacycle then controls selectivity. In the case of ethylene epoxidation, the barrier heights for these two reactions are nearly equal, and unpromoted catalysts achieve a selectivity of around 50%.[9] Both Cs and Cl promotion increase selectivity, and this effect can be explained by their impact on the barriers for these competing oxametallacycle reactions.[209]

The oxametallacycle reaction network in the epoxidation of butadiene to epoxybutene (EpB) is more complex. The principal isomerization reaction for the oxametallacycle is a 1,4-shift to form the conjugated aldehyde, crotonaldehyde. In surface science experiments products of 1,4 ring closure such as dihydrofurans are observed[210]: under the conditions of the catalytic epoxidation reaction these are dehydrogenated to furan .[211] The oxametallacycle reaction networks proposed for ethylene epoxidation and butadiene epoxidation are illustrated in Figure 6-1. Cs and Cl promotion of silver catalysts leads to EpB selectivities of 95% or greater, primarily by lowering the barrier for oxametallacycle ring closure.[210, 212]

Studies of the reaction networks of the oxametallacycles in these two cases have been facilitated by surface science experiments in which stable oxametallacycles were formed by activated ring opening of EO and EpB. Reaction paths accessible in UHV experiments could be compared with the product distributions observed over supported catalysts both with and without promoters. Unfortunately, all other examples of oxametallacycle formation in surface science experiments involve molecules with additional unsaturation such as styrene and isoprene.[213] To date, no stable oxametallacycles have been created by ring opening of alkyl olefin epoxides.

While evidence for stable oxametallacycles with alkyl substituents, as well as for the participation of such intermediates in propylene epoxidation, is lacking, there are a variety of reasons to assume that the steps involved in oxygen addition to propylene on silver are analogous to those for ethylene and butadiene. First, silver catalysts can produce PO, albeit with lower selectivity, and it is difficult to imagine how a reaction as unique as direct olefin epoxidation on silver could proceed by multiple pathways for different olefins. Second, as we have shown previously, the thermodynamics of oxametallacycle formation from alkyl olefin epoxides do not differ significantly from those for EO.[214] Recent calculations by Lei et al.[215] have suggested that oxametallacycle formation from propylene and oxygen on Ag_3 clusters is facile, with an apparent activation barrier of 12 kJ/mol. Finally, the classic experiments of Manara and Parravano [19] nearly four decades ago demonstrated clean exchange of oxygen between EO and propylene to form PO and ethylene, implying an equivalence of the C_2 and C_3 structures involved in the exchange reaction. In short, in striving to understand and to model the complex network of reactions involved in propylene epoxidation on silver catalysts, one can either begin with the fabric of theory, analogy, and circumstantial evidence that connects this chemistry to that of ethylene, or assume that these two homologs do not share a common mechanism for epoxidation.

Since relatively little attention has been paid to the network of reactions that may follow oxygen addition to propylene on silver, we have studied propylene oxide reactions on supported silver catalysts. Here we present experimental results that aim to understand the network of reactions that result from the ring opening of PO, analogous to the networks in Figure 6-1, for the selectivity-limiting branching reactions of oxametallacycles in ethylene and butadiene epoxidation. Note that unlike ethylene oxide, PO can form two oxametallacycles on Ag (Scheme 1) and thus the reaction network may be more complicated. Since some of these reaction products are subject to facile oxidation (as in the case of acetaldehyde formed from the oxametallacycle in ethylene epoxidation), we have also examined the reactions of PO co-fed with oxygen. These experiments were carried out at temperatures and oxygen flow rates resembling those for olefin epoxidation. In addition to experiments, we performed periodic, self-consistent DFT to probe the energetics of the relevant elementary reaction steps. These combined experimental and theoretical results help to develop a reaction network that connects propylene with propylene oxide and other C3 oxygenated products via surface oxametallacycle intermediates.

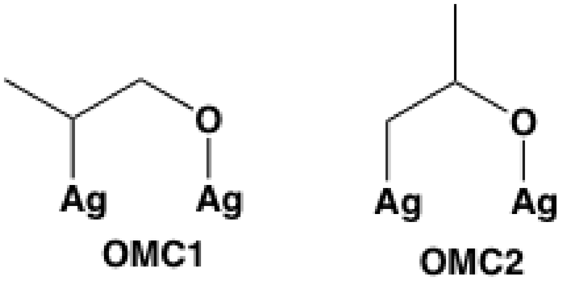

Scheme 5-1: Schematic of oxametallacycle isomers from ring opening propylene oxide.

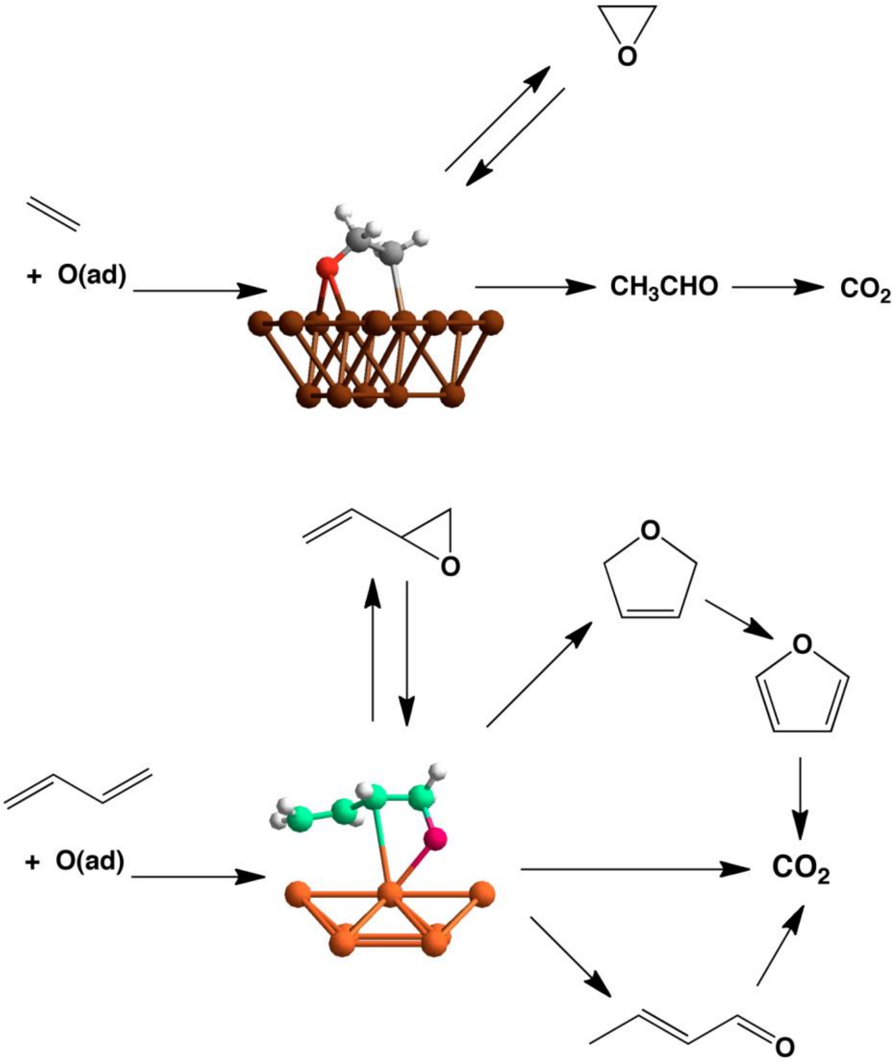

Figure 6-1 Reaction networks for ethylene and butadiene epoxidation, modified from past studies

6.2 Methods

6.2.1 Experimental Methods

The reactions of PO on Ag/α-Al_2O_3 were studied using the catalysts and reactor set-up previously described in reference [209]. The catalysts were prepared by wet-impregnation techniques. Foam monoliths (18 mm diameter x 10 mm length and 45 ppi) consisting of 99.5% α-Al_2O_3 and provided by Vesuvius Hi-Tech, were used as catalyst supports. The monoliths were first heated at 700 °C in air for 12 h to remove carbonaceous impurities, then boiled in deionized (DI) water for 2 h and dried at 363 K. The monoliths were immersed in a solution of silver nitrate ($AgNO_3$) in DI water to prepare the catalyst. The desired amount of $AgNO_3$ in solution was calculated so that the nominal loading of Ag in each catalyst was 15 wt %. The catalysts were then dried at 363 K for 12 h and calcined at 673 K in an open-air furnace for 12 h. After preparation, the catalysts were reduced in a flow of 100 sccm of 20% H_2 in He at 573 K for 12 h.

Prior to the PO decomposition experiments, catalysts were tested for propylene epoxidation by flowing a gas mixture of propylene, oxygen and nitrogen (10 sccm propylene, 10 sccm O_2 and 80 sccm N_2) to the reactor operating at 543 K and allowing the catalyst to achieve steady state with respect to conversion of propylene and the selectivity to PO. Finally, the catalysts were purged with N_2 for several hours to remove any propylene or oxygen, after which a 50 sccm stream of 1 % PO in nitrogen from a pre-mixed cylinder was introduced to the reactor at 543 K. The reactor effluent was analyzed using an HP6890 gas chromatograph with both flame ionization detector and a thermal conductivity detector. The conversion and selectivity, quantities defined here on molar basis (with respect to moles of carbon), were calculated from the calibrated peaks from the gas chromatograph. Weight hourly space velocity (WHSV) in h^{-1} was calculated by determining the density of gas mixture at reaction conditions and using it to calculate the mass of the gas components. The catalysts were also imaged by scanning electron microscopy (SEM). The images, shown in the supporting information, show the catalyst surface before and after the reduction of catalyst in H_2 flow. Additional information about typical characteristics of these monolith-supported silver catalysts, including particle sizes and oxygen uptakes, can be found in previous publications.[216-218]

6.2.2 Theoretical Methods

All DFT calculations were performed using the Vienna *ab initio* simulation package (VASP).[100, 219] The close-packed facet of Ag(111) was used as the model surface and was represented by a four-layer slab, periodically repeated in a super cell geometry with six equivalent layers of vacuum (~ 14 Å) in between any two successive metal slabs. The atoms of the top two layers of the slab were allowed to relax to their lowest energy configuration, while those of the bottom two layers were fixed in their bulk truncated positions. To accommodate the adsorbed species without significant interaction across repeated unit cells, we employed a p(3 x 3) surface unit cell, corresponding to a surface coverage of 1/9 ML for each adsorbate. Adsorption was allowed on only one of the two surfaces exposed and the electrostatic potential was adjusted accordingly.[93] We calculated the lattice constant for bulk Ag to be 4.16 Å, in good agreement with an experimental value of 4.09 Å.[203]

The electron wave function was expanded using plane waves with an energy cutoff of 400 eV, and the core electron interactions were described using the projector augmented wave method (PAW). [220, 221] The surface Brillouin zone was sampled using a 4 x 4 x 1 Monkhorst-Pack *k*-point mesh;[96] convergence was confirmed with respect to the k point set. The self-consistent PW91 generalized gradient approximation (GGA-PW91)[98, 99] was used for describing the exchange-correlation energy and potential. Minimum energy paths and respective activation energy barriers for all elementary steps were calculated using the climbing image nudged elastic band method (CI-NEB).[102] The minimum energy path for each elementary step was discretized by at least nine images, including the initial and final state. Transition states were verified by calculating the Hessian matrix[103] and identifying a single imaginary frequency along the reaction coordinate.

6.3 Results and Discussion

6.3.1 Propylene epoxidation activity of silver catalysts

The Ag/α-Al_2O_3 catalyst was essentially unselective towards epoxidation. During propylene oxidation experiments at the conditions noted above, 1.4% conversion of propylene with 98.5% selectivity to carbon dioxide (CO_2) was achieved. Production of acrolein accounted for nearly all of the balance with trace amounts of PO and propanal being detected. PO selectivities of 3 to 4% were achieved with bimetallic catalysts that have previously been shown to increase ethylene epoxidation selectivities.[216-218] However, the studies of PO reactions described hereafter were carried out on the Ag/α-Al_2O_3 catalyst only. In these studies PO decomposition was used to understand the network of reactions that lead to acetone, acrolein and propanal observed in propylene oxidation, and thus to probe sequential reactions that might contribute to low epoxidation selectivity.

Propylene Oxide Reactions

PO reaction experiments were carried out with and without oxygen co-feed. Anaerobic reactions of PO are considered first, followed by the oxygen co-feed experiments.

In the anaerobic experiments, PO concentration and feed to the reactor were kept constant (50 sccm stream with 1 % v/v PO) while the temperature was varied at a constant WHSV of 1547 h^{-1}.

The PO conversion profile as a function of temperature is shown in Figure 6-2A. At 518 K, the PO conversion was 0.8% and increased exponentially with temperature in agreement with the Arrhenius rate expression. Based on these data, the activation energy for the isomerization of PO on the Ag/α-Al_2O_3 was determined to be 116 kJ/mol. This value is similar to the energy barrier reported for the formation of an oxametallacycle intermediate from adsorbed PO. Using Density Functional Theory, Lei et al. recently calculated a value of 121.7 kJ/mol for PO ring opening on Ag nanoparticles. [215] A similar value was calculated for periodic slabs of Ag by Torres et al. [222]. These results are consistent with the hypothesis that formation of an oxametallacycle from adsorbed PO is the rate-limiting step for PO isomerization.

Figure 6-2B shows the selectivity to acrolein, propanal, acetone and allyl alcohol at different conversions of PO. At 518 K the selectivity to propanal was almost 88%, but as the temperature of the reactor was increased, selectivity to propanal decreased: at 543 K the selectivity was down to 38%. At the same time, the selectivity towards acrolein increased from 0% at 518 K to 49% at 543 K. The selectivity to acetone and allyl alcohol remained stable through this temperature range. The increase in the selectivity to acrolein occurred in parallel to the decrease in the selectivity of propanal over the same temperature range.

All of the products of PO reaction in Figure 6-2, except for allyl alcohol, are frequently reported in the literature as by-products of propylene epoxidation on silver-based catalysts [[215, 223-227]. In the absence of oxygen in this experiment, no CO_2 was detected. Note that, except for acrolein, all of the observed products are structural isomers of PO. Acrolein, having two hydrogen atoms less than the other species, was the only non-isomeric product observed in these decomposition experiments. However, no hydrogen co-product was detected by the gas chromatograph.

The formation of acetone, allyl alcohol and propanal from PO is thermodynamically favorable. Propylene oxide, having a highly strained three-member ring, has a smaller heat of formation than its isomers and thus is more reactive (see Table 6-1). Acetone is the most stable of the isomers with $\Delta H_f°$ = -217.1 kJ/mol compared to PO with a $\Delta H_f°$ = -93.7 kJ/mol and propanal and allyl alcohol are intermediate (see Table 6-1). It is not surprising that given suitable conditions, PO will isomerize into a more stable configuration. In fact, calculation of the equilibrium concentrations for the products of isomerization reveals that the reaction favors strongly the production of the isomers. The equilibrium constants for the isomerizations of PO to acetone, PO to propanal, PO to allyl alcohol and PO to acrolein and hydrogen (K_i, at 543 K) were 2.7×10^{12}, 4.1×10^{9}, 6.2×10^{4}, and 2.1×10^{5}, respectively. If the reaction were thermodynamically controlled the conversion of PO should have been larger than observed. The conversion of only 6% of the PO on the Ag catalyst and the formation of propanal as the dominant product indicate that the decomposition of PO into its isomers and acrolein is kinetically determined.

The selectivity trends for PO isomerization in Figure 6-2B provide a hint that acrolein may be a secondary product. Unlike the other products, acrolein selectivity remains low until PO conversion exceeds 3% and then increases rapidly, mainly at the expense of the dominant product, propanal.

Table 6-1 Gas Phase Standard Enthalpies of Formation of Propylene Oxide Isomers (298.15 K)

	Standard Enthalpy of Formation, $\Delta H_f°$ [kJ/mol]	Relative Stability, $\Delta H_f° - \Delta H_f°(PO)$ [kJ/mol]
Propylene Oxide	-94.7	0
Acetone	-217.5	-122.8
Propanal	-188.7	-94.0
Allyl Alcohol	-123.6	-29.9
Acrolein + H_2	-81.8	+12.9

Data from NIST Chemistry Webbook (2011)

This suggests that acrolein may be a secondary product, formed by dehydrogenation of a primary product, propanal, of PO isomerization. However, because increasing temperature was used to drive increased conversion in the experiments portrayed in Figure 6-2, these results alone are not sufficient to draw such a conclusion. It is conceivable, for example, that acrolein could also be a primary product of PO reaction, formed in parallel with, but with a somewhat higher activation barrier than, the various isomerization products. In order to distinguish between these two possibilities, it is necessary to carry out isothermal experiments at varying conversion.

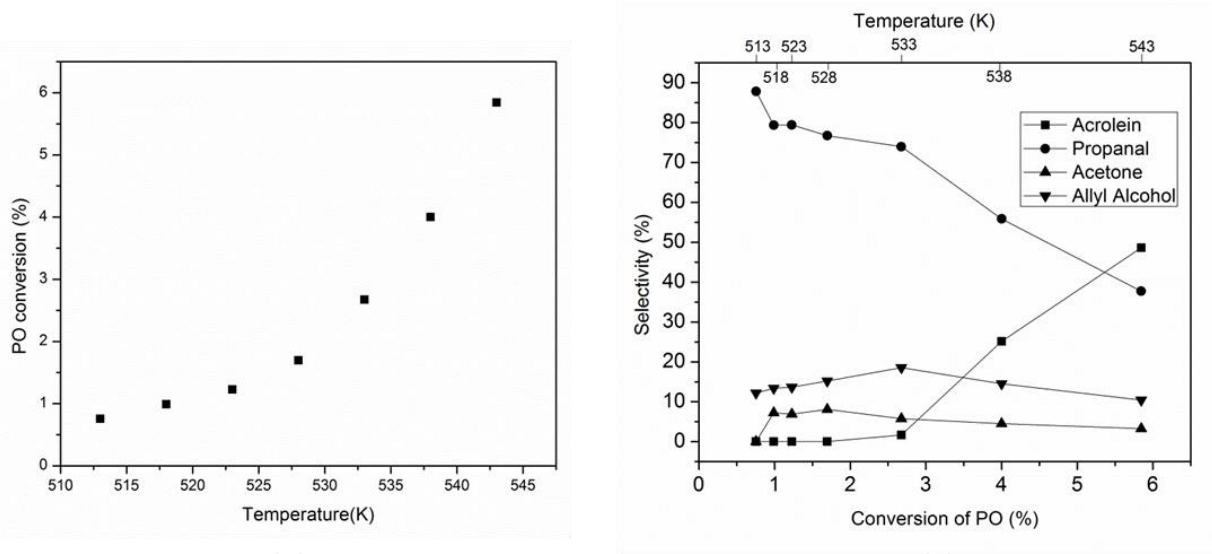

(A) (B)

Figure 6-2(A) PO conversion Ag/α-Al_2O_3 and (B) selectivity to various products from PO isomerization on Ag/α-Al_2O_3 at different temperatures.

To determine the reaction network and kinetics of PO isomerization, the reaction rank for the formation of the isomerization products was therefore investigated. In this experiment, the flow rate of PO to the reactor was varied while keeping temperature and concentration of PO in the feed constant, hence just changing the contact time with the catalyst. The PO flow was varied from 0.3 sccm to 0.8 sccm and diluted with N_2 to keep a constant 1% v/v PO in the feed. Figure 6-3 shows the selectivity of PO reactions vs. PO conversion in these experiments; PO flow rates are shown along the top axis of the figure. As conversion increased with longer contact times, the selectivity to the various products changed. Selectivity to propanal decreased substantially with a smaller reduction in the selectivity to allyl alcohol and acetone. Conversely, the selectivity to acrolein increased dramatically from its negligible level at low PO conversion. It is apparent from Figure 6-3 that acrolein is a secondary product, formed primarily by dehydrogenation of propanal, whereas the PO isomers acetone, allyl alcohol and propanal are primary products.

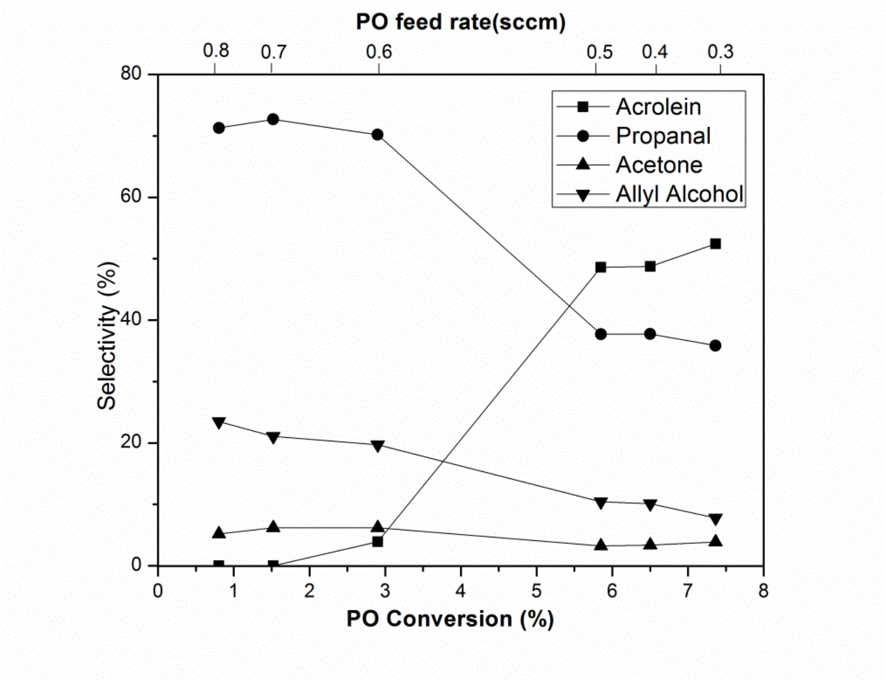

Figure 6-3. Selectivity to various products of PO isomerization on Ag/α-Al_2O_3 at 543 K at varying conversions produced by changing the PO feed rate.

By utilizing the two oxametallacycle structures in Scheme 1 as the common intermediates, one can construct a reaction network connecting propylene oxide to its primary and secondary reaction products on silver catalysts. This network is illustrated in Figure 6-4. For completeness, the formation of these two oxametallacycles from propylene and adsorbed oxygen atoms is also shown. Note the symmetry of the network with respect to propylene and PO. Depending on which C-O bond is made (in the case of propylene oxidation) or broken (by PO ring opening) either oxametallacycle can be accessed from either propylene or PO. This is not the case with the other isomers: acetone, propanal and allyl alcohol can be connected only to the oxametallacycle that contains the corresponding C-O bond in each case.

The isomers of PO can each be formed by a net hydrogen shift of one of the two oxametallacycles in Scheme 1, as shown in Figure 6-4. The two products containing a carbonyl group, propanal and acetone, can be formed by 1,2 H-shifts of the linear (OMC1) and branched (OMC2) oxametallacycles, respectively. Allyl alcohol can be formed by a net 1,4 H-shift of the linear oxametallacycle. Both 1,2 and 1,4 H-shift reactions of oxametallacycles are elementary processes in the reaction networks shown in Figure 6-1: acetaldehyde formation from EO involves a 1,2 H-shift in the corresponding oxametallacycle; crotonaldehyde formation from EpB represents a 1,4 H-shift of that oxametallacycle. However, reaction data alone are not sufficient to determine whether the 1,2 and 1,4 H-shifts of PO-derived oxametallacycles are elementary processes.

The results in Figure 6-3 clearly show that acrolein is formed as a secondary product at the expense of propanal. Close inspection of the results reveals that allyl alcohol selectivity also decreases, albeit less severely with the increased formation of acrolein. Figure 6-4 therefore shows acrolein as a dehydrogenation product of both propanal and allyl alcohol. It should be noted however that, unlike all of the other steps depicted in this figure, dehydrogenation of these molecular products is unlikely to be an elementary process.

Finally, returning to the temperature variation experiments in **Figure 6-2**, it is striking that all of the primary products of PO isomerization are present at essentially all temperatures, and absent the increasing effect of the secondary dehydrogenation, their selectivities are relatively insensitive to temperature. This suggests that the activation barriers for the two ring opening reactions are quite similar to each other; likewise the barriers to the H-shift steps must also be similar to each other.

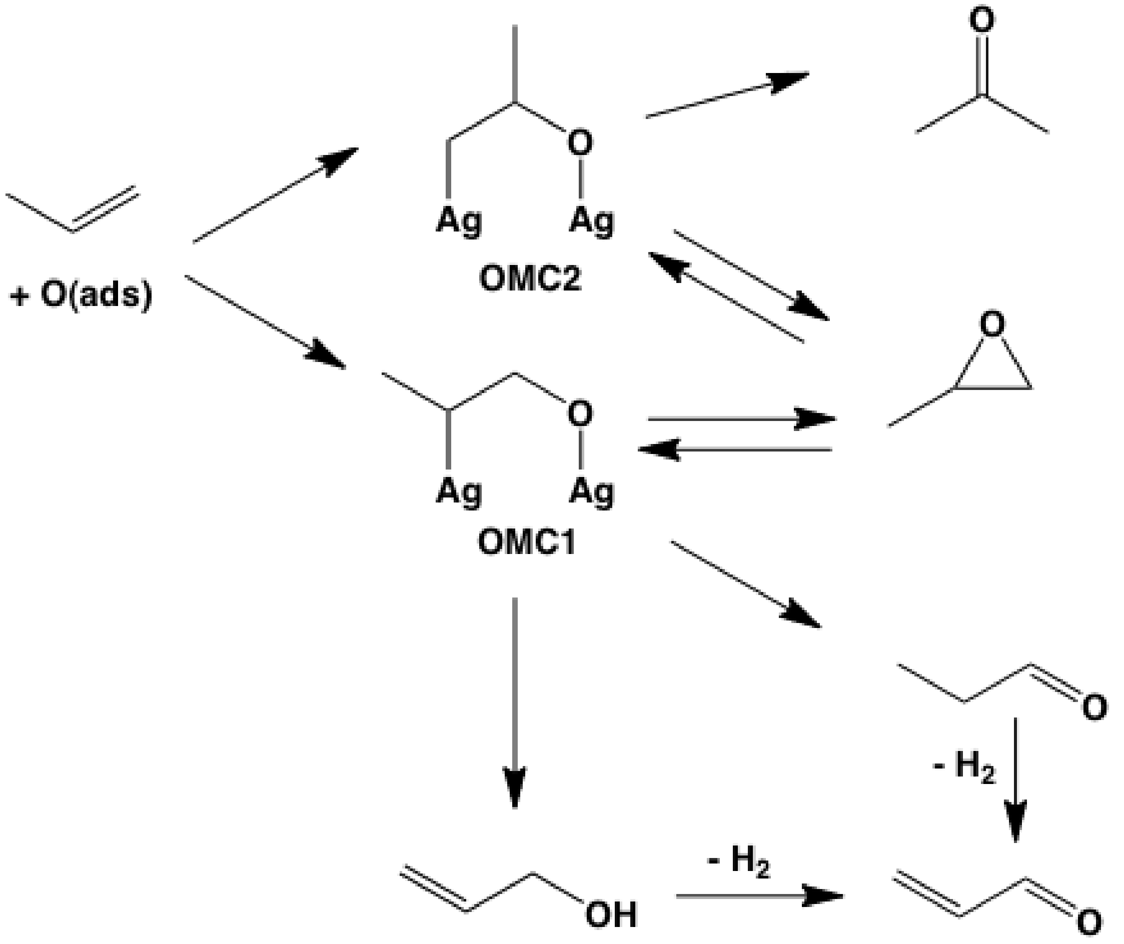

Figure 6-4 Proposed network for propylene oxide reaction under anaerobic conditions on silver catalysts.

Comparison of insights from theory and experiment

The reaction network in Figure 6-4 and the insights regarding the relative barriers of the competing reaction channels deduced from experiment provide an important framework for computational chemistry studies and for benchmarking the results of these. Conversely, by utilizing theory to test the minimum reaction network necessary to explain experimental observations, one can identify potential additional complexities in the mechanism that may not be obvious from available experimental results. This framework can thus provide the basis for further experimental and theoretical evaluation of a host of other relevant conditions, including surface structure, co-reactants and co-adsorbates, catalyst promoters, etc.

To illustrate the complementary insights into the surface reactions of propylene oxide on silver and to provide a foundation for future comprehensive studies, we have carried out DFT calculations of the barriers involved in elementary steps linking propylene, propylene oxide, and reaction products to the two oxametallacycle intermediates depicted in Figure 6-4. The most stable adsorption configurations of all reaction intermediates, along with their respective binding energies, is shown is Figure 6-5 and a schematic of the reaction coordinate is shown in Figure 6-6, with the energies of each transition state identified and of each adsorbed intermediate, all relative to the energy of propylene(ad) + O(ad), in their minimum energy coadsorbed state. While the results obtained thus far are not sufficient to produce a microkinetic model of propylene epoxidation or propylene oxide isomerization with secondary reactions, they buttress the interpretation of our anaerobic reaction experiments significantly. In particular, they demonstrate that

1. The barriers to the formation of the two oxametallacycles from propylene and oxygen are quite similar to each other;

2. The barriers to the formation of the two oxametallacycles from PO are similar, but the formation of OMC2 is more highly activated, consistent with the minor formation of acetone from PO isomerization in our experiments;

3. The barriers to ring opening of adsorbed PO are 105.9 kJ/mol (to OMC1) and 117.5 kJ/mol (to OMC2), near the observed apparent activation barrier for PO reaction (116 kJ/mol), and consistent with the hypothesis that PO ring opening is likely rate determining in the isomerization network;

4. PO formation from OMC1 has one of the lowest barriers of any of the reactions of the two oxametallacycles, suggesting that PO can be formed selectively from such intermediates;
5. The highest energy pathway from the oxametallacycles to a C_3 oxygenate product leads to acrolein + H_2, consistent with the increased formation of acrolein at higher temperatures in our experiments.

These results also provide one important caveat to the interpretation of our experimental results. We have been unable thus far to find a transition state for the 1,4 H-shift of OMC1 to produce allyl alcohol. Instead, the path to allyl alcohol appears to involve a sequence of C-H scission and O-H formation steps involving transfer of a hydrogen atom to and from the surface, and involving an allyl alkoxide intermediate. However, as shown below, for PO reaction under aerobic conditions minor amounts of allyl alcohol formed are rapidly oxidized to acrolein. Thus the 1-4 H shift reaction, whether direct or surface mediated, may ultimately be of little consequence in propylene epoxidation catalysis.

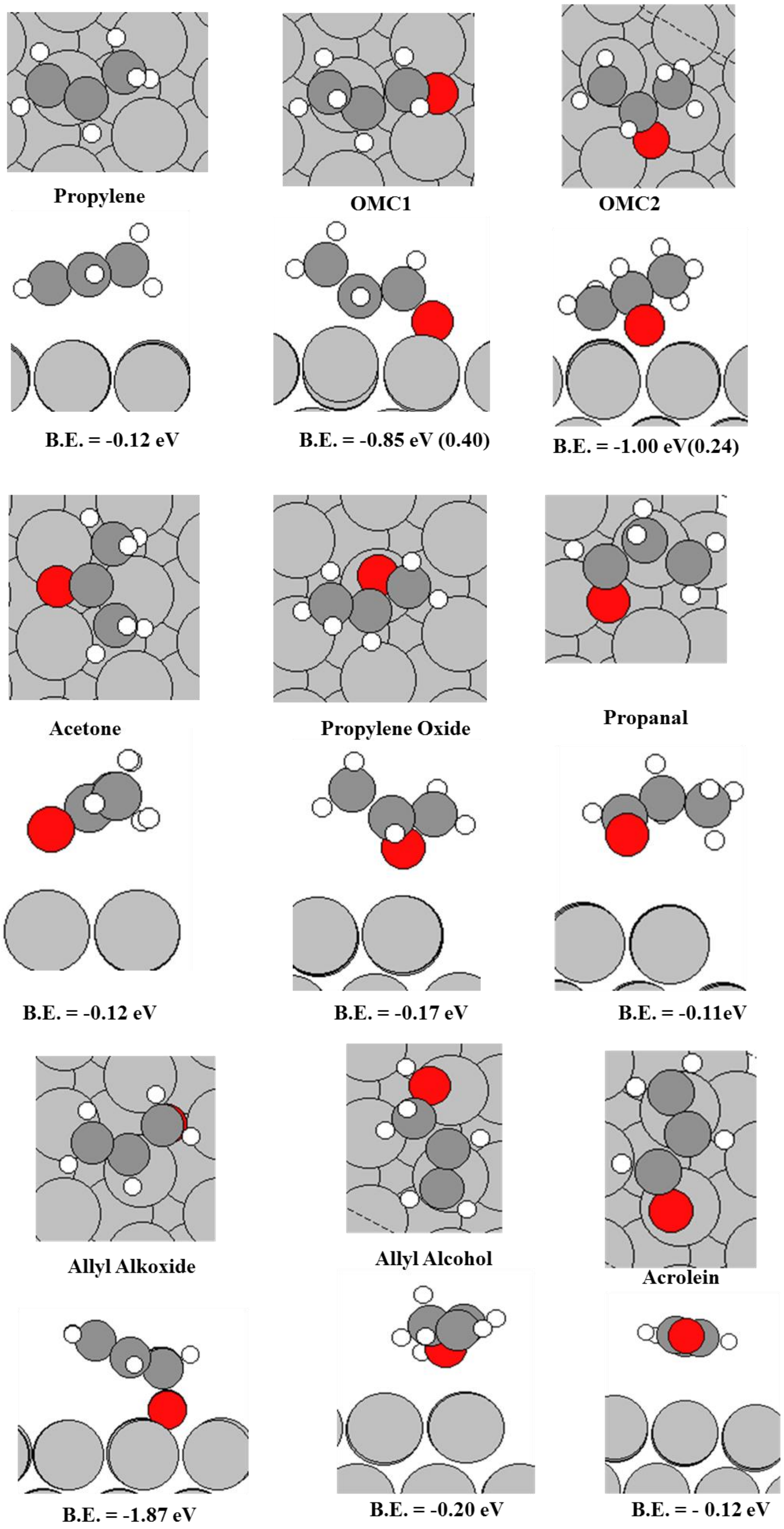

Figure 6-5 Most stable adsorption configurations and the corresponding binding energies for all the species involved in the reaction network. binding energy = $E_{adsorbed} - E_{Gasphase} – E_{Clean\ slab}$

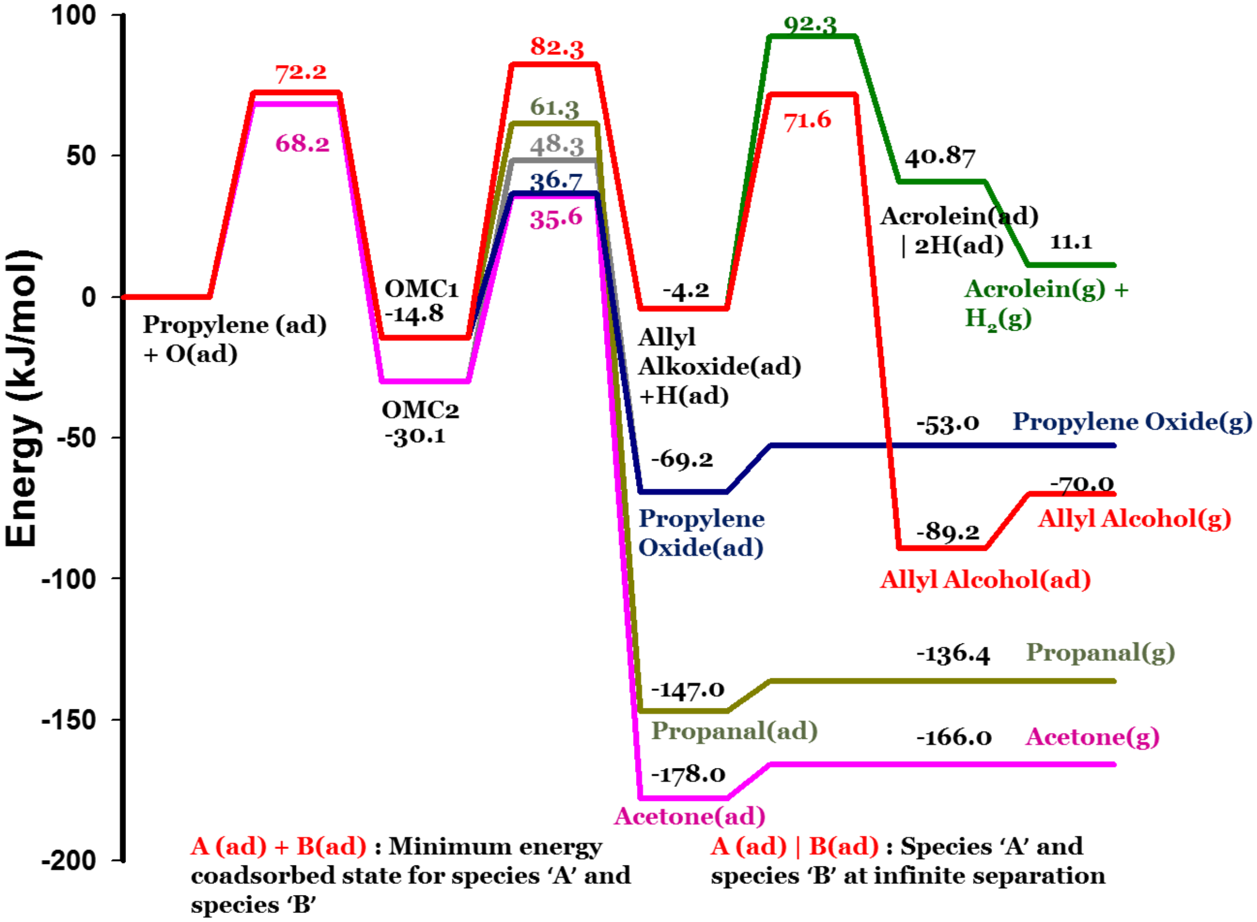

Figure 6-6 Schematic potential energy surface for reactions of propylene oxide. All energy values are with respect to Propylene (ad) + O(ad) in their minimum energy co-adsorbed state. Grey line connects PO(ad) with OMC2, with a transition state energy of 48.3 kJ/mol.

6.3.2 Effects of oxygen on the reactions of PO on Ag/α-Al_2O_3

Oxygen was introduced to the reactor along with PO to determine the effect of adsorbed oxygen on the reactivity of the oxametallacycles and the products of PO decomposition. The catalyst was allowed to reach steady state at 543 K and constant flow of 0.5 sccm PO in 50 sccm N_2. The oxygen flow was then adjusted to change the O_2/PO flow ratio to the reactor.

Oxygen affects the isomerization of PO significantly. As shown in Figure 6-7A, the conversion of PO increased from ~6% to ~10% as the O_2/PO ratio was increased from 0 to 2. The introduction of 1 sccm O_2 to the reactor almost doubled the rate of PO decomposition, and yet, further increases in the flow rate of oxygen had little effect on the PO conversion. Indeed, the conversion leveled off at ~13% even as the amount of oxygen was increased to higher levels (up to a 70:1 ratio). If these results are extrapolated to propylene oxidation conditions, they suggest that a fraction of the PO produced could end up reacting into other products. This complication poses additional constraints for the design of a selective Ag-based catalyst for propylene epoxidation. Even if combustion of propylene via allylic hydrogen abstraction can be suppressed, the catalyst must produce PO selectively and prevent its isomerization, which occurs here at noticeable levels. As shown in Figure 6-7, the reaction products in the presence of oxygen were similar to those under anaerobic conditions, with two significant differences. CO_2 became a significant product, and allyl alcohol disappeared from the product slate even at the lowest levels of oxygen utilized. The selectivities for acetone and acrolein initially increased when a small amount of oxygen was first introduced to the reactor. However, beyond this point, further increases in oxygen concentration caused both propanal and acrolein selectivities to decrease; the acetone selectivity was insensitive to the O_2/PO ratio.

It is important to consider not just selectivity trends, but also the dependence of yield on oxygen concentration in order to understand the various reaction channels. For example, the yields of both propanal and acrolein increased as more oxygen was added to the feed up to an O_2/PO ratio of 30, after which point the acrolein yield declined. This result demonstrates that at high O_2/PO ratios of 30 to 70, where PO conversion is constant, the increased production of CO_2 comes from the combustion of acrolein; propanal is surprisingly unaffected. Since both aldehydes should react readily with oxygen on silver to form surface carboxylates (which would undergo combustion) this result suggests that acrolein is preferentially adsorbed relative to propanal on the silver surface. The stronger binding of α,β-unsaturated carbonyl compounds relative to aliphatic aldehydes and ketones is expected, and has previously been deduced from studies of selective acrolein hydrogenation.[228]

The disappearance of allyl alcohol from the slate of PO isomerization products upon oxygen addition is also not surprising in view of the well-understood deprotonation of alcohols by atomic oxygen on silver.[229] Separate experiments revealed that in the presence of oxygen, allyl alcohol reacts readily to form acrolein on supported silver catalysts. This was confirmed by experiments in which the alcohol was fed by flowing nitrogen through a saturator containing liquid allyl alcohol. In the absence of oxygen a small portion of the alcohol reacted to form propanal and acrolein. The conversion of the alcohol at 543K was 4%, with no CO_2 or other products detected. When oxygen was introduced to the reactor, however, most of the allyl alcohol reacted to form acrolein and CO_2. The conversion of the alcohol in the presence of oxygen was 74%, with 80% selectivity to acrolein. This is also reflected in the results (Figure 6-7) where the slight increase in acrolein selectivity is observed with the introduction of oxygen paralleled the disappearance of allyl alcohol.

The high conversion of allyl alcohol in the presence of oxygen indicates that even if this compound is formed during propylene epoxidation, it is highly unlikely that it will be detected directly. This explains why allyl alcohol has not been reported on other propylene epoxidation studies [215, 223-227]. More importantly, this experiment confirms the pathway for the formation of acrolein established by Solomon and Madix [230]. The proposed mechanism involves the formation of an allyl alkoxide from the dehydrogenation of adsorbed allyl alcohol. This alkoxide goes through a further dehydrogenation step to produce acrolein.

The results shown in Figure 6-8 suggest that surface oxygen plays a few simple roles in the reactions of PO on silver. The relatively modest increase in PO conversion, even under highly oxidizing conditions, suggests that co-adsorbed oxygen decreases the barrier for epoxide ring opening slightly, but does not appear to react directly with PO to produce combustion products. This observation is consistent with the interaction of O(ad) and EO previously explored on the Ag(110) surface. In TPD experiments in UHV, it was observed that in the presence of co-adsorbed oxygen, a higher coverage of surface oxametallacycles was generated by EO ring opening [48]. However, the selectivity of oxametallacycle reaction channels to EO and acetaldehyde was insensitive to the presence of oxygen. The kinetics and selectivity of CO_2 formation could be accounted for entirely by secondary reactions of the acetaldehyde product.

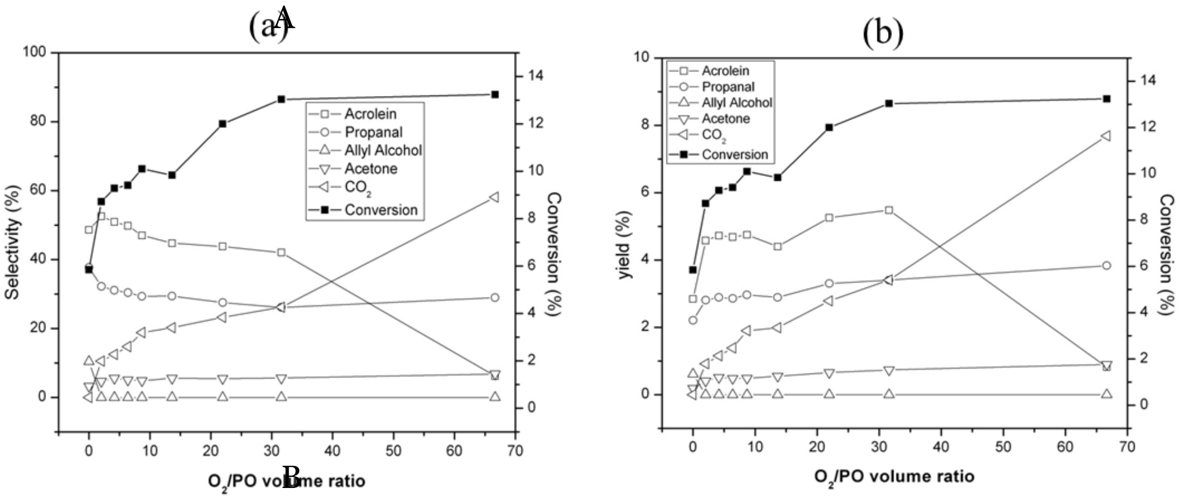

Figure 6-7 (A) PO conversion and selectivity to various products as a function of O_2/PO ratio at 543 K; (B) Corresponding trends in product yields.

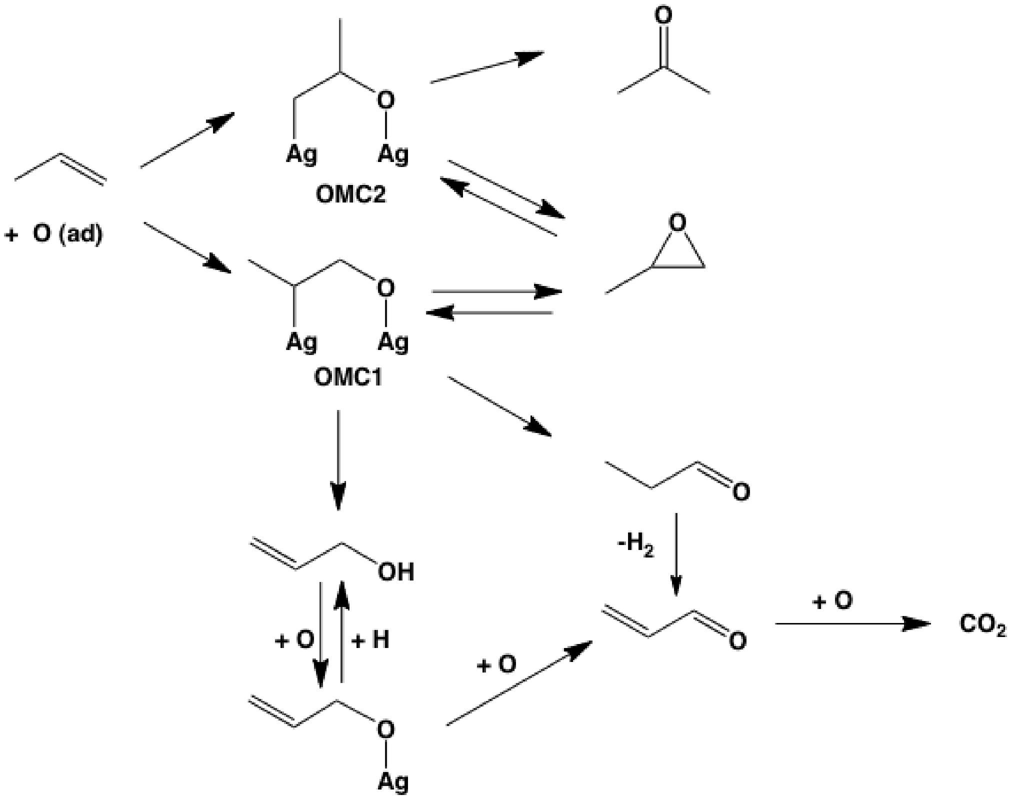

Figure 6-8 Proposed reaction network for propylene epoxidation and decomposition over silver catalysts.

The principal roles of oxygen in the present experiments appear to be to enhance acrolein formation by oxidative dehydrogenation of allyl alcohol and/or of allyl alkoxides formed from it or directly from OMC1, and to combust acrolein produced by this reaction and by the isomerization and dehydrogenation of PO. Thus to the reaction network for PO isomerization in Figure 6-4, one can add steps involving reactions of oxygen with allyl alcohol and acrolein. While it would be expected that oxygen might also participate in the dehydrogenation and/or combustion of propanal, as well, the present experiments provide little evidence for the operation of such pathways under the conditions explored. Future studies will examine changes to the potential energy surface of

Figure 6-6 with additional oxygen atoms present on the surface, however, we stress again that the experimental results described above do not give reason to expect significant perturbations.

Finally, we consider the implication of these results for the design of more selective propylene epoxidation catalysts. It is clear from previous work that the first major "fork" in the propylene oxidation network is between the pathways for oxygen addition and allylic hydrogen abstraction (which leads inexorably to combustion.) However, additional branches in the reaction network after oxygen addition lead to a variety of C_3H_6O isomers, of which PO is the least thermodynamically preferred. The manifold of reactions can be understood in terms of the formation and reactions of the two oxametallacyle intermediates depicted in Scheme 1, and all of the isomers can be accessed via ring closure or 1,2 and 1,4 H-shifts previously observed in ethylene and butadiene epoxidation. These results suggest that improvement of PO selectivity will require catalyst modifications that disfavor allyl hydrogen abstraction, but also those that favor ring closure over hydrogen shift reactions of oxametallacycles. Successful strategies for improvement of catalysts for EO and EpB production may also contribute to improved PO catalysts.

One of the perhaps surprising observations of the present work is the resistance of PO and its major isomers to oxidation with silver catalysts. While the small amount of allyl alcohol and the secondary product acrolein were both readily oxidized, there was little evidence for combustion of PO or propanal under the conditions examined. This again suggests that the design focus for improving PO selectivity should be on suppressing propylene combustion and on manipulating the branching reactions of surface oxametallacycles, rather than on sequential combustion of products.

6.4 Conclusions

The reactions of propylene oxide on silver have been studied to understand the reaction network accessible after the addition of oxygen to propylene. PO reacts on Ag catalysts under both aerobic and anaerobic conditions. Under anaerobic conditions, all of the products of isomerization are primary products; the dehydrogenation product acrolein is a secondary product. The apparent activation energy for PO isomerization is 116 kJ/mol, consistent with the energy of oxametallacycle formation from PO. Oxygen increases the conversion of PO somewhat. In the presence of oxygen, allyl alcohol readily reacts on the surface of the catalyst to form acrolein, and CO_2 is generated primarily by acrolein oxidation. These results shed light on the network of reactions involving surface oxametallacycle intermediates that can influence the selectivity of propylene epoxidation with silver catalysts.

Chapter 7

Conclusions and Suggestions for Future Work

7.1 Conclusions

The studies reported in this thesis adopt a common methodology involving the use of first-principles density functional theory calculations and microkinetic modeling, coupled with experiments, for developing a mechanistic understanding of reaction network and using this information in the discovery and design of improved heterogeneous transition metal catalysts.

The utility of this combined theoretical and experimental approach for unravelling the reaction mechanism and obtaining insights into the nature of active sites, was demonstrated first for formic acid decomposition on Au/SiC catalysts. A microkinetic model parameterized using the DFT derived initial guesses on Au(111), Au(100), and Au(211) surfaces was employed to describe the experimental FA decomposition rate and selectivity data. It was shown that FA decomposition follows the formate (HCOO) mediated path, with 100% selectivity towards the dehydrogenation products (CO_2 + H_2) under all reaction conditions in the kinetic regime explored. An analysis of the kinetic parameters suggested that an Au surface in which the coordination number of surface Au atoms is ≤ 4 may provide a better model for the active site of FA decomposition on supported Au catalysts.

This approach was then used to explore the structure sensitivity of this reaction on supported Cu catalysts. Cu(100) was shown to be the active site for FA decomposition, and the surface was predicted to have a high coverage of HCOO species. It was shown that the presence of these adsorbed intermediates can significantly affect the reaction energetics, and hence, the overall reaction rates, and that an explicit treatment of these surface poisons is important. Next, a descriptor based microkinetic modeling framework was developed to obtain two dimensional reactivity and selectivity volcano plots that led to the discovery of several potentially promising bimetallic alloy catalysts.

Finally, the reaction mechanism of propylene oxide (PO) on silver catalysts were studied to understand the network of parallel and sequential reactions that may limit the selectivity of propylene epoxidation by these catalysts. DFT calculations provided mechanistic insights for this reaction and were used to explain the low selectivity in direct propylene epoxidation with silver catalysts.

In addition to the work reported in this dissertation, similar DFT-based approaches were also adopted to study the following problems:

(1) Selective Lactic Acid Hydrogenation: The primary aim of this study was to identify the fundamental aspects that govern the selectivity in the conversion of α-hydroxy carboxylic acids to different products under hydrogenation conditions. Thermochemical trends were first obtained for this reaction on the close-packed facets of 10 transition metals; subsequently, detailed DFT calculations and reaction kinetics experiments were performed on supported Cu catalysts, and microkinetic modeling was employed to identify the reaction mechanism and nature of active sites.

(2) Steam Methane Reforming (SMR) on stepped Ni surfaces: DFT calculations were performed to map out the thermochemistry and kinetics of SMR on a stepped Ni(533) surface, and subsequently understand the role of step edges in the overall activity this reaction through microkinetic modeling. In addition, the mechanism of nucleation of graphene was also explored.

7.2 Suggestions for future work

Catalysis by gold has received significant attention over the last several decades and the remarkable activity of highly dispersed gold catalysts has been established for several reactions, like CO oxidation, acetylene hydro chlorination, selective oxidation of alcohols, and selective hydrogenation of alkenes and unsaturated aldehydes, among others. Although it is reasonably well established by now that it is perhaps the ‘small’ (< 2 nm) Au clusters that contribute to its unexpected activity, the true nature of the active site on Au catalysts hasn’t been unequivocally established. The first natural extension of our study may be to use advanced ab-initio molecular dynamics methods, together with standard DFT calculations to obtain the energetics of this reaction on highly undercoordinated Au atoms, and employ the iterative method that we had described in our study, to determine the exact nature (coordination number, charge, etc.) of the active site for FA decomposition. Recently, oxide supports have been shown to play an active role in CO oxidation on Au catalysts, and this combined AIMD-DFT approach can be particularly valuable in describing these systems. The insights from these studies can then be used to synthesize Au catalysts with high surface concentration of the desired sites, using bottom-up synthetic protocols with atomic level precision. Given the fact that Au catalysis is currently at the *hotspot* of heterogeneous catalysis, we anticipate that such an analysis may be paradigmatic for Au based catalysis, for several reactions ranging from CO oxidation to selective alkyne hydrogenation, among others.

Our analysis of formic acid decomposition on supported Cu catalysts demonstrated the importance of meticulously and explicitly incorporating surface coverage effects in the DFT calculations for obtaining accurate predictions for the active sites and surface coverages. The natural extension of this study would be for the processes that involve more reactive transition metal catalysts, for instance Pt and Pd that are prone to surface poisoning by adsorbed reaction intermediates. For the reactions (for instance, FA decomposition, water gas shift reaction, oxygen reduction reaction, ammonia and methanol electro-oxidation, NO reduction etc.), for which surface poisoning by CO/CH/NO has been well documented on these catalysts, the methodology described in this chapter may be particularly useful for ensuring that the final solutions obtained are self-consistent; i.e., the surface environment used in the DFT calculations is indeed consistent with those predicted by the microkinetic model, and observed from spectroscopic studies.

The descriptor based approach reported in Chapter 5 illustrates a catalyst design strategy that can be used for tailoring surfaces with improved catalytic properties, by utilizing the theoretical insights developed on monometallic catalysts. It should be noted here that this framework has its limitations as it was formulated using the data on close packed fcc(111) and hcp (0001), and a more open fcc(100) facets. Hence, there are several challenges that will need to be addressed before it can be adopted as a generic methodology for a wider range of heterogeneously catalyzed systems on transition metal nanoparticles. However, several advanced inorganic synthesis techniques are now available to design supported catalysts with well-defined morphology, allowing preferential exposure of specific crystal facets to the reaction environment. For such systems, this approach can arguably be extended with reasonable accuracy. Another extension of this study may be to utilize this base framework and improve the accuracy of its predictions by explicitly accounting for other crystal facets than the ones included here, accurate treatment of surface poisons, and evaluating long term catalyst stability. While several of these factors can be simulated using DFT derived microkinetic models, a versatile framework for catalyst design will require significant benchmarking of the simulations against detailed experimental studies under reaction conditions.

References

1. BP Statistical Review of World Energy. BP Statistical Review of World Energy: 2014.
2. U.S. Energy Information Administration. http://tonto.eia.doe.gov/.
3. Erisman, J. W.; Sutton, M. A.; Galloway, J.; Klimont, Z.; Winiwarter, W., How a century of ammonia synthesis changed the world. *Nature Geoscience* 2008, 1, 636-639.
4. Schlogl, R., Catalytic synthesis of ammonia - A "never-ending story"? *Angewandte Chemie-International Edition* 2003, 42, 2004-2008.
5. Kaspar, J.; Fornasiero, P.; Hickey, N., Automotive catalytic converters: current status and some perspectives. *Catalysis Today* 2003, 77, 419-449.
6. Gokhale, A. A.; Dumesic, J. A.; Mavrikakis, M., On the mechanism of low-temperature water gas shift reaction on copper. *Journal of the American Chemical Society* 2008, 130, 1402-1414.
7. Madon, R. J.; Braden, D.; Kandoi, S.; Nagel, P.; Mavrikakis, M.; Dumesic, J. A., Microkinetic analysis and mechanism of the water gas shift reaction over copper catalysts. *Journal of Catalysis* 2011, 281, 1-11.
8. Nilekar, A. U.; Alayoglu, S.; Eichhorn, B.; Mavrikakis, M., Preferential CO Oxidation in Hydrogen: Reactivity of Core-Shell Nanoparticles. *Journal of the American Chemical Society* 2010, 132, 7418-7428.
9. Linic, S.; Barteau, M. A., Control of ethylene epoxidation selectivity by surface oxametallacycles. *Journal of the American Chemical Society* 2003, 125, 4034-4035.
10. Mavrikakis, M.; Doren, D. J.; Barteau, M. A., Density functional theory calculations for simple oxametallacycles: Trends across the periodic table. *Journal of Physical Chemistry B* 1998, 102, 394-399.
11. Greeley, J.; Mavrikakis, M., On the role of subsurface oxygen and ethylenedioxy in ethylene epoxidation on silver. *Journal of Physical Chemistry C* 2007, 111, 7992-7999.
12. Grabow, L. C.; Mavrikakis, M., Mechanism of Methanol Synthesis on Cu through CO2 and CO Hydrogenation. *Acs Catalysis* 2011, 1, 365-384.
13. Logadottir, A.; Norskov, J. K., Ammonia synthesis over a Ru(0001) surface studied by density functional calculations. *Journal of Catalysis* 2003, 220, 273-279.
14. Honkala, K.; Hellman, A.; Remediakis, I. N.; Logadottir, A.; Carlsson, A.; Dahl, S.; Christensen, C. H.; Norskov, J. K., Ammonia synthesis from first-principles calculations. *Science* 2005, 307, 555-558.
15. Ojeda, M.; Nabar, R.; Nilekar, A. U.; Ishikawa, A.; Mavrikakis, M.; Iglesia, E., CO activation pathways and the mechanism of Fischer-Tropsch synthesis. *Journal of Catalysis* 2010, 272, 287-297.
16. Greeley, J.; Jaramillo, T. F.; Bonde, J.; Chorkendorff, I. B.; Norskov, J. K., Computational high-throughput screening of electrocatalytic materials for hydrogen evolution. *Nature Materials* 2006, 5, 909-913.
17. Knudsen, J.; Nilekar, A. U.; Vang, R. T.; Schnadt, J.; Kunkes, E. L.; Dumesic, J. A.; Mavrikakis, M.; Besenbacher, F., A Cu/Pt near-surface alloy for water-gas shift catalysis. *Journal of the American Chemical Society* 2007, 129, 6485-6490.

18. Adzic, R. R.; Zhang, J.; Sasaki, K.; Vukmirovic, M. B.; Shao, M.; Wang, J. X.; Nilekar, A. U.; Mavrikakis, M.; Valerio, J. A.; Uribe, F., Platinum monolayer fuel cell electrocatalysts. *Topics in Catalysis* 2007, 46, 249-262.

19. Nilekar, A. U.; Xu, Y.; Zhang, J.; Vukmirovic, M. B.; Sasaki, K.; Adzic, R. R.; Mavrikakis, M., Bimetallic and ternary alloys for improved oxygen reduction catalysis. *Topics in Catalysis* 2007, 46, 276-284.

20. Studt, F.; Abild-Pedersen, F.; Bligaard, T.; Sorensen, R. Z.; Christensen, C. H.; Norskov, J. K., Identification of non-precious metal alloy catalysts for selective hydrogenation of acetylene. *Science* 2008, 320, 1320-1322.

21. Andersson, M. P.; Bligaard, T.; Kustov, A.; Larsen, K. E.; Greeley, J.; Johannessen, T.; Christensen, C. H.; Norskov, J. K., Toward computational screening in heterogeneous catalysis: Pareto-optimal methanation catalysts. *Journal of Catalysis* 2006, 239, 501-506.

22. Dumesic, J. A.; Rudd, D. F.; Aparicio, L. M.; Rekoske, J. E.; Treviño, A. A., The Microkinetics of Heterogeneous Catalysis (ACS Professional Reference Book). 1993.

23. Ovesen, C. V.; Clausen, B. S.; Hammershoi, B. S.; Steffensen, G.; Askgaard, T.; Chorkendorff, I.; Norskov, J. K.; Rasmussen, P. B.; Stoltze, P.; Taylor, P., Microkinetic analysis of the water-gas shift reaction under industrial conditions. *Journal of Catalysis* 1996, 158, 170-180.

24. Linic, S.; Barteau, M. A., Construction of a reaction coordinate and a microkinetic model for ethylene epoxidation on silver from DFT calculations and surface science experiments. *Journal of Catalysis* 2003, 214, 200-212.

25. Gokhale, A. A.; Kandoi, S.; Greeley, J. P.; Mavrikakis, M.; Dumesic, J. A., Molecular-level descriptions of surface chemistry in kinetic models using density functional theory. *Chemical Engineering Science* 2004, 59, 4679-4691.

26. Mhadeshwar, A. B.; Vlachos, D. G., Is the water-gas shift reaction on Pt simple? Computer-aided microkinetic model reduction, lumped rate expression, and rate-determining step. *Catalysis Today* 2005, 105, 162-172.

27. Grabow, L. C.; Gokhale, A. A.; Evans, S. T.; Dumesic, J. A.; Mavrikakis, M., Mechanism of the water gas shift reaction on Pt: First principles, experiments, and microkinetic modeling. *Journal of Physical Chemistry C* 2008, 112, 4608-4617.

28. Blaylock, D. W.; Ogura, T.; Green, W. H.; Beran, G. J. O., Computational Investigation of Thermochemistry and Kinetics of Steam Methane Reforming on Ni(111) under Realistic Conditions. *Journal of Physical Chemistry C* 2009, 113, 4898-4908.

29. Singh, S.; Li, S.; Carrasquillo-Flores, R.; Alba-Rubio, A. C.; Dumesic, J. A.; Mavrikakis, M., Formic acid decomposition on Au catalysts: DFT, microkinetic modeling, and reaction kinetics experiments. AIChE Journal: 2014; Vol. 60, pp 1303-1319.

30. Rackemann, D. W.; Doherty, W. O. S., A review on the production of levulinic acid and furanics from sugars. *Proceedings of the 34th Conference of the Australian Society of Sugar Cane Technologists held at Cairns, Queensland, Australia, 1-4 May 2012* 2012, 20-M 20.

31. Rice, C.; Ha, S.; Masel, R. I.; Wieckowski, A., Catalysts for direct formic acid fuel cells. *Journal of Power Sources* 2003, 115, 229-235.

32. Alonso, D. M.; Bond, J. Q.; Dumesic, J. A., Catalytic conversion of biomass to biofuels. *Green Chemistry* 2010, 12, 1493-1513.

33. Tilman, D.; Socolow, R.; Foley, J. A.; Hill, J.; Larson, E.; Lynd, L.; Pacala, S.; Reilly, J.; Searchinger, T.; Somerville, C.; Williams, R., Beneficial Biofuels-The Food, Energy, and Environment Trilemma. *Science* 2009, 325, 270-271.

34. Bozell, J. J.; Petersen, G. R., Technology development for the production of biobased products from biorefinery carbohydrates-the US Department of Energy's "Top 10" revisited. *Green Chemistry* 2010, 12, 539-554.

35. Boddien, A.; Loges, B.; Junge, H.; Gaertner, F.; Noyes, J. R.; Beller, M., Continuous Hydrogen Generation from Formic Acid: Highly Active and Stable Ruthenium Catalysts. *Advanced Synthesis & Catalysis* 2009, 351, 2517-2520.

36. Fellay, C.; Yan, N.; Dyson, P. J.; Laurenczy, G., Selective Formic Acid Decomposition for High-Pressure Hydrogen Generation: A Mechanistic Study. *Chemistry-a European Journal* 2009, 15, 3752-3760.

37. Fellay, C.; Dyson, P. J.; Laurenczy, G., A viable hydrogen-storage system based on selective formic acid decomposition with a ruthenium catalyst. *Angewandte Chemie-International Edition* 2008, 47, 3966-3968.

38. Gan, W.; Dyson, P. J.; Laurenczy, G., Hydrogen storage and delivery: immobilization of a highly active homogeneous catalyst for the decomposition of formic acid to hydrogen and carbon dioxide. *Reaction Kinetics and Catalysis Letters* 2009, 98, 205-213.

39. Fukuzumi, S., Bioinspired energy conversion systems for hydrogen production and storage. *European Journal of Inorganic Chemistry* 2008, 1351-1362.

40. Boddien, A.; Gaertner, F.; Jackstell, R.; Junge, H.; Spannenberg, A.; Baumann, W.; Ludwig, R.; Beller, M., ortho-Metalation of Iron(0) Tribenzylphosphine Complexes: Homogeneous Catalysts for the Generation of Hydrogen from Formic Acid. *Angewandte Chemie-International Edition* 2010, 49, 8993-8996.

41. Johnson, T. C.; Morris, D. J.; Wills, M., Hydrogen generation from formic acid and alcohols using homogeneous catalysts. *Chemical Society Reviews* 2010, 39, 81-88.

42. Zhang, T.; Wyman, C. E., Integrated production of levulinic acid and furfural from cellulosic biomass. *Abstracts of Papers of the American Chemical Society* 2011, 241.

43. Girisuta, B.; Janssen, L. P. B. M.; Heeres, H. J., Kinetic study on the acid-catalyzed hydrolysis of cellulose to levulinic acid. *Industrial & Engineering Chemistry Research* 2007, 46, 1696-1708.

44. Bond, J. Q.; Alonso, D. M.; Wang, D.; West, R. M.; Dumesic, J. A., Integrated Catalytic Conversion of gamma-Valerolactone to Liquid Alkenes for Transportation Fuels. *Science* 2010, 327, 1110-1114.

45. Braden, D. J.; Henao, C. A.; Heltzel, J.; Maravelias, C. T.; Dumesic, J. A., Production of liquid hydrocarbon fuels by catalytic conversion of biomass-derived levulinic acid. *Green Chemistry* 2011, 13, 1755-1765.

46. Serrano-Ruiz, J. C.; Braden, D. J.; West, R. M.; Dumesic, J. A., Conversion of cellulose to hydrocarbon fuels by progressive removal of oxygen. *Applied Catalysis B-Environmental* 2010, 100, 184-189.

47. Columbia, M. R.; Thiel, P. A., The interaction of formic-acid with transition-metal surfaces, studied in ultrahigh-vacuum. *Journal of Electroanalytical Chemistry* 1994, 369, 1-14.

48. Madix, R. J., Surface-reaction modifiers - general overview. *Abstracts of Papers of the American Chemical Society* 1980, 180, 26-PHYS.

49. Larson, L. A.; Dickinson, J. T., Decomposition of formic-acid on Ru(1010). *Surface Science* 1979, 84, 17-30.

50. Sun, Y. K.; Weinberg, W. H., Catalytic decomposition of formic-acid on Ru(001) - transient measurements. *Journal of Chemical Physics* 1991, 94, 4587-4599.

51. Solymosi, F.; Kiss, J.; Kovacs, I., Adsorption of HCOOH on Rh(111) and its reaction with preadsorbed oxygen. *Surface Science* 1987, 192, 47-65.

52. Jorgensen, S. W.; Madix, R. J., Active oxygen on group VIII metals - activation of formic-acid and formaldehyde on Pd(100). *Journal of the American Chemical Society* 1988, 110, 397-400.

53. Bulushev, D. A.; Beloshapkin, S.; Ross, J. R. H., Hydrogen from formic acid decomposition over Pd and Au catalysts. *Catalysis Today* 2010, 154, 7-12.

54. Solymosi, F.; Koos, A.; Liliom, N.; Ugrai, I., Production of CO-free H-2 from formic acid. A comparative study of the catalytic behavior of Pt metals on a carbon support. *Journal of Catalysis* 2011, 279, 213-219.

55. Ying, D. H. S.; Madix, R. J., Thermal-desorption study of formic-acid decomposition on a clean Cu(110) surface. *Journal of Catalysis* 1980, 61, 48-56.

56. Boddien, A.; Mellmann, D.; Gaertner, F.; Jackstell, R.; Junge, H.; Dyson, P. J.; Laurenczy, G.; Ludwig, R.; Beller, M., Efficient Dehydrogenation of Formic Acid Using an Iron Catalyst. *Science* 2011, 333, 1733-1736.

57. Koos, A.; Solymosi, F., Production of CO-Free H-2 by Formic Acid Decomposition over Mo2C/Carbon Catalysts. *Catalysis Letters* 2010, 138, 23-27.

58. Flaherty, D. W.; Berglund, S. P.; Mullins, C. B., Selective decomposition of formic acid on molybdenum carbide: A new reaction pathway. *Journal of Catalysis* 2010, 269, 33-43.

59. McCarty, J.; Madix, R. J., Study of kinetics and mechanism of decomposition of formic-acid on carburized and graphitized Ni(110) using AES, LEED and flash desorption. *Journal of Catalysis* 1975, 38, 402-417.

60. Kubota, J.; Bandara, A.; Wada, A.; Domen, K.; Hirose, C., IRAS study of formic acid decomposition on NiO(111)/Ni(111) surface: Comparison of vacuum and catalytic conditions. *Surface Science* 1996, 368, 361-365.

61. Dilara, P. A.; Vohs, J. M., TPD and HREELS investigation of the reaction of formic-acid on ZrO_2(100). *Journal of Physical Chemistry* 1993, 97, 12919-12923.

62. Larsson, R.; Jamroz, M. H.; Borowiak, M. A., On the catalytic decomposition of formic acid. I. The activation energies for oxide catalysis. *Journal of Molecular Catalysis a-Chemical* 1998, 129, 41-51.

63. Senanayake, S. D.; Mullins, D. R., Redox pathways for HCOOH decomposition over CeO2 surfaces. *Journal of Physical Chemistry C* 2008, 112, 9744-9752.

64. Peng, X. D.; Barteau, M. A., Acid-base properties of model MgO surfaces. *Langmuir* 1991, 7, 1426-1431.

65. Outka, D. A.; Madix, R. J., Acid-base and nucleophilic chemistry of atomic oxygen on the Au(110) surface - reactions with formic-acid and formaldehyde. *Surface Science* 1987, 179, 361-376.

66. Lin, C.-H.; Chen, C.-L.; Wang, J.-H., Mechanistic Studies of Water-Gas-Shift Reaction on Transition Metals. *Journal of Physical Chemistry C* 2011, 115, 18582-18588.

67. Davis, B. H. B. H.; Jacobs, G.; Patterson, P. M. P. M.; Graham, U. M. U. M.; Crawford, A. C. A. C., Low temperature water gas shift: the link between the catalysis of

WGS and formic acid decomposition over Pt/ceria. *International Journal of Hydrogen Energy* 2005, 30, 1265-76.

68. Liu, C.; Chen, M.; Du, C.; Zhang, J.; Yin, G.; Shi, P.; Sun, Y., Durability of Ordered Mesoporous Carbon Supported Pt Particles as Catalysts for Direct Formic Acid Fuel Cells. *International Journal of Electrochemical Science* 2012, 7, 10592-10606.

69. Yu, X. W.; Pickup, P. G., Codeposited PtSb/C catalysts for direct formic acid fuel cells. *Journal of Power Sources* 2011, 196, 7951-7956.

70. Yinghui, P.; Ruiming, Z.; Blair, S. L., Anode poisoning study in direct formic acid fuel cells. *Electrochemical and Solid-State Letters* 2009, 12, B23-6.

71. Markovic, N. M.; Ross, P. N., Surface science studies of model fuel cell electrocatalysts. *Surface Science Reports* 2002, 45, 121-229.

72. Xingwen, Y.; Pickup, P. G., Recent advances in direct formic acid fuel cells (DFAFC). *Journal of Power Sources* 2008, 182, 124-32.

73. Choi, J.-H.; Jeong, K.-J.; Dong, Y.; Han, J.; Lim, T.-H.; Lee, J.-S.; Sung, Y.-E., Electro-oxidation of methanol and formic acid on PtRu and PtAu for direct liquid fuel cells. *Journal of Power Sources* 2006, 163, 71-75.

74. Brandon, N. P.; Skinner, S.; Steele, B. C. H., Recent advances in materials for fuel cells. *Annual Review of Materials Research* 2003, 33, 183-213.

75. Xu, J. B.; Zhao, T. S.; Liang, Z. X., Carbon supported platinum-gold alloy catalyst for direct formic acid fuel cells. *Journal of Power Sources* 2008, 185, 857-861.

76. Sheng, Z.; Yuyan, S.; Geping, Y.; Yuehe, L., Facile synthesis of PtAu alloy nanoparticles with high activity for formic acid oxidation. *Journal of Power Sources* 2010, 195, 1103-6.

77. Haruta, M.; Kobayashi, T.; Sano, H.; Yamada, N., Novel gold catalysts for the oxidation of carbon-monoxide at a temperature far below 0-degrees-c. *Chemistry Letters* 1987, 405-408.

78. Hutchings, G. J., Vapor-phase hydrochlorination of acetylene - correlation of catalytic activity of supported metal chloride catalysts. *Journal of Catalysis* 1985, 96, 292-295.

79. Sa, J.; Goguet, A.; Taylor, S. F. R.; Tiruvalam, R.; Kiely, C. J.; Nachtegaal, M.; Hutchings, G. J.; Hardacre, C., Influence of Methyl Halide Treatment on Gold Nanoparticles Supported on Activated Carbon. *Angewandte Chemie-International Edition* 2011, 50, 8912-8916.

80. Guzman, J.; Gates, B. C., Gold nanoclusters supported on MgO: Synthesis, characterization, and evidence of Au(6). *Nano Letters* 2001, 1, 689-692.

81. Janssens, T. V. W.; Clausen, B. S.; Hvolbaek, B.; Falsig, H.; Christensen, C. H.; Bligaard, T.; Norskov, J. K., Insights into the reactivity of supported Au nanoparticles: combining theory and experiments. *Topics in Catalysis* 2007, 44, 15-26.

82. Gong, J., Structure and Surface Chemistry of Gold-Based Model Catalysts. *Chemical Reviews* 2012, 112, 2987-3054.

83. Coquet, R.; Howard, K. L.; Willock, D. J., Theory and simulation in heterogeneous gold catalysis. *Chemical Society Reviews* 2008, 37, 2046-2076.

84. Davis, R. J., All that glitters is not Au-0. *Science* 2003, 301, 926-927.

85. Bond, G. C.; Thompson, D. T., Catalysis by gold. *Catalysis Reviews-Science and Engineering* 1999, 41, 319-388.

86. Hashmi, A. S. K.; Hutchings, G. J., Gold catalysis. *Angewandte Chemie-International Edition* 2006, 45, 7896-7936.

87. Guzman, J.; Anderson, B. G.; Vinod, C. P.; Ramesh, K.; Niemantsverdriet, J. W.; Gates, B. C., Synthesis and reactivity of dimethyl gold complexes supported on MgO: Characterization by infrared and x-ray absorption spectroscopies. *Langmuir* 2005, 21, 3675-3683.

88. Yi, N.; Saltsburg, H.; Flytzani-Stephanopoulos, M., Hydrogen Production by Dehydrogenation of Formic Acid on Atomically Dispersed Gold on Ceria. *Chemsuschem* 2013, 6, 816-819.

89. Ojeda, M.; Iglesia, E., Formic Acid Dehydrogenation on Au-Based Catalysts at Near-Ambient Temperatures. *Angewandte Chemie-International Edition* 2009, 48, 4800-4803.

90. Gazsi, A.; Bansagi, T.; Solymosi, F., Decomposition and Reforming of Formic Acid on Supported Au Catalysts: Production of CO-Free H-2. *Journal of Physical Chemistry C* 2011, 115, 15459-15466.

91. Hammer, B.; Hansen, L. B.; Norskov, J. K., Improved adsorption energetics within density-functional theory using revised Perdew-Burke-Ernzerhof functionals. *Physical Review B* 1999, 59, 7413-7421.

92. Greeley, J.; Norskov, J. K.; Mavrikakis, M., Electronic structure and catalysis on metal surfaces. *Annual Review of Physical Chemistry* 2002, 53, 319-348.

93. Neugebauer, J.; Scheffler, M., Adsorbate-substrate and adsorbate-adsorbate interactions of na and k adlayers on Al(111). *Physical Review B* 1992, 46, 16067-16080.

94. Bengtsson, L., Dipole correction for surface supercell calculations. *Physical Review B* 1999, 59, 12301-12304.

95. Chadi, D. J.; Cohen, M. L., SPECIAL POINTS IN BRILLOUIN ZONE. *Physical Review B* 1973, 8, 5747-5753.

96. Monkhorst, H. J.; Pack, J. D., Special Points for Brillouin-Zone Integrations. *Physical Review B* 1976, 13, 5188-5192.

97. Vanderbilt, D., Soft self-consistent pseudopotentials in a generalized eigenvalue formalism. *Physical Review B* 1990, 41, 7892-7895.

98. Perdew, J. P.; Chevary, J. A.; Vosko, S. H.; Jackson, K. A.; Pederson, M. R.; Singh, D. J.; Fiolhais, C., Atoms, molecules, solids, and surfaces - applications of the generalized gradient approximation for exchange and correlation. *Physical Review B* 1992, 46, 6671-6687.

99. White, J. A.; Bird, D. M., Implementation of gradient-corrected exchange-correlation potentials in car-parrinello total-energy calculations. *Physical Review B* 1994, 50, 4954-4957.

100. Kresse, G.; Furthmuller, J., Efficiency of ab-initio total energy calculations for metals and semiconductors using a plane-wave basis set. *Computational Materials Science* 1996, 6, 15-50.

101. Donohue, J. I., The Structures of the Elements. *Wiley: New York* 1974, 222.

102. Henkelman, G.; Uberuaga, B. P.; Jonsson, H., A climbing image nudged elastic band method for finding saddle points and minimum energy paths. *Journal of Chemical Physics* 2000, 113, 9901-9904.

103. Greeley, J.; Mavrikakis, M., A first-principles study of surface and subsurface H on and in Ni(111): diffusional properties and coverage-dependent behavior. *Surface Science* 2003, 540, 215-229.

104. Chakarova-Kack, S. D.; Schroder, E.; Lundqvist, B. I.; Langreth, D. C., Application of van der Waals density functional to an extended system: Adsorption of benzene and naphthalene on graphite. *Physical Review Letters* 2006, 96.
105. Sauer, J.; Ugliengo, P.; Garrone, E.; Saunders, V. R., Theoretical-study of van-der-waals complexes at surface sites in comparison with the experiment. *Chemical Reviews* 1994, 94, 2095-2160.
106. Lopez, N.; Janssens, T. V. W.; Clausen, B. S.; Xu, Y.; Mavrikakis, M.; Bligaard, T.; Norskov, J. K., On the origin of the catalytic activity of gold nanoparticles for low-temperature CO oxidation. *Journal of Catalysis* 2004, 223, 232-235.
107. Hu, C.; Ting, S.-W.; Chan, K.-Y.; Huang, W., Reaction pathways derived from DFT for understanding catalytic decomposition of formic acid into hydrogen on noble metals. *International Journal of Hydrogen Energy* 2012, 37, 15956-15965.
108. Campbell, C. T.; Daube, K. A., A surface science investigation of the water-gas shift reaction on cu(111). *Journal of Catalysis* 1987, 104, 109-119.
109. Vanherwijnen, T.; Dejong, W. A., Kinetics and mechanism of the co shift on cu-zno .1. Kinetics of the forward and reverse co shift reactions. *Journal of Catalysis* 1980, 63, 83-93.
110. Edwards, J. F.; Schrader, G. L., Infrared-spectroscopy of cu/zno catalysts for the water-gas shift reaction and methanol synthesis. *Journal of Physical Chemistry* 1984, 88, 5620-5624.
111. Bowker, M.; Hadden, R. A.; Houghton, H.; Hyland, J. N. K.; Waugh, K. C., The mechanism of methanol synthesis on copper-zinc oxide alumina catalysts. *Journal of Catalysis* 1988, 109, 263-273.
112. Neophytides, S. G.; Marchi, A. J.; Froment, G. F., Methanol synthesis by means of diffuse reflectance infrared fourier-transform and temperature-programmed reaction spectroscopy. *Applied Catalysis a-General* 1992, 86, 45-64.
113. Sakakini, B.; Tabatabaei, J.; Watson, M. J.; Waugh, K. C.; Zemicael, F. W., Identification of the intermediate involved in methanol synthesis by gaseous titration. *Faraday Discussions* 1996, 105, 369-376.
114. Senanayake, S. D.; Stacchiola, D.; Liu, P.; Mullins, C. B.; Hrbek, J.; Rodriguez, J. A., Interaction of CO with OH on Au(111): HCOO, CO3, and HOCO as Key Intermediates in the Water-Gas Shift Reaction. *Journal of Physical Chemistry C* 2009, 113, 19536-19544.
115. Meunier, F. C.; Goguet, A.; Hardacre, C.; Burch, R.; Thompsett, D., Quantitative DRIFTS investigation of possible reaction mechanisms for the water-gas shift reaction on high-activity Pt- and Au-based catalysts. *Journal of Catalysis* 2007, 252, 18-22.
116. Nishimura, K.; Kunimatsu, K.; Machida, K.; Enyo, M., Electrocatalysis of pd + au alloy electrodes .4. Ir spectroscopic studies on the surface species derived from formaldehyde and formate in alkaline-solutions. *Journal of Electroanalytical Chemistry* 1989, 260, 181-192.
117. Xu, J.; Chen, L.; Tan, K. F.; Borgna, A.; Saeys, M., Effect of boron on the stability of Ni catalysts during steam methane reforming. *Journal of Catalysis* 2009, 261, 158-165.
118. Duan, S.; Ji, Y.-F.; Fang, P.-P.; Chen, Y.-X.; Xu, X.; Luo, Y.; Tian, Z.-Q., Density functional theory study on the adsorption and decomposition of the formic acid catalyzed

by highly active mushroom-like Au@Pd@Pt tri-metallic nanoparticles. *Physical Chemistry Chemical Physics* 2013, 15, 4625-4633.

119. Zhong, W.; Liu, Y.; Zhang, D., Theoretical Study of Methanol Oxidation on the PtAu(111) Bimetallic Surface: CO Pathway vs Non-CO Pathway. *Journal of Physical Chemistry C* 2012, 116, 2994-3000.

120. Greeley, J.; Mavrikakis, M., Surface and subsurface hydrogen: Adsorption properties on transition metals and near-surface alloys. *Journal of Physical Chemistry B* 2005, 109, 3460-3471.

121. Huang, S.-C.; Lin, C.-H.; Wang, J. H., Trends of Water Gas Shift Reaction on Close-Packed Transition Metal Surfaces. *Journal of Physical Chemistry C* 2010, 114, 9826-9834.

122. Yu, Y.; Wang, X.; Lim, K. H., A DFT Study on the Adsorption of Formic Acid and Its Oxidized Intermediates on (100) Facets of Pt, Au, Monolayer and Decorated Pt@Au Surfaces. *Catalysis Letters* 2011, 141, 1872-1882.

123. Barton, D. G.; Podkolzin, S. G., Kinetic study of a direct water synthesis over silica-supported gold nanoparticles. *Journal of Physical Chemistry B* 2005, 109, 2262-2274.

124. Ford, D. C.; Nilekar, A. U.; Xu, Y.; Mavrikakis, M., Partial and complete reduction of O-2 by hydrogen on transition metal surfaces. *Surface Science* 2010, 604, 1565-1575.

125. Jalili, S.; Isfahani, A. Z.; Habibpour, R., Atomic oxygen adsorption on Au (100) and bimetallic Au/M (M = Pt and Cu) surfaces. *Computational and Theoretical Chemistry* 2012, 989, 18-26.

126. Xu, Y.; Mavrikakis, M., Adsorption and dissociation of O-2 on gold surfaces: Effect of steps and strain. *Journal of Physical Chemistry B* 2003, 107, 9298-9307.

127. Mehmood, F.; Kara, A.; Rahman, T. S.; Henry, C. R., Comparative study of CO adsorption on flat, stepped, and kinked Au surfaces using density functional theory. *Physical Review B* 2009, 79.

128. Ojifinni, R. A.; Froemming, N. S.; Gong, J.; Pan, M.; Kim, T. S.; White, J. M.; Henkelman, G.; Mullins, C. B., Water-enhanced low-temperature CO oxidation and isotope effects on atomic oxygen-covered Au(111). *Journal of the American Chemical Society* 2008, 130, 6801-6812.

129. Liu, S.; Jin, P.; Zhang, D.; Hao, C.; Yang, X., Reaction mechanism for methanol oxidation on Au(1 1 1): A density functional theory study. *Applied Surface Science* 2013, 265, 443-451.

130. Bi, Q.-Y.; Du, X.-L.; Liu, Y.-M.; Cao, Y.; He, H.-Y.; Fan, K.-N., Efficient Subnanometric Gold-Catalyzed Hydrogen Generation via Formic Acid Decomposition under Ambient Conditions. *Journal of the American Chemical Society* 2012, 134, 8926-8933.

131. Grabow, L. C.; Hvolbaek, B.; Norskov, J. K., Understanding Trends in Catalytic Activity: The Effect of Adsorbate-Adsorbate Interactions for CO Oxidation Over Transition Metals. *Topics in Catalysis* 2010, 53, 298-310.

132. Flytzani-Stephanopoulos, M.; Gates, B. C., Atomically Dispersed Supported Metal Catalysts. *Annual Review of Chemical and Biomolecular Engineering, Vol 3* 2012, 3, 545-574.

133. Fu, Q.; Weber, A.; Flytzani-Stephanopoulos, M., Nanostructured Au-CeO2 catalysts for low-temperature water-gas shift. *Catalysis Letters* 2001, 77, 87-95.

134. Deng, W. L.; De Jesus, J.; Saltsburg, H.; Flytzani-Stephanopoulos, M., Low-content gold-ceria catalysts for the water-gas shift and preferential CO oxidation reactions. *Applied Catalysis a-General* 2005, 291, 126-135.
135. Gates, B. C., Supported gold catalysts: new properties offered by nanometer and sub-nanometer structures. *Chemical Communications* 2013, 49, 7876-7877.
136. Campbell, C. T., Finding the rate-determining step in a mechanism - Comparing DeDonder relations with the "degree of rate control". *Journal of Catalysis* 2001, 204, 520-524.
137. Campbell, C. T., Micro- and macro-kinetics: their relationship in heterogeneous catalysis. *Topics in Catalysis* 1994, 1, 353-366.
138. Dumesic, J. A., Analyses of reaction schemes using De Donder relations. *Journal of Catalysis* 1999, 185, 496-505.
139. Shekhar, M.; Wang, J.; Lee, W.-S.; Akatay, M. C.; Stach, E. A.; Delgass, W. N.; Ribeiro, F. H., Counting Au catalytic sites for the water-gas shift reaction. *Journal of Catalysis* 2012, 293, 94-102.
140. Shekhar, M.; Wang, J.; Lee, W.-S.; Williams, W. D.; Kim, S. M.; Stach, E. A.; Miller, J. T.; Delgass, W. N.; Ribeiro, F. H., Size and Support Effects for the Water-Gas Shift Catalysis over Gold Nanoparticles Supported on Model Al2O3 and TiO2. *Journal of the American Chemical Society* 2012, 134, 4700-4708.
141. Williams, W. D.; Shekhar, M.; Lee, W.-S.; Kispersky, V.; Delgass, W. N.; Ribeiro, F. H.; Kim, S. M.; Stach, E. A.; Miller, J. T.; Allard, L. F., Metallic Corner Atoms in Gold Clusters Supported on Rutile Are the Dominant Active Site during Water-Gas Shift Catalysis. *Journal of the American Chemical Society* 2010, 132, 14018-14020.
142. Sanchez, A.; Abbet, S.; Heiz, U.; Schneider, W. D.; Hakkinen, H.; Barnett, R. N.; Landman, U., When gold is not noble: Nanoscale gold catalysts. *Journal of Physical Chemistry A* 1999, 103, 9573-9578.
143. Wang, J. L.; Wang, G. H.; Zhao, J. J., Density-functional study of Au-n(n=2-20) clusters: Lowest-energy structures and electronic properties. *Physical Review B* 2002, 66.
144. Idrobo, J. C.; Walkosz, W.; Yip, S. F.; Oeguet, S.; Wang, J.; Jellinek, J., Static polarizabilities and optical absorption spectra of gold clusters (Au-n, n=2-14 and 20) from first principles. *Physical Review B* 2007, 76.
145. Ferrando, R.; Fortunelli, A.; Johnston, R. L., Searching for the optimum structures of alloy nanoclusters. *Physical Chemistry Chemical Physics* 2008, 10, 640-649.
146. Marx, D.; Hutter, J., Ab initio molecular dynamics: Theory and Implementation. *Modern Methods and Algorithms of Quantum Chemistry* 2000, 301-449.
147. Zhai, Y. P.; Pierre, D.; Si, R.; Deng, W. L.; Ferrin, P.; Nilekar, A. U.; Peng, G. W.; Herron, J. A.; Bell, D. C.; Saltsburg, H.; Mavrikakis, M.; Flytzani-Stephanopoulos, M., Alkali-Stabilized Pt-OHx Species Catalyze Low-Temperature Water-Gas Shift Reactions. *Science* 2010, 329, 1633-1636.
148. Mager-Maury, C.; Chizallet, C.; Sautet, P.; Raybaud, P., Platinum Nanoclusters Stabilized on gamma-Alumina by Chlorine Used As a Capping Surface Ligand: A Density Functional Theory Study. *Acs Catalysis* 2012, 2, 1346-1357.

149. Fu, Q.; Kudriavtseva, S.; Saltsburg, H.; Flytzani-Stephanopoulos, M., Gold-ceria catalysts for low-temperature water-gas shift reaction. *Chemical Engineering Journal* 2003, 93, 41-53.

150. Guzman, J.; Gates, B. C., Structure and reactivity of a mononuclear gold-complex catalyst supported on magnesium oxide. *Angewandte Chemie-International Edition* 2003, 42, 690-693.

151. Guzman, J.; Gates, B. C., Simultaneous presence of cationic and reduced gold in functioning MgO-supported CO oxidation catalysts: Evidence from X-ray absorption spectroscopy. *Journal of Physical Chemistry B* 2002, 106, 7659-7665.

152. Guzman, J.; Gates, B. C., Oxidation states of gold in MgO-supported complexes and clusters: Characterization by X-ray absorption spectroscopy and temperature-programmed oxidation and reduction. *Journal of Physical Chemistry B* 2003, 107, 2242-2248.

153. Loges, B.; Boddien, A.; Gaertner, F.; Junge, H.; Beller, M., Catalytic Generation of Hydrogen from Formic acid and its Derivatives: Useful Hydrogen Storage Materials. *Topics in Catalysis* 2010, 53, 902-914.

154. Grasemann, M.; Laurenczy, G., Formic acid as a hydrogen source - recent developments and future trends. *Energy & Environmental Science* 2012, 5, 8171-8181.

155. Enthaler, S.; von Langermann, J.; Schmidt, T., Carbon dioxide and formic acid-the couple for environmental-friendly hydrogen storage? *Energy & Environmental Science* 2010, 3, 1207-1217.

156. Hull, J. F.; Himeda, Y.; Wang, W.-H.; Hashiguchi, B.; Periana, R.; Szalda, D. J.; Muckerman, J. T.; Fujita, E., Reversible hydrogen storage using CO2 and a proton-switchable iridium catalyst in aqueous media under mild temperatures and pressures. *Nature Chemistry* 2012, 4, 383-388.

157. Jiang, H.-L.; Singh, S. K.; Yan, J.-M.; Zhang, X.-B.; Xu, Q., Liquid-Phase Chemical Hydrogen Storage: Catalytic Hydrogen Generation under Ambient Conditions. *Chemsuschem* 2010, 3, 541-549.

158. Rees, N. V.; Compton, R. G., Sustainable energy: a review of formic acid electrochemical fuel cells. *Journal of Solid State Electrochemistry* 2011, 15, 2095-2100.

159. Uhm, S.; Lee, H. J.; Lee, J., Understanding underlying processes in formic acid fuel cells. *Physical Chemistry Chemical Physics* 2009, 11, 9326-9336.

160. Wettstein, S. G.; Bond, J. Q.; Alonso, D. M.; Pham, H. N.; Datye, A. K.; Dumesic, J. A., RuSn bimetallic catalysts for selective hydrogenation of levulinic acid to gamma-valerolactone. *Applied Catalysis B-Environmental* 2012, 117, 321-329.

161. Iglesia, E.; Boudart, M., Unimolecular and bimolecular formic-acid decomposition on copper. *Journal of Physical Chemistry* 1986, 90, 5272-5274.

162. Columbia, M. R.; Crabtree, A. M.; Thiel, P. A., The temperature and coverage dependences of adsorbed formic-acid and its conversion to formate on pt(111). *Journal of the American Chemical Society* 1992, 114, 1231-1237.

163. Wachs, I. E.; Madix, R. J., Oxidation of H2CO on a copper(110) surface. *Surface Science* 1979, 84, 375-386.

164. Bowker, M.; Madix, R. J., XPS,UPS and thermal-desorption studies of the reactions of formaldehyde and formic-acid with the cu(110) surface. *Surface Science* 1981, 102, 542-565.

165. Baber, A. E.; Mudiyanselage, K.; Senanayake, S. D.; Beatriz-Vidal, A.; Luck, K. A.; Sykes, E. C. H.; Liu, P.; Rodriguez, J. A.; Stacchiola, D. J., Assisted deprotonation of

formic acid on Cu(111) and self-assembly of 1D chains. *Physical Chemistry Chemical Physics* 2013, 15, 12291-12298.

166. Bowker, M.; Haq, S.; Holroyd, R.; Parlett, P. M.; Poulston, S.; Richardson, N., Spectroscopic and kinetic studies of formic acid adsorption on Cu(110). *Journal of the Chemical Society-Faraday Transactions* 1996, 92, 4683-4686.

167. Bowker, M.; Rowbotham, E.; Leibsle, F. M.; Haq, S., The adsorption and decomposition of formic acid on Cu{110}. *Surface Science* 1996, 349, 97-110.

168. Poulston, S.; Bennett, R. A.; Jones, A. H.; Bowker, M., STM study of formic acid adsorption on Cu(110). *Physical Review B* 1997, 55, 12888-12891.

169. Bowker, M.; Poulston, S.; Bennett, R. A.; Stone, P.; Jones, A. H.; Haq, S.; Hollins, P., A combined STM molecular beam study of formic acid oxidation on Cu(110). *Journal of Molecular Catalysis a-Chemical* 1998, 131, 185-197.

170. Bowker, M.; Bennett, R. A.; Poulston, S.; Stone, P., Insights into surface reactivity: formic acid oxidation on Cu(110) studied using STM and a molecular beam reactor. *Catalysis Letters* 1998, 56, 77-83.

171. Youngs, T. G. A.; Haq, S.; Bowker, M., Formic acid adsorption and oxidation on Cu(110). *Surface Science* 2008, 602, 1775-1782.

172. Iglesia, E.; Boudart, M., Decomposition of formic-acid on copper, nickel, and copper nickel-alloys .2. Catalytic and temperature-programmed decomposition of formic-acid on cu sio2, cu al2o3, and cu powder. *Journal of Catalysis* 1983, 81, 214-223.

173. Iglesia, E.; Boudart, M., Catalytic and temperature programmed decomposition of formic-acid on copper-catalysts. *Abstracts of Papers of the American Chemical Society* 1985, 189, 92-COLL.

174. Iglesia, E.; Boudart, M., Decomposition of formic-acid on copper, nickel, and copper nickel-alloys .1. Preparation and characterization of catalysts. *Journal of Catalysis* 1983, 81, 204-213.

175. Quinn, D. F.; Taylor, D., Decomposition of formic acid and methanol on copper-nickel alloys. *Journal of the Chemical Society* 1965, 5248-&.

176. Volter, J.; Alsdorf, E., Surface composition and catalytic activity of nickel-copper alloys. *Zeitschrift Fur Anorganische Und Allgemeine Chemie* 1971, 380, 303-&.

177. Rundell, D. N.; Saltsburg, H. M.; Smith, W. D., The role of multiple gas-solid collisions in the catalytic decomposition of formic-acid. *Chemical Engineering Science* 1980, 35, 1113-1119.

178. Schwab, G. M.; Watson, A. M., Isotope effect in catalytic formic-acid dehydrogenation. Royal Society of Chemistry: Trans. Faraday Soc., 1964; Vol. 60, pp 1833 - 1846.

179. Howe, R. F.; Metcalfe, A., dehydrogenation of formic acid by Cu3Au. *Journal of Catalysis* 1969, 14, 55-&.

180. Schwab, G. M.; Schmidt, R., Influence of plastic-deformation on catalytic properties of metals. *Zeitschrift Fur Physikalische Chemie-Frankfurt* 1972, 82, 174-184.

181. Dowden, D. A.; Reynolds, P. W., Some reactions over alloy catalysts. *Discussions of the Faraday Society* 1950, 8, 184-190.

182. Inglis, H. S.; Taylor, D., Decomposition of formic acid on titanium, vanadium, chromium, manganese, iron, cobalt, nickel, and copper. *Journal of the Chemical Society a -Inorganic Physical Theoretical* 1969, 2985-&.

183. Bennett, R. A.; Poulston, S.; Bowker, M., Elevated temperature scanning tunneling microscopy study of formic acid adsorption and reaction on oxygen (2x1) covered Cu(110). *Journal of Chemical Physics* 1998, 108, 6916-6922.
184. Nakamura, I.; Nakano, H.; Fujitani, T.; Uchijima, T.; Nakamura, J., Synthesis and decomposition of formate on Cu(111) and Cu(110) surfaces: Structure sensitivity. *Journal of Vacuum Science & Technology a-Vacuum Surfaces and Films* 1999, 17, 1592-1595.
185. Nakano, H.; Nakamura, I.; Fujitani, T.; Nakamura, J., Structure-dependent kinetics for synthesis and decomposition of formate species over Cu(111) and Cu(110) model catalysts. *Journal of Physical Chemistry B* 2001, 105, 1355-1365.
186. Rubert-Nason, P.; Mavrikakis, M.; Maravelias, C. T.; Grabow, L. C.; Biegler, L. T., Advanced solution methods for microkinetic models of catalytic reactions: A methanol synthesis case study. *Aiche Journal* 2014, 60, 1336-1346.
187. *CRC Handbook of Chemistry and Physics*. 76 ed.; CRC Press: New York, 1996.
188. Ulitsky, A.; Elber, R., A new technique to calculate steepest descent paths in flexible polyatomic systems. *Journal of Chemical Physics* 1990, 92, 1510-1511.
189. Mills, G.; Jonsson, H.; Schenter, G. K., Reversible work transition-state theory - application to dissociative adsorption of hydrogen. *Surface Science* 1995, 324, 305-337.
190. Montgomery, J. A.; Frisch, M. J.; Ochterski, J. W.; Petersson, G. A., A complete basis set model chemistry. VI. Use of density functional geometries and frequencies. *Journal of Chemical Physics* 1999, 110, 2822-2827.
191. Chinchen, G. C.; Hay, C. M.; Vandervell, H. D.; Waugh, K. C., The measurement of copper surface-areas by reactive frontal chromatography. *Journal of Catalysis* 1987, 103, 79-86.
192. Hansen, P. L.; Wagner, J. B.; Helveg, S.; Rostrup-Nielsen, J. R.; Clausen, B. S.; Topsoe, H., Atom-resolved imaging of dynamic shape changes in supported copper nanocrystals. *Science* 2002, 295, 2053-2055.
193. Lin, S.; Johnson, R. S.; Smith, G. K.; Xie, D.; Guo, H., Pathways for methanol steam reforming involving adsorbed formaldehyde and hydroxyl intermediates on Cu(111): density functional theory studies. *Physical Chemistry Chemical Physics* 2011, 13, 9622-9631.
194. Zuo, Z.-J.; Wang, L.; Han, P.-D.; Huang, W., Insights into the reaction mechanisms of methanol decomposition, methanol oxidation and steam reforming of methanol on Cu(111): A density functional theory study. *International Journal of Hydrogen Energy* 2014, 39, 1664-1679.
195. Fujitani, T.; Choi, Y.; Sano, M.; Kushida, Y.; Nakamura, J., Scanning tunneling microscopy study of formate species synthesized from CO2 hydrogenation and prepared by adsorption of formic acid over Cu(111). *Journal of Physical Chemistry B* 2000, 104, 1235-1240.
196. Sotiropoulos, A.; Milligan, P. K.; Cowie, B. C. C.; Kadodwala, M., A structural study of formate on Cu(111). *Surface Science* 2000, 444, 52-60.
197. Tang, Q.-L.; Chen, Z.-X.; He, X., A theoretical study of the water gas shift reaction mechanism on Cu(111) model system. *Surface Science* 2009, 603, 2138-2144.
198. Lin, S.; Xie, D.; Guo, H., Methyl Formate Pathway in Methanol Steam Reforming on Copper: Density Functional Calculations. *Acs Catalysis* 2011, 1, 1263-1271.

199. Wang, G.-C.; Nakamura, J., Structure Sensitivity for Forward and Reverse Water-Gas Shift Reactions on Copper Surfaces: A DFT Study. *Journal of Physical Chemistry Letters* 2010, 1, 3053-3057.

200. Wang, G. C.; Jiang, L.; Zhou, Y. H.; Cai, Z. S.; Pan, Y. M.; Zhao, X. Z.; Li, Y. W.; Sun, Y. H.; Zhong, B.; Pang, X. Y.; Huang, W.; Xie, K. C., Investigation of the kinetic properties for the forward and reverse WGS reaction by energetic analysis. *Journal of Molecular Structure-Theochem* 2003, 634, 23-30.

201. Ferrin, P.; Mavrikakis, M., Structure Sensitivity of Methanol Electrooxidation on Transition Metals. *Journal of the American Chemical Society* 2009, 131, 14381-14389.

202. Greeley, J.; Mavrikakis, M., A first-principles study of methanol decomposition on Pt(111). *Journal of the American Chemical Society* 2002, 124, 7193-7201.

203. Ashcroft, N. W.; Mermin, N. D., *Solid state physics*. Holt: New York,, 1976; p xxi, 826 p.

204. SRI Consulting (2011) World Petrochemicals Report.

205. Sheldon, R. A., Synthetic and mechanistic aspects of metal-catalyzed epoxidations with hydroperoxides. *Journal of Molecular Catalysis* 1980, 7, 107-126.

206. Zemichael, F. W.; Palermo, A.; Tikhov, M. S.; Lambert, R. M., Propene epoxidation over K-promoted Ag/CaCO3 catalysts: the effect of metal particle size. *Catalysis Letters* 2002, 80, 93-98.

207. Erley, W.; Wagner, H., Thermal-decomposition of co on a stepped ni surface. *Surface Science* 1978, 74, 333-341.

208. Monnier, J. R.; Peters, K. T.; Hartley, G. W., The selective epoxidation of conjugated olefins containing allylic substituents and epoxidation of propylene in the presence of butadiene. *Journal of Catalysis* 2004, 225, 374-380.

209. Linic, S.; Barteau, M. A., On the mechanism of Cs promotion in ethylene epoxidation on Ag. *Journal of the American Chemical Society* 2004, 126, 8086-8087.

210. Medlin, J. W.; Barteau, M. A.; Vohs, J. M., Oxametallacycle formation via ring-opening of 1-epoxy-3-butene on Ag(110): a combined experimental/theoretical approach. *Journal of Molecular Catalysis a-Chemical* 2000, 163, 129-145.

211. Monnier, J. R., The selective epoxidation of non-allylic olefins over supported silver catalysts. *3rd World Congress on Oxidation Catalysis* 1997, 110, 135-149.

212. Medlin, J. W.; Monnier, J. R.; Barteau, M. A., Deuterium kinetic isotope effects in butadiene epoxidation over unpromoted and Cs-promoted silver catalysts. *Journal of Catalysis* 2001, 204, 71-76.

213. Piao, H.; Enever, M. C. N.; Adib, K.; Hrbek, J.; Barteau, M. A., High resolution X-ray photoelectron spectroscopy of styrene oxide adsorption and reaction on Ag(111). *Surface Science* 2004, 571, 139-145.

214. Medlin, J. W.; Mavrikakis, M.; Barteau, M. A., Stabilities of substituted oxametallacycle intermediates: Implications for regioselectivity of epoxide ring opening and olefin epoxidation. *Journal of Physical Chemistry B* 1999, 103, 11169-11175.

215. Lei, Y.; Mehmood, F.; Lee, S.; Greeley, J.; Lee, B.; Seifert, S.; Winans, R. E.; Elam, J. W.; Meyer, R. J.; Redfern, P. C.; Teschner, D.; Schlogl, R.; Pellin, M. J.; Curtiss, L. A.; Vajda, S., Increased Silver Activity for Direct Propylene Epoxidation via Subnanometer Size Effects. *Science* 2010, 328, 224-228.

216. Dellamorte, J. C.; Barteau, M. A.; Lauterbach, J., Opportunities for catalyst discovery and development: Integrating surface science and theory with high throughput methods. *Surface Science* 2009, 603, 1770-1775.
217. Dellamorte, J. C.; Lauterbach, J.; Barteau, M. A., Effect of Preparation Conditions on Ag Catalysts for Ethylene Epoxidation. *Topics in Catalysis* 2010, 53, 13-18.
218. Dellamorte, J. C.; Lauterbach, J.; Barteau, M. A., Palladium-silver bimetallic catalysts with improved activity and selectivity for ethylene epoxidation. *Applied Catalysis a-General* 2011, 391, 281-288.
219. Kresse, G.; Furthmuller, J., Efficient iterative schemes for ab initio total-energy calculations using a plane-wave basis set. *Physical Review B* 1996, 54, 11169-11186.
220. Blochl, P. E., Projector augmented-wave method. *Physical Review B* 1994, 50, 17953-17979.
221. Kresse, G.; Joubert, D., From ultrasoft pseudopotentials to the projector augmented-wave method. *Physical Review B* 1999, 59, 1758-1775.
222. Torres, D.; Lopez, N.; Illas, F.; Lambert, R. M., Low-basicity oxygen atoms: A key in the search for propylene epoxidation catalysts. *Angewandte Chemie-International Edition* 2007, 46, 2055-2058.
223. Yao, W.; Guo, Y.; Liu, X.; Guo, Y.; Wang, Y.; Wang, Y.; Zhang, Z.; Lu, G., Epoxidation of propylene by molecular oxygen over the Ag-Y2O3-K2O/alpha-Al2O3 catalyst. *Catalysis Letters* 2007, 119, 185-190.
224. Lu, J. Q.; Bravo-Suarez, J. J.; Takahashi, A.; Haruta, M.; Oyama, S. T., In situ UV-vis studies of the effect of particle size on the epoxidation of ethylene and propylene on supported silver catalysts with molecular oxygen. *Journal of Catalysis* 2005, 232, 85-95.
225. Luo, M. F.; Lu, J. Q.; Li, C., Epoxidation of propylene over Ag-CuCl catalysts using air as the oxidant. *Catalysis Letters* 2003, 86, 43-49.
226. Bettahar, M. M.; Costentin, G.; Savary, L.; Lavalley, J. C., On the partial oxidation of propane and propylene on mixed metal oxide catalysts. *Applied Catalysis a-General* 1996, 145, 1-48.
227. Takahashi, A.; Hamakawa, N.; Nakamura, I.; Fujitani, T., Effects of added 3d transition-metals on Ag-based catalysts for direct epoxidation of propylene by oxygen. *Applied Catalysis a-General* 2005, 294, 34-39.
228. Brandt, K.; Chiu, M. E.; Watson, D. J.; Tikhov, M. S.; Lambert, R. M., Chemoselective Catalytic Hydrogenation of Acrolein on Ag(111): Effect of Molecular Orientation on Reaction Selectivity. *Journal of the American Chemical Society* 2009, 131, 17286-17290.
229. Liu, X.; Madix, R. J.; Friend, C. M., Unraveling molecular transformations on surfaces: a critical comparison of oxidation reactions on coinage metals. *Chemical Society Reviews* 2008, 37, 2243-2261.
230. Solomon, J. L.; Madix, R. J., kinetics and mechanism of the oxidation of allyl alcohol on Ag(110). *Journal of Physical Chemistry* 1987, 91, 6241-6244.

Appendix

A-1 Significant Quantum Effects in Hydrogen Activation[4]

Introduction

The making and breaking of bonds involving hydrogen atoms at the surfaces of materials plays a major role in nature. It is also relevant to heterogeneous catalysis, sensing, energy storage, and chemical reactions in the interstellar medium.[1-6] Therefore, understanding the adsorption and reaction dynamics of hydrogen on solid surfaces is of widespread importance and central to process improvement and materials engineering. The light mass of hydrogen makes it subject to quantum behavior, which can strongly affect its reactivity.[7] It has been demonstrated both experimentally and theoretically that quantum tunneling plays a role in a variety of reactions including conformational inversions, eliminations, and enzymatic reactions involving hydrogen.[7-9] While it is known that quantum effects can have a significant effect on the rate of reactions involving hydrogen, our understanding of the regimes in which these quantum effects are important in is currently not well developed.

Heterogeneously catalyzed hydrogenation reactions often employ metals and alloys based on platinum, ruthenium, palladium, or nickel. These metals allow for the facile dissociation of molecular hydrogen due to a relatively low reaction barrier. In contrast, coinage metals like Cu

---

[4] Adapted from “Significant Quantum Effects in Hydrogen Activation”, G. Kyriakou, E. R. M. Davidson, G. Peng, L. T. Roling, S. Singh, M. B. Boucher, M. D. Marcinkowski, M. Mavrikakis, A. Michaelides, E. C. H. Sykes, *ACS Nano* 8, 4827 (2014)

and Au exhibit a higher barrier for the dissociation of molecular hydrogen and are less reactive towards hydrogen.[10-12] Many surface science studies have examined the quantum behavior of hydrogen.[13-30] Experimental work has focused on the quantum tunneling-enabled diffusion of single hydrogen atoms on a variety of surfaces using field emission microscopy,[15] helium spin-echo spectroscopy,[16] optical diffraction,[17-19] and scanning tunneling microscopy (STM).[20-22] Recently, quantum tunneling was found to allow 2D self assembly of hydrogen atoms at low temperature (5 K) on Cu(111).[23] The key observable difference between classical and tunneling reaction pathways is the temperature dependence of the reaction rate and divergence from classical behavior is often detected through careful examination of kinetic isotope effects in chemical reactions.[7, 17, 27, 28, 31]

We recently reported that addition of just 1% of a monolayer of Pd to the surface of Cu can promote the dissociation of hydrogen.[32-34] These single atom Pd sites lower the energy barrier to hydrogen uptake, allowing it to dissociate and then spill over onto the bare Cu terraces.[32-34] Despite careful use of density functional theory (DFT) calculations, a number of recent studies could not explain these results.[35-38] Here we use a well-defined model system and an array of sophisticated theoretical approaches that allow us to understand and quantify the precise role of quantum effects in hydrogen dissociation. We studied the uptake of hydrogen and deuterium using temperature programmed desorption (TPD), DFT, path integral based DFT approaches to account for quantum nuclear effects, and kinetic Monte Carlo (KMC). The dissociative adsorption of molecular hydrogen and deuterium reveals vastly different rates and temperature dependence for the two species. The rate of hydrogen activation is higher at lower sample temperature, whereas deuterium activation slows down as the temperature is lowered. The dramatically different behavior observed in these experiments originates from the different extent of quantum tunneling for H_2 and D_2. In both cases our calculations indicate that tunneling is relevant. In the case of H_2, the contribution from tunneling is so significant that the effective barrier is reduced to the point that H_2 uptake becomes dominated by thermodynamic effects. On the contrary, tunneling through the D_2 barrier is not as significant, and the D_2 uptake rate is dictated kinetically by the effective height of the barrier.

Materials and Methods

Experimental

Measurements were carried out in two UHV chambers, both of which have been described in detail elsewhere.[23, 33, 34] The first UHV chamber was operated at a base pressure of $<1x10^{-10}$ mbar and was equipped with a quadrupole mass spectrometer, used for temperature programmed desorption measurements as well as LEED and AES capabilities. The Cu(111) crystal could be resistively heated to 775 K and cooled to 73 K**.** Normally the crystal could only be cooled to 83 K with liquid nitrogen, but lower temperatures were reached by bubbling helium gas through the cryogenic dewar. The sample was cleaned by cycles of Ar sputtering (1.5 kV, 11 μA) followed by annealing at 725 K. The second chamber, an Omicron Nanotechnology LT-UHV STM was operated at a base pressure of $<5 \times 10^{-11}$ mbar. The instrument incorporated a preparation chamber in which sample cleaning, annealing and Pd deposition were performed. Pd deposition was performed in both UHV systems using flux monitored Omicron Nanotechnology Focus EFM 3 electron beam evaporators with the Cu(111) samples held at 380 K during deposition. Pd coverages were calibrated using both AES and TPD of CO. Hydrogen 99.999% (AirGas) and Deuterium (99.999%) (AirGas) were used in our study. Hydrogen coverage calculations were based on a saturation coverage of unity when hydrogen was adsorbed on a 5 monolayer (ML) Pd film, assuming that the film terminates as Pd(111).

Theoretical

Calculations of the classical barrier and pathway for H_2/D_2 dissociation were performed using the VASP code[48] with projector augmented wave (PAW) potentials.[49] Van der Waals dispersion forces were accounted for through the optB88-vdW functional,[41] which accounts for dispersion forces within the non-local vdW-DF scheme[42] and has been implemented in VASP by Klimes et al.[50] The electronic states were expanded using plane waves with an energy cutoff of 600 eV. The Pd/Cu(111) surface was modeled by a five-layer slab with a (3×3) surface unit cell with a Cu atom at the top layer substituted by a Pd atom. A vacuum layer equivalent of six atomic layers was used. The Brillouin zone was sampled using a (8×8×1) k-point mesh based on the Monkhorst-Pack scheme.[51] The two bottom-most Cu(111) layers were fixed during relaxation. All structures were fully relaxed until the Hellmann-Feynman forces acting on the atoms were smaller than 0.01 eV/Å. The climbing image nudged elastic band (CI-NEB) method[52] was used to calculate the classical H_2/D_2 activation energy barrier. ZPE corrections to the classical barrier were obtained simply by taking the difference between the sum of real-valued harmonic vibrational frequencies at the transition state and at the physisorbed (initial) state.

Quantum tunneling effects were accounted for using two path integral based approaches. Most results reported have been obtained from the harmonic quantum transition state theory method (also known as instanton) on an analytic potential fitted to the underlying DFT potential energy surface. Specifically fitted to a DFT potential energy surface in which the atoms in the substrate were fixed at the positions they adopt prior to H_2 dissociation. Fixing the surface in this manner is an approximation but it also gives a sensible reaction coordinate as quantum effects frequently result in corner-cutting of the classical minimum energy path during reactions. Here the fixed surface results in a chemisorption barrier of 468 meV, only 6 meV higher than the barrier obtained when the surface is allowed to fully relax during the dissociation process. We used 200 beads in our instanton calculations, which were converged by comparing to 100 and 500 bead test calculations. AIPIMD simulations were also performed using 16 imaginary time-slices (known as beads) propagated by Langevin dynamics at 85 K and forces computed on-the-fly using DFT. For efficiency reasons we used a slightly less expensive computational set-up than the barrier height calculations above, in particular a three-layer slab was used with the bottom layer fixed, and the Brillouin zone was sampled with a (4×4×1) k-point mesh. These reduced settings result in a classical chemisorption barrier of 465 meV, which is a very good representation of the fully converged system.

The kmos[53] framework was used for the implementation of Kinetic Monte Carlo (KMC) simulations. From a given state of the system, the KMC algorithm determines the probability of all possible transitions to other states according to the user-defined rates of all available elementary reaction steps. A reaction step is then chosen in accordance with this probability distribution, and the system assumes the new state determined by that reaction step. The simulation has no memory; that is, the probability of undergoing a particular transition is determined only by the current state of the system and not by any prior configuration. The simulation time step after each transition is selected randomly from a Poisson distribution with a mean that equals the sum of the rates of all available transitions from the original state. Simulations are allowed to proceed until the desired simulation time is reached (50 s for H_2,200 s for D_2, same as the dosing times in the experiments).The code input comprises the lattice structure, binding energies and minimum energy configurations of all the species involved in the reaction mechanism, activation energy barriers and pre-exponential factors for all elementary steps, simulation time, and the reaction temperature and pressure. All simulations were performed on a Pd/Cu catalytic surface represented as a lattice in which all types of atop (Pd, Cu) and three-fold hollow (Pd/Cu, Cu) sites were explicitly taken into account (see Figure S2). In particular, the lattice structure was represented by a 20x20 Cu(111) grid with periodic boundary conditions. 1% of the surface Cu atoms were randomly substituted by Pd atoms with the restriction that they could not be nearest neighbors. This is in agreement with studies that have shown that Pd atoms disperse in the surface layer of Cu(111)[54] and that the most stable configurations for alloys with low Pd content (and coverages below X_{Pd} = 0.4) are those where the surface Pd atoms are surrounded by Cu atoms[32]. This is also consistent with STM observations reported in past experimental studies.[55, 56] H_2 (D_2) molecular precursors were only allowed to adsorb atop surface atoms, while H (D) adatoms occupied only hollow sites, consistent with our DFT calculations indicating that adsorption of H adatoms is ~0.4 eV more stable on the hollow sites than the atop sites. Our DFT calculations show that adsorption of H (D) adatoms is thermodynamically favorable in up to three hollow sites around a single metal surface atom. Adsorption of a fourth, fifth, or sixth H (D) adatom around a metal surface atom is energetically unfavorable, with substantially weaker binding compared to that on other surface sites. The KMC simulations therefore allowed adsorption in up to three hollow sites around each metal surface atom. Simulations were performed at similar conditions as experiments: the surface coverage of H (D) was recorded after dosing with 10^{-10} atm H_2 for 50 s (10^{-9} atm D_2 for 200 s) at fixed temperatures in the range 75 K – 195 K. Each KMC simulation was performed a total of 25 times to obtain an average value of final surface coverage for each experimental condition being simulated.

All the model parameters, with the exception of sticking coefficients for H_2 (D_2), were rigorously derived from our DFT calculations. The sticking coefficients for the H_2(D_2) adsorption steps were assumed to be 1. The enthalpy estimates for the surface species and transition states were obtained by correcting the electronic energies, as obtained from our DFT calculations, for zero point energy (ZPE) contributions and temperature variations. The temperature-dependent activation energy barriers for the H_2/D_2 dissociation steps on Pd (Table 1, Step 3) were obtained from the HQTST calculations. For our modeling purposes, these quantum tunneling barriers were approximated to be linear functions of temperature until they reach their classical values, as shown in Figure S3. The classical activation energy barrier for the H_2 (D_2) dissociation step on Cu (Table S1, Step 4) was obtained using the CI-NEB method[52]; the barriers for all the surface diffusion steps (Table S1, Step 5-9) were found to be insensitive parameters for the KMC simulations and were fixed at 0.12 eV, in agreement with our earlier studies.[57] The entropy values were directly calculated from the vibrational frequencies of the respective states, and the pre-exponential factors were calculated from entropy differences between the initial and transition states of the respective elementary steps. The rate constants for reactions involving bond-formation or bond-scission were calculated using transition state theory; collision theory was employed to calculate the rate constants for the adsorption-desorption steps.[58, 59]

Results and Discussion

The uptakes of hydrogen and deuterium on single atom alloy Pd/Cu surfaces as a function of temperature were obtained using TPD experiments, as shown in Figure 1a and b. The measurements were performed on the 0.01 ML Pd/Cu(111) alloy surface, which consists of 1% Pd in the form of individual, isolated Pd atoms substituted into the Cu(111) lattice.[32-34] The surface was exposed to either hydrogen or deuterium at a selected sample temperature in the range of 75-193 K. The sample was subsequently warmed or cooled to 83 K, followed by the thermal desorption measurement. The 75 – 193 K temperature range reflects: (i) the minimum temperature to which our sample could be cooled; and (ii) the maximum temperature we could heat the sample to without desorption of gaseous hydrogen or deuterium. It is immediately clear that the uptakes of the two isotopes on the 0.01 ML Pd/Cu(111) surface are very different. Critically, the uptake of hydrogen *decreases* when the temperature is raised while deuterium's uptake *increases* at higher sample temperature. Isotope effects that lead to different rates of H vs. D reactions are common, however, the completely opposite behavior observed here as a function of temperature is exceptional. Figure 1(c) shows a natural log plot of the two uptake curves shown in Figures 1(a) and (b) as a function of inverse temperature. These plots were used to extract the apparent activation energy for the dissociative adsorption process. In the case of deuterium, the apparent activation energy was found to be 0.045 ± 0.005 eV and for hydrogen it was -0.023 ± 0.005 eV. The small negative apparent activation barrier of hydrogen on 0.01 ML Pd/Cu(111) suggests that the dissociation process involves more than a single step. Typically, negative apparent activation barriers in Arrhenius plots are indicative of the presence of a precursor state[26, 39, 40], however, we will show later in our analysis that it relates to the thermodynamics of H uptake.

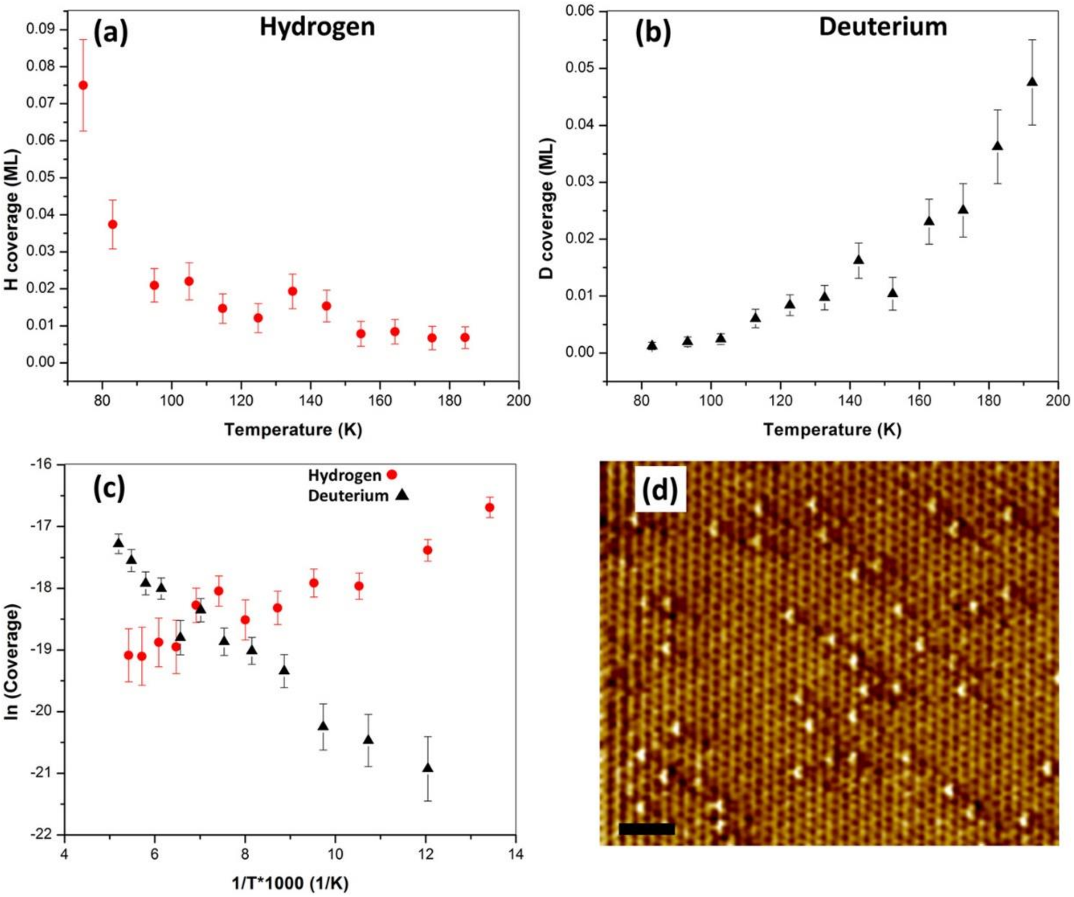

Figure 1. The uptake of hydrogen and deuterium on 0.01 ML Pd/Cu(111). (a) Uptake of hydrogen atoms on the alloy surface after an exposure of 5 L of molecular hydrogen at different temperatures. (b) Uptake of deuterium atoms on the alloy surface after an exposure of 200 L of molecular deuterium at different sample temperatures. The exposures of H_2/D_2 (5 L/200 L) were chosen to yield comparable surface coverages over the temperature range examined. (c) Arrhenius plots for the data shown in (a) and (b). Circles represent hydrogen data points and triangles are deuterium data points. (d) STM image of the 0.01 ML Pd/Cu(111) alloy showing that at this coverage Pd exists as single atoms which appear as protrusions in the Cu(111) surface. Scanning conditions: I = 0.04 nA, V = 0.08 V, Scale Bar = 1 nm.

To elucidate the underlying mechanism and differences of the H_2/D_2 dissociation process on Pd/Cu(111) we performed DFT calculations for the process. The specific exchange-correlation functional used was the optB88-vdW functional[41], which accounts for van der Waals (vdW) dispersion forces within the non-local vdW-DF scheme.[42] Full details of the computational setup are given in the Methods section. The classical DFT potential energy barrier for H_2 dissociation was calculated on a Cu(111)-(3x3) surface with a single Pd atom substitution (Figure 2(a)). Along the minimum energy pathway of H_2 dissociation, a weak physisorption well was identified, with H_2 found 1.9 Å above Pd. Starting from this physisorbed state (with a binding energy of about -

0.1 eV relative to a H_2 molecule in the gas phase), the H—H bond dissociation occurs above the Pd atom with an energy barrier of 0.46 eV. The barrier obtained here with the optB88-vdW functional is slightly higher than that obtained in previous DFT calculations using a standard generalized gradient approximation functional and both barriers are much too high to account for the experimental observations.[35]

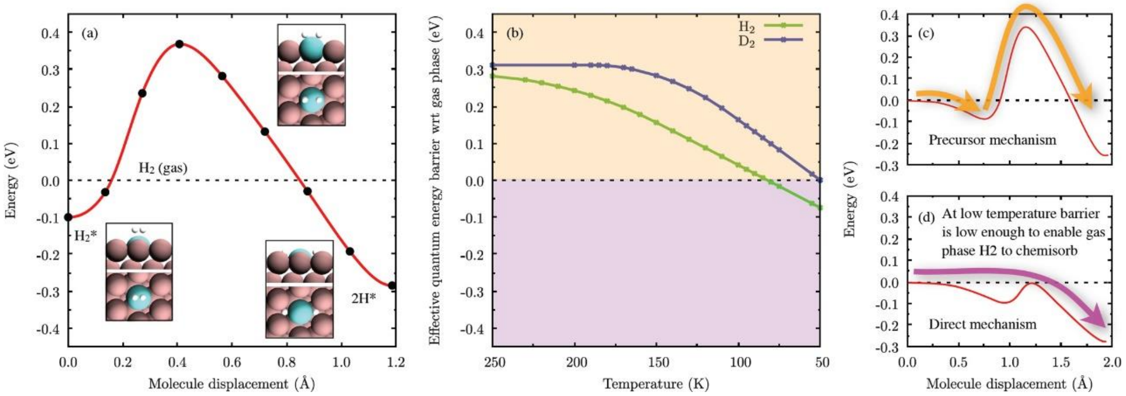

Figure 2. (a) Potential energy surface for H_2 dissociation from the physisorbed precursor state on the Pd/Cu(111) substrate. The total energy of the clean surface and the H_2 in the gas phase is used as the energy zero. Insets are top and side views of initial physisorbed precursor state (H_2*), transition state (TS), and final state (2H*). White, brown, and cyan spheres indicate H, Cu, and Pd atoms, respectively. (b) Temperature dependence of the effective quantum energy barrier (relative to the gas phase) obtained from harmonic quantum transition state theory calculations that take into account tunneling through the chemisorption barrier and zero point energies. It can be seen that below the quantum crossover temperature (260 K for H_2, 190 K for D_2) the effective energy barrier decreases as the temperature is lowered. The orange/pink regions of the graph correspond to two different mechanisms for chemisorption below 80 K for H_2 or 50 K for D_2. These two routes to chemisorption are the precursor-mediated process (c), or below 80 K for H_2 (50 K for D_2) a direct chemisorption for H_2 incident on a Pd site (d).

Bearing in mind that the computed DFT barrier is too high to account for the facile activation of H_2 below 100 K, as observed in experiments, we now consider how quantum nuclear effects may alter our physical picture of the dissociation process. The simplest and traditional first step is to consider how zero point energy (ZPE) will alter the energetics of the process. When we consider the effect of ZPE corrections, we do indeed find that they lower the energy barrier to dissociation. However, the reduction is small and the barriers remain too high at 0.37 eV for H_2 and 0.39 eV for D_2, as compared to the experimentally observed apparent barriers (-0.023 eV and 0.045 eV for H_2 and D_2, respectively) This indicates that the experimental results cannot be explained through a simple consideration of the ZPE effect and that instead quantum mechanical tunneling is likely to play an important role in this process.

To account for quantum tunneling effects in this system, we have used two path integral based approaches. Specifically most calculations reported were obtained with harmonic quantum transition state theory (HQTST) (otherwise known as instanton theory)[43] although the more sophisticated ab initio path integral molecular dynamics (AIPIMD)[44,45] approach was also used. The HQTST method is an efficient path-integral based approach that includes quantum tunneling by considering the spread of a "necklace" of beads over the top of the dissociation barrier. The beads are connected by mass and temperature-dependent springs, such that the classical limit (with all beads contracted to a single point) is recovered at high temperature and/or high mass. As the temperature is lowered, these springs weaken and the beads sample lower energy states on either side of the classical saddle point, resulting in a lowering of the quantum energy barrier due to tunneling through the classical potential. The HQTST calculations were performed on an analytical one-dimensional potential constructed to resemble our DFT energy profile for dissociative adsorption (Figure 2(a)). Figure 2(b) shows some of the key results of the HQTST calculations wherein the effective dissociation barriers for both H_2 and D_2 are plotted as a function of temperature. It can be seen that below the quantum-classical crossover temperature (which is the temperature below which classical and quantum mechanics diverge – in this system 260 K for H_2, 190 K for D_2), the effective quantum energy barrier decreases as the temperature is lowered. A lower barrier will result in more facile chemisorption of H_2 from the physisorbed state following the precursor mechanism shown in Figure 2(c). At 80 K (50 K) the effective quantum barrier for H_2 (D_2) to dissociatively chemisorb reaches zero (relative to H_2 or D_2 in the gas phase). This indicates that below these temperatures an incident molecule at a Pd site could undergo barrierless dissociation if, prior to doing so, it does not get trapped in the physisorbed state, as illustrated schematically in Figure 2(d).

The HQTST calculations reveal that it is mainly tunneling that leads to the substantial reductions in the effective quantum dissociation barriers. To test this conclusion we performed a separate set of AIPIMD simulations in which the quantum delocalization of the breaking H_2 bond was examined at various points along the classical dissociation pathway. In AIPIMD the forces on the atoms are computed "on the fly" and it does not rely on a pre-determined potential energy surface. A snapshot from an 85 K AIPIMD simulation with the centre of mass of the H_2 fixed at the classical saddle point is shown in Figure 3. Clearly there is a large spread of the path integral beads associated with the two hydrogen atoms. Delocalization of the beads along the dissociation reaction coordinate is a signature for quantum tunneling through the potential barrier. The extent of the delocalization observed in the AIPIMD simulations is similar to the spreading observed in the HQTST calculations at the same temperature (Figure S1).

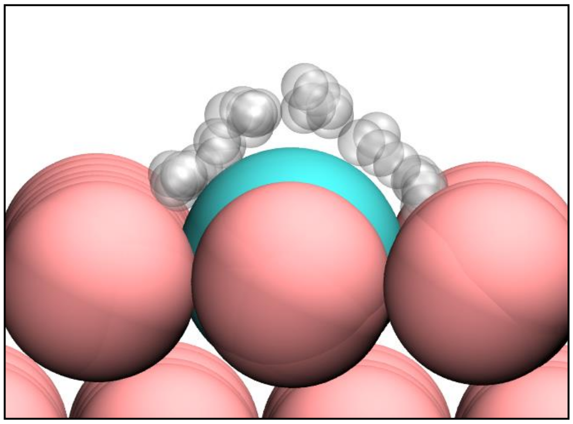

Figure 3. Side view of a snapshot from an 85 K ab initio path integral molecular dynamics simulation of a single H_2 at the classical saddle point for dissociation on the Pd/Cu(111) surface. In this simulation each H atom of the two H atoms is represented by 16 path integral replicas ("beads"). The large spread of the beads along the dissociation reaction coordinate indicates that at this temperature the H_2 molecule can tunnel through the dissociation barrier.

The path integral based DFT calculations reveal significant tunneling through the dissociation barrier at experimentally relevant temperatures, with a greater extent of tunneling for H_2 versus D_2

dissociation. To gain further insight into the experimentally observed differences in the H_2/D_2 uptake we performed a series of KMC simulations, making use of the data and insight gained from the various DFT calculations. With no adjustments to the DFT-derived parameters (energetics and reaction pre-factors), these simulations predict no quantifiable uptake of H (D) adatoms for the two cases that employ: (a) a DFT-derived (classical) activation energy barrier; and (b) a temperature-dependent quantum tunneling barrier obtained via the HQTST simulations. Therefore, to capture the experimentally-observed trends, systematic adjustments to the model parameters were performed until a reasonable agreement between the experimentally measured and model predicted surface coverages was reached. These adjustments were small (0.20 eV or less) and were within the typical error bars associated with DFT calculations of processes at surfaces. A more detailed account of these adjustments can be found in the supporting information (Figure S5, Table S1). In particular we found that the coverages predicted by our KMC simulations are very sensitive to the binding energy of H_2 (D_2) on the Pd sites. Perturbations as small as 0.005 eV (stabilization) of H_2 (D_2) can cause the surface coverages to increase by as much as 20% from their original values, thereby indicating that the binding strength of the precursor state plays a critical role in the overall reaction. Accordingly, the correct treatment of the weak interaction of H_2/D_2 with the metal surface is highly desirable for the detailed understanding of the phenomena studied here.

Figure 4 shows the results from the KMC simulations for H_2/D_2 uptake, plotted against the experimental observations. The surface coverage of H (D) adatoms is found to decrease (increase) monotonically with an increase in temperature, consistent with the experimental trends. Our results suggest that these opposite trends for the surface coverages of H/D adatoms with increasing temperature are due to the fact that H_2 dissociation is *thermodynamically controlled,* while D_2 dissociation is *kinetically controlled* over the entire temperature regime.

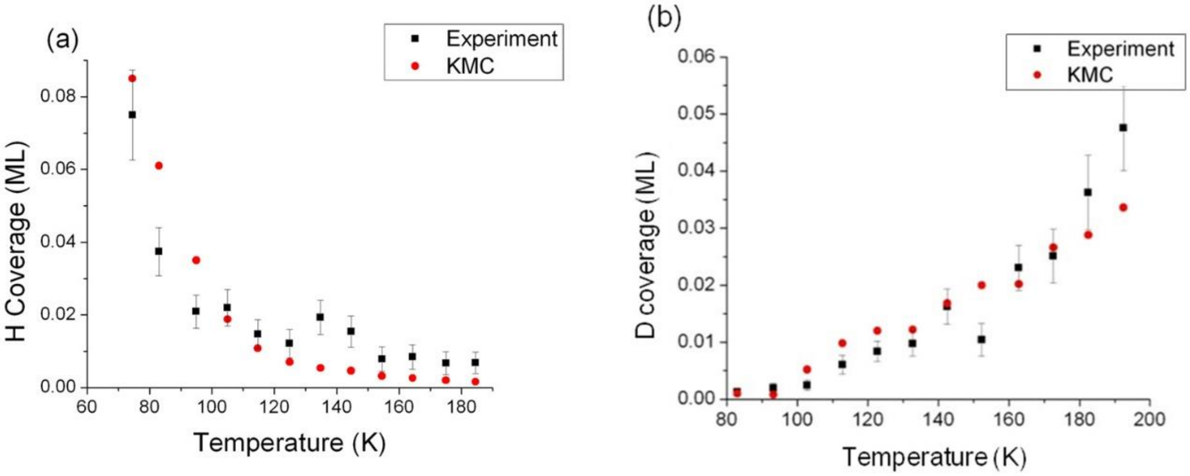

Figure 4. KMC simulations results for (a) H_2 uptake and (b) D_2 uptake, and their comparison with the experimentally measured values. For parameter values used to obtain these results.

In the case of H_2, it is observed that the decreasing trend of H adatom surface coverage with temperature is dictated by the thermodynamics, and not by the kinetics, of H_2 dissociation at surface Pd sites. In other words, the temperature-dependent activation energy barrier for this step is too small under all experimental conditions for it to be of great kinetic relevance, and the H surface coverage is governed by the thermodynamic driving force, i.e., the reaction free energy of this step. Since this is an exothermic step, an increase in temperature is expected to disfavor H_2 dissociation. In particular, the reaction free energy of this elementary step increases with an increase in temperature, which results in a monotonically decreasing equilibrium constant. The decreasing H surface coverage, and hence the negative apparent activation energy barrier, is a direct consequence of this phenomenon.

Contrary to the H_2 case just described, the monotonically increasing trend in D adatom surface coverage is due to the fact that D_2 dissociation is kinetically controlled. The temperature-dependent activation energy barrier for D_2 dissociation at surface Pd sites (Table S1, Step 3) is large enough to ensure that it is the kinetically relevant rate controlling step over the entire temperature regime. Consequently, the D surface coverage is governed by the kinetics of this elementary step, thereby resulting in a monotonically increasing surface coverage with increasing temperature. In order to quantify this, we obtained the overall rate of D_2 dissociation from our model (total number of D_2 dissociation events, as obtained from our KMC model: 'E_{net}'). Plotting the natural log of E_{net} against 1/T, (where T = temperature (K)), yields the apparent activation energy barrier of the overall reaction, as shown in Figure 5.. This apparent activation energy barrier, as obtained from this analysis, is 0.032 eV, consistent with its experimental value (0.045±0.005eV).

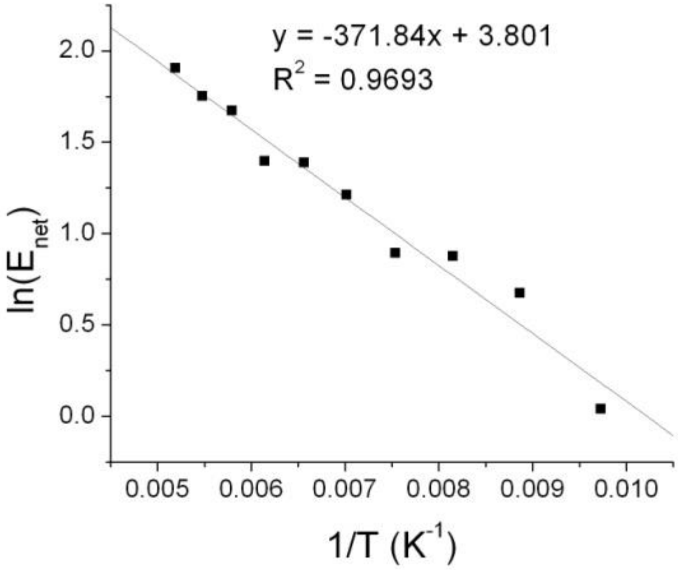

Figure 5. Determination of apparent activation energy barrier for KMC simulations of D_2 uptake. The logarithm of total number of D_2 dissociation events (E_{net}) is plotted against the inverse temperature. The apparent activation energy barrier, as calculated from the slope of the best-fit line, is 0.032 eV, consistent with the experimentally-determined value of 0.045 ± 0.005 eV.

The results of our KMC simulations suggest that both H_2 and D_2 dissociation proceed through the same reaction pathway. The dissociation of H_2 (D_2) to give surface H(D) adatoms occurs exclusively over Pd sites; for the temperature range employed in our experiments, no dissociation is observed over Cu sites because of the prohibitively high activation energy barrier. H_2 (D_2) must land directly on or adjacent to surface Pd atoms, as the precursor states in the vicinity of Cu atoms are extremely short-lived and prefer to desorb at all temperatures rather than diffuse across the surface to a Pd site. This was verified by reducing the rate constants for H_2 (D_2) diffusion steps by several orders of magnitude from the calculated values and observing that the final results were essentially independent of the diffusion rates.

Finally, we note that our calculations indicate that dissociation can occur through two distinct processes, each due to the combination of van der Waals interactions and quantum tunneling. The first process involves the trapping of H_2 in the physisorbed state, which acts as a precursor to the dissociative chemisorption process (Figure. 2(a) and sketched in Figure. 2(c)). The second mechanism may become possible at very low temperatures when quantum effects are so pronounced that the effective chemisorption barrier drops below the gas phase H_2 energy zero (sketched in Figure 2(d)). Our HQTST calculations predict that this can happen at less than ~80 K for H_2 and less than ~50 K for D_2. This direct dissociation process occurs at lower temperatures than we have been able to probe in the current TPD experiments but it is an intriguing implication of the calculations that we hope to examine in future studies. More generally, the results of this study suggest a novel approach for inducing selective reactions or isotope separations that utilize the vastly different rates of bond cleavage involving hydrogen and deuterium. For example, many important surface-catalyzed reactions involve C-H or O-H bond cleavage.[46, 47] If the C or O atom remains at the same surface site before and after the bond breaks and most of the motion is of the light H atom, similar temperature-dependent activation barriers may occur and novel ways to control bond breaking developed.

Conclusions

We have shown experimentally that the dissociation of H_2 and D_2 molecules at single Pd atom surface sites in a Pd/Cu alloy occur at vastly different rates and with opposite trends as a function of sample temperature. Traditional DFT-based methods for modeling dissociation barriers are inadequate for explaining these results. Our experimental observations motivated us to take a theoretical approach using path integral based DFT simulations that account for the role of quantum nuclear effects in H_2/D_2 dissociation, coupled with KMC to model the dissociation rates over the relevant range of temperatures. Our data reveal that the dissociation barriers are strongly temperature-dependent and that H_2/D_2 dissociation is dictated by totally different thermodynamic/kinetic parameters. Within our theoretical framework, we see a positive slope in Arrhenius plots for H_2 uptake, which originates from temperature-dependent quantum tunneling aided by a precursor state, and a negative slope for D_2 which can be explained by a scheme in which thermally assisted barrier crossing dominates tunneling and the effect of the precursor state. The breaking of chemical bonds involving H atoms is ubiquitous in nature, and our results provide a unique insight into the highly temperature-dependent quantum effects that dictate these rates. We also hope to apply this refined theoretical approach to other light-atom systems in order to search for regimes where important chemistry may become more controllable once quantum effects are fully understood and quantified.

References

1. Graetz, J. New approaches to hydrogen storage. *Chem. Soc. Rev.* **2009,** *38,* 73-82.

2. Armbruster, M.; Kovnir, K.; Friedrich, M.; Teschner, D.; Wowsnick, G.; Hahne, M.; Gille, P.; Szentmiklosi, L.; Feuerbacher, M.; Heggen, M.; Girgsdies, F.; Rosenthal, D.; Schlogl, R.; Grin, Y. $Al_{13}Fe_4$ as a low-cost alternative for palladium in heterogeneous hydrogenation. *Nat. Mater.* **2012,** *11,* 690-3.

3. Eliaz, N.; Eliezer, D.; Olson, D. L. Hydrogen-assisted processing of materials. *Mater. Sci. Eng.: A* **2000,** *289,* 41-53.

4. Shegai, T.; Johansson, P.; Langhammer, C.; Kall, M. Directional scattering and hydrogen sensing by bimetallic Pd-Au nanoantennas. *Nano Lett.* **2012,** *12,* 2464-9.

5. Sakintuna, B.; Lamaridarkrim, F.; Hirscher, M. Metal hydride materials for solid hydrogen storage: A review. *Int. J. Hydrogen Energy* **2007,** *32,* 1121-1140.

6. Le Bourlot, J.; Le Petit, F.; Pinto, C.; Roueff, E.; Roy, F. Surface chemistry in the interstellar medium. *Astron. Astrophys.* **2012,** *541,* A76.

7. McMahon, R. J. Chemistry. Chemical reactions involving quantum tunneling. *Science* **2003,** *299,* 833-4.

8. Masgrau, L.; Roujeinikova, A.; Johannissen, L. O.; Hothi, P.; Basran, J.; Ranaghan, K. E.; Mulholland, A. J.; Sutcliffe, M. J.; Scrutton, N. S.; Leys, D. Atomic description of an enzyme reaction dominated by proton tunneling. *Science* **2006,** *312,* 237-41.

9. Schreiner, P. R.; Reisenauer, H. P.; Ley, D.; Gerbig, D.; Wu, C. H.; Allen, W. D. Methylhydroxycarbene: Tunneling Control Of A Chemical Reaction. *Science* **2011,** *332,* 1300-3.

10. Bettens, F. L.; Bettens, R. P. A.; Brown, R. D.; Godfrey, P. D. The Microwave Spectrum, Structure, and Ring-Puckering of the Cyclic Dipeptide Diketopiperazine. *J. Am. Chem. Soc.* **2000,** *122,* 5856-5860.

11. Pan, M.; Brush, A. J.; Pozun, Z. D.; Ham, H. C.; Yu, W. Y.; Henkelman, G.; Hwang, G. S.; Mullins, C. B. Model Studies Of Heterogeneous Catalytic Hydrogenation Reactions With Gold. *Chem. Soc. Rev.* **2013,** *42,* 5002-13.

12. Hayden, B. E.; Hodgson, A. Dissociation dynamics on ordered surface alloys. *J. Phys.: Condens. Matter* **1999,** *11,* 8397-8415.

13. McIntosh, E. M.; Wikfeldt, K. T.; Ellis, J.; Michaelides, A.; Allison, W. Quantum Effects in the Diffusion of Hydrogen on Ru(0001). *J. Phys. Chem. Lett.* **2013,** *4,* 1565-1569.

14. Waluyo, I.; Ren, Y.; Trenary, M. Observation of Tunneling in the Hydrogenation of Atomic Nitrogen on the Ru(001) Surface to Form NH. *J. Phys. Chem. Lett.* **2013,** *4,* 3779-3786.

15. Dharmadhikari, C.; Gomer, R. Diffusion of hydrogen and deuterium on the (111) plane of tungsten. *Surf. Sci.* **1984,** *143,* 223-242.

16. Jardine, A. P.; Lee, E. Y.; Ward, D. J.; Alexandrowicz, G.; Hedgeland, H.; Allison, W.; Ellis, J.; Pollak, E. Determination of the quantum contribution to the activated motion of hydrogen on a metal surface: H/Pt(111). *Phys. Rev. Lett.* **2010,** *105,* 136101.

17. Lee, A.; Zhu, X. D.; Deng, L.; Linke, U. Observation of a transition from over-barrier hopping to activated tunneling diffusion: H and D on Ni(100). *Phys. Rev. B* **1992,** *46,* 15472-15476.

18. Wong, A.; Lee, A.; Zhu, X. D. Coverage dependence of quantum tunneling diffusion of hydrogen and deuterium on Ni(111). *Phys. Rev. B* **1995,** *51,* 4418-4425.

19. Wang, X.; Fei, Y. Y.; Zhu, X. D. Classical and quantum diffusion of hydrogen atoms on Cu(111). *Chem. Phys. Lett.* **2009,** *481,* 58-61.

20. Lauhon, L. J.; Ho, W. Direct observation of the quantum tunneling of single hydrogen atoms with a scanning tunneling microscope. *Phys. Rev. Lett.* **2000,** *85,* 4566-9.

21. Kua, J.; Lauhon, L. J.; Ho, W.; Goddard, W. A. Direct comparisons of rates for low temperature diffusion of hydrogen and deuterium on Cu(001) from quantum mechanical calculations and scanning tunneling microscopy experiments. *J.Chem. Phys.* **2001,** *115,* 5620-5624.

22. Heinrich, A. J.; Lutz, C. P.; Gupta, J. A.; Eigler, D. M. Molecule cascades. *Science* **2002,** *298,* 1381-7.

23. Jewell, A. D.; Peng, G.; Mattera, M. F.; Lewis, E. A.; Murphy, C. J.; Kyriakou, G.; Mavrikakis, M.; Sykes, E. C. Quantum tunneling enabled self-assembly of hydrogen atoms on Cu(111). *Acs Nano* **2012,** *6,* 10115-21.

24. Okuyama, H.; Siga, W.; Takagi, N.; Nishijima, M.; Aruga, T. Path and mechanism of hydrogen absorption at Pd(100). *Surf. Sci.* **1998,** *401,* 344-354.

25. Groß, A. Quantum effects in the dissociative adsorption of hydrogen. *J. Chem. Phys.* **1999,** *110,* 8696-8702.

26. Hakanoglu, C.; Hawkins, J. M.; Asthagiri, A.; Weaver, J. F. Strong Kinetic Isotope Effect in the Dissociative Chemisorption of H2 on a PdO(101) Thin Film. *The J. Phys. Chem. C* **2010,** *114,* 11485-11497.

27. Muto, H.; Matsuura, K.; Nunome, K. Large isotope effect due to quantum tunneling in the conversion reaction of electrons to hydrogen and deuterium atoms in irradiated water/heavy water ice. *J. Phys. Chem.* **1992,** *96,* 5211-5213.

28. Berger, H. F.; Leisch, M.; Winkler, A.; Rendulic, K. D. A search for vibrational contributions to the activated adsorption of H2 on copper. *Chem. Phys. Lett.* **1990,** *175,* 425-428.

29. Sundell, P. G.; Wahnström, G. Hydrogen tunneling on a metal surface: A density-functional study of H and D atoms on Cu(001). *Surf. Sci.* **2005,** *593,* 102-109.

30. Sundell, P.; Wahnström, G. Quantum motion of hydrogen on Cu(001) using first-principles calculations. *Phys. Rev. B* **2004,** *70,* 081403.

31. Lee, A.; Zhu, X. D.; Wong, A.; Deng, L.; Linke, U. Observation of diffusion of H and D on Ni(111) from over-barrier hopping to nonactivated tunneling. *Phys. Rev. B* **1993,** *48,* 11256-11259.

32. Tierney, H. L.; Baber, A. E.; Kitchin, J. R.; Sykes, E. C. Hydrogen dissociation and spillover on individual isolated palladium atoms. *Phys. Rev. Lett.* **2009,** *103,* 246102.

33. Kyriakou, G.; Boucher, M. B.; Jewell, A. D.; Lewis, E. A.; Lawton, T. J.; Baber, A. E.; Tierney, H. L.; Flytzani-Stephanopoulos, M.; Sykes, E. C. Isolated metal atom geometries as a strategy for selective heterogeneous hydrogenations. *Science* **2012,** *335,* 1209-12.

34. Marcinkowski, M. D.; Jewell, A. D.; Stamatakis, M.; Boucher, M. B.; Lewis, E. A.; Murphy, C. J.; Kyriakou, G.; Sykes, E. C. Controlling a spillover pathway with the molecular cork effect. *Nat. Mater.* **2013,** *12,* 523-8.

35. Ramos, M.; Martinez, A. E.; Busnengo, H. F. H2 dissociation on individual Pd atoms deposited on Cu(111). *Phys. Chem. Chem. Phys.* **2012,** *14,* 303-10.

36. Fu, Q.; Luo, Y. Catalytic Activity of Single Transition-Metal Atom Doped in Cu(111) Surface for Heterogeneous Hydrogenation. *J. Phys. Chem. C* **2013,** *117,* 14618-14624.

37. Fu, Q.; Luo, Y. Active Sites of Pd-Doped Flat and Stepped Cu(111) Surfaces for H_2 Dissociation in Heterogeneous Catalytic Hydrogenation. *Acs Catal.* **2013,** *3,* 1245-1252.

38. Farías, D.; Minniti, M.; Al Taleb, A.; Miranda, R. Initial Sticking Coefficient of H2 on the Pd–Cu(111) Surface Alloy at very Low Coverages. *Z. Phys. Chem.***2013,** *227,* 2196-7156.

39. Ertl, G.; Lee, S. B.; Weiss, M. Kinetics of nitrogen adsorption on Fe(111). *Surf. Sci.***1982,** *114,* 515-526.

40. Mortensen, J. Nitrogen Adsorption and Dissociation on Fe(111). *J. Catal.* **1999,** *182,* 479-488.

41. Klimes, J.; Bowler, D. R.; Michaelides, A. Chemical accuracy for the van der Waals density functional. *J. Phys. Condens. Matter* **2010,** *22,* 022201.

42. Dion, M.; Rydberg, H.; Schroder, E.; Langreth, D. C.; Lundqvist, B. I. van der Waals density functional for general geometries. *Phys. Rev. Lett.* **2004,** *92,* 246401.

43. Andersson, S.; Nyman, G.; Arnaldsson, A.; Manthe, U.; Jónsson, H. Comparison of Quantum Dynamics and Quantum Transition State Theory Estimates of the H + CH_4 Reaction Rate. *J. Phys. Chem. A* **2009,** *113,* 4468-4478.

44. Marx, D.; Parrinello, M. Ab initio path-integral molecular dynamics. *Z. Phys. B* **1994,** *95,* 143-144.

45. Marx, D.; Parrinello, M. Ab initio path integral molecular dynamics: Basic ideas. *J. Chem. Phys.* **1996,** *104,* 4077-4082.

46. Michaelides, A.; Hu, P. A density functional theory study of the reaction of C+O,C+N, and C+H on close packed metal surfaces. *J. Chem. Phys.***2001,** *114,* 5792-5795.

47. Michaelides, A.; Hu, P. Insight into microscopic reaction pathways in heterogeneous catalysis. *J. Am. Chem. Soc.* **2000,** *122,* 9866-9867.

48. Kresse, G. Efficient iterative schemes for ab initio total-energy calculations using a plane-wave basis set. *Phys. Revi. B* **1996,** *54,* 11169-11186.

49. Kresse, G. From ultrasoft pseudopotentials to the projector augmented-wave method. *Phys. Rev. B* **1999,** *59,* 1758-1775.

50. Klimeš, J.; Bowler, D. R.; Michaelides, A. Van der Waals density functionals applied to solids. *Phys. Rev. B* **2011,** *83,* 195131.

51. Monkhorst, H. J.; Pack, J. D. Special points for brillouin-zone integrations. *Phys. Rev. B* **1976,** *13,* 5188-5192.

52. Henkelman, G.; Uberuaga, B. P.; Jonsson, H. A climbing image nudged elastic band method for finding saddle points and minimum energy paths. *J. Chem. Phys.* **2000,** *113,* 9901-9904.

53. Hoffmann, M. J. (to be published), kmos, {http://mhoffman.github.com/kmos}. **2012**.

54. Ruban, A. V.; Skriver, H. L. Calculated surface segregation in transition metal alloys. *Comput. Mater. Sci.* **1999,** *15,* 119-143.

55. Bellisario, D. O.; Han, J. W.; Tierney, H. L.; Baber, A. E.; Sholl, D. S.; Sykes, E. C. H. Importance of Kinetics in Surface Alloying: A Comparison of the Diffusion Pathways of Pd and Ag Atoms on Cu(111). *J. Phys. Chem. C* **2009,** *113,* 12863-12869.

56. Aaen, A. B.; Laegsgaard, E.; Ruban, A. V.; Stensgaard, I. Submonolayer growth of Pd on Cu(111) studied by scanning tunneling microscopy. *Surf. Sci.* **1998,** *408,* 43-56.

57. Nilekar, A. U.; Greeley, J.; Mavrikakis, M. A simple rule of thumb for diffusion on transition-metal surfaces. *Angew. Chem. In.t Ed.* **2006,** *45,* 7046-9.

58. Cortright, R. D.; Dumesic, J. A. Kinetics of heterogeneous catalytic reactions: Analysis of reaction schemes. *Adv. Catal.* **2001,** *46,* 161-264.

59. Dumesic, J. A.; Rudd, D. F.; Aparicio, L. M.; Rekoske, J. E.; Treviño, A. A. The Microkinetics of Heterogeneous Catalysis (ACS Professional Reference Book). **1993**.